Influence of Load Frequency and Fiber Orientation on the Fatigue Behavior of Short Glass Fiber-Reinforced Thermoplastics

Einfluss der Beanspruchungsfrequenz und der Faserorientierung auf das Ermüdungsverhalten kurzglasfaserverstärkter Thermoplaste

Von der Fakultät für Maschinenwesen
der Rheinisch-Westfälischen Technischen Hochschule Aachen
zur Erlangung des akademischen Grades eines Doktors
der Ingenieurwissenschaften genehmigte Dissertation

vorgelegt von

Hakan Çelik

Berichter: Universitätsprofessor Dr.-Ing. Christian Hopmann
Honorarprofessor Dr. rer. nat. Rudolf Stauber

Tag der mündlichen Prüfung: 26.05.2025

Diese Dissertation ist auf den Internetseiten der Universitätsbibliothek online verfügbar.

Vorwort

Die vorliegende Arbeit entstand während meiner Tätigkeiten als wissenschaftlicher Mitarbeiter und Abteilungsleiter am Institut für Kunststoffverarbeitung (IKV) an der Rheinisch-Westfälischen Technischen Hochschule Aachen in den Jahren 2017 bis 2024.

Mein besonderer Dank gilt Herrn Prof. Dr.-Ing. Christian Hopmann für das entgegengebrachte Vertrauen, die mir gewährten Freiräume für meine Forschungen und die Möglichkeit, in einer so tollen Forschungseinrichtung wie dem IKV, einer „Spielwiese“ für Kunststofftechniker, arbeiten zu dürfen. Erst dadurch wurde die Durchführung dieser Arbeit ermöglicht. Ebenso möchte ich mich bei Hon.-Prof. Dr. rer. nat. Rudolf Stauber für die Übernahme des Koreferats und bei Univ.-Prof. Dr.-Ing. Uwe Reisgen für den Prüfungsvorsitz bedanken.

Danken möchte ich auch allen Kolleginnen, Kollegen, Mitarbeiterinnen und Mitarbeitern des IKV, die während meiner Tätigkeit am Institut durch ihren Einsatz direkt oder indirekt zum Entstehen dieser Arbeit beigetragen haben. Den Kolleginnen und Kollegen der Abteilung Strukturberechnung und Werkstofftechnik, besser bekannt als „Bunker“, danke ich in besonderem Maße für das äußerst angenehme Arbeitsklima, die große Hilfsbereitschaft und die kreativen Kaffeepausen, die uns immer wieder fachlich, aber auch freundschaftlich zusammengebracht haben. Mein besonderer Dank geht an Johannes Marder, Richard Frohberg, Noah Mentges, Christoph Zimmermann, Simon Wurzbacher, Maiko Ersch, Suveni Kreimeier, Prof. Dr. rer. nat. Rainer Dahlmann und Nuno Correia. Danken möchte ich ebenfalls meinem Vorgänger Pascal Brandt, der mir spannende Projekte hinterlassen hat, die die Grundlage für diese Arbeit bilden.

Ebenfalls gilt mein außerordentlicher Dank den StuWi-Arbeitenden sowie den studentischen Hilfskräften meiner Arbeitsgruppe. Ohne sie wäre diese Arbeit weder möglich noch eine Freude gewesen. Ein großes Dankeschön an das gesamte Team mit Felix Arand, Anton Baker, Marco Baumann, Darius Blatton, Alexander Breitenstein-Attach, Daniel Fritsche, Emil Gladik, Timur Gönül, Edwin Gordes, Vera Hauser, Sandra Heymann, Moritz Kuster, Marie Langner, Luiz Lise, Noah Mentges, Minh Phong, Henry Poppe, Roman Schmohl, Jonas Siegberg, Deniz Sönmez, Anton Stefer, Jacqueline Steinhauer, Raphael Stoppok, Fabian Wilhelm und Felix Zimmermann für den unermüdlichen Einsatz und den unzähligen Stunden an Prüfmaschinen, CAD-Konstruktionen und Simulationsrechnern.

Ein besonderer Dank gilt meinen Eltern und meinen Geschwistern, die mir meinen Werdegang erst ermöglicht und mich auf dem gesamten Weg zu jeder Zeit unterstützt haben. Ein letzter und ausdrücklicher Dank gilt meiner wundervollen Frau Melissa und meiner bezaubernden Tochter Alara für ihre immerwährende, liebevolle Unterstützung und die Zeit, die sie mir für diese Arbeit zur Verfügung gestellt haben. You two are my greatest treasures!

Aachen, im September 2024 *Hakan Çelik*

Soru sormasını bilen insan yetiştirecek bir eğitim gerekiyor…

Oktay Sinanoğlu

Die in dieser Arbeit vorgestellten Untersuchungen wurden zu einem Teil durch öffentliche Mittel im Rahmen der Vorhaben 19419 N und 20556 N durch die Forschungsvereinigung Kunststoffverarbeitung über die AiF im Rahmen der Industrielle Gemeinschaftsforschung und -entwicklung (IGF) durch das Bundesministerium für Wirtschaft und Klimaschutz (BMWK) aufgrund eines Beschlusses des Deutschen Bundestages und von der Deutschen Forschungsgemeinschaft (DFG) im Vorhaben mit der Projektnummer 495573874 (HO 4776/82-1) finanziell gefördert. Ihnen gilt unser ausdrücklicher Dank!

1 ABSTRACT 1

2 SUMMARY 2

3 ZUSAMMENFASSUNG 3

4 INTRODUCTION 4

4.1 Definition of the scientific question 5
4.2 Objectives and methodological approach 7

5 FUNDAMENTALS OF SHORT FIBER-REINFORCED THERMOPLASTICS 9

5.1 Multiscale material morphology of short fiber-reinforced thermoplastics 9
5.2 Micro-mechanical damage progression induced by dynamic-cyclic loads 11
5.3 Characterization of the macroscopic and anisotropic fatigue behavior 13

6 CHARACTERIZING THE FREQUENCY-DEPENDENT FATIGUE BEHAVIOR 15

6.1 Effects on the fatigue characterization procedure to enable the investigation of the frequency effect through experimental testing 17
6.2 Revision of the testing machine and the development of the peripheral equipment 23
6.3 Manufacturing and preparation of test specimens for the fatigue investigations 31

7 LOAD AND FREQUENCY INDUCED TEMPERATURE INFLUENCE ON THE FATIGUE BEHAVIOR 36

7.1 Characterization of the fatigue life of PBT-GF30 under varying frequencies 39
7.2 Experimental evaluation of the temperature development during dynamic-cyclic loading under varying frequencies 43
7.3 Quantitative analysis of the temperature development due to dynamic-cyclic load 49
7.4 Preliminary conclusion regarding frequency-dependent fatigue and resulting temperature development 63

8 QUASI-STATIONARY ISOTHERMAL FATIGUE CHARACTERIZATION 65

8.1 Development of a thermo-adaptive cooling system for enabling quasi-stationary isothermal material characterization under dynamic-cyclic load application 66
8.2 Verification of the homogeneous temperature distribution within the specimen during quasi-stationary isothermal material characterization 71
8.3 Load and frequency-dependent material characterization applying extended dynamic mechanical analysis (EDMA) 74
8.4 Conclusion on the thermo-adaptive test methodology for quasi-stationary isothermal material characterization and dynamic-cyclic material behavior of PBT 85

9 DESCRIPTION OF THE FREQUENCY-DEPENDENT FATIGUE LIFE 86

9.1 Characterization of frequency-dependent fatigue behavior under isothermal conditions 87
9.2 Derivation of a phenomenological model for the frequency-dependent shift in describing and predicting cyclic fatigue life.....92
9.3 Accelerated fatigue life characterization of short fiber-reinforced thermoplastics.....99
9.4 Conclusion on the isothermal characterization and the phenomenological modeling of the frequency-dependent fatigue life.....100

10 NOVEL METHODOLOGY FOR MANUFACTURING SPECIMENS WITH UNIFORM AND HIGH FIBER ORIENTATION 103

10.1 Formation of fiber orientation distributions in injection molding.....106
10.2 Conceptual process design and mold development for uniform and high fiber orientation.....115
10.3 Numerical analysis for the determination of the process parameters to manufacture specimen plates with uniform and highly oriented fiber orientation.....118
10.4 Experimental validation of the open-end injection molding process 125
10.5 Conclusion on the developed novel injection molding process for specimen plates with uniform and high fiber orientation.....134

11 INFLUENCE OF FIBER ORIENTATION DISTRIBUTION ON THE FATIGUE BEHAVIOR 136

11.1 Isothermal fatigue characterization of specimens with uniform and high fiber orientation across the thickness.....136
11.2 Influence of fiber orientation state on the cyclic fatigue performance 141
11.3 Fractographic analysis for understanding fatigue damage progression and the influence of creep 145
11.4 Conclusions on the fiber orientation distribution and its impact on cyclic fatigue behavior.....150

12 CONCLUSIONS AND OUTLOOK..... 151

13 ABBREVIATIONS, SYMBOLS, INDICES..... 154

13.1 Abbreviations.....154
13.2 Symbols 155
13.3 Indices.....157

14 LITERATURE..... 159

15 APPENDIX 169

15.1 Processing parameters for specimen plate production 169
15.2 Thermodynamic framework for thermo-mechanical interactions during dynamic-cyclic loading 169

1 ABSTRACT

The mechanical behavior of short fiber-reinforced thermoplastics is complex due to their heterogeneous structure and the viscoelastic properties of the matrix. Understanding fatigue under dynamic-cyclic loads is challenging since damage occurs across multiple material scales, which is why the effects of load, temperature, and frequency are difficult to quantify. For this reason, methods are being developed in this thesis that will allow the material behavior and damage mechanisms to be investigated at the macro level individually, without interaction. A thermo-adaptive methodology has been developed to suppress self-heating at high frequencies, allowing isothermal characterization. In addition, a new injection molding process has been developed that enables the production of uniform, highly oriented specimens, whereby the influence of the orientation of the meso-behavior can be examined in macroscopic tests. It was found that, under isothermal conditions, the tolerable load cycles increase with frequency and converge at high frequencies. It can, therefore, be assumed that there is a material-dependent upper limit for the solely cyclic fatigue life.

2 SUMMARY

The mechanical behavior of short glass fiber-reinforced thermoplastics is complex due to their process-dependent, heterogeneous material structure, characterized not only by fiber mass content and length distribution but also by fiber orientation and a matrix exhibiting time- and temperature-dependent viscoelastic properties. Under dynamic-cyclic loads, interactions and damage progression occur across all material scales, making it significantly challenging to achieve a comprehensive understanding of the fatigue behavior. While the primary influencing factors (load, temperature, and frequency) are known, their exact impact on the fatigue is challenging to quantify. Load frequency, in particular, plays a critical role by linking applied load cycles to load duration and determining the material's hysteretic self-heating behavior.

To improve the understanding of damage processes, direction-dependent fatigue tests were conducted across a frequency range of 2 Hz to 90 Hz using specimens extracted from injection molded plates. In addition to fatigue life, the temperature evolution was experimentally and quantitatively investigated. The fatigue behavior is superimposed by the thermal response of the material, with two regimes identified: one showing the progressive temperature increase due to hysteretic self-heating and another with stabilized temperature.

Given that temperature changes significantly influence mechanical behavior and damage mechanisms, thereby complicating the investigation of fatigue processes, a thermo-adaptive testing methodology was developed to suppress self-heating, enabling characterization under quasi-isothermal conditions. This approach revealed that, although the loss energy per cycle decreases with increasing frequency, the loss power rises with frequency, leading to self-heating under conventional thermal boundary conditions. Fatigue tests performed with this new method demonstrated that, under isothermal conditions, the material's cyclic lifespan increases with frequency and appears to converge at higher frequencies. A phenomenological frequency shift function was derived to quantitatively describe this behavior, introducing a solely cyclic intrinsic fatigue life unaffected by creep. Additionally, a methodology was presented that reduces the test duration from 25 days to 5 compared to classical industry-standard fatigue tests.

Since the damage mechanisms largely depend on the multiscale and heterogeneous material structure, and the fiber orientation distribution across the thickness does not allow for definitive conclusions regarding orientation dependence, a new injection molding process was developed. This process enables the production of specimen plates with a uniform and high fiber orientation across the thickness, eliminating the typical layered structure. Isothermal fatigue tests were also conducted on these specimens at different frequencies, clearly demonstrating that fatigue strength does not scale with the degree of orientation as it does with quasi-static strength, indicating differing damage mechanisms between quasi-static and fatigue load.

3 ZUSAMMENFASSUNG

Das mechanische Verhalten kurzglasfaserverstärkter Thermoplaste ist aufgrund der verarbeitungsbedingten heterogenen Werkstoffstruktur und der zeit- und temperaturabhängigen viskoelastischen Eigenschaften der Matrix komplex. Insbesondere die Beanspruchungsfrequenz spielt dabei eine kritische Rolle, da sie die aufgebrachten Lastzyklen mit der Beanspruchungsdauer verknüpft und maßgeblich zur Eigenerwärmung betragen kann.

Im Rahmen der vorliegenden Untersuchungen wurde das frequenz- und orientierungsabhängige Ermüdungsverhalten von Proben, welche aus spritzgegossenen Platten entnommen wurden, in einem Frequenzbereich von 2 Hz bis 90 Hz mittels Schwingversuchen analysiert. Die durchgeführten Untersuchungen haben verdeutlicht, dass das frequenzabhängige Ermüdungsverhalten ebenfalls von thermischen Wechselwirkungen im Werkstoff beeinflusst wird.

Aufgrund des signifikanten Einflusses von Temperaturänderungen auf die Schädigungsmechanismen und der daraus resultierenden Herausforderung, einzelne Schädigungsmechanismen wechselwirkungsfrei untersuchen zu können, wurde eine neue thermoadaptive Prüfmethodik entwickelt, die eine Charakterisierung unter quasi-isothermen Bedingungen ermöglicht, indem die Eigenerwärmung gezielt unterdrückt wird. Mit dieser Methode konnte gezeigt werden, dass die Verlustleistung mit der Frequenz zunimmt, obwohl die Verlustenergie pro Zyklus mit steigender Frequenz abnimmt. Darüber hinaus haben Ermüdungsversuche mit dieser neuen Methode ergeben, dass unter isothermen Bedingungen die zyklische Lebensdauer des Werkstoffs mit steigender Frequenz zunimmt und sich bei höheren Frequenzen einem Grenzwert nähert. Eine phänomenologische Frequenzverschiebungsfunktion wurde hergeleitet, um dieses Verhalten quantitativ zu beschreiben. Des Weiteren wurde eine rein zyklische intrinsische Ermüdungslebensdauer eingeführt, die nicht von Kriechprozessen beeinflusst wird. Mit der thermo-adaptiven Prüfmethodik kann ebenfalls die Prüfdauer im Vergleich zu klassischen industrieüblichen Ermüdungsprüfungen von ca. 25 Tagen auf 5 Tage reduziert werden.

Des Weiteren wurde ein neues Spritzgießverfahren entwickelt, das die Herstellung von Probenplatten mit einer gleichmäßigen und hohen Faserorientierung über die gesamte Dicke ermöglicht. An diesen hochorientierten Proben wurden ebenfalls isotherme Ermüdungsversuche bei verschiedenen Frequenzen durchgeführt, die eindeutig zeigen, dass die Ermüdungsfestigkeit nicht wie die quasistatische Festigkeit mit dem Grad der Orientierung skaliert, was auf unterschiedlich ablaufenden Schädigungsmechanismen zwischen quasistatischer und Ermüdungs-beanspruchung hinweist.

4 INTRODUCTION

Short fiber-reinforced thermoplastics (SFRT) are widely used as engineering materials for semi-structural applications in technical components due to their good weight-specific properties, potential for functional and component integration, and cost-effective manufacturing through injection molding. When designing such injection molded structural components, two factors must be considered: the local stress and deformation behavior under diverse applied load and displacement boundary conditions and the appropriate dimensioning framework for evaluating the induced stress or strain states at the material level.

Regardless of the process-dependent heterogeneous material morphology and the resulting complex interactions among constituents due to multi-scale characteristics, the anisotropic deformation behavior can be predicted through integrative methodologies that combine injection molding simulations with homogenization techniques within mechanical analyses [Bra06, Haa18, HS20, Tuc22]. The resulting local stress state must be evaluated depending on the application boundary conditions against appropriate dimensioning parameters. In addition to traditional stress-based dimensioning using strength data, alternative methodologies for dimensioning based on strain exist, with different advantages and disadvantages. Nevertheless, for quasi-static and long-term load conditions, sufficiently accurate methods have been developed and are now considered as solved at a level sufficient for component dimensioning [Bra06, Dil19, Haa18, Kai13, SSK18].

However, when a component is subjected to complex dynamic-cyclic loads, a design verification for operational load conditions is necessary before its field deployment. Currently, this verification is typically conducted in the later stages of the development process through expensive component testing. Although the fatigue properties of SFRT materials can be characterized through mechanical testing, these tests are time-consuming and costly. In addition, due to the complex material structure and viscoelastic properties, it is challenging to interpret and extrapolate the obtained fatigue data to other load scenarios. Furthermore, the actual load-case scenarios include fluctuating thermo-mechanical loads that cannot be adequately represented by material tests conducted under constant load conditions [Hai06]. Translating these load scenarios into load collectives and appropriately taking into account in damage accumulation hypotheses remains unfeasible in a material-appropriate manner [DJB+09, Har77, HÇ21, HMB11]. This is due to the incomplete understanding of the fatigue mechanisms of SFRT, which arises not only from the complex material structure but also from the lack of comprehensive methods to fully isolate and analyze single damage mechanisms at different scales [BDB+07, Gün13, Kan15, KSO+18, Len16, PKE+20a, SDH+14, SZS15].

Hence, there is a knowledge gap in understanding the fatigue behavior of SFRT materials, which this work seeks to address.

4.1 Definition of the scientific question

The mechanical behavior of short fiber-reinforced thermoplastics under dynamic-cyclic load is governed by both the intrinsic properties of individual constituents and the micro-mechanical configuration of the composite material (see Fig. 4.1) [FHY99, MMQ10, Sch17]. The flow conditions induced while injection molding and geometric design of the component result in spatially heterogeneous fiber orientation distributions (FOD) characterized by bidirectional layered structures along the thickness direction. This leads to pronounced meso- and macroscopic anisotropy within the material [Bau17, KLC+20, PG21b, Tuc22]. Although computational methodologies for predicting resultant fiber orientations have advanced significantly [CK02, TCH17, Tuc22], the inherent complexity and variability of micro-mechanical interactions persist, particularly under dynamic-cyclic load conditions.

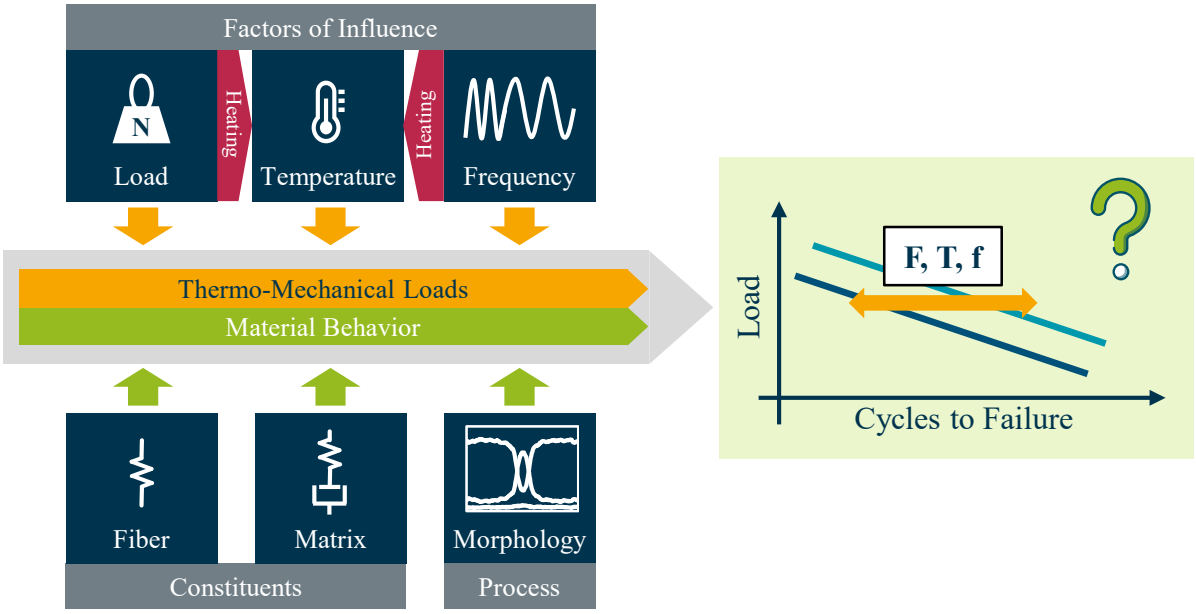

Fig. 4.1: Effects of thermo-mechanical loads (stress, frequency, and temperature) and material characteristics (morphology and constituents) on the fatigue life of short fiber-reinforced thermoplastics.

This complexity is further increased by the time- and temperature-dependent behavior of the thermoplastic matrix, which plays a critical role in the mechanisms of damage accumulation and progression [Gün13, PMP+11, RSL+16, RSR+18]. Micro-structural damage evolution is manifested through the gradual reduction of the dynamic stiffness and the increase in dissipated energy per load cycle at the macroscopic scale [BCR14b, BK09, SML+20]. However, accurately describing the concurrently or sequentially occurring damage mechanisms and deriving universally applicable constitutive relationships for material-specific fatigue

prediction remains an unresolved challenge. Specifically, the non-uniform fiber orientation across the thickness induces complex local stress states during micro-mechanical damage initiation and propagation, making precise characterization and transfer to other micro-configurations regarding the fiber orientation difficult [Gün13, KMA+21, Len16, NLB15, Son04]. Furthermore, the bidirectional connection between micro-level and macroscopic material behavior continues to be a significant challenge.

In addition to the inherent material properties, the load type has a substantial influence on the fatigue life of the material (compare Figure 4.1). When short fiber-reinforced thermoplastics are subjected to stresses approaching their quasi-static strength, the material undergoes plastic flow, and the primary damage mechanism remains plasticity-dominated despite the oscillatory load conditions. To differentiate between fracture and plastic flow under dynamic-cyclic loading, a static long-term test at an equivalent high load can be employed [KKG16, PG21b]. The critical parameter is the time to failure, which signifies material flow. If a dynamic-cyclic load results in an extended time to failure, the dominant failure mechanism is characterized by plastic flow, as the load duration is the primary driving factor. Conversely, when the time to failure determined in the oscillatory test falls below the maximum loading duration achievable in the long-term test, damage due to fracture becomes more dominant [KKG16].

Cyclic damage progression resulting from dynamic-cyclic loads is also influenced by the creep behavior of the thermoplastic matrix once the load deviates from purely alternating stresses [MFM+15, PG21a]. Fatigue tests conducted under varying load ratios and loading frequencies have demonstrated that crack propagation is qualitatively associated with the applied number of load cycles, while creep is related to the load duration [KKG16, MFM+15, PG21a]. The applied frequency connects the number of load cycles and the load duration.

Additionally, it is important to consider that the viscoelastic properties of the matrix result in the dissipation of a fraction of the applied kinetic energy as thermal energy due to internal friction at the molecular level and internal crack surfaces with each applied load cycle [AML+13, BCR14b, Chr12]. Since plastics exhibit lower thermal conductivity compared to other materials, the generated thermal energy can accumulate within the material, leading to self-heating. As a consequence of sustained material stressing and the associated temperature increase of the material, thermally induced flow occurs. The magnitude and frequency of the applied load directly influence the dissipated power [BK09, Chr12].

As a result, all these parameters interact with each other, which significantly complicates the precise characterization and understanding of the underlying fatigue mechanisms and the prediction of cyclic lifetime (compare Figure 4.1). However, the load frequency has a particularly important role, as it controls both competing effects of dynamic-cyclic load

application and the load duration, which is why it can be used to gain a better understanding of fatigue behavior for SFRT materials for tensile-tensile load cases.

4.2 Objectives and methodological approach

The aim of this thesis is to investigate and quantify the influence of the frequency on the fatigue behavior of short fiber-reinforced thermoplastics under load-controlled tensile-tensile states depending on the prevailing fiber orientations and to understand the effects of creep and dynamic-cyclic loads on the achievable fatigue life.

This work examines an industrial-grade polybutylene terephthalate reinforced with 30 wt.% glass fibers (PBT-GF30). However, the primary objective is to develop universally applicable methodologies that can be applied to other fiber-reinforced thermoplastics grades.

The thesis is structured as follows:

In the first step, the temperature evolution as a function of load frequency is examined in fatigue characterization experiments similar to those conducted in the industry to assess the dynamic-cyclic strength for the dimensioning of technical components. The fatigue tests are performed within a frequency range of 2 Hz to 90 Hz, with the temperature development due to hysteretic self-heating in the specimens being measured and correlated with the resulting fatigue life to evaluate its effect on fatigue behavior. The experiments are conducted on specimens extracted from injection-molded plates, oriented longitudinally and transversally to the melt flow direction.

To investigate the influence of load frequency on the material and fatigue behavior without the effect of self-heating, a novel thermo-adaptive test methodology is developed. This methodology ensures that the specimen maintains a constant temperature throughout the entire test duration, regardless of the applied load, frequency, or damage-induced change of the hysteresis behavior. By applying this approach, the dynamic-cyclic deformation behavior is investigated dependent on load, frequency, and temperature to assess whether it undergoes significant changes across the tested frequency range and to determine whether the micro-mechanical stress state, as the driving force for damage progression and material fatigue, remains constant within the frequency range, or if the frequency leads to an identifiable influence due to strain-rate dependent material behavior. Subsequently, isothermal fatigue tests are conducted to investigate the impact of load frequency while eliminating the effects of self-heating, ensuring consistent viscoelastic material behavior and damage mechanisms unaltered by any temperature changes.

The damage progression is influenced by interactions within the process-induced material morphology, particularly due to the varying fiber orientation across the thickness. To address

this, a novel injection molding methodology is developed, enabling the production of specimen plates with a uniform and highly oriented fiber orientation distribution (UH-FOD) throughout the thickness. This approach allows for an interaction-free investigation of the orientation-dependent meso-mechanical behavior of SFRT materials through macroscopic experiments.

With these UH-FOD specimens, isothermal fatigue tests are conducted to investigate the frequency-dependent fatigue life solely as a function of the meso-level orientation state at a material temperature of 23 °C in longitudinal and transversal direction, and the results are compared with previously obtained data and insights using specimens with conventional fiber orientation distributions.

The outcome of these investigations provides fundamental methods for independently characterizing and analyzing the complex mechanical interactions within SFRT materials. This enables a detailed study and deeper understanding of the material fatigue and its individual mechanisms at the meso-scale using macroscopic experimental techniques. Additionally, the influence of load frequency is quantified, and the effects of cyclic and creep-driven fatigue mechanisms are examined and modeled phenomenologically.

5 FUNDAMENTALS OF SHORT FIBER-REINFORCED THERMOPLASTICS

In this chapter, the mechanical properties of short fiber-reinforced thermoplastics are discussed, with an emphasis on their multiscale structure and the damage mechanisms that contribute to failure under dynamic-cyclic loading conditions.

5.1 Multiscale material morphology of short fiber-reinforced thermoplastics

Short fiber-reinforced thermoplastics are characterized by their heterogeneous, multiscale material structure. The material behavior, including deformation and mechanical degradation, is largely dependent on the interaction of individual constituents at the micro-level, as well as the resulting interactions at the meso- and macro-levels (compare Figure 5.1). By understanding these scale-spanning interactions, the mechanical properties of SFRPs can be adjusted to meet specific application requirements.

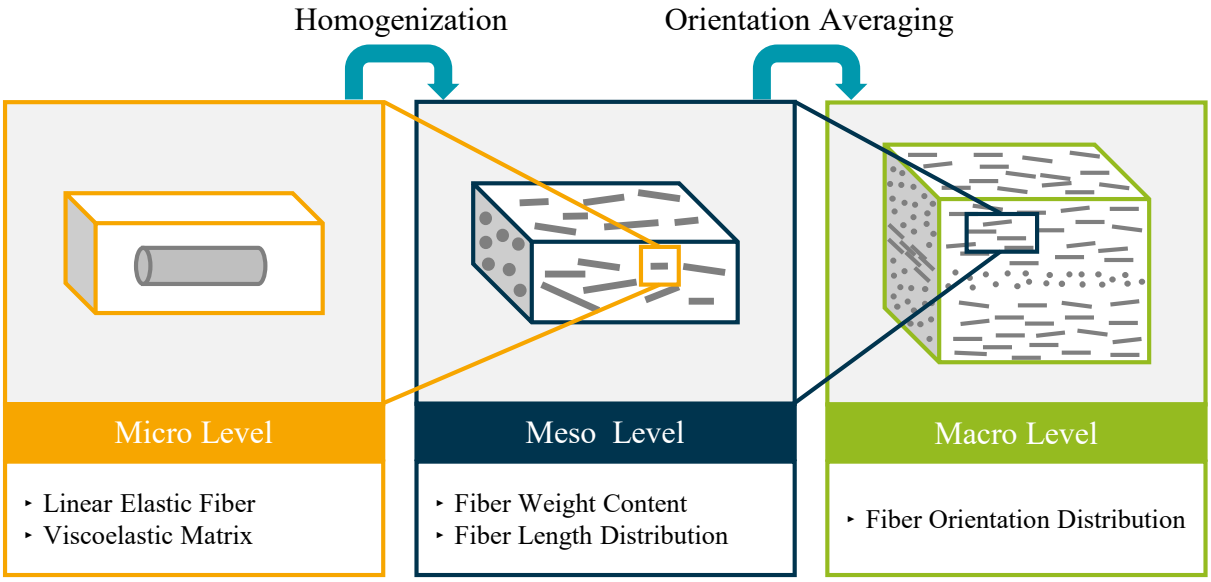

Fig. 5.1: Heterogeneous, multi-scale morphology of injection molded short fiber-reinforced thermoplastics.

At the micro-level, the behavior is mainly governed by the fiber and matrix properties. The behavior of the glass fibers, which are typically the primary reinforcement, can be approximated by ideal elastic deformation while neglecting temperature effects on the properties [Sch07]. Although the tensile strength of glass fibers is significantly higher than that of the thermoplastic matrix, the fibers in the compound do not reach their strength limits. This is due to the mechanical load transfer between the matrix and the fibers through shear stresses, which requires a certain fiber length. The average fiber length in the compound is below 1 mm [FLM19, MO12, Tuc22]. Nevertheless, the resulting mechanical properties of the compound

primarily result from the thermo-mechanical viscoelastic deformation behavior of the thermoplastic matrix and its interaction with the fibers [Bra06, Dil19, Haa18].

However, it is important to consider that the material constitution and polymer morphology of the thermoplastic matrix are also a function of the injection molding process. Accordingly, the melt flow and the cooling rate influence the orientation of polymer chains and the resulting degree of crystallinity in semi-crystalline matrices [DHM22, MO12]. Additionally, the fibers themselves act as nucleation points within the matrix, leading to the formation of a trans-crystalline zone around the fibers, where crystals grow perpendicular to the fiber surface [Sch17, SZS15]. Consequently, the matrix behaves differently in the immediate vicinity of the fibers compared to the bulk matrix areas. Furthermore, the process and mechanical properties can be modified using additives. Thus, the injection molding process significantly affects also the state and the properties of the thermoplastic matrix material.

On the next higher scale, the meso-level, the fiber weight content (FWC) and the fiber length distribution (FLD) significantly influence the resulting homogenized properties from micro-mechanics. The fiber content is set gravimetrically during compounding. However, fiber-matrix separation can occur during cavity filling, leading to local variations in fiber content, particularly in long fiber-reinforced thermoplastics [GO18]. The injection molding process induces high shear stresses, especially during the plastification of the compound due to interactions between the plastification screw and the melt, causing fiber length reduction resulting in a fiber length distribution [PAK+13, Tuc22]. On the mesoscopic scale, it can be assumed that most of the fibers are aligned in one direction, leading to the mechanical properties being characterized by transversely isotropic behavior [Sch07, SSK18].

On the macroscopic scale, the material properties are significantly influenced by the fiber orientation distribution. Injection molding typically results in a characteristic fiber orientation distribution across the thickness, consisting of seven distinct layers, with three of these layers occupying the largest fraction of the cross-section [MO12, Tuc22]. Thereby, two thin outer layers exhibit a randomly arranged in-plane fiber orientation distribution. Adjacent to these outer layers are two thicker layers, primarily oriented in the main flow direction of the melt during cavity filling. This orientation significantly contributes to the mechanical properties regarding the stiffness and strength of the compound material. Moving inward, there are two thin transition layers where the fiber orientation gradually changes direction as it approaches the core layer. At the core, the fiber orientation is primarily transverse to the main flow direction of the melt [Tuc22]. Due to fiber-fiber interactions during mold-cavity filling, some fibers may also exhibit random orientation throughout the material thickness. The mechanisms responsible for the development of the distinct fiber orientation distribution during injection molding are discussed in detail in Chapter 10.

Given the complex heterogeneous material structure, various material configurations that affect the anisotropic stiffness and strength properties must be taken into account during component dimensioning. In recent years, numerous methods have been developed for modeling the anisotropic deformation behavior accurately using integrative simulation chains to link both process and structural mechanics [Bra06, Dil19, Haa18, HS20]. These methods commonly use a two-step approach to represent the complex material morphology. Micro-mechanical approaches can be applied to homogenize the matrix and stiffness properties depending on the micro-scale configuration to derive the resulting meso-scale properties [Bra06, SSK18, Tuc22]. These meso-scale properties exhibit transversely isotropic behavior. In a subsequent step, orientation averaging at the macroscopic level forms the fiber orientation distribution across the material thickness [AT87]. The local fiber orientation distribution can be calculated numerically for each component using injection molding simulations.

When subjected to loads, the heterogeneous material structure of short fiber-reinforced thermoplastics undergoes interactions across all relevant scales. Even under the application of homogeneous and constant external loads, a complex stress state is induced within the material at the micro-mechanical level. Time-dependent mechanisms within the viscoelastic matrix become activated, resulting in localized relaxation and retardation phenomena [Haa18]. Under high load intensities or, for example, dynamic-cyclic loading conditions, additional fracture events are initiated primarily at the micro-level, thereby influencing the material behavior on all three micro-, meso- and macroscopic scales.

5.2 Micro-mechanical damage progression induced by dynamic-cyclic loads

Induced by dynamic-cyclic loads, progressive damage initiation and accumulation occur, which can result in the failure of the SFRT composite even under external loads below its quasi-static strength. Depending on the load conditions concerning load magnitude, frequency, and ambient temperature, the material can withstand varying numbers of load cycles. In isotropic materials, it has been observed that after damage initiation in the form of micro-crack formation, each subsequent load cycle contributes to crack propagation, progressively reducing the load-bearing cross-section. Upon reaching a critical crack length, the structural cohesion of the material is compromised, and the applied stress induces abrupt crack growth, ultimately leading to macroscopic failure [GS11]. The damage process itself can be approximated using Linear Elastic Fracture Mechanics (LEFM), for instance. A fundamental assumption of LEFM is that far-field loads induce a stress singularity at the crack front [GS11, Mur12]. Although stress reduction occurs due to plasticity or viscoelasticity, this phenomenon is neglected in the brittle fracture theory of LEFM. The intensity of the crack tip stress fields is characterized by stress intensity factors K. When the material-specific fracture toughness K_C is exceeded, crack

propagation continues. The various and multi-axial load conditions can be comprehensively described by combining the fundamental fracture modes (I, II, and III) [GS11, Mur12].

Under dynamic-cyclic load conditions, fatigue crack growth can be initiated even below the critical stress intensity thresholds. This phenomenon arises from complex inelastic processes occurring directly within the crack process zone, whereby rapid, repetitive loads induce fluctuating residual stress fields and result in material degradation with each cycle, characterized by the crack growth rate. Consequently, a cyclic stress intensity factor ΔK is defined for periodic loading scenarios. The crack growth rate can thus be empirically described using *Paris* law [GS11, Gün13]. Building upon LEFM, additional frameworks such as elastoplastic fracture mechanics and creep fracture mechanics have been developed to more accurately account for material behavior beyond the linear elastic regime [Mur12].

However, due to the heterogeneous material structure, the fatigue behavior of fiber-reinforced plastics significantly differs from that of isotropic materials with nearly homogeneous morphologies. The reinforcing fibers distributed within the matrix can act as barriers to propagating cracks, necessitating a differentiated examination of crack growth behavior and the accompanying damage development [Len16, RSL+16, RSR+18]. Fatigue loads induce the formation of numerous individual micro-cracks at the fiber ends and debondings along the fiber/matrix interface, which do not immediately lead to macroscopic failure [LMN09, RSR+18]. Instead, each micro-crack results in a localized reduction in stiffness, prompting continuous stress redistribution at the micro-mechanical material level [LMN09]. Through the accumulation of damage, cracks coalesce under the applied load until the undamaged material portion can no longer bear the applied load, leading to failure [KKS+91, RSR+18].

The fiber/matrix interface in short fiber-reinforced thermoplastics results in three fundamentally distinct failure modes at the micro-scale (compare Figure 5.2) [Sch11]. The fiber/matrix boundary constitutes the most significant weak point in the composite material, as load transfer to the fibers occurs through the interface driven by the stiffness difference of the phases [FM15, LMH87, RSR+18, Sch11]. Interface failure leads to partial fiber debonding or complete separation through fiber pull-out. Characterizing the interfacial properties, particularly determining the shear strength at the interface, poses a considerable challenge. Various testing methods have been employed for thermosetting plastics [SVG16], such as single fiber fragmentation [ZT00], micro-droplet testing [GGJ+15], and single fiber pull-out [PB81]. Additionally, the crack growth rate at the fiber/matrix interface has been measured using single fiber test specimens under dynamic-cyclic loads [PGB+13]. Pure matrix failure can also occur, characterized by crazing and shear bands [Gus09, LMH87, LMN09, Sch11]. Matrix stressing is more pronounced at the micro-scale due to the limited free matrix length between fibers, resulting in high local strains under stress. As the fiber weight fraction

increases, the free matrix length at the micro-scale decreases. The third micro-mechanical failure mode is fiber breakage, which is the most desirable yet least frequent of the micro-mechanical failure mechanisms [Sch07, Sch11].

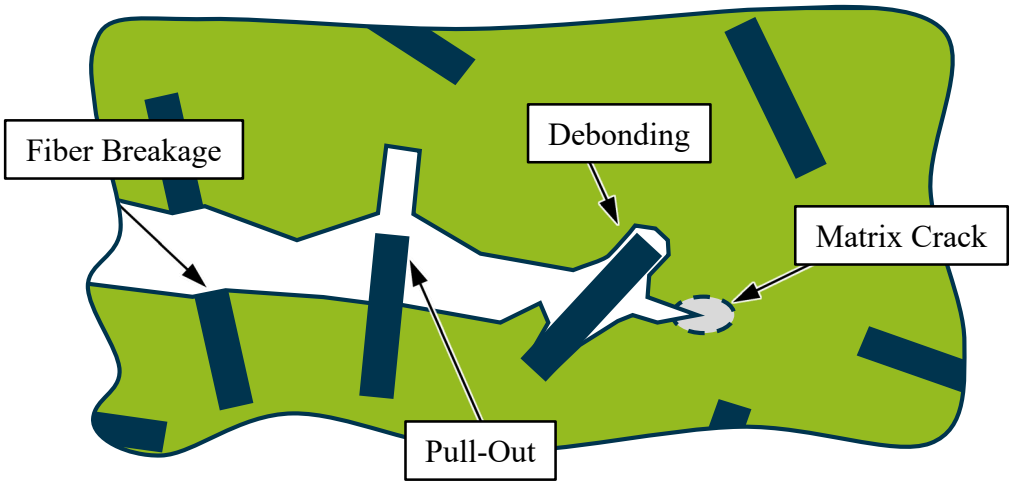

Fig. 5.2: Micro-mechanical failures within short fiber-reinforced thermoplastics [Sch11].

The prevailing damage mechanism is highly dependent on the load conditions and, in particular, on the orientation of the fibers. For instance, when the entire fatigue process is examined at the micro-scale for longitudinally oriented fibers, the progressive damage begins with the formation of micro-cracks at the fiber ends [LMN09, RSR+18, Sch11]. Due to the locally high stresses and the limited bonding area at the fiber tips, the material is first damaged at these points on the micro-scale. With each additional load cycle, crack growth progresses. The interaction of individual fibers at the micro-scale leads to matrix stretching [LMH87]. In the case of transversely oriented fibers, fiber/matrix debonding is the dominant mechanism, resulting in crack growth along the fibers. With continued loading, the cracks further propagate, reducing the load-bearing cross-section until the material fully yields. This damage process is also influenced by the phenomena in adjacent layer structures, as the SFRT caries the external loads at the macro-scopic level and the local load depends on the spatial stiffness distribution at the micro-mechanical level [RSR+18, Sch11]. However, investigating interactions of different fiber orientations, as it is conducted with continuous fiber-reinforced plastics, is hindered in short glass fiber-reinforced thermoplastics due to the lack of a quantitative description methodology of the interaction-free fiber-orientation dependent behavior. Although imaging techniques, as described in [RSR+18], can be integrated into the fatigue testing machine, the actual induced stress state at the micro-scale remains unknown.

5.3 Characterization of the macroscopic and anisotropic fatigue behavior

For the dimensioning process of components subjected to fatigue loads, the material behavior can be characterized through *Wöhler* tests, wherein standardized specimens are subjected to

defined and steady dynamic-cyclic loads to determine the number of cycles to failure [Hai06, HM80]. The fatigue life information of the material can be represented in stress versus cycles to failure diagrams, commonly referred to as an SN curve. The load conditions (load ratio, frequency, waveform, temperature, etc.) are maintained constant throughout the entire test. Depending on the application, characterization is conducted analogously to long-term tests in plastics (relaxation/retardation) and is performed either force-controlled or displacement-controlled [HM80, RV07]. Depending on the component requirements, specific criteria, such as not only specimen fracture but also a defined reduction in material stiffness or exceeding a specified material damping, can be selected as failure criteria [RV07].

To explicitly account for fiber orientation, the master-SN curve concept was developed for continuous fiber-reinforced plastics, enabling the generation of a fiber-orientation-independent SN curve and enabling practical fatigue assessment for component dimensioning [Kaw04]. This approach is based on the hypothesis that the influence of material configuration and, thus, anisotropy applies equally to both dynamic-cyclic and quasi-static load cases. Therefore, a dynamic stress factor is defined as the ratio between fatigue strength and quasi-static strength. This procedure is conducted for different material orientations. The resulting normalized stress/cycles tofailure curves are subsequently averaged, which leads to the master-SN curve. The local component stress level can be estimated using corresponding equipotential conditions and, hence, be evaluated using the master-SN curve. This approach has also been applied to short fiber-reinforced plastics. [BDB+07, HÇ21, SDB14+]. However, the issue remains that the entire fatigue process is reduced to a bearable number of cycles. Furthermore, the testing effort increases significantly because the material must be characterized quasi-statically and in *Wöhler* tests for different orientations.

Additional phenomenological damage models, such as residual strength or residual stiffness models, describe fatigue by equating the damage state with the reduction of material properties [DP01, PD02]. During material testing, hysteresis behavior can also be examined. With progressive damage, changes in dynamic stiffness and dissipated energy per load cycle become observable. Creep or relaxation effects of loading can be identified by the drift of the hysteresis loop in the stress-strain space [BK09]. There are approaches aiming to correlate dissipated energy with fatigue to estimate life (heat build-up) [JMS+13, SML+17].

However, the task of material-based description of parallel and successive damage mechanisms in short fiber-reinforced thermoplastics under fatigue loads is complex and remains a topic of ongoing research. The primary challenges arise from the inherent complexity of the material's micro-structure, the multiscale interactions, and the presence of multiple competing and superimposed damage mechanisms like cyclic crack growth or creep depending on the load states (stress, frequency, temperature, etc.)

6 CHARACTERIZING THE FREQUENCY-DEPENDENT FATIGUE BEHAVIOR

The purpose of this work is to understand the influence of test frequency on the fatigue process of technical thermoplastics, taking into account fiber orientation and determining the driving mechanisms that lead to material failure. However, investigating characteristics, properties, and the state of the material through experimental testing presents numerous challenges. For evaluating material responses, it is crucial to ensure that the tested specimen accurately reflects the intrinsic behavior of the investigated material. Nevertheless, the necessity of characterizing the material through a specimen that has undergone additional processing and preparation can already lead to discrepancies and deviations between the experimentally determined properties and the actual prevailing material properties in an injection molded component [Erik90, GS15]. Furthermore, it is important to recognize that the test conditions during the material characterization significantly impact the results. Due to the nature of fatigue testing, where cumulative damage is successively introduced to the material through a large number of mechanical load cycles, the test procedure and material response are highly sensitive to inconsistencies and variations. In addition, fatigue tests are time-consuming and costly, making it impractical to repeat tests without further ado in the event of any issues. Consequently, it is critical to identify and understand which influencing factors can negatively impact the experimental procedure, particularly if, as in this study, it is aimed to identify and understand the sensitivities and the impact of the material constitution and load frequencies on the fatigue process [GS15].

Therefore, before conducting experimental tests to investigate the frequency effect, the available testing equipment was thoroughly reviewed and redesigned, and the testing procedure was refined to ensure the reproducibility and reliability of the fatigue tests. The diagrams in Figure 6.1 present in advance the outcome of the revision of the test methodology. The improvements themselves are discussed in Chapter 6.2. The left diagram shows three SN datasets for the PBT-GF30 material tested in this work. The shown SN datasets were generated using two different servo-hydraulic testing machines: the Schenck VHF7 and the Schenck PCN, both from Instron Testing Systems GmbH, Darmstadt, Germany. For investigating the frequency effect on the fatigue behavior in this work, the VHF7 is chosen for its higher frequency range (compare Chapter 6.2). Therefore, a revision of the test methodology is conducted for this system. The test machine configuration before the revision is labeled "OC" for "Old Configuration" while the configuration after the improvements is labeled "NC" for "New Configuration". It should be noted that the tested specimens shown in Figure 6.1 come from two different production batches, which may result in variations in material morphology, such as fiber orientation distributions, thereby affecting the fatigue life. Since no conclusions are drawn about the behavior of the material at this point, a qualitative comparison is

nevertheless presented here. The specimens tested with the PCN and VHF7-OC originate from the same production batch. The specimens tested on the VHF7-NC were taken from the same specimen batch used to investigate the frequency effect in this work.

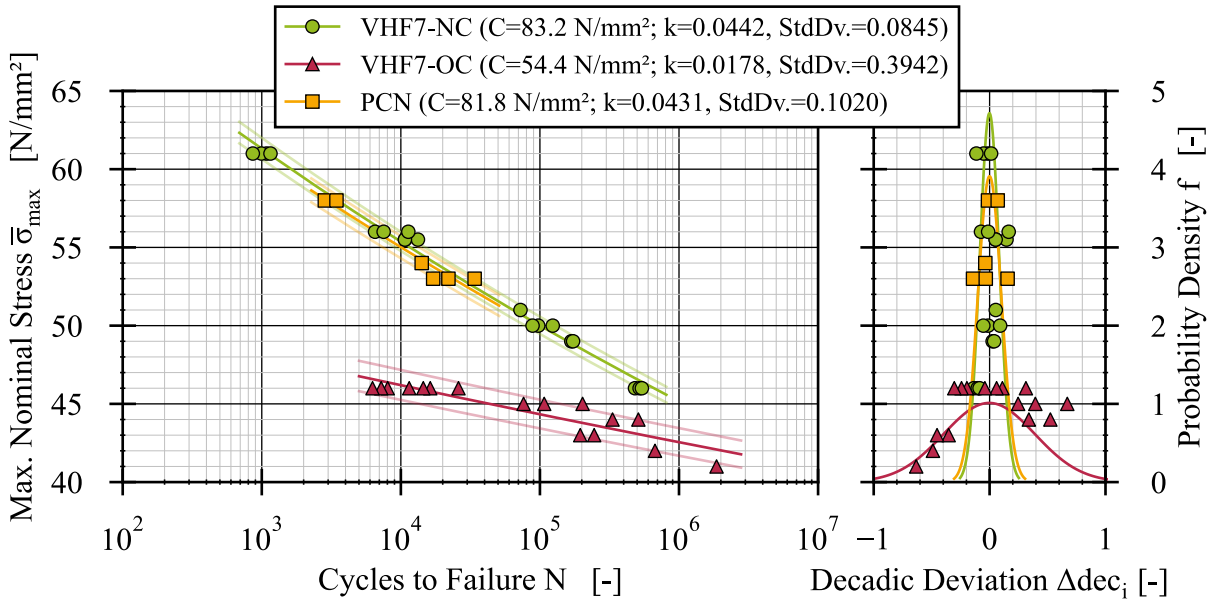

Fig. 6.1: Left: Experimentally determined SN datasets to compare different test setups. The tested material is a PBT-GF30 at a frequency of 5 Hz under transversal load. The lighter lines correspond to the 10th and 90th percentiles of each Basquin fit. Right: Statistical scattering of the decadic deviation of the determined cycles to failure.

Comparing the results of Figure 6.1, left, it is evident that the configuration and the different testing machines have an impact on the generated fatigue data. Firstly, the fatigue experiments with the testing machines VHF7-NC and PCN result in comparable fatigue limits, although it needs to be taken into account that only five experiments were conducted on the PCN testing machine. Both *Basquin* coefficients for the slope k and load level adjustment C of the SN datasets for VHF7-NC and PCN are very comparable. However, the fatigue results of the VHF7-OC deviate significantly from the other results. A comparison of the *Basquin* coefficients shows that both the slope k, and the load level factor C, are significantly decreased, indicating that the material appears to withstand a lower number of load cycles for the same stresses.

In addition, the resulting fatigue data of the VHF7-OC testing machine is highly scattered. To illustrate the deviation of the results, the achieved load cycles are statistically evaluated (compare Figure 6.1, right). To achieve this, the logarithm of the tested cycle to failure N_i for each specimen was calculated and then subtracted from the corresponding predicted fatigue life $N_p(\bar{\sigma}_{max,i})$ using the *Basquin* fit (compare Equation 6.1 and 6.2). This procedure enables the statistical comparison of all experimental data over the decadic deviation Δdec_i of each test within the scatter range, regardless of the tested load level and the achieved load cycles, since

the experimentally determined datasets are only shifted without losing or changing the statistical nature of the results.

$$\Delta dec_i = log(N_i) - log\left(N_p(\bar{\sigma}_{max,i})\right) \quad \textit{(Eq. 6.1)}$$

$$\Delta dec_i = log(N_i) - log\left(\left(\frac{\bar{\sigma}_{max,i}}{C}\right)^{-\frac{1}{k}}\right) \quad \textit{(Eq. 6.2)}$$

When comparing these results, it is evident that the decadic standard deviation of the determined SN dataset using VHF7-OC is approximately 4.66 times higher than the standard deviation of the other test setups. The maximum decadic deviation range, determined by the difference between the lowest and highest load cycle count, is at 1.30 for the VHF7-OC. This means that the bearable load cycles for a single tested stress level can deviate by a factor of approximately 20 ($10^{1.3} \approx 19.95$). Hence, with this setup, it is not expected that the frequency effect on the fatigue of short glass fiber-reinforced plastics can be adequately investigated. Consequently, the entire testing methodology is systematically revised, as detailed in the following sections.

In section 6.1, the factors influencing fatigue behavior characterization are discussed in detail, along with potential influences that can affect testing accuracy and quality. Section 6.2 provides a comprehensive description of the testing machines and equipment developed for fatigue characterizations in this work. The chapter concludes with a description of the production and preparation of test specimens.

6.1 Effects on the fatigue characterization procedure to enable the investigation of the frequency effect through experimental testing

To ensure high accuracy and reproducibility of the experimental fatigue characterization method, the available testing machine and equipment are reviewed and redesigned, and the testing procedure is improved. For this purpose, the test methodology is systematically analyzed, and various influencing factors are identified. The sensitivities of the experimental determination of the fatigue behavior are illustrated by aggregating the main factors in an *Ishikawa* diagram (compare Figure 6.2) based on descriptions and discussions of the fatigue testing in the DIN 50100 standard for fatigue characterization of metals [NN16], the DIN 53442 with specifications for the conduction of fatigue tests on specimens made of plastics under alternating bending stress [NN90], the literature [GS15, Hai06, McK16, Sch08] and to a significant extent by the experiences gathered during the generation of experimental data in the course of this work.

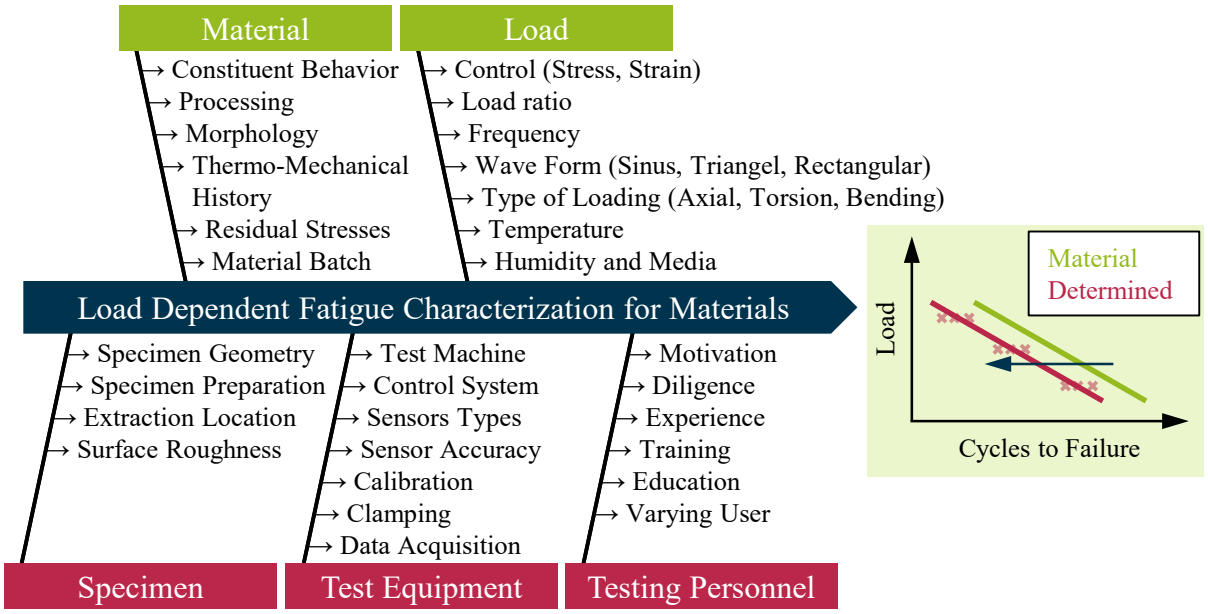

Fig. 6.2: Main factors that influence the experimental determination of fatigue behavior.

The main influencing factors impacting the characterization of fatigue life are divided into five main categories. The first two categories, ***material*** and ***load***, are inherently linked to the fatigue process of materials, while the remaining three categories, ***specimen***, ***test equipment***, and ***test personnel***, relate to the testing methodology. The following provides a more detailed explanation of the factors that influence the five categories.

The fatigue life depends on the properties and the mechanical response of the ***material***. Short fiber-reinforced thermoplastics exhibit complex material behavior due to the heterogeneous multi-scale material structure. Although the constituents, i.e., fiber and matrix, can be clearly described, the material behavior is characterized by its morphology, which can vary depending on the process of injection molding. This is reflected, for example, in local crystallinity or melt flow-dependent fiber orientations [Sch17, Tuc22]. Additionally, residual stresses may be present within the material, for instance, due to temperature gradients, shrinkage, or different thermal contractions of the constituents during the cooling resulting in a reduction of the stress that can be applied to the material before material cohesion deteriorates [DHM22, MO12].

Furthermore, the manner in which the ***load*** is applied and perceived by the material is crucial for the characterization process, the determined material-specific properties, and the fatigue process itself. The type of load control is particularly important, as the material exhibits different behavior under stress-controlled and strain-controlled conditions due to its inherent viscoelastic properties [HM80, RV07]. Additionally, the load ratio r significantly influences the induced stress state in the material. It describes the ratio between the minimum and maximum stress $r = \sigma_{Min}/\sigma_{Max}$ or in strain-controlled tests, the ratio between the minimum and maximum strain $r = \varepsilon_{Min}/\varepsilon_{Max}$ Consequently, the load ratio r quantifies the nature of the

dynamic-cyclic loads. For example, when the load ratio is $0 < r < 1$, the material is applied with tension-tension loads. This indicates that both the minimum and maximum stresses are in the tensile range, causing the material to experience only oscillating tensile stresses without entering into a compression state. In the case of the load ratio is $-1 < r < 0$, the material is subjected to tension-compression loads. Analogously, when the load ratio $r > 1$, the material will experience purely compression-compression loads [GS15, Hai06, HM80]. Depending on the induced load state, different failure mechanisms will be triggered and, thus affect the damage progress of the material.

In addition to the direction of the stress (tension or compression), the induced stress state is also influenced by whether the load is applied uniaxially or multiaxially. Although multiaxial stress states are prevalent in most structural components, fatigue tests are typically conducted under uniaxial loading conditions depending on the material directions. While methods for multiaxial fatigue testing do exist [Kai13, MMJ+10], they are not widely used due to the complexity involved in producing specimens and conducting the tests. Furthermore, even if the stress state of the material is structurally induced via axial, torsional, or bending loads, the local stress state is unambiguously described by normal and shear stresses on the material level. Therefore, in material characterization, such as in fatigue tests, a defined stress state is aimed to be induced as homogeneously as possible by uniaxial load application, even though this approach does not account for the multiaxiality of the material. The multiaxiality can then be described, for instance, using material-appropriate strength hypotheses, which consist of enveloping functions based on uniaxial values in different directions [Len16, SSK18].

Furthermore, the wave shape of the oscillation has an influence on the fatigue behavior of materials. Although the amplitude, mean level of the load, and frequency can be used to describe the loading and unloading averaged over the applied cycles, the wave shape of the oscillation will determine the actual stress state within each cyclic. Consequently, the wave shape of the oscillation defines the rates and the duration of the applied loads and, thus, will affect the material response. Sinusoidal waves apply stresses smoothly, whereas square waves introduce stresses more abruptly, leading to a reduction in the number of cycles the material withstands under fatigue loading [HM80, JGM08].

Temperature, humidity, and the media to which the material is exposed also significantly impact fatigue behavior. Variations in temperature can alter the mechanical properties of the material, either softening or embrittling it, which in turn can alter the damage mechanisms of the materials and affect the fatigue life of the material. Additionally, the material can heat up during cyclic loading due to dissipation mechanisms within the material, depending on the heat exchange with the environment (compare Chapter 7). Humidity and media, such as aggressive

environments, can accelerate material degradation and crack initiation, further negatively influencing the material's fatigue performance [HM80].

Given these various load-dependent influencing factors, it is important to ensure that the induced stress state in the experimental characterization aligns with the actual stress state in the specific component being developed, or at the very least, that the taken dimensioning limits are sufficiently conservative.

In summary, the fatigue response is a function of both the ***material*** and the ***load*** application. However, the ***specimen***, the ***test equipment***, and the ***personnel*** conducting the experiments of the fatigue characterization also influence the determined fatigue data, potentially leading to differences between the test data and the actual fatigue life of the material (compare Figure 6.2). It should be noted that factors influencing the test procedure usually result in a shorter measured fatigue life compared to the actual fatigue life of the material (compare Figure 6.1), as these factors often negatively impact the damage progression unless the test is conducted incorrectly with parameters that are less damaging than intended.

The ***specimen*** itself is a fundamental element of the experimental characterization of materials, particularly for fatigue testing. The geometry of the specimen, including its shape and dimensions, is crucial since features like sharp corners, notches, and varying cross-sections can create stress concentrations that impact the fatigue life of the tested material. The geometries of specimens vary depending on the required characteristic values and the methodological approach of interest. For instance, a compact tension test specimen differs significantly from a 1BA test specimen [GS15, NN12]. The compact tension specimen has a pre-existing crack, and loading introduces stress concentrations around this crack and, thus, leads to controlled crack evolution, providing data motivated by fracture mechanics. In contrast, the 1BA specimen has no intentionally induced pre-existing crack, and a homogeneous stress distribution is intended to deliver fatigue data in terms of continuum mechanics.

The adequate production and preparation of the specimen are crucial for the characterization of fatigue behavior. For example, the injection molding process must be in a steady state, and the process parameters must remain consistent throughout the entire manufacturing process of the specimens or specimen plates. Even if the machine settings are not changed, external influences such as temperature fluctuations in the environment or the state of the compound, such as its dryness, can alter the resulting process parameters and, consequently, the material morphology.

Furthermore, specimen preparation usually involves cutting, machining, and finishing, which need to be conducted carefully to ensure consistency and avoid introducing unintended damage that could affect the mechanical behavior and, consequently, the fatigue performance of the material. Additionally, the surface roughness of the specimen is a critical factor. Rougher

surfaces can serve as initiation points for cracks, especially for brittle materials, thus reducing overall fatigue life [Erik90]. Lastly, the location from which the specimen is extracted from the specimen plates matters, especially if fiber-reinforced plastics are to be tested, for which a distinct orientation dependency is evident. Even the extraction of several specimens from a single specimen plate can lead to different mechanical response behaviors or higher scattering if the morphology and the state of the material are not homogeneous throughout the extraction positions within the plates. Since the cavity-filling process already causes a pressure loss over the flow path length, a property gradient along the flow path is always to be expected in injection-molded specimen plates [GGO+16, TCH13].

In addition to the specimens used, the reliability and precision of the ***test equipment*** are decisive for obtaining accurate fatigue data. The performance of the test machine, which applies the dynamic-cyclic loads onto the material, must be both accurate and consistent across each individual test and throughout all tests. The control system used to maintain load application conditions over the entire test should be precise and reliable to ensure that the loads, frequencies, and other parameters are correctly applied. Fatigue experiments are particularly sensitive compared to other mechanical tests, as even small and one-time inconsistencies can significantly affect the entire experiment.

The accuracy of the test machine also depends on the set PID control parameters, but the control behavior of the test system is not solely impacted by the testing machine itself. Rather, it is also influenced by the mechanical behavior of the specimen within the control loop. Hence, the PID values need to be adapted for the specimen, material, and test setup (clamping, load cell, etc.) to ensure good agreement between the setpoint and the actual signal. It is also important to note that the testing machine is in a steady state during the entire test. For instance, if a servo-hydraulic testing machine is used, the viscosity of the hydraulic oil depends on the operating temperature of the testing cylinder. To prevent any negative influences from the testing machine, it is essential to warm up the testing machine before each test. This requirement must also be taken into account when a specimen is changed. After the failure of the specimen, the testing piston comes to a standstill, leading to its cooling and, consequently, a change in oil viscosity and piston behavior.

As discussed before, thermoplastics exhibit significant temperature sensitivity, meaning their mechanical properties can vary drastically with changes in temperature. This sensitivity necessitates the use of a temperature chamber during testing to maintain a controlled thermal environment [GS15]. Consistency in temperature is important to ensure accurate and reproducible results. However, it is not only the stability of the temperature that matters but also the heating and cooling rate of the chamber, as it directly influences the heat exchange between the temperature chamber and the test specimen. This is particularly important for

fatigue tests at higher frequencies, as different temperatures can develop within the material despite a constant ambient temperature of the chamber, depending on the prevailing heat exchange rate (compare Chapter 7).

In addition to load application in a controlled environment, the measurement of the mechanical response is also important. The types of sensors used to measure load, strain, piston displacement, and other variables are vital, as their accuracy and calibration directly affect the reliability of the experimentally determined data. The load cell sensitivity should be within a suitable force range to ensure high accuracy. Additionally, the load cell must be appropriately selected to match the expected load range of the test to avoid overloading or also underloading, which could compromise measurement accuracy and sensor integrity.

The method of specimen clamping in the test machine can also influence the results. Improper clamping can introduce unwanted stresses or cause the specimen to slip, which is particularly problematic for viscoelastic materials that tend to creep, reducing the clamping force and changing the load introduction into the specimen. One challenge relevant to fatigue assessment is the oscillating load, which is why conventional clamping with wedge-screw grips is not a preferable option, as the clamping force depends on the load currently applied to the test specimen. Also, it is essential to clamp the specimen in exactly the same position and with the same clamping force each time to ensure consistency throughout all fatigue tests. Furthermore, the data acquisition system must be capable of accurately capturing high-frequency signals to facilitate effective analysis of fatigue behavior. This is especially important, for instance, to capture the hysteresis of the material at high frequencies.

Furthermore, in addition to the material and technical aspects, the human factor significantly influences the experimentally determined results. The skills and diligence of the ***personnel*** conducting the experiments are critical to ensuring the reliability of the fatigue characterization. This is particularly important when a large number of different people are involved in the testing process. Motivated personnel are more likely to perform thorough and accurate testing. Diligence in respecting the testing protocol and attention to detail can prevent errors and ensure consistent results. Furthermore, experience plays a significant role, as experienced personnel can better manage unexpected issues and accurately interpret data while testing. Proper training ensures that the personnel is familiar with the equipment, procedures, and safety protocols. A solid educational background provides the theoretical understanding necessary to understand fatigue mechanisms and testing methods.

By carefully considering these factors (specimen characteristics, test equipment reliability, and competence of the testing personnel), it is possible to obtain accurate and reliable fatigue life data very close, if not identical, to the material's actual fatigue life. This ensures that material

effects can be investigated and distinguished without negative influence, allowing for a precise assessment of material behavior under dynamic-cyclic load conditions.

6.2 Revision of the testing machine and the development of the peripheral equipment

The following section contains a detailed description of the test setup for the investigations of fatigue behavior under various frequencies and material orientations. The experimental tests in this thesis are carried out on a servo-hydraulic mechanical testing machine, Schenck VHF7 of Instron Testing Systems GmbH, Darmstadt, Germany. The hydro pulse cylinder of the testing machine can apply a mechanical test frequency of up to 1 kHz. The load application for the static case can be up to ±7 kN, and for the dynamic-cyclic case, up to ±5.6 kN [NN15]. The maximum stroke of the testing cylinder is at ±10 mm, whereby it should be noted that the amplitude stroke decreases with increasing frequency and load. For example, at a frequency of 100 Hz and full load (5.6 kN), only an amplitude stroke of approximately ±1 mm can be achieved [NN15]. The testing machine is operated with an updated control and data acquisition system of the type testControl II from Zwick GmbH & Co. KG, Ulm, Germany. The data acquisition system can record up to 400 kHz and has a bus interface of 10 kHz [NN15]. This limitation is crucial when using high test frequencies since the stress-strain data needs to be recorded with a high resolution to be able to analyze the material response accurately, especially when the hysteresis behavior of the material is aimed to be investigated. Therefore, the data acquisition and write-out for all mechanical tests is set to record 100 points per cycle, requiring a data rate of 10 kHz for a mechanical load frequency of 100 Hz.

The testing machine is equipped with a Zwick GmbH & Co. KG, Ulm, Germany, load cell of the type DR-F, with a nominal force of 5 kN. The load cell's operating range is ±230 % of the nominal force. Before the start of the mechanical investigations and fatigue tests for this work, the load cell was calibrated with test nominal weights by Zwick GmbH & Co. KG, Ulm, Germany. The calibration was carried out along the entire measurement chain of the testing machine.

For strain measurement, the testing machine is equipped with two EXA 20 axial extensometers manufactured by Sandner Messtechnik GmbH, Biebesheim am Rhein, Germany, with two different maximum measuring displacements of ±1.25 mm and ±5 mm. Both extensometers have a gauge base length of 20 mm, allowing strains of ±6.125 % and ±25 % to be measured. The extensometer knives are fixed on the specimen by using spring cotters, which press both extensometer knives onto the specimen. It is important that the spring cotters are placed in such a way that the extensometer knives are pressed evenly on the specimen surface so that there is no notch formation at the edges of the specimen, which can negatively affect the experiments and lead to false indications of the fatigue life of the tested material. A calibrated gauge block

is used to ensure that the distance of the extensometer knives matches the gauge base length and is maintained while placing the extensometer on the specimen. Before the fatigue test is started, the gauge block must be removed so that the knives can follow the elongation of the specimen.

To ensure that the extensometer is positioned on the specimen in the same manner for each specimen throughout all experimental tests, a positioning fixture is developed. Furthermore, the positioning fixture ensures the consistent positioning of the specimen within the specimen clamping of the testing machine. The positioning fixture consists of three parts: the base and the two wings, referred to as the right wing and the left wing, respectively (compare Figure 6.3, left). The two wings are guided on the base and can be translated relative to each other. The test specimen is placed between the two wings and clamped by them. The base has an end stop for each wing, ensuring that the specimen is always positioned in the center of the base. Furthermore, two magnets are attached to the wing sections to prevent the test specimen from losing its position after it has been positioned within the positioning fixture. The extensometer can be mounted subsequent to the positioning of the test specimen. This is achieved by placing the extensometer with the mounted gauge block within the positioning fixture in the provided guides for the extensometer knives. As previously stated, it is essential that the measuring knives are positioned exactly centered relative to the specimen width. This is necessary due to the tactile measurement of the elongation of the specimen. Not positioning the measuring knives and the spring cotters centered can result in notches forming on the surface of the specimen. The relative fixation of the test specimen and the spring cotters to each other is achieved by means of a stopper on the left wing of the positioning fixture (compare Figure 7.2, right).

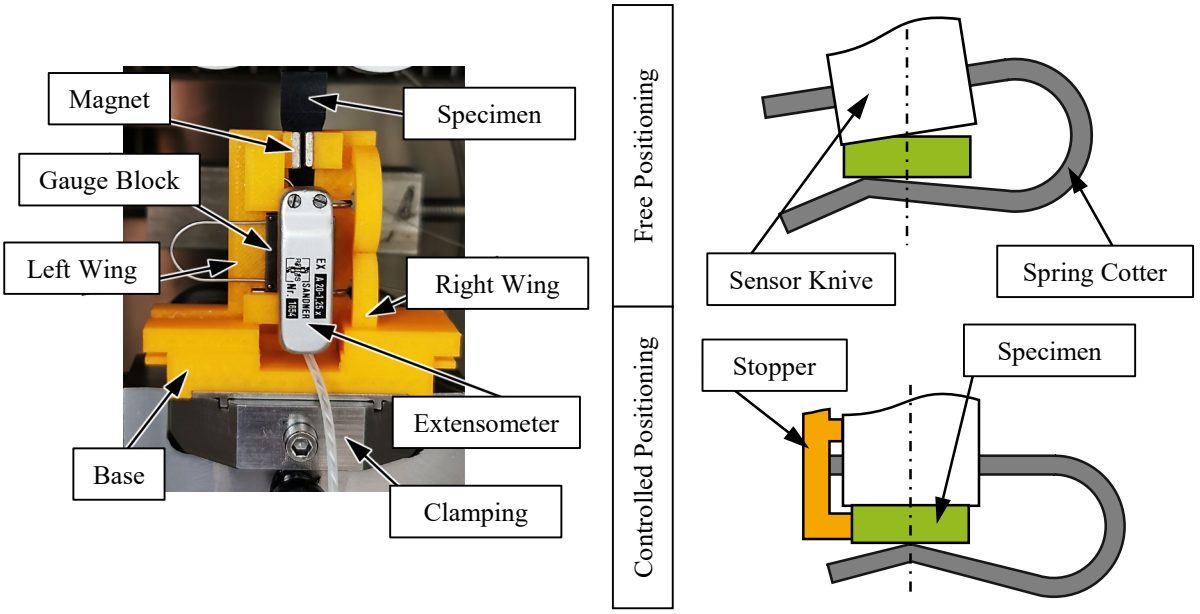

Fig. 6.3: Left: The positioning fixture ensures the precise and repeatable positioning of the extensometer and specimen. Right: The positioning of the measuring knives and spring cotters is achieved by using stoppers at the positioning fixture.

After the extensometer is attached and the spring cotters lock the position relative to the specimen, the positioning fixture is inserted into the bottom clamp of the testing machine. To ensure that the specimens are always centered in the clamp, guides and magnets are also used here to ensure reproducible positioning for all tests. After successfully positioning the fixture, the clamp is tightened, and the two wings are removed by translational displacement to the right and left. Subsequently, the base can also be removed without displacing the test specimen or the extensometer.

One of the most important factors in mechanical testing and, particularly for experimental fatigue characterization, is the introduction of force into the test specimen to induce a homogeneous stress state. It must be ensured throughout the entire testing period that the specimen does not slip within the clamping fixture and that the force application remains constant, even when a large number of load cycles (> 10^6) are applied to the specimen. The specimen is secured in the clamping fixture by applying forces in normal direction to the surface at the shoulders of the specimen. This ensures that the specimen is clamped between grips and the force is subsequently introduced into the specimen through shear stresses by means of friction. Therefore, the clamping force is of great importance for the force introduction. However, due to their viscoelastic properties, technical thermoplastics are prone to creep, causing the clamping force to decrease over time if the clamping is realized through displacement control. Although pressure-controlled hydraulic grips can be used to ensure that creep is compensated for and a constant force is applied throughout the entire test duration, these grips are usually associated with expensive auxiliary equipment and high weights of the clamping fixtures.

The following section will address the influence of the weight of the clamping fixture, particularly in the context of high-frequency testing, as it is an additional load that must be managed by the control system during the test. The force F_{Clamp} induced by the oscillatory movement of the clamping fixture comprises two components: the static weight force F_{Static} and the dynamic component $F_{Dynamic}$ resulting from the varying acceleration of the fixture (compare Equation 6.3).

$$F_{Clamp} = F_{Static} \pm F_{Dynamic} \qquad \textit{(Eq. 6.3)}$$

The static weight force F_{Static} results from the product of the mass m and the acceleration due to gravity g (compare Equation 6.4).

$$F_{Static} = m\, g \qquad \textit{(Eq. 6.4)}$$

The dynamic force $F_{Dynamic}$ generated by the weight m of the clamping fixture can be approximated by considering the acceleration $a(f, s_{Amp})$ caused by its dynamic-cyclical

movement at a certain frequency f and amplitude stroke s_{Amp} of the piston (compare Equation 6.5).

$$F_{Dynamic} = m\, a(f, s_{Amp}) \qquad \textit{(Eq. 6.5)}$$

Assuming a sinusoidal movement, the peak acceleration $a(f, s_{Amp})$ is given by Equation 6.6:

$$a = (2\pi f)^2 \cdot s_{Amp} \qquad \textit{(Eq. 6.6)}$$

Consequently, the maximum total force $F_{Clamp,Max}$ introduced by the weight of the clamping fixture under cyclic loading conditions is the sum of the static weight force F_{Static} and the dynamic force $F_{Dynamic}$ described by Equation 6.5.

$$F_{Clamp,Max} = m\left(g + (2\pi f)^2 \cdot s_{Amp}\right) \qquad \textit{(Eq. 6.7)}$$

In Figure 6.4, Equation 6.7 is evaluated for an amplitude stroke s_{Amp} of 0.6 mm, which corresponds to a strain of approximately 2 % for a 1BA test specimen according to DIN ISO 574 [NN12], for different weights m ranging from 1 to 9 kg within a frequency range up to 100 Hz. The horizontal 10 % and 25 % lines represent the relative force compared to the maximum applicable dynamic force (±5.6 kN) of the hydraulic test cylinder.

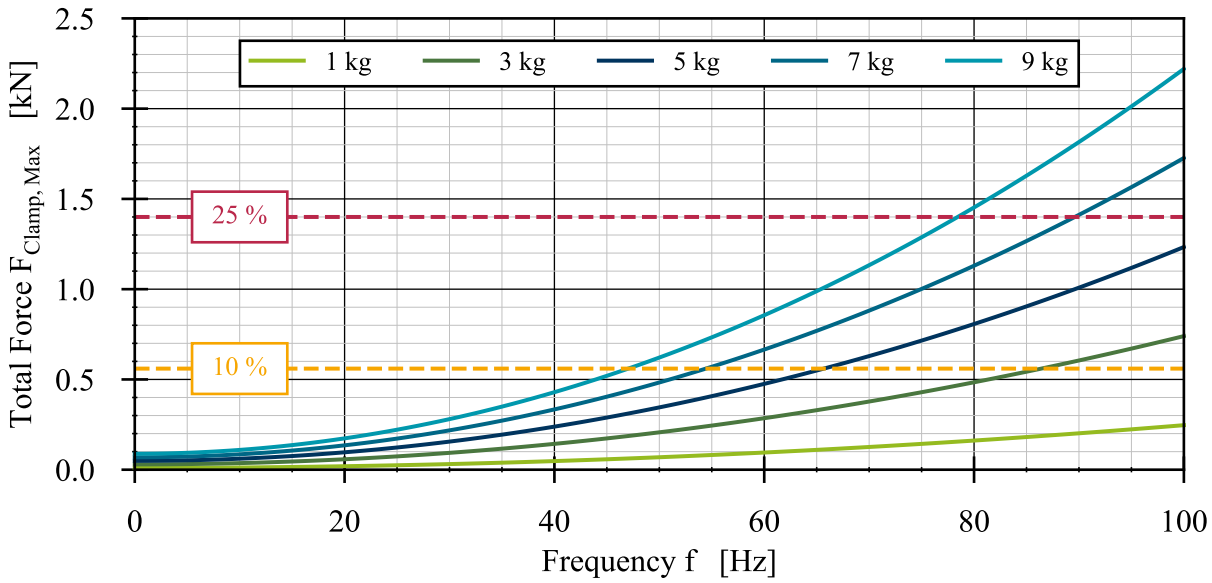

Fig. 6.4: Evaluation of the total force for an amplitude stroke of 0.6 mm, corresponding to a strain of approximately 2 % for a 1BA test specimen, across different weights from 1 to 10 kg within a frequency range up to 100 Hz.

For comparison, a standard 10 kN screw clamping fixture made by Zwick GmbH & Co. KG, Ulm, Germany, with a weight of 8.6 kg can be considered. With such a clamping fixture, at a frequency of 100 Hz, a load of over 2 kN would be additionally induced by its oscillatory movement while conducting a fatigue test, which would need to be compensated by the testing cylinder. This represents over 40 % of the maximum applicable force of the testing cylinder. Furthermore, the additional load can be interpreted as a disturbance in the control loop.

Consequently, it would be necessary to verify the PID parameters of the control system every time when the frequency is changed, and a clamping fixture with high weights is used to ensure that the target load can still be induced in the test specimen.

A new clamping system is developed to minimize the possible negative effects of the clamping fixture at low and high frequencies over the entire load and duration range for the aimed fatigue tests to investigate the frequency effect (compare Figure 6.5). This system is capable of inducing a constant clamping force over the entire test duration despite material creep and is reproducible over all tests. The fundamental principle of the clamping system is that the clamping force is generated by compressing disc springs, thereby securing the specimen between the two gripping elements. Disc springs, also known as *Belleville* springs, are a type of spring that features a conical shape. They can support high loads with relatively small deflections, and their compact size allows them to be used in applications with limited space. This enables the provision of the necessary force within a small design space.

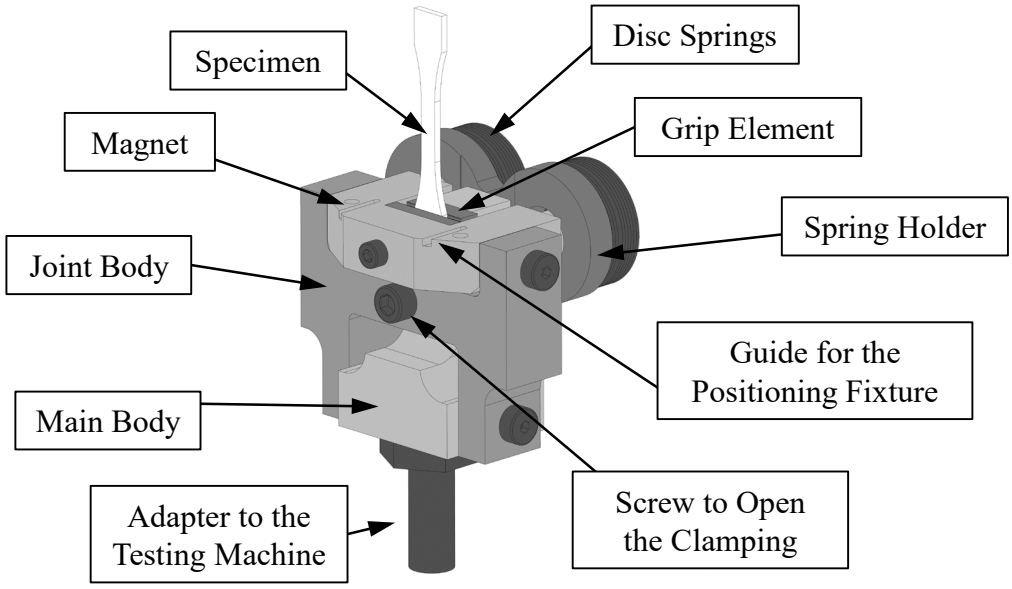

Fig. 6.5: Assembly and design of the newly developed clamping fixture for fatigue characterization under various loads and frequencies.

The load-deflection curve, hence, the stiffness behavior of disc springs, is non-linear and degressive, meaning that the force increases more slowly with a higher deflection as long as the disc springs are not completely flattened and the spring effect is no longer available. This characteristic is advantageous for specimen clamping purposes since once a force is established by the disc springs, deviations in deflection do not significantly impact the force generated by the disc springs. Therefore, when, for instance, testing thermoplastic materials, even if the specimen material undergoes creep due to the clamping force, the reduction in clamping force will be negligible. Furthermore, disc springs can be stacked in various configurations (parallel,

series, or combination) to achieve desired load-deflection characteristics. Stacking in parallel increases the load capacity while stacking in series increases the deflection range.

The clamping system is designed in such a way that the main body and joint body are always pressed against each other. This is why the springs have to be packed in series, as the springs essentially require further compression to open the clamping fixture for changing the specimen. Hence, two parallel spring packages, each consisting of nine disc springs connected in series, are used to ensure even and steady force application on the surface of the specimen. The disc springs conform to DIN 17222, are characterized by an applicable force of 1,750 N at a compression of 0.94 mm and an outer diameter of 34 mm. Consequently, this configuration can apply a maximum force of 3500 N, achieved when compressing the spring packages by approximately 8.6 mm. It is important to note that the maximum applicable compression through the grips is also influenced by the friction between the grip elements and the specimen surface. Therefore, the surfaces of the grip elements were serrated as usual for mechanical testing grips to enhance the friction. Before the application of the newly developed clamping system in fatigue tests, quasi-static tensile tests were conducted, during which tensile loads exceeding 1200 N were successfully applied without any slipping of the specimens. Hence, the functionality and suitability of the clamping system and the spring assembly configuration are successfully validated.

As previously discussed, the weight of the clamping fixture significantly affects the dynamically induced loads during testing, necessitating adaption by the control system and the hydraulic piston. Therefore, it is essential to design a compact clamping fixture to reduce these effects. The newly developed clamping fixture, including all screws and springs, has a mass of approximately 1.11 kg, resulting in maximum induced inertial forces by the oscillatory movement below 250 N for the aimed test frequencies and load levels (compare Figure 6.4).

Additionally, positioning guides and magnets for the specimen positioning fixture are integrated into the clamping fixture, as illustrated in Figure 6.5. This ensures that the relative positions of these components are both secured and reproducible.

Hence, a revised clamping and specimen positioning setup has been developed to meet the mechanical requirements for fatigue characterization under different frequencies and load levels.

Given the significant influence of temperature on the mechanical behavior of thermoplastic materials, all experiments are conducted in a temperature-controlled chamber of the Type TEE21/40 X, manufactured by Brabender Realtest GmbH, Moers, Germany. This chamber, equipped with an updated digital temperature controller, ensures a stable ambient temperature and can be set to a range from -40 °C to 250 °C. It should be noted that the process-dependent

working range of the temperature chamber is highly influenced by the environmental temperature and the cooling of the compressor. Although the target temperature can be achieved and maintained by the temperature chamber, the necessary cooling and heating rates can vary due to these external influencing factors. To position the temperature chamber relative to the testing machine, a fixed frame system was developed. This system allows the temperature chamber to be translationally moved as needed. Defined stops ensure that the chamber is positioned consistently relative to the testing machine and, consequently, aligned with the axis of the testing cylinder.

While the temperature chamber ensures that the fatigue testing occurs in a temperature-controlled environment, the actual specimen temperature is additionally monitored throughout the entire duration of the experiments for each specimen using an infrared pyrometer. The CSmicro LT22H CF pyrometer from Optris GmbH, Berlin, Germany, is used for this purpose, with a measurement range of -50 °C to 1030 °C. With a reaction time of 150 ms, it is possible to measure temperature changes nearly instantaneously. For the testing setup, it is crucial that the distance between the pyrometer and the specimen accounts for the pyrometer's focal point, ensuring that the measurement spot is accurately directed at the specimen's surface. The pyrometer used in this setup is characterized by a measurement spot of 2.3 mm in diameter at a distance of 50 mm. Additionally, the infrared pyrometer features an internal thermometer that can continuously monitor the ambient temperature. The pyrometer is securely mounted and precisely aligned within the temperature chamber. Given that the temperature chamber maintains a defined relative position to the test axis, and all specimens are clamped using the positioning fixture and the newly developed clamping system, the measurement spot of the pyrometer remains consistently centered on the test area of each specimen across all tests. This ensures accurate and reproducible temperature measurements for all specimens throughout the experimental series.

The appropriate setting of the emissivity value is crucial for accurate temperature measurement using a pyrometer. Therefore, an experimental test is conducted in which specimens are clamped without being subjected to any load. Subsequently, the temperature chamber is set to three different temperatures: 5 °C, 25 °C, and 55 °C. The resulting temperatures are then measured using the pyrometer and its internal temperature sensor, and these recordings are compared to ensure accuracy. An emissivity value of 0.95, as recommended by the pyrometer manufacturer for the material, was used during these measurements. The measurements were analyzed after thermal equilibrium was reached.

The recorded data is presented exemplarily for a duration of eight minutes in Figure 6.6. The upper plot illustrates the difference between the set temperature of the chamber and the internal sensor of the pyrometer, which does not require a calibration like the pyrometer sensor.

However, it is important to note that the output of the internal temperature sensor does not show short-term fluctuations. Across all three set temperatures (5 °C, 25 °C, and 55 °C), the deviations remain close to zero with minor fluctuations. Specifically, the deviations are within ±0.25 °C at 5 °C and 25 °C, and within ±0.1 °C at 55 °C. Taking also measurement inaccuracies into account, this indicates that the temperature control within the chamber is stable.

In the lower plot, the data illustrates the difference between the pyrometer and its internal sensor. The observed deviations show the sensor's precision in capturing the surface temperature of the specimen in comparison to the internal temperature readings. At 5 °C, the differences fall within ±0.5 °C, while at 25 °C and 55 °C, they remain within ±0.2 °C. Despite the inherent response delay of the internal sensor, the pyrometer measurements exhibit sufficiently accurate temperature capturing across all three temperature settings. The variations are generally negligible, affirming the pyrometer's capabilities to measure the actual specimen temperature, thereby ensuring dependable data for fatigue testing and analysis.

According to DIN ISO 291, class 1 thermal stability allows a deviation of ±1°C, and class 2 stability allows a deviation of ±2°C. The recorded deviations fall well within these specified limits [NN08].

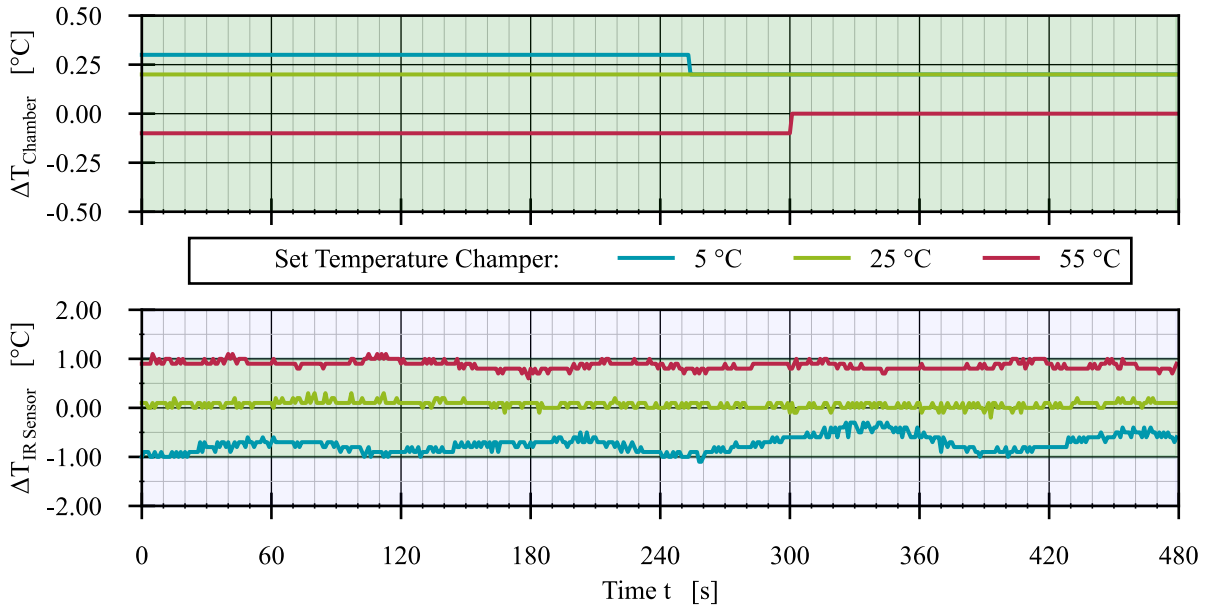

Fig. 6.6: Top: Difference between the set temperature of the temperature chamber and the internal sensor of the pyrometer. Bottom: Difference between the pyrometer and its internal sensor at the same set temperatures.

As a result, a controlled temperature environment and temperature monitoring setup have been established to meet the requirements for determining the effects of temperature while the load and frequency-dependent fatigue behavior is characterized.

6.3 Manufacturing and preparation of test specimens for the fatigue investigations

Although the fatigue behavior is highly material-specific, especially since the thermoplastic matrix of various types of plastics can behave very differently depending on the used polymer and additives, this study focuses on investigating only one type of material to have a thorough and consistent analysis. Polybutylene terephthalate with 30-weight percent of short glass fibers of the type Pocan® B3235 and the corresponding non-reinforced polybutylene terephthalate of the type Pocan® B1305 provided by Envalior GmbH, Düsseldorf, Germany, are used to investigate the effect of the frequency on the fatigue procedure.

Both materials are processed through injection molding using a fully electric injection molding machine, IntElect 100/520-340 Smart, manufactured by Sumitomo Demag Plastics Machinery GmbH, located in Schwaig, Germany. Specimen plates are produced, from which the test specimens for the fatigue experiments and further analyses (micro-computed tomography, differential scanning calorimetry, conductivity, etc.) are subsequently extracted. The injection molding parameters are chosen according to the manufacturer's recommendations (compare Appendix 15.1). Only one set of manufacturing parameters is used to produce the specimen plates since it is not aimed to investigate the influence of manufacturing parameters on the fatigue procedure. After molding each specimen plate (compare Figure 6.7), the manifold area for ensuring the parallel flow front is removed immediately after the specimen plate is ejected to prevent warpage, which is induced by shrinkage due to the higher wall thickness compared to the plate area.

The selection of the specimen plate with dimensions of 115 mm x 115 mm x 2 mm is based on several considerations regarding the mechanical characterization of the material under various frequencies in fatigue tests and load directions. This plate size provides sufficient area to extract 1BA specimens in accordance with the DIN ISO 527 standard. The 1BA specimens have a shoulder width of 10 mm, a width of 5 mm in the test section, and an overall length of approximately 75 mm (compare Figure 6.7). It is important to note that longer specimens require more elongation to achieve the same material strain than shorter specimens. Given the constrained space within the temperature chamber (compare Chapter 6.1), the small geometry of the 1BA specimen offers handling advantages.

To ensure that the process-dependent morphologies of the specimens are as identical as possible for the material property characterization and evaluation, the specimens are extracted only from one position from each plate and orientation. Even minor deviations in fiber orientation between individual specimens can significantly influence the mechanical properties and, consequently, the fatigue properties since the impact of the fibers on the stiffness and strength of the compound material is substantial. Therefore, maintaining consistency in fiber orientation is

decisive for obtaining reliable and comparable fatigue data and for avoiding misinterpretation of results caused by morphological variation throughout the tested specimens. Given that the influence of fiber orientation is also to be investigated, specimens with three different fiber orientations (longitudinal (0°), diagonal (45°), and transversal (90°)) with respect to the main flow direction are extracted from the plates, as illustrated in Figure 6.7. The diagonal orientation is only used for quasi-static tensile tests. Positioning aids are used for precise specimen extraction, and the specimens are machined from the plates using a computer-controlled milling machine. This approach allows for an accurate assessment of how different fiber orientations affect the mechanical properties under various loading conditions and frequencies, respectively.

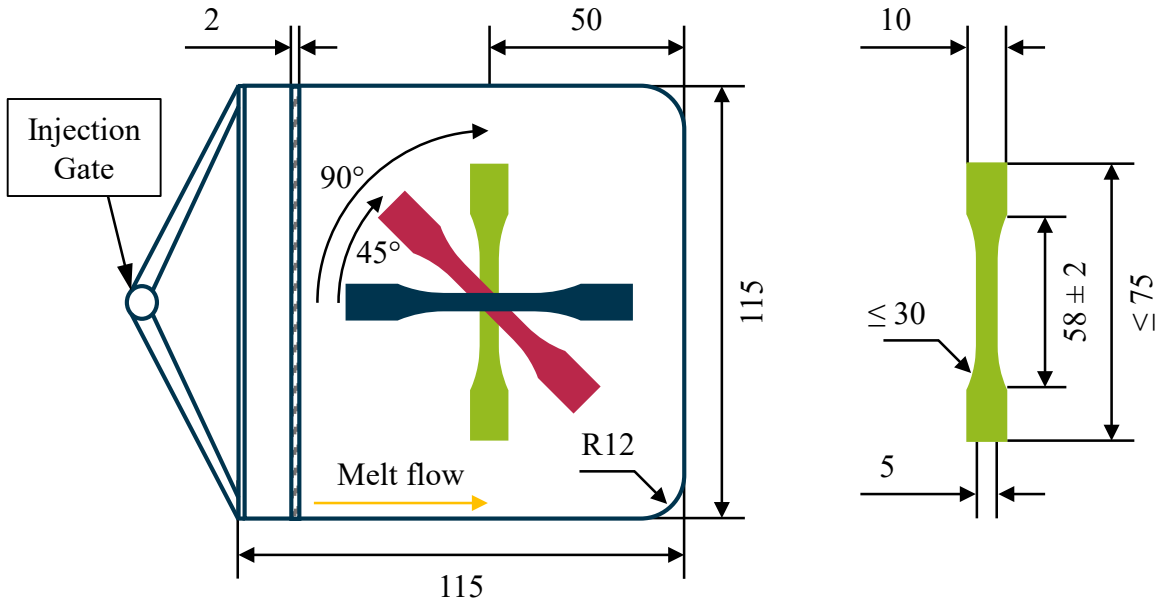

Fig. 6.7: Dimensions of the specimen plate and the 1BA specimen according to DIN EN ISO 527, including extracting position.

To quantify the fiber orientation distribution across the thickness of the manufactured PBT-GF30 specimen plates, micro-computed tomography (µCT) scans are conducted. The fiber orientation distribution of two different specimen plates, one produced at the beginning and one at the end of the production series, is measured. Four different positions of each specimen plate are analyzed. The µCT scans were performed using the SKYSCAN 1172 X-ray micro-computed tomography scanner from Bruker Corporation, Billerica, Massachusetts, USA. The geometric dimensions of the test specimens depend on the required resolution. For analyzing a short glass fiber-reinforced thermoplastic with a fiber mass content of 30-weight percent, a high resolution (4000 px x 2664 px) is necessary to distinguish the fibers. Consequently, square specimens with an edge length of 5 mm based on previous experiences are used. To ensure the extraction direction can be traced, the specimens are chamfered on a defined edge. The specimen is mounted in the holder of the µCT-scanner, which then moves towards the detector. During the scanning process, the specimen is rotated by a total of

180 degrees. After each rotation, the specimen is moved upward, and the scanning process is repeated. The scanner creates a three-dimensional depiction of the micro-structure based on the layer-by-layer density distribution determined for the specimen. Using an evaluation script [Haa18], the distribution function of the fibers is extracted from the individual slice images of the µCT scan. From this data, the second-order orientation tensors $\boldsymbol{A}$, which quantify the orientation state, are derived. For a second-order orientation tensor $\boldsymbol{A}$, the entries A_{ij} are referred to as components. Each index i and j denotes a spatial axis [Tuc22]. The off-diagonal values A_{12}, A_{13} and A_{23} of the second-order orientation tensor are negligible small, indicating that the primary orientation system of the tensor is aligned with the orientation of the specimen plate, which is why they are not shown here. The diagonal values A_{11}, A_{22} and A_{33} of the second-order orientation tensor obtained from the µCT measurements are shown in Figure 6.8.

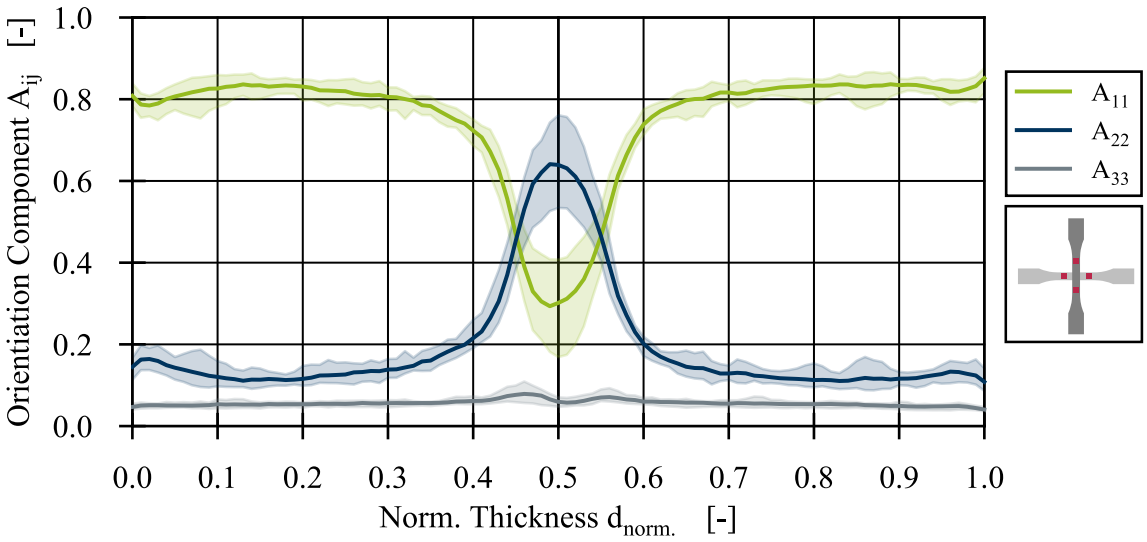

Fig. 6.8: µCT evaluation of the fiber orientation of the specimen plates, showing the characteristic distribution for injection molded compound materials. Averaged results of two plates for each of four positions.

The eight scanned specimens, which were taken from the same areas of the specimen plate as the test regions for the 1BA specimens are located, exhibit the typical orientation distribution for injection-molded short fiber-reinforced thermoplastics. The light-colored shaded areas represent the deviations within these eight scanned specimens. However, it should be noted that the outer images of the µCT-scans may be missing in the measurements due to limitations in accurately setting the analysis boundaries of these areas during image processing. This can lead to higher fluctuations, especially in regions with steep orientation gradients, as the eight orientation distributions may be slightly misaligned relative to each other. For the injection-molded specimen plates, a fiber orientation in the main flow direction, quantified as $A_{11} > 0.8$, is observed over approximately 70 % of the specimen thickness. The fibers are predominantly

oriented in the in-plane direction, as indicated by an out-of-plane orientation value of $A_{33} > 0.05$, which is uniformly distributed across the entire thickness. Thus, with specimen plates of a thickness of 2 mm, a fiber orientation distribution is obtained that allows the influence of macroscopic anisotropy on fatigue to be investigated.

To evaluate the quality of the specimens, quasi-static tensile tests are conducted, providing initial indications of the deviations regarding the mechanical behavior. The influence of fiber orientation on the *Young's* modulus E and tensile strength R is determined by testing five different specimens for each orientation. The tensile tests are performed using a Z150 universal testing machine from Zwick GmbH & Co. KG, Ulm, Germany, in accordance with DIN EN ISO 527. The clamping length of the specimens is 60 mm, and the length of the test section is 30 mm. The strain is measured using tactile extensometers throughout the entire test duration. For the determination of the *Young's* modulus, the crosshead speed of the universal testing machine is set to 0.25 mm/min. After reaching a strain of $\varepsilon = 0{,}3$, the crosshead speed is increased to 5 mm/min and maintained constant until fracture occurs. The results of the tensile test are shown in Figure 6.9 and the averaged values and the standard deviations in parentheses for the stiffness and strength are in Table 6.1.

Orientation	Young's Modulus E [N/mm²]		Tensile Strength R [N/mm²]	
Longitudinal - 0°	8047.90	(118.15)	120.11	(0.44)
Diagonal - 45°	5099.98	(111.07)	78.31	(0.43)
Transversal - 90°	4618.07	(66.93)	67.29	(1.40)

Table 6.1: Tensile test results for specimens made of PBT-GF30 at 0°, 45°, and 90° orientations, including the standard deviations.

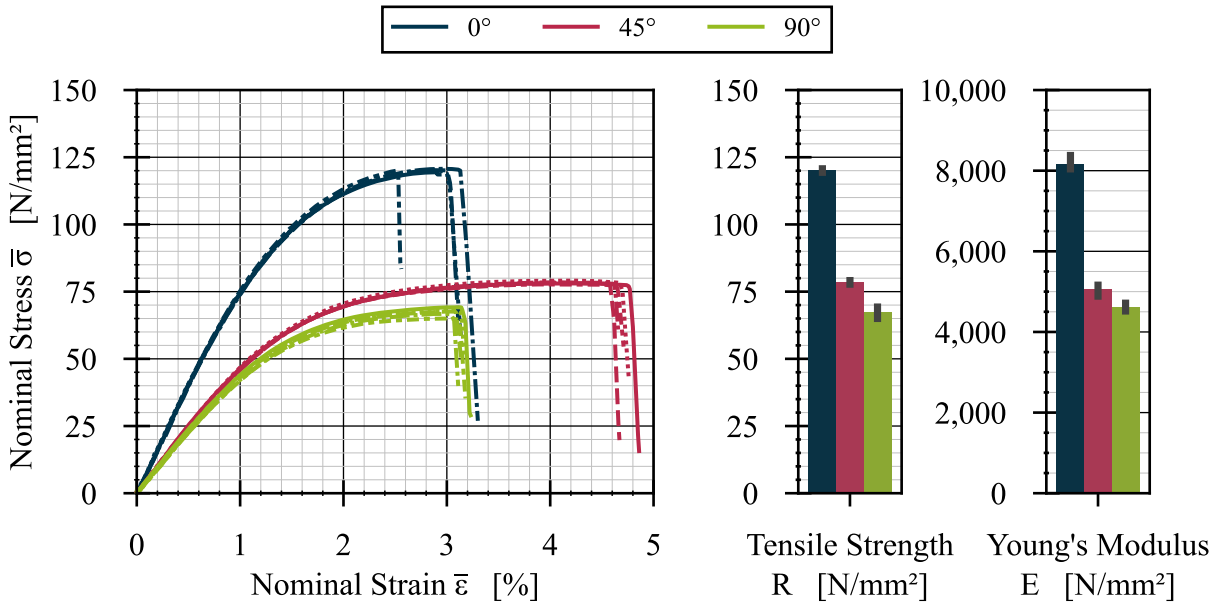

Fig. 6.9: Tensile test results for specimens made of PBT-GF30 at 0°, 45°, and 90° orientations relative to the main flow direction. Left: Stress-strain curves, Middle: Tensile strength, and Right: Young's modulus.

The tensile test results of the PBT-GF30 material confirm the influence of fiber orientation on the mechanical properties of short glass fiber-reinforced thermoplastics. Specimens at 0° exhibit the highest tensile strength and stiffness, while those at 90° show the lowest values. The tensile behavior of both longitudinal and transverse specimens is significantly affected by the mainly bidirectional fiber orientation distribution across the thickness. Additionally, it can be seen that the strain at failure with $\varepsilon_F \approx 3{,}0\ \%$ is at a similar level for the longitudinal and transversal direction of the material. Due to the shear stresses induced within the material during the tensile testing, the diagonal specimens exhibit a different deformation behavior, achieving a strain at failure of almost $\varepsilon_F \approx 4{,}7\ \%$. This further highlights the substantial impact of fiber orientation distribution on the material's mechanical deformation behavior. The results not only confirm the validity of the specimen preparation process but also ensure that the collected data is consistent and reliable. However, the further investigations are focused the longitudinal and transversal directions.

As previously discussed, the specimen plates have a thickness of 2 mm, which is advantageous for both the development of fiber orientation distribution and fatigue testing at high frequencies. During high-frequency fatigue tests, the effective heat dissipation and the resulting self-heating of the material are also critical. The resulting temperature is influenced not only by applied stresses and frequencies but also by the heat exchange with the environment and the geometric ratio between surface area and volume. A thickness of 2 mm ensures a surface-to-volume ratio, adequate for heat transfer (compare Chapter 8.2) and maintaining the integrity of the material under test conditions. The effects on self-heating and the geometric parameters are analyzed and discussed in the following sections.

7 LOAD AND FREQUENCY INDUCED TEMPERATURE INFLUENCE ON THE FATIGUE BEHAVIOR

In the following chapter, the influence of frequency and the resulting temperature evolution of the material due to dynamic-cyclic stress will be investigated both experimentally and analytically, thereby establishing the foundation for subsequent investigations in Chapter 8 and the following chapters. First, however, a brief literature review of the state of the research regarding the effect of frequency and temperature on the fatigue behavior of non-reinforced and fiber-reinforced thermoplastic materials is presented.

In 1975, *Crawford* and *Benham* investigated the influence of frequency on non-reinforced thermoplastics, specifically polypropylene (PP), polycarbonate (PC), and polymethyl methacrylate (PMMA) [CB75]. In their study the frequency is varied in the range of 0.167 Hz to 10 Hz. The study shows a temperature increase in dependency on load and frequency. At higher frequencies and load levels, the temperature in the material is progressively increased until the failure of the specimen occurs. Conversely, at lower frequencies and applied loads, the specimen reached thermal equilibrium, maintaining a temperature higher than the ambient temperature but stable over the duration of dynamic-cyclic load application. The experimentally generated SN data shows that the data points for final failure at lower frequencies and loads are mainly aligned on a single curve, indicating that the cycles to failure of tested materials do not depend on the frequency. However, deviating points are interpreted as thermally induced failures and not cyclic-crack controlled.

Handa et al. studied the fatigue behavior of polyamide 6.6 (PA66) with a 33 % glass fiber content and moisture content below 0.2 % by weight at frequencies of 5 Hz, 20 Hz, and 50 Hz across a temperature range from 0 °C to 120 °C [HKN99]. The study shows that the slope of the SN curves decreases with increasing temperature up to the glass transition temperature, after which the slope remains consistent. Additionally, higher frequencies lead to a decrease in the SN curve slopes. However, it should be noted that the SN data for the different frequencies intersect each other. The study also indicates that higher frequencies result in increased specimen temperatures, suggesting that fatigue behavior varies with both frequency and temperature, even under similar constant ambient conditions.

In a different study [JK98], polyamide 6 (PA6) and polyamide 6.6 (PA66) with a 33 % glass fiber content and dry-as-molded were tested at three different temperatures (-40 °C, 23 °C, and 121 °C) under tension-tension loading. A sensitivity analysis reveals a significant temperature increase at frequencies above 5 Hz, leading to all tests being conducted at 5 Hz. The results demonstrate a substantial reduction in fatigue life with increasing temperature and a corresponding decrease in the slope of the SN curves.

In the study of [ZM06], the fatigue behavior of PA66-GF33 (undefined conditioning state) was investigated at various frequencies (0.01 Hz to 20 Hz) and different specimen orientations relative to the main melt flow direction. The hysteresis loops were analyzed to distinguish between thermal and fatigue failure. At low frequencies, the hysteresis loop slope, representing the dynamic stiffness, remained nearly constant. However, increasing the frequency reduced the dynamic stiffness, likely due to a noticeable temperature rise caused by energy dissipation. The study also shows that the cyclic fatigue life increases with frequencies up to 2 Hz, beyond which it decreases, an effect attributed by the authors to the temperature increase through self-heating within the specimen.

In a study conducted by [MFM+15], the temperature and frequency-dependent fatigue of two non-reinforced thermoplastics (PP and PP/elastomer blend) and two glass fiber-reinforced plastics (PA6-GF35 and PBT-GF30) were analyzed, covering a frequency range from 0.063 Hz up to 20 Hz. The polyamide specimens were conditioned for seven days in distilled water. The findings indicate that a 10 °C change in temperature significantly reduces the fatigue life. Furthermore, a linear relationship between frequency and temperature increase was established.

Bernasconi et al. investigated the effect of frequency on PA6 with 30 % glass fiber content after conditioning the samples to account for the changing mechanical behavior depending on the absorbed water content [BK09]. The results show that the cyclic fatigue life decreases with increasing frequency. Three frequencies (1 Hz, 2 Hz, and 4 Hz) were investigated, while the temperature of the specimen at a frequency of 4 Hz reached up to 27 °C above room temperature (T_{Room} = 23 °C). Additionally, a correlation between strain rate and fatigue life is shown, independent of the prevailing temperature.

A significant amount of work by *Quaresimin*, *De Monte*, and *Moosbrugger* [MMJ+10, MMQ10, PCD+20, SM08] focuses on the fatigue behavior in short glass fiber-reinforced thermoplastics, examining the effects of fiber orientation, temperature, and frequency. Their studies included both uniaxial and multiaxial fatigue tests on PA66-GF35 (dry and not-conditioned), varying the r factors. It was observed that fatigue life decreased by 55 - 60 % when testing at 130 °C compared to experiments at 23 °C, regardless of the type of loading state of the material. The lowest bearable cycles were recorded for combined tension and torsion stress states [MMJ+10].

Sonsino and *Moosbrugger* further demonstrated that even at high loads, frequencies as low as 5 Hz and 8 Hz could lead to significant self-heating, causing temperature rises from 30 °C to 90 °C in tension-tension tests. Also, at a stress ratio of $r = \sigma_{Min}/\sigma_{Max} = -1$, where the mean stress is zero, considerable temperature increases of up to 72 °C were observed [SM08].

In [MMQ10], temperature increases of approximately 20 °C at 10 Hz were observed, particularly for 90 ° specimens. Furthermore, an inhomogeneous temperature distribution along the specimen was also noticed, with differences of up to 10 °C and notable higher temperatures in the shoulder transition area, which negatively influenced the damage location of the specimen and possibly falsified the obtained results.

Govaert et al. contribute extensively to the failure and, especially, to the fatigue behavior of technical thermoplastics [EAT+21, JGM08, Kan15, KKG16, Past19, PG21a, PG21b, PKE+20a]. Their research includes both non-reinforced and fiber-reinforced thermoplastics (PC, ABS, PMMA, PEI, HD-PE and PP), emphasizing the application of the time-dependent *Eyring's* flow theory. Therefore, they describe the lifespan of the materials using time to failure instead of the bearable number of cycles to failure, regardless of whether a static or dynamic cyclic load is applied to the material. Their studies consistently show that with increasing frequency, the failure-indicating curves (stress over time to failure) are shifted parallelly towards shorter times to failure but without altering the slope, supporting the concept that the load frequency significantly affects the fatigue behavior of thermoplastic materials.

The literature clearly indicates that frequency has a profound impact on the fatigue behavior of thermoplastics, primarily through temperature increases within the material induced by cyclic dissipation. As the frequency increases, the specimen temperature also rises, resulting in decreased fatigue life and notable alterations in material properties. The most important findings of the presented literature are summarized below:

- **Temperature increase:** The temperature within the material increases with rising frequency and load, leading to higher dissipation and, hence, self-heating within the specimen.
- **Change of cyclic lifespan:** The cyclic lifespan initially increases with rising frequency but then decreases beyond a threshold, primarily due to the increasing temperature within the material.
- **Constant slope of the fatigue data:** The slope of the fatigue data remains constant despite increasing frequency.
- **Decrease of time to failure:** With increasing frequency, the failure-indicating fatigue line shifts consistently to shorter lifespans when depicted over time to failure.

In the next subchapter, the influence of different frequencies on the PBT-GF30 specimens using the revised test equipment (compare Chapter 6) is investigated, focusing on the findings of the literature review.

7.1 Characterization of the fatigue life of PBT-GF30 under varying frequencies

For the experimental investigations, four load levels were initially defined based on previous studies conducted at 5 Hz for the same material to cover the cyclic lifespan range between 10^3 and 10^6 cycles. This applies to specimens extracted from the specimen plate both longitudinally and transversally relative to the flow direction. As a result, a total of eight load levels were selected for the following fatigue characterization, as outlined in Table 7.1. This data already indicates that transversal specimens can withstand a significantly higher number of load cycles compared to those oriented longitudinally to the flow direction when similar dynamic-cyclic loads relative to the quasi-static strength are applied.

	Longitudinal specimen		**Transversal specimen**	
Targeted number of cycles to failure N [-]	**Applied loads F_i [N]**	**Relative to the quasi-static strength F_i/R_L [-]**	**Applied loads F_i [N]**	**Relative to the quasi-static strength F_i/R_T [-]**
10^3	925	0.770	610	0.907
10^4	780	0.649	555	0.825
10^5	685	0.570	500	0.743
10^6	620	0.516	460	0.684

Table 7.1: Defined load levels for evaluation of the frequency effect on the fatigue behavior for longitudinal and transversal specimen.

In this work, the focus is on the fatigue behavior under tension-tension loading conditions, usually characterized by a load ratio of $r = \sigma_{Min}/\sigma_{Max} = F_{Min}/F_{Max} = 0$. However, to ensure that all applied loads remain within the tension-tension regime and to avoid any unintentional compressive loadings on the specimen due to control or other material-related fluctuations for instance caused by damage progression, a minimum load $F_{Min} = 20\ N$ is applied instead of $F_{Min} = 0\ N$. For comparison reasons, according to *Euler's* buckling theory (*Euler* case 4) $F_{crit.} = \pi^2\ EI/l_{eff.}^2$ with the material stiffness E, moment of inertia I and buckle effective length $l_{eff.}$, buckling would occur for the less stiff, transversely oriented specimen at a compressive load of approximately $F_{crit.} = 168\ N$ under the same clamping conditions used for the fatigue characterization [GHS+18]. Therefore, the load fluctuation must be significant to induce a possible buckling failure in the specimen, yet the minimum force, defined as $F_{Min} = 20\ N$, is maintained throughout all tests to ensure that the failure mechanisms remain consistent in the tension-tension regime. At the specimen level, this minimum load equates to a stress of 2 N/mm². Consequently, the actual applied load ratios are $r_{L,max} = 0.0322$ and $r_{T,max} = 0.043$ for the longitudinal and the transversal specimen.

The experimental fatigue tests are conducted at six different frequencies ranging from 2 Hz to 90 Hz. As a result, the frequency dependency within approximately two decades can be analyzed. Given the extended length from the hydraulic piston to the load cell of the experimental setup due to the required integration of the temperature chamber, it is crucial to ensure that no additional interfering vibrations occur at the applied frequencies. To address this, the entire experimental setup was analyzed across the full applied frequency range using a high-speed camera (Fastcam SA 1.1 from Photron USA, Inc., San Diego, USA) (compare [Fri21]). The frequency analysis revealed an additional transversal movement of the load introducing upper clamping, with the issue starting to become noticeable at test frequencies around 70 Hz. This transverse oscillation intensifies as the test frequency increases. It is assumed that the natural frequencies of the testing setup are being excited, leading to this oscillatory interference. However, since the setup cannot be easily modified - owing to the required length for being able to use the temperature chamber and the need for recalibration if the flange connection to the load cell would be replaced - the fatigue testing is proceeded with this test configuration. Consequently, the fatigue characterization at 90 Hz is conducted with the understanding that the additional oscillation can influence the material's fatigue behavior and must be carefully examined. The multi-axial loading induced by this transversal oscillation is anticipated to generate additional shearing within the specimen, potentially leading to a reduced fatigue life compared to a solely uniaxial stress state. All experiments are conducted at a set ambient temperature of the chamber of 23 °C.

Due to the large number of testing points generated by the four load levels, six frequencies, and two orientations, only two to three experiments are conducted per test point. This approach prioritizes the investigation of a broader parameter range, though it comes at the cost of reduced statistical reliability. As a consequence of the revision of the experimental test equipment (compare Chapter 6), it is expected that the degree of scattering will be reduced. Furthermore, the circumstance of necessary test duration emerges as a significant factor limiting the number of repetitions for the characterization of fatigue behavior.

The results of these fatigue tests under varying frequencies are depicted in Figures 7.1 and 7.2 for longitudinal and transversal specimens, respectively. The resulting experimental data successfully spans the targeted cyclic fatigue life range from 10^3 to 10^6 load cycles. Despite the limited number of repetitions per test point, the obtained data exhibits minimal scattering, suggesting that the experimental results are sufficiently robust to assess material effects. To enhance visual interpretation, failure points are approximated by guiding lines using power law fits, which deviate from the traditional *Basquin* equation and can also have curved forms.

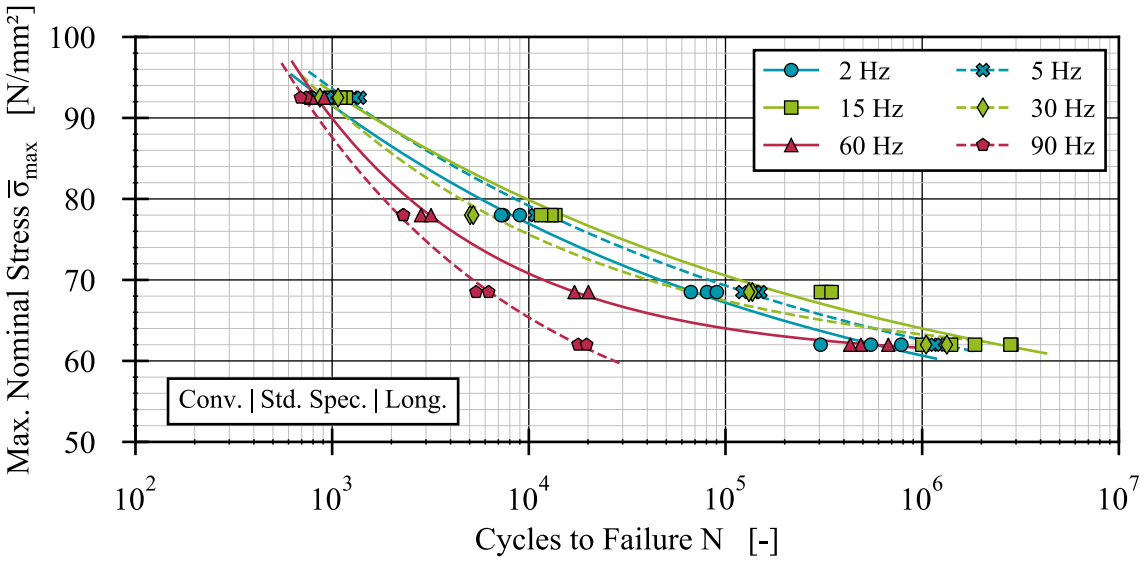

Fig. 7.1: Cyclic fatigue results for varying frequencies between 2 Hz and 90 Hz for the longitudinal specimens made of PBT-GF30. Markers are experimental data and lines are guides to the eye.

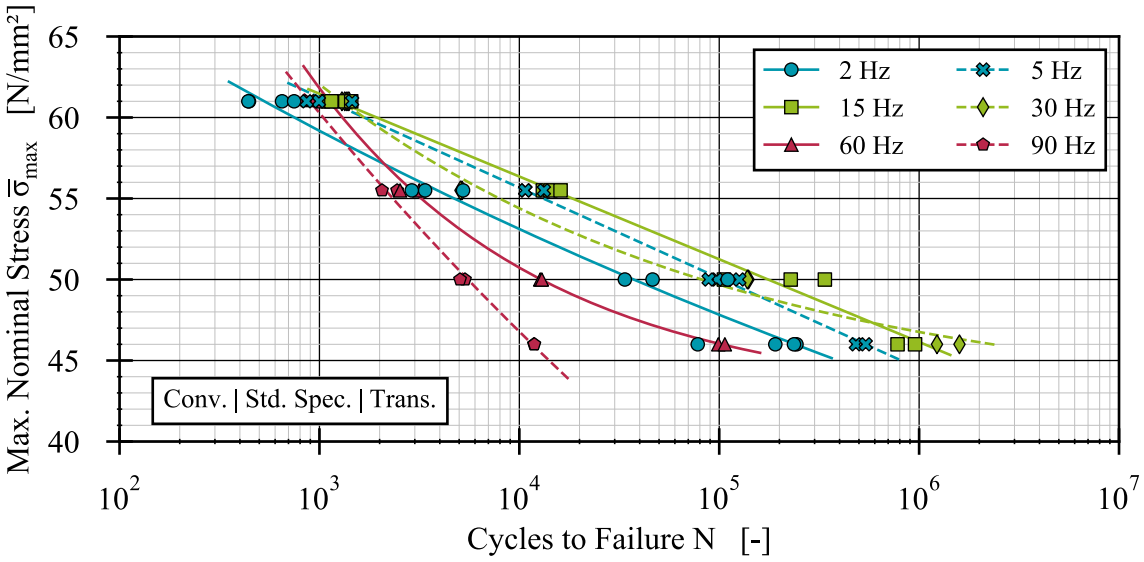

Fig. 7.2: Cyclic fatigue results for varying frequencies between 2 Hz and 90 Hz for the transversal specimens made of PBT-GF30. Markers are experimental data and lines are guides to the eye.

The results for the longitudinal specimens show two distinct clusters of data points corresponding to the highest and lowest load levels. At a load of 92.5 N/mm^2, all specimens fail after approximately 10^3 load cycles, with a scattered range within half a decade. In contrast, at a load of 62.0 N/mm^2, the scattering width is more pronounced, extending over a full decade. Particularly notable is the deviation of failure points at a load frequency of 90 Hz, where the cyclic lifespan at the same load level of 62.0 N/mm^2 drops to about $2 \cdot 10^4$ cycles. This indicates that increasing the loading frequency by a factor of four can result in a reduction of cyclic lifespan by approximately two decades. In addition, the fatigue life between the highest and lowest load levels decreases significantly as the frequency increases, resulting in a visible

curvature of the approximated guiding lines. It is noteworthy that the cyclic lifespan initially exhibits an increase with frequency, reaching a peak at 15 Hz, before a subsequent decrease at higher frequencies. This observation suggests that the highest cyclic lifespan for longitudinal specimens is achieved at a loading frequency of 15 Hz.

For the transversal specimens, a similar clustering of lifespan around 10^3 load cycles is observed at the highest load level of 61.0 N/mm^2. However, the scattering of data points at lower load levels is much more pronounced across the different frequencies compared to the longitudinal specimens. The “guide to the eye” fits show less curvature at lower frequencies compared to higher frequencies starting from 30 Hz. It should be noted that the range of the achieved cycles to failure is comparable to the longitudinal results across tests conducted at 15 Hz and 90 Hz. Furthermore, the highest cyclic lifespan is also achieved at 15 Hz for transversal specimens.

This finding aligns with previously discussed research [ZM06], which identified a reversal point in cyclic lifespan when a frequency range was investigated. For the tested PBT-GF30, this reversal point occurs at 15 Hz for both longitudinal and transversal specimens.

The same fatigue data is reinterpreted using a time to failure approach, as practiced by *Govaert’s* research group (compare Figure 7.3 and 7.4). The general trends remain consistent across load levels for each frequency, meaning that the slopes of the fatigue life indicating curves are identical to the ones for cycles to failure. However, these curves are shifted along the x-axis in accordance with the time-scaled lifespan. Both longitudinal and transversal specimens exhibit a clear decrease in time to failure with increasing frequency without showing the previously observed characteristic reversal point for the cycle to failure depiction anymore. Additionally, the deviation in lifespan becomes more pronounced at lower load levels. For example, at the lowest tested load levels, specimens subjected to a frequency of 2 Hz can withstand the dynamic cyclic load for up to 100 hours, whereas at the same load level but with a frequency of 90 Hz, the SFRT material can only sustain the load for a few minutes before a failure occurs.

Given that the prior literature review has demonstrated the significant impact of ambient temperature and temperature development on the achievable material fatigue lifespan under dynamic-cyclic loading, characterized by load level and frequency, in the following sections, the temperature developments observed during the experimental characterization are analyzed in detail.

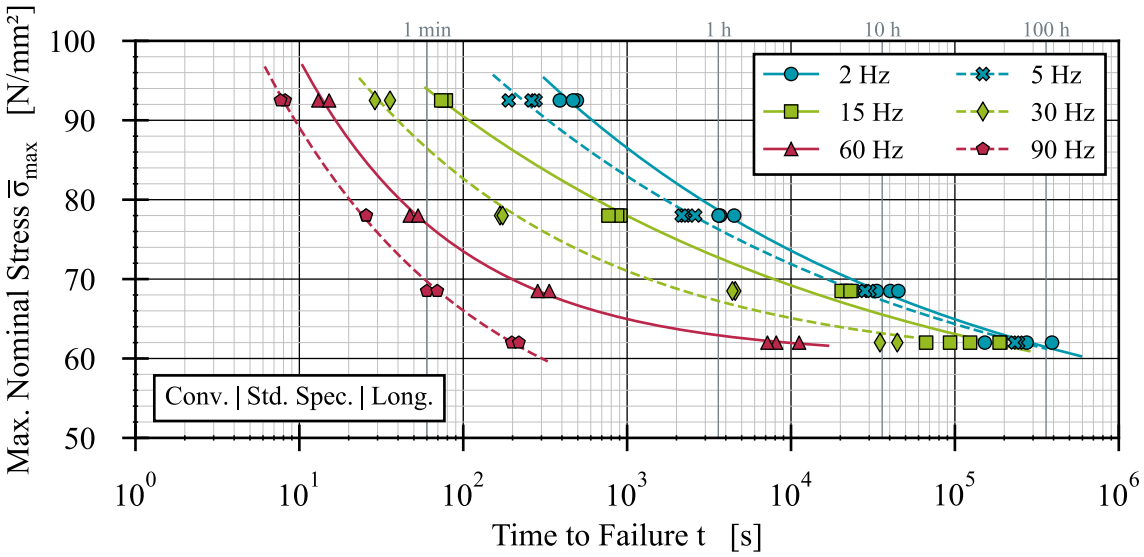

Fig. 7.3: Fatigue results over time to failure for varying frequencies between 2 Hz and 90 Hz for the longitudinal specimens made of PBT-GF30. Markers are experimental data and lines are guides to the eye.

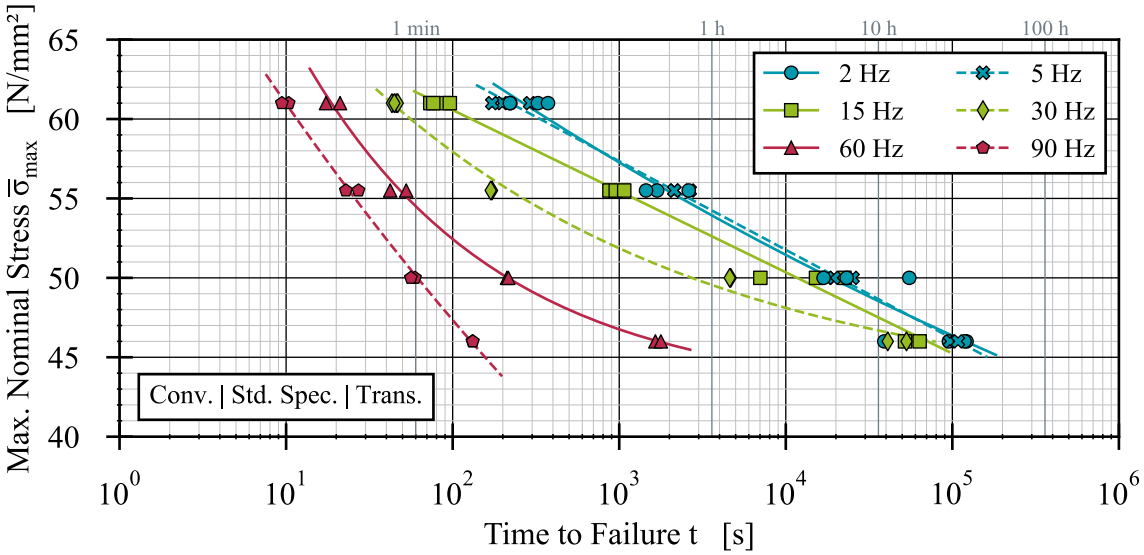

Fig. 7.4: Fatigue results over time to failure for varying frequencies between 2 Hz and 90 Hz for the transversal specimens made of PBT-GF30. Markers are experimental data and lines are guides to the eye.

7.2 Experimental evaluation of the temperature development during dynamic-cyclic loading under varying frequencies

As previously described, the surface temperature of the specimens is continuously recorded during all tests using an infrared pyrometer (compare Chapter 6.2). The following section will evaluate and analyze this temperature data to understand its influence on the experimentally obtained frequency-dependent fatigue life data discussed before.

The temperature data obtained from the infrared pyrometer is initially evaluated to assess its suitability as a representative measurement of the specimen temperature during the tests. The

infrared pyrometer measures the surface temperature of the specimen at a single point with a diameter of approximately 2.3 mm in the center of the specimen's testing area. For comparison, the 1BA specimen has a width of 5 mm. Hence, it is necessary to verify how representative the obtained pyrometer data is for the temperature distribution across the entire surface of the stressed area of the specimen. To assess the representativeness of the pyrometer data, the temperature distribution over the surface and the development over the test duration are also recorded and analyzed using a thermographic camera (FLIR A 600 Series, FLIR Systems Inc., Wilsonville, USA). Exemplary test points, particularly in the high-frequency range, are investigated. For all test points, a homogeneous temperature distribution is observed throughout the entire duration of the tests. However, after a certain load time, the temperature distribution begins to change, and local hot spots usually appear. In most cases, the specimens fail precisely at these thermal hot spots. It is assumed that damage localization occurs at these points, leading to increased energy dissipation and the formation of thermal hot spots.

In Figure 7.5, an exemplary comparison of temperature development for test parameters at a frequency of 30 Hz and a load level of 78.0 N/mm² is shown. Over the course of the test, the maximum local temperature deviates from the temperature measured by the pyrometer. Nevertheless, until just before fracture, the temperature difference remains at around under 3 °C to 4 °C. However, at the moment of fracture, the maximum temperature difference for this load reaches approximately 32 °C. This indicates that in the event of significant damage localization occurring outside the infrared pyrometer's designated measurement point, the resulting temperature increase cannot be accurately captured by the infrared pyrometer. It is important to note that at the time of this significant divergence, the material damage has already progressed substantially, and the specimen is in the final stages of failure.

Furthermore, on the right side of Figure 7.5, histograms of the temperature distribution recorded by the thermographic camera at three different time points are shown. The maximum temperature of the surface and the pyrometer data are indicated by the vertical lines. The temperature measured by the infrared pyrometer can accurately reflect the average surface temperature of the specimen. It is important to note that only the surface temperature can be assessed here, and the actual volumetric temperature distribution within the specimen can deviate from the surface temperature. In addition, the distribution width of the temperature can be attributed to the rectangular cross-section of the specimen, where the surface-to-volume ratio is greater at the edges than in the center of the specimen, causing the surface near the edges to be slightly cooler compared to the rest of the specimen's surface. However, based on these investigations, it can be concluded that the pointwise recording of the surface temperature using the infrared pyrometer can be taken as the representative temperature of the entire specimen surface for the analysis.

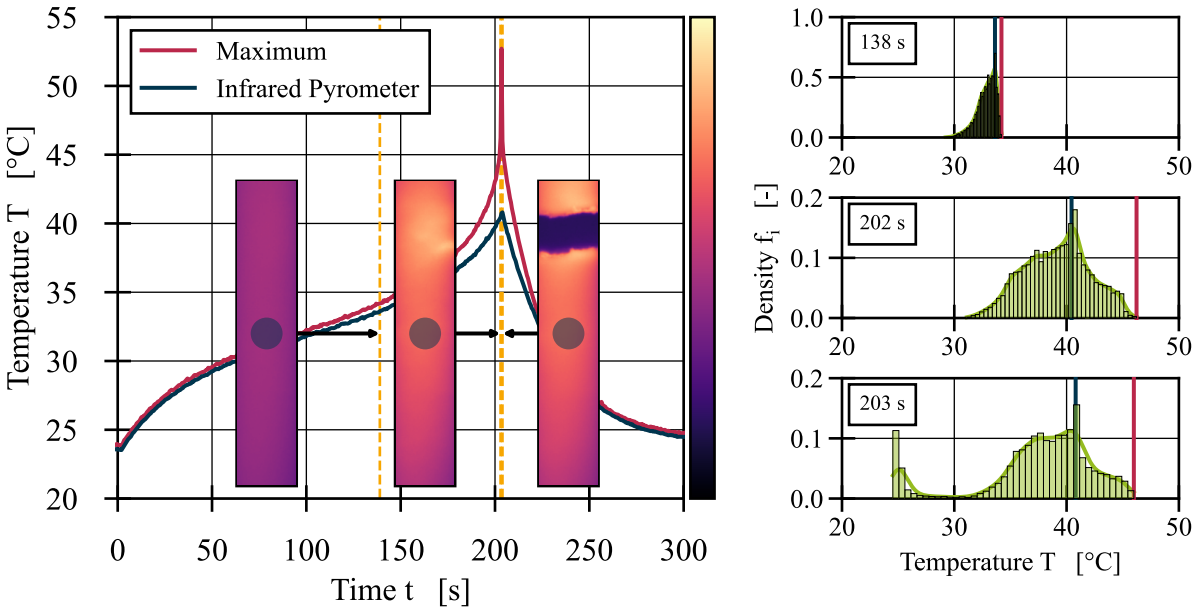

Fig. 7.5: Left: Comparison of the maximum temperature of the determined temperature distribution over the specimen surface measured by the thermographic camera and the local temperature data determined by the infrared pyrometer. Right: Temperature distribution over the entire test area surface of the specimen. The shown exemplary data is measured at a frequency of 30 Hz and a load of 78.0 N/mm² using a longitudinal specimen.

Figure 7.6 shows the time-dependent temperature development for single exemplary tests for each frequency and load combination, specifically for the longitudinal specimens. It is important to note that all tests were conducted in a temperature-controlled chamber set to an ambient temperature of 23 °C (compare Chapter 6). The data clearly shows that significant heat development can occur within the specimens, depending on the applied frequency and load level. The maximum recorded surface temperatures of the specimens reach up to approximately 75 °C, which is observed during the test at 90 Hz with the lowest applied load level of 62.0 N/mm².

Two distinct patterns, **progressive** and **stabilized** temperature developments, can be identified, each characterized by different temperature profiles over time. The progressive pattern is observed especially at higher frequencies, where a progressive behavior due to accelerated temperature increase is seen throughout the entire duration of the test. This type of temperature rise is notable for almost all test conditions at 60 Hz and 90 Hz and at high loads at 15 Hz, with a temperature increase of at least over 10 °C. This progressive heating can be assumed to clearly indicate a thermally induced failure caused by the dynamic-cyclic load application. The second pattern is characterized by either small or barely detectable stabilized temperature increases compared to the ambient temperature. In these cases, the temperature stabilizes over the time course of the test, rather than continuing to rise significantly. A turning point can often be observed in the temporal temperature profile, characterized by the rate of temperature decelerating after an initial progressive rise, eventually stabilizing. Despite this stabilization, a

slight but still noticeable increase in temperature over the test duration can be observed. As seen for the frequency of 30 Hz and a load level of 68.5 N/mm², towards the end of the test, just before failure occurs, the temperature typically rises again more sharply. In the tests conducted at frequencies of 2 Hz and 5 Hz, a maximum temperature increase of a few degrees is noticeable for the low load levels.

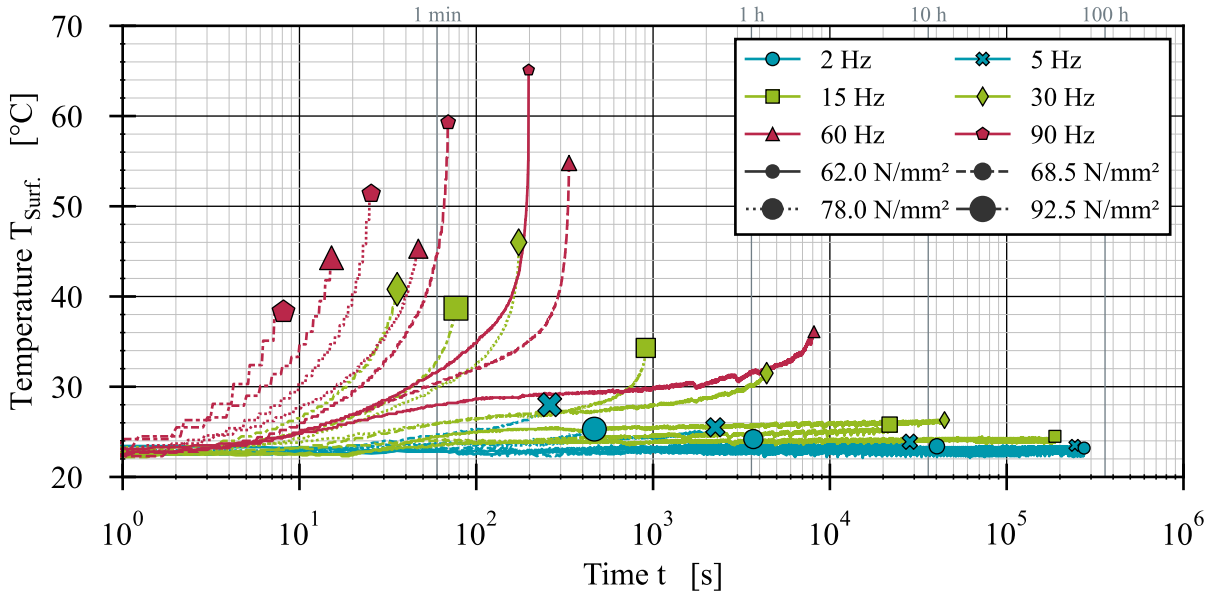

Fig. 7.6: Exemplary data for depiction of the temperature development for different load levels and frequencies for the longitudinal specimens made of PBT-GF30. Markers indicate the measured temperature at failure and the lines the temperature development over time.

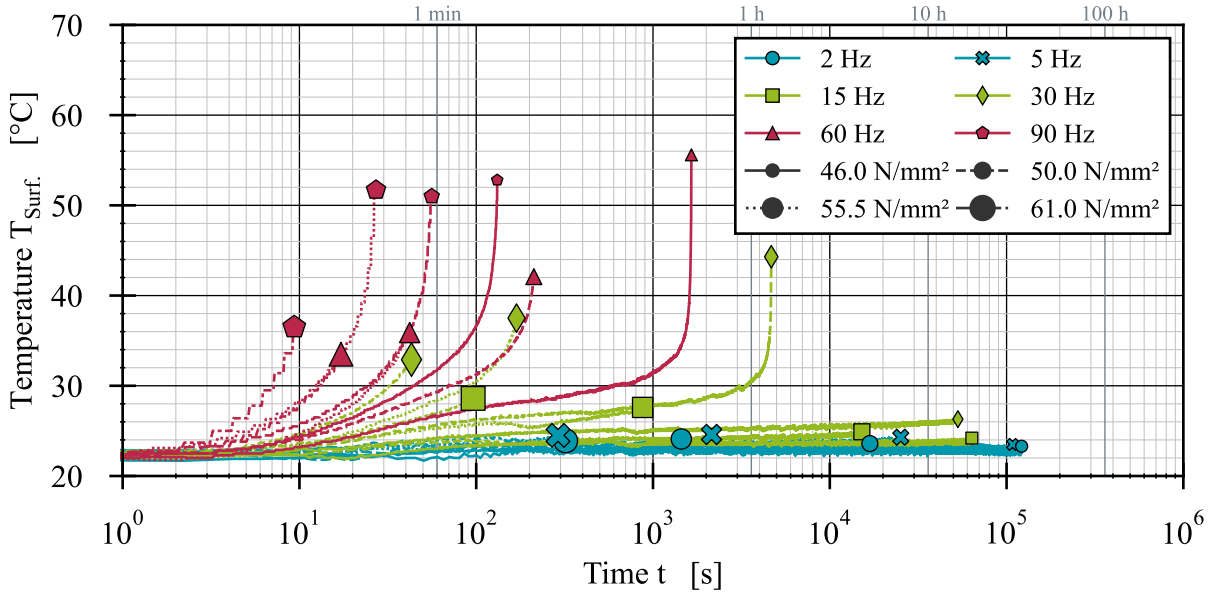

Fig. 7.7: Exemplary data for depiction of the temperature development for different load levels and frequencies for the transversal specimens made of PBT-GF30. Markers indicate the measured temperature at failure and the lines the temperature development over time.

Analogous to the temperature developments observed in the longitudinal specimens, the same conclusions can also be drawn for the transversal specimens (compare Figure 7.6). A detailed analysis of the temperature evolution over time allows the same distinction between progressive and stabilized temperature increases of the transversal-oriented specimens.

Figures 7.8 and 7.9 show the maximum temperatures measured during the fatigue tests for all longitudinal and transversal specimens. In the stabilized temperature development region, the lowest temperature increases are observed in specimens subjected to the lowest frequencies and load levels. For instance, at the lowest tested frequency of 2 Hz and a load of 62.0 N/mm², no significant temperature change is detected, suggesting that the specimen maintained approximately the same temperature as the ambient environment throughout the testing duration. As either the frequency or the load level is increased, a corresponding rise in temperature is observed, accompanied by a reduction in the material's lifespan. However, the frequency exerts a more pronounced influence on temperature than an increase in load level.

A contradictory trend is observed in the progressive temperature development region. In this region, the highest temperatures are recorded at lower load levels. For instance, surface temperatures ranging from 65 to 75°C were recorded for a load of 62 N/mm² at a frequency of 90 Hz. As the load level is increased, the achieved maximum temperature at failure decreases progressively. Consequently, the lowest temperatures were observed during the 90 Hz tests at the highest load level of 92.0 N/mm². Similar trends can be observed for the transversal specimens (see Figure 7.9).

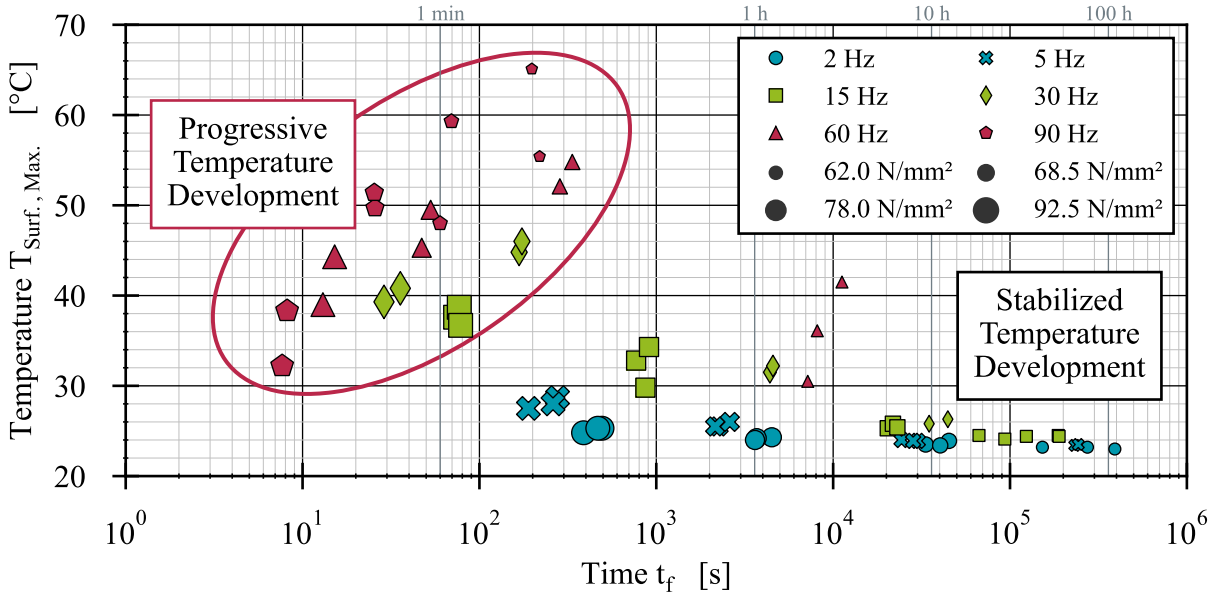

Fig. 7.8: Exemplary data for depiction of the temperature development for different load levels and frequencies for the longitudinal specimens made of PBT-GF30. Markers indicate the measured temperature at failure.

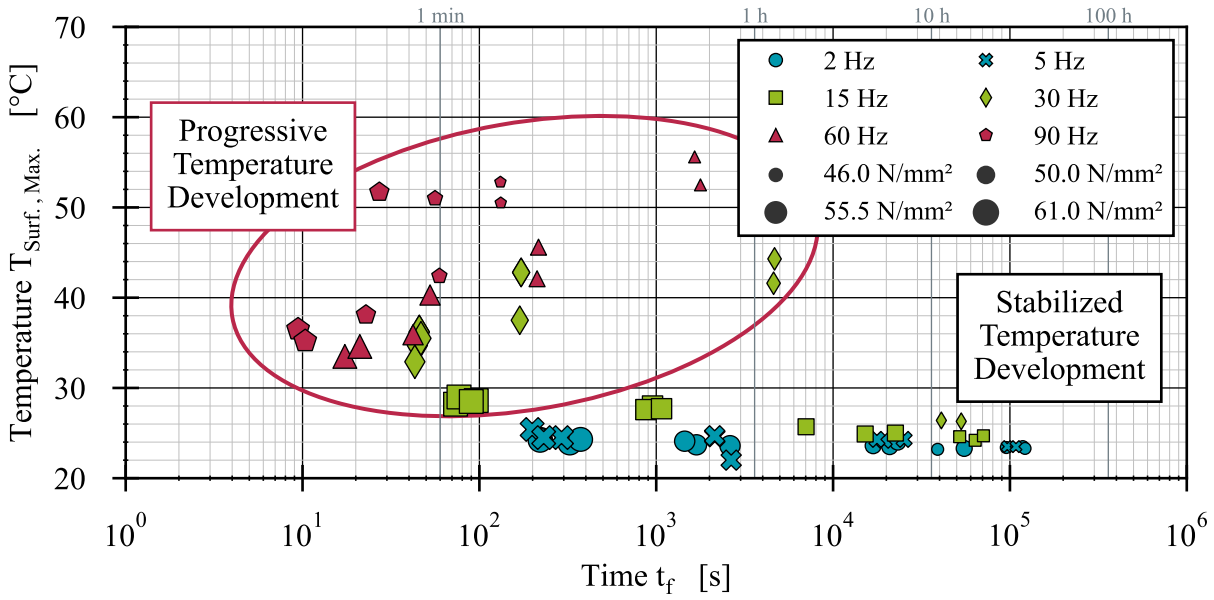

Fig. 7.9: Exemplary data for depiction of the temperature development for different load levels and frequencies for the transversal specimens made of PBT-GF30. Markers indicate the measured temperature at failure.

This behavior becomes even more apparent in the heatmap shown in Figure 7.10, where the average of the highest recorded surface temperatures is calculated across the repetitions for the different test parameter combinations. As the frequency increases for each load level, there is a general rise in temperature for all load levels. It is important to note that the infrared pyrometer is not able to capture every time the absolute highest occurring temperatures as described before. When the load level is increased for each frequency, there is a successive but less pronounced temperature increase up to frequencies of 15 Hz. However, at higher frequencies, this trend is reversed, and the highest temperatures are observed at the lowest load levels.

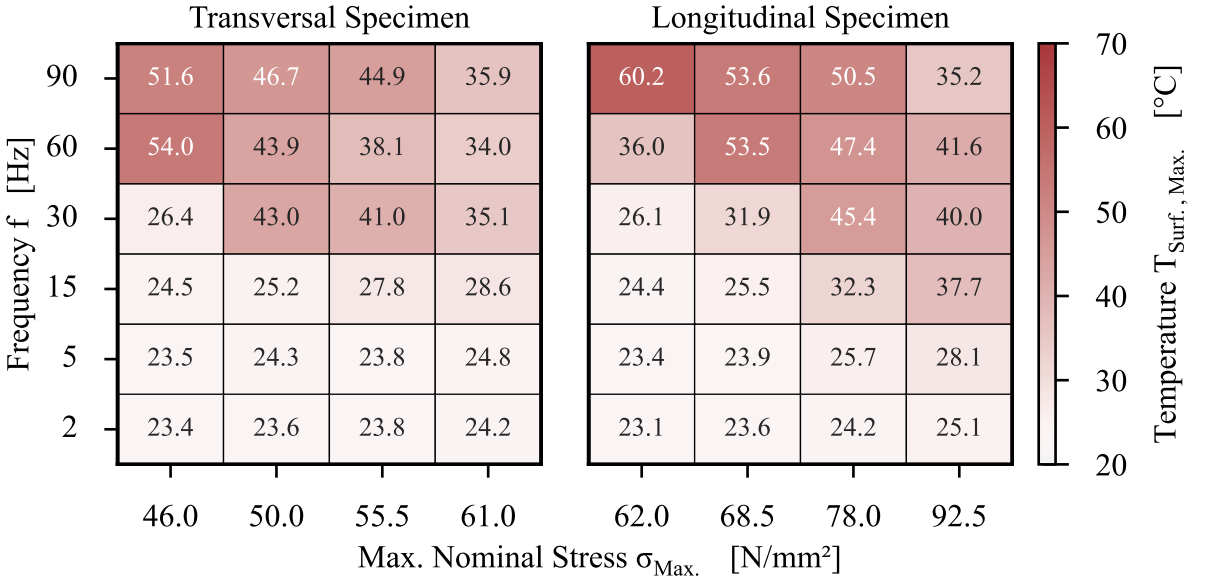

Fig. 7.10: Heatmap depicting the averaged maximum temperature measured at the failure of the specimens depending on the applied load level and frequency.

From the material's perspective, this behavior can be explained by the temperature-dependent strength properties of thermoplastic materials. As the temperature within the material increases, its strength decreases. This indicates that despite the fact that elevated loads result in increased heat dissipation within the specimen, the tests do not reach higher temperatures due to failing before higher temperatures can be achieved. Furthermore, this behavior can be taken to distinguish between progressive and stable temperature development. This boundary can be drawn at approximately 15 Hz. As can be seen in Figures 7.1 and 7.2, the reversal point of the cyclical lifespan is also at this frequency.

When comparing these temperature data with the failure points illustrated in Figures 7.3 and 7.4, it is evident that material failure occurs significantly earlier at test points where the material temperature exceeds the ambient temperature by more than 10 °C. This results in a curvature of the SN lines. Fatigue tests with minimal temperature increases are well-approximated by linear models, such as the *Basquin* fit, which is commonly employed in fatigue analysis. Consequently, a curved failure line indicates a thermally induced failure behavior. However, the inverse is not necessarily true since a linear failure line does not rule out thermally induced failure, as demonstrated by the failure line for transversal specimens tested at a frequency of 90 Hz (compare Figure 7.4).

Given that the frequency- and load-dependent fatigue lifespans for longitudinal and transverse specimens, along with the resulting significant temperature development, have been experimentally determined, the following section will examine the factors influencing temperature development in detail.

7.3 Quantitative analysis of the temperature development due to dynamic-cyclic load

In the following section, the temperature evolution within the material during dynamic-cyclic loads is discussed depending on the boundary conditions of the thermal environment maintained by the temperature chamber in which the fatigue tests are conducted. Therefore, it is essential to describe the temperature evolution under fatigue load conditions in terms of energetic relationships and properties, including changes resulting from damage progression.

During dynamic-cyclic loading, mechanical energy is introduced into the material and stored as elastic strain energy. However, a small fraction of this energy is irreversibly lost due to material internal losses. Upon unloading, the material also cannot fully recover the stored strain energy because of these dissipative effects. The energy difference between the loading and unloading phases results in energy dissipation in the form of heat, often referred to as hysteresis losses [BCR14b, WS12]. If the dissipated energy accumulates faster than it can be transferred to the environment, this behavior can lead to a temperature increase within the material. The rate of heat transfer is primarily influenced by the material's thermal conductivity and the

efficiency of thermal exchange with the surrounding environment [BCR14a, BCR14b, MFM+15].

To describe this thermal behavior quantitatively, an energetic relationship must be formulated using the first and second laws of thermodynamics. This relationship is detailed in Appendix 15.2, where the derivation of the equation describing the temperature evolution in mechanically loaded materials, treated as a closed system interacting with its environment, is explained step by step by applying the thermodynamic framework. Accordingly, Equation 7.1 provides the energetic foundation for the subsequent analysis. The time-dependent change in temperature $\dot{T}$ is a function of mechanically, thermally, and thermo-mechanically induced energy fractions as well as material parameters such as the density ρ and heat capacity c_p of the material under mechanical loads.

$$\rho c_p \dot{T} = \left\{ \boldsymbol{\sigma} : \dot{\boldsymbol{\varepsilon}}_{\boldsymbol{p}} - \rho \frac{\partial \psi}{\partial \boldsymbol{V}_{\boldsymbol{k}}} : \dot{\boldsymbol{V}}_{\boldsymbol{k}} \right\}_{mech.} + \{-div(\boldsymbol{q})\}_{therm.} + \left\{ T \left(\frac{\partial \boldsymbol{\sigma}}{\partial T} : \dot{\boldsymbol{\varepsilon}}_{\boldsymbol{e}} + \rho \frac{\partial^2 \psi}{\partial T \partial \boldsymbol{V}_{\boldsymbol{k}}} : \dot{\boldsymbol{V}}_{\boldsymbol{k}} \right) \right\}_{therm-mech.} \quad \textit{(Eq. 7.1)}$$

In this context, the solely mechanical contribution is defined by the mechanically induced product of stress $\boldsymbol{\sigma}$ and the inelastic strain rate $\dot{\boldsymbol{\varepsilon}}_{\boldsymbol{p}}$, in addition to the change in *Helmholtz* free energy $\rho \frac{\partial \psi}{\partial \boldsymbol{V}_{\boldsymbol{k}}} : \dot{\boldsymbol{V}}_{\boldsymbol{k}}$ resulting from material alterations. The internal material variables $\boldsymbol{V}_{\boldsymbol{k}}$ are established to describe dissipative processes occurring within the material, including alterations at the molecular level, dislocation configurations, or defect distributions [Chr12, LC94, Mur12]. The concept of the internal variable $\boldsymbol{V}_{\boldsymbol{k}}$ is discussed in detail in the Appendix 15.3. It should be noted that the term $\boldsymbol{\sigma} : \dot{\boldsymbol{\varepsilon}}_{\boldsymbol{p}}$ can also be interpreted by the change of the *Helmholtz* free energy ψ over the internal material variables $\boldsymbol{V}_{\boldsymbol{k}}$. However, for the understanding of this discussion, it is formulated here using direct mechanical quantities. The thermal component refers to the heat exchange $div(\boldsymbol{q})$ within the material and with the environment. Additionally, there are the thermo-mechanical components, which describes the thermoelastic effect $T \frac{\partial \boldsymbol{\sigma}}{\partial T} : \dot{\boldsymbol{\varepsilon}}_{\boldsymbol{e}}$ and the change in *Helmholtz* free energy $\rho T \frac{\partial^2 \psi}{\partial T \partial \boldsymbol{V}_{\boldsymbol{k}}} : \dot{\boldsymbol{V}}_{\boldsymbol{k}}$ with respect to temperature T and internal variables $\boldsymbol{V}_{\boldsymbol{k}}$ [BCR14b, Chr12, LC94, Mur12].

Accordingly, the time-dependent evolution of temperature is a function of five distinct energetically motivated terms. To simplify the equation, the following assumptions are made: It is reasonable to neglect the term $\frac{\partial^2 \psi}{\partial T \partial \boldsymbol{V}_{\boldsymbol{k}}}$, given that no significant temperature-induced changes in the material's morphological structure are anticipated during fatigue testing that would lead to substantial temperature variations of the material.

Additionally, the thermoelastic effect is neglected. When a material with a *Poisson's* ratio less than 0.5 undergoes elastic deformation, its volume decreases, causing a temperature change in an adiabatic system due to entropy elasticity. For materials with a positive thermal expansion coefficient, this results in a detectable temperature decrease; a material with a negative coefficient shows the opposite effect [LC94, SML+17]. However, considering the *Clausius-Duhem* inequality in Equation 15.18 for dissipation, it becomes evident that the thermoelastic effect is not included as a dissipation contributor, as it represents a reversible temperature change dependent on the immediate stress state of the material. Thus, under dynamic-cyclic loading, the thermoelastic effect does not contribute to the averaged net temperature increase and can be neglected in long-term temperature evolution analysis. Nevertheless, the thermoelastic effect is briefly addressed at this point. As noted in the literature [Chr12, PP03], the thermoelastic effect is often used to validate thermodynamically consistent material models. However, in the context of the fatigue experiments conducted in this study, the surface temperature of the specimens is measured using the infrared pyrometer at a sampling rate of 1 Hz. This rate is insufficient to capture temperature fluctuations within cycles at frequencies of 2 Hz and 90 Hz. Regardless, it is observed that at the beginning of the tests, while applying the mean load right before the dynamic-cyclic load phase started, a temperature decrease is noticed (see Figure 7.11). Nevertheless, a reversible temperature reduction of approximately 0.3 °C is insignificant in the context of this work. Therefore, for the subsequent analyses, the thermoelastic effect is neglected and will not be addressed further.

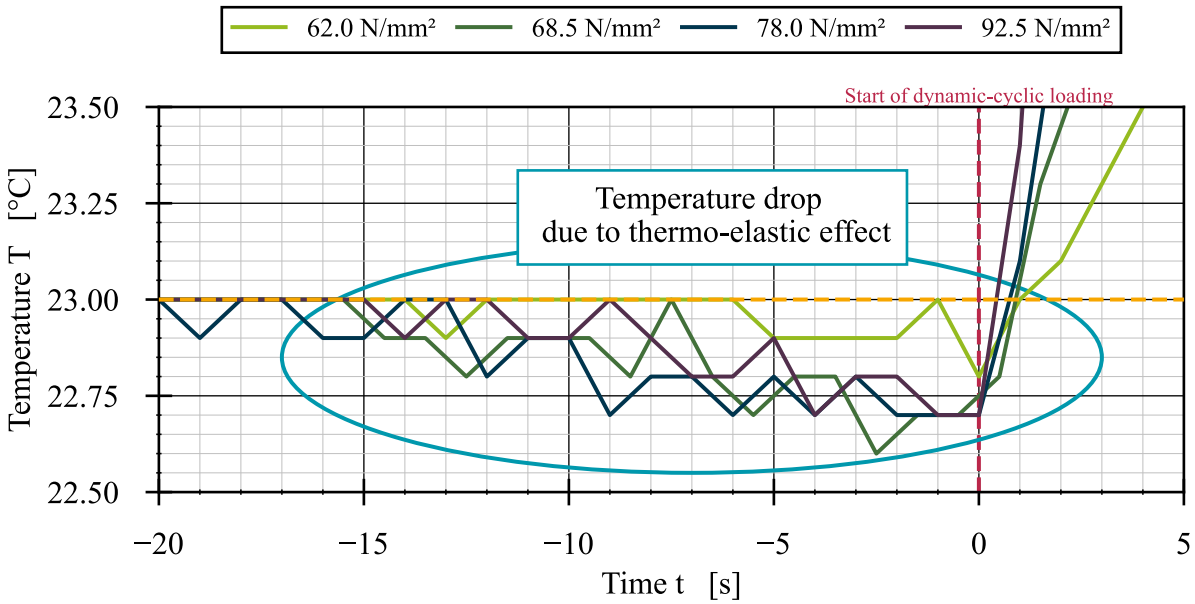

Fig. 7.11: Temperature decrease due to the thermoelastic effect when approaching the mean load is shown for different load levels at a test frequency of 60 Hz.

Since the *Helmholtz* free energy and internal variables cannot be directly determined but are defined as material dissipation as stated by the *Clausius-Duhem* relationship, the entire

mechanical contribution can be approximated by a parameter representing the homogenized dissipation rate $\{\dot{\Delta}\}_{mech.}$ that includes all material effects (viscoelasticity, plasticity, damage etc.) (compare Equation 7.2).

$$\left\{\boldsymbol{\sigma}:\dot{\boldsymbol{\varepsilon}}_{\boldsymbol{p}}-\rho\left(\frac{\partial\psi}{\partial\boldsymbol{V}_{\boldsymbol{k}}}:\dot{\boldsymbol{V}}_{\boldsymbol{k}}\right)\right\}_{mech.}=\{\dot{\Delta}\}_{mech.} \qquad \textit{(Eq. 7.2)}$$

This approach significantly simplifies the relationship describing the time-dependent temperature evolution of the stressed material, which can be represented by equation 7.3.

$$\rho c_p\dot{T}=\{\dot{\Delta}\}_{mech.}+\{-div(\boldsymbol{q})\}_{therm.} \qquad \textit{(Eq. 7.3)}$$

At this stage, the hysteresis behavior and the resultant dissipation rate are explained in terms of internal material behavior. When a thermoplastic material is subjected to dynamic-cyclic loading, it experiences repeated cycles of stress and strain, during which kinetic energy is continuously introduced into the system. This energy is partially converted into potential energy, which is stored within the material's structure as it deforms elastically. The remaining portion of the energy is dissipated as heat due to several factors, including internal friction, molecular-level interactions, and the initiation or propagation of micro-damages within the material. As the material is unloaded, some of the stored potential energy is released and converted back into kinetic energy, allowing the material to partially recover its original shape. However, not all of the stored energy is recoverable. A fraction of it is also dissipated during the unloading process, further contributing to heat generation. This ongoing cycle of energy input, storage, dissipation, and recovery leads to the formation of a hysteresis loop when plotting stress against strain (compare Figure 7.12).

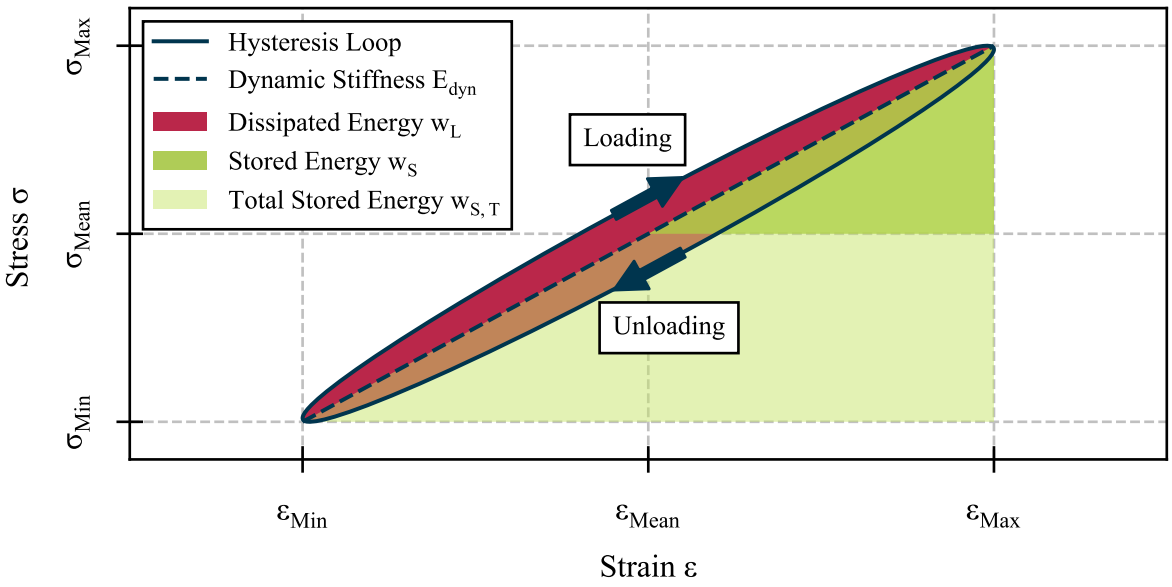

Fig. 7.12: Schematic depiction of the hysteresis loop while dynamic-cyclic load application. The shown description of the total stored energy is valid for the tensile-tensile load case.

The hysteresis loop can be ideally approximated by the time t and frequency f dependent trigonometric expressions in Equations 7.4 and 7.5. When a stress amplitude σ_{Amp} is applied to a material, the strain response ε_A lags behind due to dissipation mechanism, resulting in a phase shift quantified by the phase angle δ. If $\delta = 0$, the stress $\sigma(t)$ and strain $\varepsilon(t)$ are perfectly in phase, indicating purely elastic behavior with no energy loss, thus reducing the hysteresis loop to a straight line. For the further analysis, due to simplification reasons, the mean stress σ_{Mean} and strain ε_{Mean} are neglected.

$$\varepsilon(t) = \varepsilon_{Amp}\, sin(2\,\pi\, f\, t) + \varepsilon_{Mean} \qquad \textit{(Eq. 7.4)}$$

$$\sigma(t) = \sigma_{Amp}\, \sin(2\,\pi\, f\, t + \delta) + \sigma_{Mean} \qquad \textit{(Eq. 7.5)}$$

The slope of the hysteresis loop is described by the dynamic stiffness E_{dyn}, which serves as a material parameter distinct from *Young's* modulus obtained in quasi-static tensile tests. The dynamic stiffness E_{dyn} is defined as the ratio of the difference between the maximum and minimum stresses to the corresponding strain difference (see Equation 7.6).

$$E_{dyn} = \frac{\sigma_{Max} - \sigma_{Min}}{\varepsilon_{Max} - \varepsilon_{Min}} = \frac{\sigma_{Amp}}{\varepsilon_{Amp}} \qquad \textit{(Eq. 7.6)}$$

However, the dynamic stiffness E_{dyn} provides only a linear approximation of the stress-strain relationship under dynamic-cyclic loads and does not account for the energy dissipation. Assuming linear behavior, an oscillating signal can be decomposed into its real and imaginary components using *Euler's* formula [WS12]. This approach expresses the actual behavior with complex numbers, leading to the representation of the complex modulus E^* (Equation 7.7).

$$E^* = E' + iE'', \qquad \textit{(Eq. 7.7)}$$

The complex modulus E^* is usually used to represent the viscoelastic behavior of plastics. The elastic component is characterized by the storage modulus E', while the viscous behavior is represented by the loss modulus E''. The relationship between the loss modulus $E''$and the storage modulus E' can also be quantified by the phase angle δ (compare Equation 7.8).

$$\delta \approx tan\delta = \frac{E''}{E'} \qquad \textit{(Eq. 7.8)}$$

Both moduli uniquely define the energy contributions under dynamic-cyclic loads. To quantify the stored energy w_S and the loss energy w_L, Equations 7.4 and 7.5 are integrated over a load cycle. The stored energy w_S corresponds to the volume-specific potential energy stored in the deformation at the maximum strain amplitude ε_{Amp} during a load cycle (Equation 7.9) [WS12].

$$w_S = \frac{1}{2} E' \varepsilon_{Amp}^2 \qquad \textit{(Eq. 7.9)}$$

The stored energy calculated from Equation 7.9 significantly differs from the actual stored energy when the material is subjected to non-zero mean stress σ_{Mean}. For instance, the actual

total stored energy $w_{S,T}$ for a tensile-tensile load case (r = 0) is four times of w_S (compare Figure 7.12). Nevertheless, the established relationship for phase shift and energy dissipation ratio remains valid regardless of the load ratio, and therefore, this definition for the stored energy is used for the general framework to describe the material behavior.

The loss energy w_L, on the other hand, represents the energy dissipated as heat during the same load cycle. This dissipated energy is associated with the internal friction, molecular interactions, and other irreversible processes within the material that occur during cyclic loading. The loss energy is proportional to the loss modulus E'' and the square of the maximum strain amplitude ε_{Amp}^2, as described by Equation 7.10 [DHM22, WS12]:

$$w_L = \pi E'' \varepsilon_{Amp}^2 \qquad \textit{(Eq. 7.10)}$$

As the material undergoes extended load cycles, damage accumulates leading to changes in its behavior. This is directly reflected in the hysteresis , as the relationship between dynamic-cyclic stress and strain changes. Figure 7.13 illustrates the hysteresis behavior at different time points while applying dynamic-cyclic loads, clearly showing how the hysteresis loop changes over the duration of the testing. The dissipated energy w_L increases with the mechanical degradation of the material, as crack formation releases energy and creates new surfaces within the material, leading to additional friction under dynamic-cyclic loading. Therefore, the hysteresis loop thus not only describes the viscoelastic behavior but also all other dissipative processes in the material. At the same time, also the reduction in dynamic stiffness is typically used as a damage parameter to indicate the state of the material under fatigue loads [PD01, PD02].

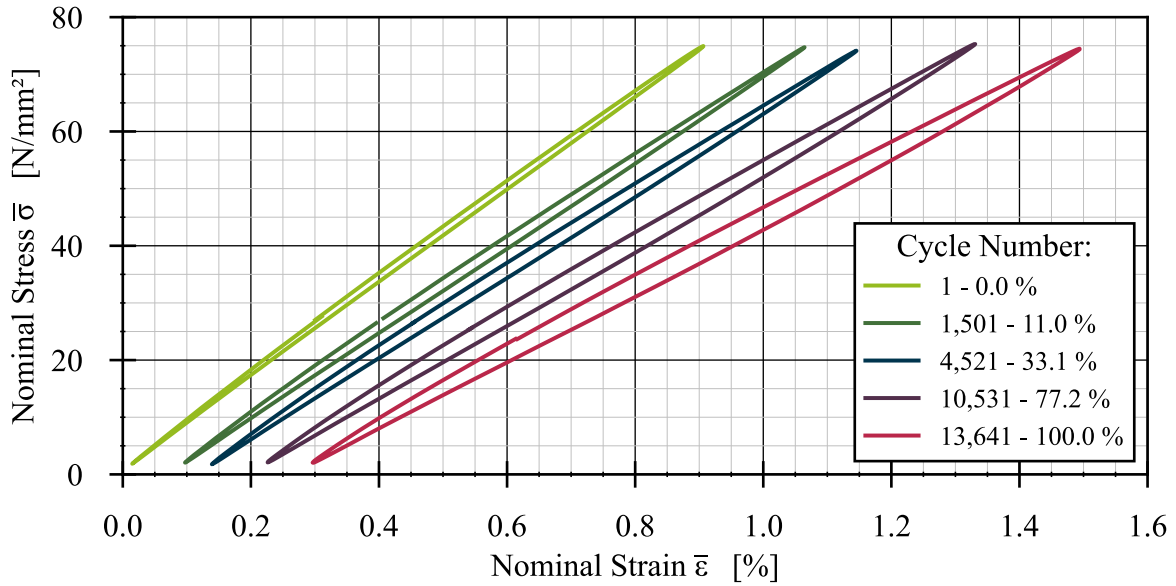

Fig. 7.13: Exemplary measured hysteresis over fatigue lifespan for a longitudinal specimen at a frequency of 15 Hz and a maximum stress of 78.0 N/mm². Specimen failed after 13,641 cycles.

Hence, the loss energy w_L, serves as a key parameter for describing the mechanically induced dissipation within the material. However, to accurately describe the time-dependent temperature evolution of the material, it is essential to consider the dissipation power, defined as the rate of energy dissipation over time, along with the applied loading frequency (see Equation 7.11). Together, these factors determine how much heat can accumulate in the material over time, influencing the overall thermal response.

$$\{\dot{\Delta}\}_{mech.} = f \cdot w_L \qquad \textit{(Eq. 7.11)}$$

To accurately describe the temperature evolution resulting from dynamic-cyclic loading, it is essential to consider not only the energy dissipation mechanisms within the material but also the heat exchange processes that occur within the material and between the environment (compare Equation 7.3).

Before analyzing temperature changes in a material, it is essential to determine whether the internal temperature distribution needs to be considered in detail or if it can be adequately approximated by the average temperature of the entire body. To make this evaluation, the *Biot* number, a dimensionless parameter in heat transfer, can be used. The *Biot* number *Bi* represents the ratio of the thermal resistance for heat conduction within the body to the resistance for the convection at the surface of the body [BW15, HM19]. It is calculated using the following Equation 7.12:

$$Bi = \frac{\alpha}{\lambda} l_C \qquad \textit{(Eq. 7.12)}$$

In this equation, α denotes the external convective heat transfer coefficient, which measures how effectively heat is transferred from the body's surface to the surrounding environment. The geometric parameter l_C is the characteristic length of the body, often defined as the ratio of the body's volume to its surface area $l_C = V/A$, reflecting the geometry of the considered body [BW15, HM19]. The thermal conductivity of the material is described by λ, indicating how well the material conducts heat internally.

A small *Biot* number, indicating that the external heat transfer coefficient is lower than the internal thermal conductivity, suggests minimal temperature differences between the surface, the average temperature, and the core of the body. For *Biot* numbers less than 0.5, it is generally accurate to assume a uniform temperature throughout the body for calculations [BW15].

To calculate the *Biot* number, the external heat transfer coefficient must first be determined, as it depends on the convective heat dissipation to the environment. In the context of this study, this coefficient is influenced by the cooling capacity and airflow conditions within the temperature chamber and must be experimentally measured.

The most straightforward experimental method to assess the cooling behavior of the specimens within the temperature chamber, driven by external convective heat transfer, is to analyze the temperature profiles over time immediately after specimen failure occurs. During the frequency-dependent fatigue tests previously discussed (Chapter 7.2), the specimens reach significantly higher temperatures than the set ambient temperature due to material dissipation. Once failure occurs and there is no further energy dissipation within the material, the cooling process becomes solely dependent on external convective heat transfer. To determine the heat transfer coefficient α, the time-dependent temperature change must be described. This can be conducted using Equation 7.13, which represents the normalized temperature decrease as a function of the dimensionless time τ. Here, T is the current temperature of the object of interest, T_{Max} is the temperature at the start of cooling, and T_{Amb} is the ambient temperature:

$$\frac{T - T_{Amb}}{T_{Max} - T_{Amb}} = e^{-\tau} = e^{-\frac{t}{t_0}} \qquad \textit{(Eq. 7.13)}$$

The geometry and material parameters that primarily govern the cooling behavior, and consequently the external heat transfer coefficient α, are defined in t_0. This parameter can be further specified as follows:

$$t_0 = \frac{\rho\, c_p}{\alpha} \cdot \frac{V}{A} = \frac{\rho\, c_p}{\alpha} \cdot \frac{1}{2} \cdot \frac{w \cdot d}{w + d} \qquad \textit{(Eq. 7.14)}$$

Here, ρ is the material density, c_p is the specific heat capacity at constant pressure, A is the surface area, V is the volume, w is the width, and d is the thickness of the specimen. The geometric parameters are defined by the specimen‘s geometry. Additionally, material properties such as density and specific heat capacity are required. At this point, the temperature-dependent density for PBT-GF30 is assumed to be constant with $\rho = 1{,}550\ kg/m^3$ (determined at $T = 23\ °C$), according to the material data sheet [NN19]. Differential scanning calorimetry (DSC) tests were conducted to determine the specific heat capacity, resulting in approximately $c_p = 1{,}425\ J/kg\ K$ (averaged for the temperature range of 20 °C to 50 °C). Using the experimentally measured cooling curves, Equation 7.13 can be fitted via regression analysis, allowing the external convective heat transfer coefficient α, hence, the cooling performance of the temperature chamber, to be determined based on the material and geometric parameters of the specimen. However, it should be noted that this approach already assumes that the measured surface temperature is representative for the entire test specimen.

For the determination of the external heat transfer coefficient α, only experiments conducted in the frequency range of 30 Hz - 90 Hz, where a maximum temperature of over 30 °C is reached, are used. Figure 7.14, left presents six exemplary cooling curves with corresponding regression fits, accurately capturing the temperature decrease over time. In Figure 7.14, right, the derived external convective heat transfer coefficients for both specimen orientations are depicted. These

coefficients range from 56.61 W/m²K to 100.00 W/m²K, with pronounced clustering around 63 W/m²K and a secondary less distinct cluster near 95 W/m²K. The mean value over all considered tests is 69.78 W/m²K. Due to fluctuations in the operating conditions of the temperature chamber, coefficients exceeding 75 W/m²K are treated as outliers. Consequently, a mean value of 63 W/m²K will be used in subsequent analyses.

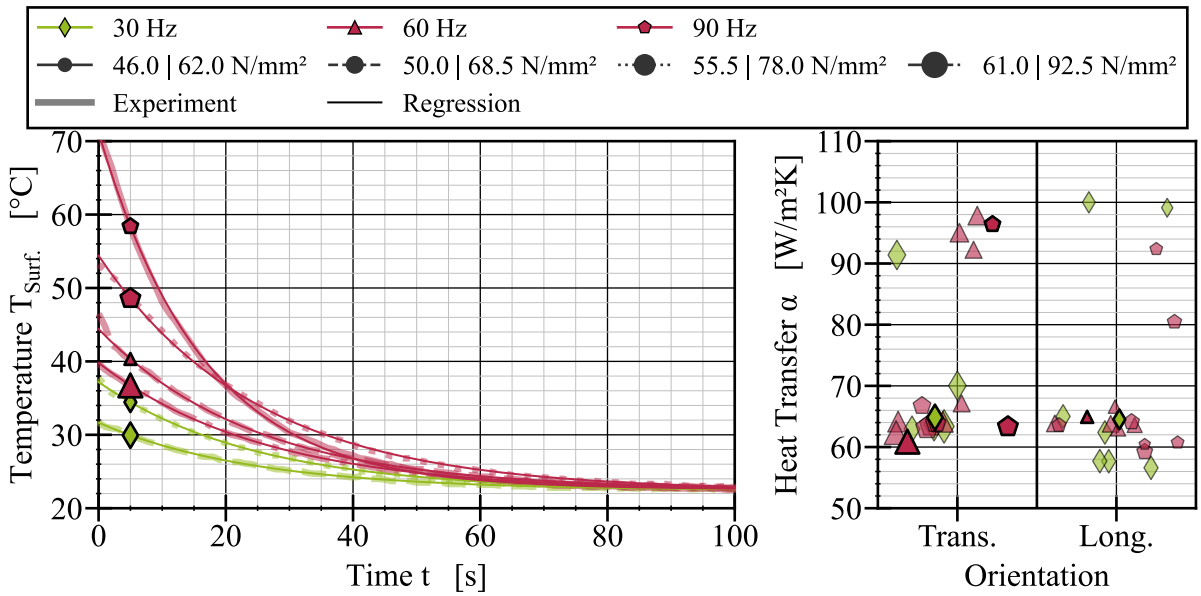

Fig. 7.14: Left: Exemplary time course of the cooling curves. Right: Determined external convective heat transfer coefficients. The analysis included all tests that exhibited an initial temperature above 30 °C.

To accurately calculate the *Biot* number, it is essential to determine the thermal conductivity of the material being studied. In this investigation, thermal conductivity measurements are performed using a light flash analyzer (LFA) on the LFA 467 HyperFlash, manufactured by NETZSCH-Gerätebau GmbH, Selb, Germany. The tests are conducted within a temperature range of 20 °C to 50 °C, providing conditions that closely approximate the operating environment of the material. It should be noted that the LFA initially measures the thermal diffusivity. The thermal conductivity is then derived using the material's density and specific heat capacity. The resulting thermal conductivity averaged for the temperature range of 20 °C to 50 °C is $\lambda = 0.278\ W/mK$.

For the 1BA specimen used here, the characteristic length, which represents the ratio of the body's volume to its surface area, is calculated to be $l_c = 0.714\ mm$. With this information, the *Biot* number is determined to be $Bi = 0.162$. This value is notably below the threshold of 0.5, indicating that the internal heat transfer within the material is much higher than the external thermal heat transfer at its surface. At first, this might seem counterintuitive since plastics are typically characterized by low thermal conductivity compared to other materials like metals. However, it is important to consider that the specimen used in this study has a thickness of only

2 mm, allowing for fast internal heat transfer and thermal homogenization. Consequently, the temperature distribution within the specimen can be considered relatively uniform, and the influence of internal temperature gradients is assumed to be minimal. Therefore, it is justified to approximate the specimen temperature distribution $T(x, y, z)$ with an average temperature $\bar{T}$ in subsequent thermal analyses and thermal conductivity within the specimen does not need to be considered (compare Equation 7.15).

$$\rho c_p \dot{\bar{T}} = f \cdot w_L + \{-div(\boldsymbol{q})\}_{therm.} \qquad \textit{(Eq. 7.15)}$$

In addition to convective and conductive heat transfer, heat can also be exchanged through radiation. Therefore, it is necessary to evaluate whether radiative heat transfer should be considered in the analysis of the material's temperature evolution during the investigations in this work. To assess this, the radiation and convection ratio (RCR) can be analyzed, which compares the radiative heat transfer to the convective heat transfer, as stated in Equation 7.16. This ratio helps determine the significance of radiation in the overall heat transfer process [Cen04, HM19].

$$RCR = \frac{\dot{Q}_{Radiation}}{\dot{Q}_{Convection}} = \frac{\epsilon\, \sigma_{SB}\, A \left(T_{Surf}^4 - T_{Amb}^4\right)}{\alpha\, A \left(T_{Surf} - T_{Amb}\right)} \qquad \textit{(Eq. 7.16)}$$

The radiative heat transfer is influenced by several key factors, including the material's emissivity ϵ, which represents its ability to emit thermal radiation relative to a perfect blackbody. The *Stefan-Boltzmann* constant σ_{SB}, a physical constant that defines the power radiated per unit area of a blackbody in terms of its temperature, is also essential in this calculation. The surface area A of the material, which is the total area exposed to the surrounding environment, directly affects both radiative and convective heat transfer [BW15, Cen04, HM19].

The surface temperature T_{Surf} of the material is critical in determining the amount of heat radiation and convection to the surrounding domain characterized by the ambient temperature as it drives the temperature difference with the ambient environment T_{Amb}. Additionally, the previously discussed convective heat transfer coefficient α takes place in Equation 7.16.

By analyzing the RCR, it can be determined whether radiative heat transfer is negligible or significant in the context of the overall heat transfer process. If the RCR is much less than 1, radiation can be ignored, whereas an RCR close to or greater than 1 indicates that radiation must be considered in the analysis [Cen04, HM19]. To estimate the radiation to convection ratio, a maximum surface temperature of 70 °C and an ambient temperature of 23 °C are assumed. Additionally, for a conservative estimate, an emissivity value of 1.0 is used, representing the material as a perfect emitter of thermal radiation [Cen04]. With these assumptions, the calculated RCR for the thermal case study under investigation results in a

value of $RCR = 0.072$. This low RCR indicates that radiative heat transfer is minimal compared to convective heat transfer, justifying the focus primarily on convection in the thermal analysis. Furthermore, it should be noted that Equation 7.16 only considers the radiated power from the object under consideration. The radiation from the chamber onto the test specimen would also affect the temperature development if the heat transfer mechanism via radiation would be dominant here, which is not the case due to the occurring low temperatures.

The time-dependent temperature behavior of the specimen under the frequency-dependent dynamic-cyclic loading can be described by the following first-order differential Equation 7.17:

$$\rho c_p V \dot{\bar{T}} = Vf \cdot w_L - \alpha A (\bar{T} - T_{Amb}) \qquad \textit{(Eq. 7.17)}$$

This first-order differential equation balances the heat generated within the material due to mechanical dissipation $Vf \cdot w_L$ with the heat lost to the environment through convection $\alpha A (\bar{T} - T_{Amb})$. The term $\rho c_p V \dot{\bar{T}} =$ on the left-hand side, represents the rate of change of the internal energy of the specimen, which is directly related to the rate of temperature change over time. After rearranging the variables, Equation 7.18 results.

$$\frac{\rho c_p}{\alpha} \frac{V}{A} \dot{\bar{T}} + \bar{T} = \frac{1}{\alpha} \frac{V}{A} f \cdot w_L + T_{Amb} \qquad \textit{(Eq. 7.18)}$$

By solving this differential equation, the time evolution of the average temperature $\bar{T}(t)$ under dynamic-cyclic loading can be predicted, providing insights into the thermal response of the material. This equation is particularly useful for understanding how the interplay between internal heat generation and external heat dissipation influences the thermal stability of the specimen under the specified loading conditions. As previously discussed, the experimental results for temperature development presented in Chapter 7.2 revealed two distinct types of temperature evolution: progressive and stabilized temperature development. Equation 7.18 can now be employed to quantitatively differentiate between these two forms. To do so, the derivative $\dot{\bar{T}} = \frac{d\bar{T}}{dt} = 0$ can be set, assuming a quasi-steady-state temperature. This implies that, after an initial rise in temperature, a thermal equilibrium is reached where the heat generated by dissipation balances the heat transfer to the environment. The resulting steady-state temperature can be expressed as in Equation 7.19 stated.

$$\bar{T} = \frac{1}{\alpha} \cdot \frac{V}{A} \cdot f \cdot w_L + T_{Amb} \qquad \textit{(Eq. 7.19)}$$

By applying this equation, the steady-state temperature of the specimen under specific loading conditions can be accurately predicted. If the steady-state temperature remains relatively low, the temperature development is classified as stabilized, indicating that heat dissipation is effectively balancing the heat generated.

In this equation, the primary material parameter influencing the outcome is the loss energy w_L. However, it is important to recognize that the mechanical properties of materials, particularly polymers, are highly sensitive to temperature. For instance, the viscoelastic behavior of polymers, which significantly impacts their damping characteristics and energy dissipation, is inherently temperature-dependent [DHM22, MO12, WS12]. As a result, the loss energy w_L is strongly dependent on the prevailing temperature. Due to this temperature dependence, solving Equation 7.19 requires iterative methods that take into account the variable nature of loss energy in response to the temperature conditions during testing. Moreover, due to the viscoelastic behavior of polymers, the loss energy is also influenced by the rate of loading (or strain rate) and the magnitude of the applied load. Therefore, loss energy w_L is not only temperature-dependent but also varies with the frequency f of the dynamic-cyclic loading and the specific stress state $\boldsymbol{\sigma}$ applied to the material. Additionally, as previously discussed, the degree of energy dissipation is further affected by the material's damage state, meaning that the progressive accumulation of damage during cyclic loading can also alter the loss energy w_L over the time of load application.

This interdependence reveals that Equation 7.19, which might initially appear straightforward, is actually quite complex due to the multiple factors influencing the loss energy w_L. Solving this equation analytically is challenging because the loss energy is a function of several variables, including stress $\boldsymbol{\sigma}$, frequency f, temperature T, and the damage state D of the material as written in Equation 7.20.

$$w_L = w_L(\boldsymbol{\sigma}, f, T, D) \qquad \textit{(Eq. 7.20)}$$

If the energy loss w_L is known at each point during the fatigue test, the temperature evolution can be predicted with without further ado using the previously discussed material properties and thermal heat transfer characteristics. Since in the experiments every tenth cycle is measured during the tests, capturing 100 data points for each hysteresis, these data can be used to calculate the temperature progression over time. For the purposes of verification, this analysis is performed using the finite element analysis software Abaqus/CAE 2020 from Dassault Systèmes Simulia Corp., Johnston, USA. The simulation predicted accurately the temperature evolution with a maximum deviation of 0.5 °C below the actual measured temperature, as shown in Figure 7.15. Only for the test at 78 N/mm² is the temperature peak not accurately reproduced. However, it should be noted that the hysteresis behavior is determined using an extensometer, meaning the measured dissipation is averaged over the area between the two measurement points of the extensometer. As a result, increases in dissipation due to localized damage events cannot be captured. The details of the model and the computational approach are not discussed in detail here, as they do not provide significant new insights into the

material's behavior and understanding. For further details, *Fritsche's* work is referenced here [Fri21].

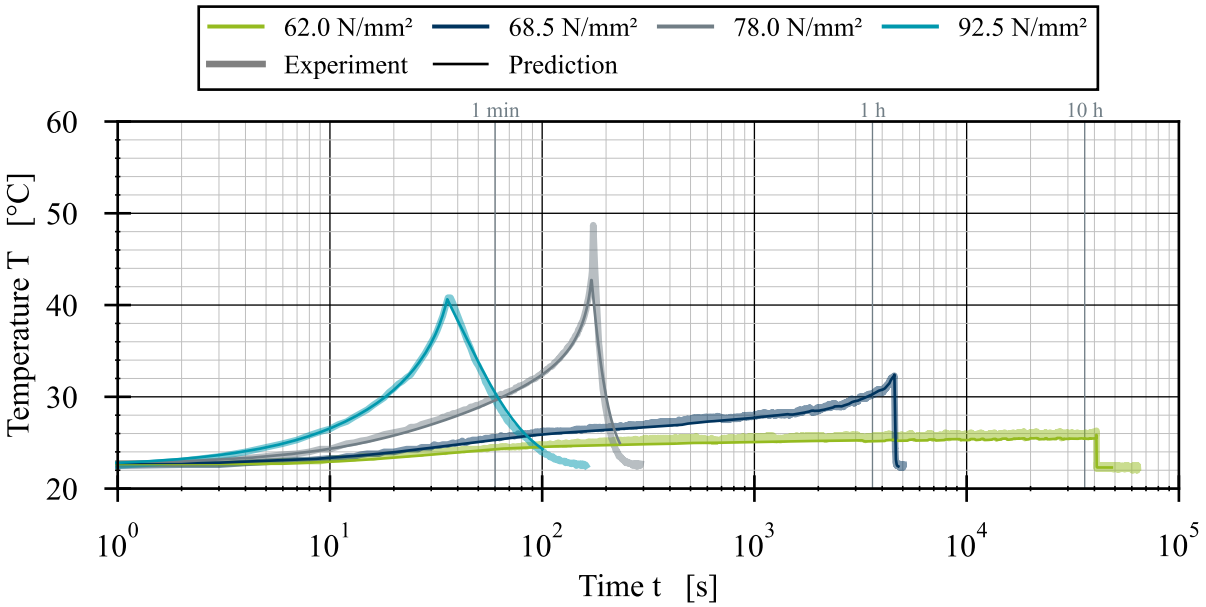

Fig. 7.15: Time-dependent temperature evolution of longitudinal specimens subjected to different stress levels and a frequency of 30 Hz under dynamic-cyclic loading. The graph compares experimental data with model predictions via FEM. A maximum deviation of ca. 0.5 K is observable (except for the temperature peak for 78.0 N/mm²).

To illustrate the dependencies and sensitivities between loss energy w_L, frequency f, and temperature T, Figure 7.16 compares the measured data for loss energy w_L, dissipated power $f \cdot w_L$, and the resulting surface temperature T at a stress level of 68.5 N/mm², across frequencies of 2 Hz, 30 Hz and 60 Hz, for longitudinal specimens. It should be noted that the loss energy and prevailing material temperature are in a direct, bidirectional interaction with each other. As the temperature increases, the material's viscous properties become more pronounced, leading to a higher dissipation of energy. This, in turn, requires more energy to be transferred to the surrounding environment to maintain the temperature. In the case of an inability to transfer the generated heat to the surrounding environment, an increase in temperature within the material will occur. However, the heat transfer mechanism is also driven by the difference in temperature between the material and the environment, which may cause the specimen to eventually reach a quasi-steady-state temperature (stabilized temperature progression). If the thermal equilibrium cannot be reached, a progressive temperature development will result.

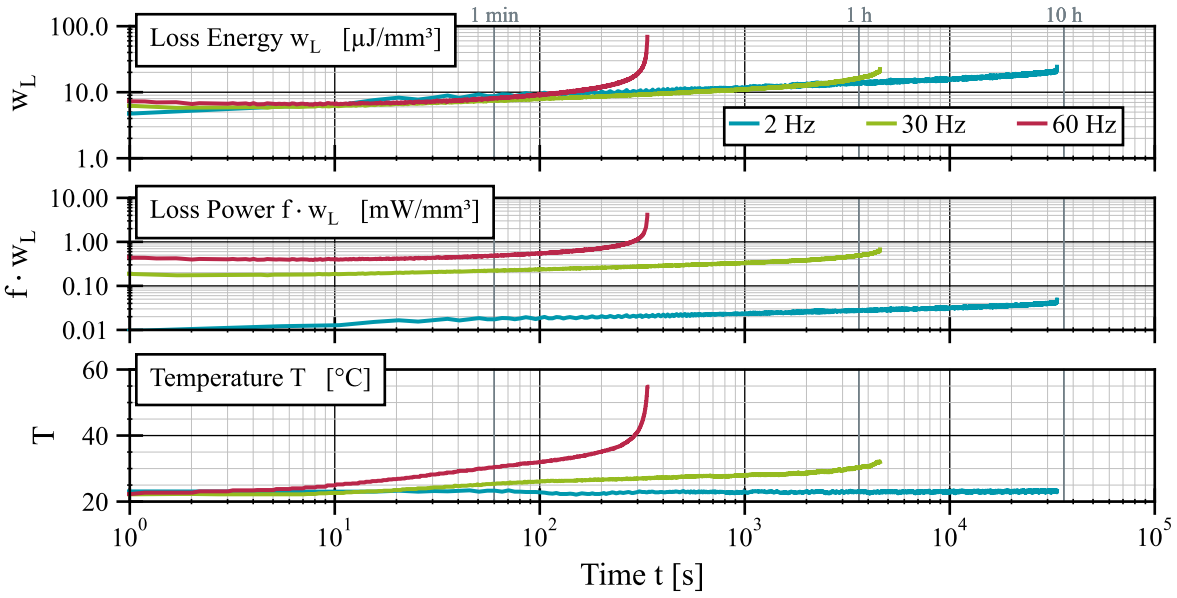

Fig. 7.16: Time-dependent evolution of the measured loss energy, loss power, and surface temperature for longitudinal specimens under dynamic-cyclic loading at 2 Hz, 30 Hz, and 60 Hz.

The diagrams in Figure 7.16 clearly show that, across different frequencies, the loss energy generated within the material remains at a similar level, but increases over time due to damage progression. However, the dissipated power, which is directly proportional to the frequency, is the main factor driving the increase in temperature within the material. Hence, if the loss energy increases over time, also the loss power will increase equally. Nevertheless, at 2 Hz, this increase appears to remain below a critical threshold, resulting in no significant temperature rise. At 30 Hz, a higher temperature within the material is initially established, and as the dissipated energy increases due to progressive damage, a gradual temperature rise occurs. Towards the end, this temperature rise accelerates due to intensified damage progress, eventually leading to material failure. At 60 Hz, the higher and progressively increasing loss energy corresponds to a more pronounced and rapid temperature rise until the specimen ultimately fails.

The bidirectional interaction between temperature and loss energy complicates the quantitative analysis of causality. As the temperature increases, the material's strength decreases due to its temperature dependence, further influencing the overall response. In the 90 Hz test, the pronounced and rapid temperature increase suggests that the premature failure is likely due to thermally induced weakening of the material, leading to a reduction in strength.

This detailed explanation underlines the importance of considering the relationships between temperature, loss of energy, and material properties in dynamic-cyclic loading scenarios. It also illustrates the challenges involved in isolating specific causal factors when multiple variables are interacting, emphasizing the necessity for a comprehensive approach to material analysis.

7.4 Preliminary conclusion regarding frequency-dependent fatigue and resulting temperature development

In summary, this study confirms many findings from the existing literature. Notably, it was observed that increasing the frequency initially leads to an increase in the number of load cycles the material can withstand, but beyond a specific frequency threshold (identified as 15 Hz in this work for the tested PBT-GF30), the cyclic fatigue life begins to decrease. When plotting the experimental data against time to failure, a subsequent reduction in time to failure with increasing frequency was also found.

Especially the significant impact of self-heating on the fatigue strength of short fiber-reinforced thermoplastics under continuous dynamic-cyclic load was determined. As the material heats up, its strength decreases leading to a decline in fatigue lifespan once notable heating occurs. However, at higher load levels, the material fails before substantial heating can occur, resulting in a curved SN line across the load range, which may indicate thermally induced failure.

However, stabilized and progressive temperature development can be clearly distinguished in the investigations. Stabilized temperature development occurs when the thermal equilibrium is reached, while the progressive development is characterized by a continuous, accelerated rise in temperature. Although the primary goal of fatigue characterization was to determine the dynamic strengths and corresponding lifespans, this study demonstrates that accurate temperature predictions can be made if the material's loss energy and heat exchange with the environment are known.

The influence of the heat convection is also evident. Ideally, SFRT material tests should be conducted in temperature-controlled chambers to ensure constant ambient temperatures. However, these chambers maintain temperature through forced convective heat exchange, resulting in high heat transfer coefficients due to air circulation. In contrast, natural convection, which is present when a body is at a higher temperature than its surrounding non-moving fluid (air), leads to significantly lower heat transfer rates [Cen04]. This discrepancy implies that the temperatures and lifespans determined under idealized conditions in the temperature chamber may not reflect real-world scenarios. This discrepancy also poses challenges for the comparability of fatigue results, even when morphologically and geometrically identical specimens are tested on identical machines but in temperature chambers with different cooling capacities or air circulation. These differences likely result in varying material temperatures under the same frequency leading to unfavorable fatigue outcomes.

Furthermore, understanding material damage under fatigue loading requires isolating the interaction processes occurring during fatigue. The loss energy is a crucial material parameter for describing heating behavior and understanding the damage process within the material.

Thereby, the damage progress can fundamentally be described with the reduction of *Helmholtz* free energy from a continuum mechanics perspective. However, due to the parallel and interdependent damage processes occurring at different scales, the hysteresis behavior and, hence, the loss energy provide important material characteristics. Ideally, the loss energy should be studied under isolated boundary conditions. Given that temperature is a key driver, in the following, a methodology is developed to eliminate the temperature influence, allowing for the investigation of the material behavior under fatigue loads solely due to load state characterized by frequency, stress-level and also damage progression.

8 QUASI-STATIONARY ISOTHERMAL FATIGUE CHARACTERIZATION

As previously discussed, the hysteresis behavior of SFRT materials can not only serve as an indicator of damage mechanisms and material states but also significantly influences the resulting material temperature when the dissipated energy cannot be released efficiently into the environment. This, in turn, affects the dynamic-cyclic material behavior, creating a feedback loop with the hysteresis itself. Therefore, to better understand the damage mechanisms and the resulting fatigue behavior, it is essential to develop a methodology that simplifies these interactions, allowing the study of the fatigue process without the interfering influence of temperature. In this chapter, a new characterization method is introduced to eliminate the influence of temperature increase due to self-heating, enabling the investigation of dynamic-cyclic deformation behavior and damage progression solely under the effects of loading frequency, load amplitude, prevailing fiber orientation distribution and preset material temperature. Before presenting this new approach, a brief review of the literature on the role of hysteresis in the fatigue behavior of fiber-reinforced plastics is provided.

In the work of [MML+15], the correlation between the loss energy and the resulting temperature increase is used to determine the dissipation of SBR-rubber under varying frequencies. The temperature increase while testing is measured and used to calculate the loss energy of the material depending on the load state via reverse-engineering. However, the loss energy due to dissipation is also measured by the testing machine recording the applied force and movement of the traverse, respectively stress and strain of the material.

In the studies of [JML+12, JMS+13], the fatigue lifetime of short carbon fiber-reinforced PEEK thermoplastic composite and PA66-GF50 is characterized using the same procedure as in [MML+15], but named the methodology “heat build-up protocol”. During the heat build-up procedure, the temperature of the specimen is measured, and changes in temperature are used to determine the dissipated energy of the material depending on the applied stress levels. The obtained values are then plotted against applied stresses and correlated with fatigue life data, and this method is applied as a criterion for predicting fatigue. However, it is important to note that dissipated energy naturally increases with the applied stress level, and in the heat build-up test, only the hysteresis behavior of undamaged specimens is assessed without considering changes in hysteresis behavior through damage progression. Essentially, the stress state is correlated with the fatigue life through the intermediate step of dissipated energy, which does not establish any causality regarding the fatigue life.

In the work of *Chen* [Che23], a master curve methodology for fatigue prediction under dynamic-cyclic shear loading in continuous fiber-reinforced thermoset materials was developed. The damage was also homogenized using continuum mechanical approaches.

However, numerical Representative Volume Element (RVE) models representing the microstructure of the material were developed and applied to determine the homogenized loss energy induced by cyclic damage progression. This numerically calculated energy loss was then used as an input for the master curve. The developed energy approach for the master curve was experimentally validated.

Furthermore, in the research of *Hopmann et al.* [HKF+20], dissipated energy is used to develop damage accumulation hypothesis not only for different load spectra but also for frequency-specific and mixed load-frequency spectra. The developed hypothesis is motivated by the loss energy characterized through the hysteresis loop rather than solely by the number of load cycles. Unlike the previously discussed publications, this study used the cumulative dissipated energy over the entire test duration as the assessment metric for different load phases. Hence, the effect of the damage progression on the hysteresis behavior is taken into account. This approach yielded for PA6-GF15 comparable results to traditional damage accumulation hypotheses. The key advantage of this approach, compared to conventional ones, is that no parameter calibration is required. The accumulation hypothesis relies solely on energy losses directly measured from experiments. Hence, although the experimental effort remains the same, there is no need for subsequent adjustments of material data using calibration parameters like in conventional damage accumulation hypotheses.

As previously discussed, temperature and hysteresis loops are interrelated through dissipation, preventing an independent, interaction-free investigation of the damage progression induced by fatigue loads at different frequencies. Therefore, based on the insights from the previous chapters, an alternative approach is developed in this thesis. Typically, heat convection is considered a given, non-changeable condition that must be characterized and determined every time. According to the literature [AML+13, JMS+13, MML+15, SML+17], it can be used to determine the loss energy using temperature data. Nevertheless, in the new approach developed here, heat convection is utilized as an adaptable control variable to maintain thermal equilibrium, preventing any temperature change despite increased frequency. This enables the investigation of frequency effects in isothermal fatigue tests.

8.1 Development of a thermo-adaptive cooling system for enabling quasi-stationary isothermal material characterization under dynamic-cyclic load application

To maintain the specimen's temperature within controlled limits during high-frequency dynamic-cyclic loading, where significant heat dissipation occurs, a thermo-adaptive cooling system is developed. This system is designed to prevent progressive temperature increases and ensure the accuracy of characterization and fatigue tests by minimizing temperature fluctuations caused by environmental factors or intrinsic material behavior and damage progression.

In the previously discussed investigations on temperature evolution, Equation 7.17 was derived, and the physical significance of its terms was explained. Besides the material-induced dissipated power stated as $f \cdot w_L$, two other key factors in the equation govern the thermal energy balance: the ambient temperature T_{Amb} and the convective heat transfer coefficient α. While material characterization, the ambient temperature is determined by the temperature chamber and, ideally, fluctuates minimally around a set temperature. Also, the ambient temperature acts as a static offset factor for the temperature evolution described by the additive term in Equation 7.17.

In contrast, the convective heat transfer coefficient α is a function of the fluid motion along the material's surface. By altering the airflow (forced convection), the convective heat transfer can be adjusted. Specifically, the convective heat transfer coefficient is proportional to ${v_{Fluid}}^{1/2}$ for the laminar and ${v_{Fluid}}^{4/5}$ for the turbulent case, as shown in Equation 8.1 [HM19]. This relationship indicates that increasing airspeed v_{Air} enhances convective cooling. Due to the exponents being less than one, the coefficient shows a degressive progression with increasing flow velocity v_{Fluid}. Nevertheless, varying v_{Air} allows for controlled manipulation of the thermal balance of the material.

$$\bar{\alpha} \sim \begin{matrix} {v_{Fluid}}^{1/2}, & laminar \\ {v_{Fluid}}^{4/5}, & turbulent \end{matrix} \qquad \textit{(Eq. 8.1)}$$

For targeted quasi-stationary isothermal material characterization, where the temperature change over time is zero $\left(\dot{\bar{T}} = \frac{dT}{dt} = 0\right)$ and the material temperature constant ($\bar{T} = const$), Equation 7.18 can be modified as follows (see Equation 8.2).

$$\bar{T} - T_{Amb} = \frac{1}{\bar{\alpha}(v_{Air})} \cdot \frac{V}{A} \cdot f \cdot w_L(\boldsymbol{\sigma}, f, T, D) \qquad \textit{(Eq. 8.2)}$$

This equation demonstrates that as long as any dissipation in from of loss energy w_L is generated within the material, a temperature rise above the ambient temperature will occur. However, the degree of this temperature increase can be controlled through the forced convection. If the dissipated energy within the material increases due to factors such as damage evolution, a corresponding increase in air velocity v_{Air} can dynamically compensate the effect of the higher dissipation regarding the temperature. If adjusting the convection rate $\bar{\alpha}(v_{Air})$ is insufficient due to limitations on increasing the air velocity, the ambient temperature T_{Amb} can serve as an additional parameter that may be reduced to maintain the target material temperature.

Thus, three key points can be stated. First, whenever dissipative processes occur within the material, a temperature difference relative to the ambient temperature will arise. Second, the

extent of the temperature increase depends on the dissipated energy, the ratio of volume to surface area of the material, and the forced convection. Finally, to keep the desired material temperature during the entire load application while testing constant, the ambient temperature can be adjusted to control the static temperature difference, while dynamic changes in dissipation, such as those caused by material damage progression, can be compensated by modifying the forced convection through dynamically increasing the velocity of the airflow around the tested specimen.

The convective heat transfer coefficient α determined experimentally in Chapter 7.3 is mainly influenced by the airflow conditions within the temperature chamber. A large fan within the chamber ensures high air circulation, which facilitates a uniform temperature distribution. By adjusting the fan's rotational speed, the convective heat transfer coefficient $\bar{\alpha}(v_{Air})$ could be manipulated. However, such adjustments would require modifications to the temperature chamber's electronics and an assessment of the fan's operational range. Additionally, any alteration could potentially disrupt the design of the temperature control system's design and functionality of the chamber.

To address this, an additional fan system is developed and integrated into the chamber to ensure that the specimen is exposed to airflow directly and in a controlled manner. By adapting the fan speed, the heat transfer of the forced convection can be adjusted as needed. The system draws in the air thermally preconditioned by the temperature chamber and accelerates it using axial fans. The developed experimental setup is shown in Figure 8.1.

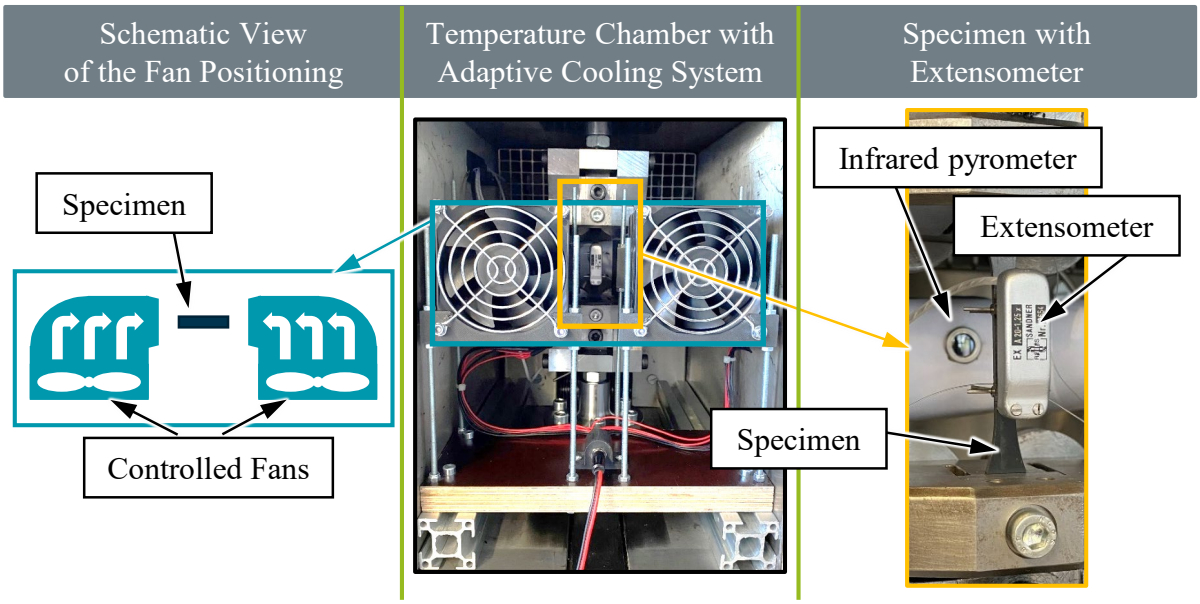

Fig. 8.1: Setup of the thermo-adaptive cooling system to enable quasi-stationary isothermal material characterization under dynamic-cyclic load application.

The fans are positioned on both sides of the specimen, with air deflectors precisely directing the accelerated airflow onto the specimen to ensure that both large surfaces are parallelly

exposed to the airflow. This two-sided configuration is chosen to achieve a uniform and symmetrical airflow, ensuring a homogeneous temperature distribution across the specimen.

To maintain the specimen's temperature at a constant level, the airflow must be dynamically adapted according to the momentary dissipated energy by the material. Therefore, an Arduino-based control unit is developed (Arduino Uno R3, Arduino S.r.l., Monza, Italy), which adjusts the fan speed through pulse-width modulation (PWM) of the fan's input voltage. For effective PWM control, the system needs to continuously assess the required level of fan speed respectively heat convection to keep the specimen's temperature constant. This is achieved through a control loop (compare Figure 8.2) in which the current temperature, measured by the infrared pyrometer, is fed into the control system as input. The infrared pyrometer, which continuously and instantaneously monitors the specimen's surface temperature, provides real-time feedback to the developed Arduino system. When the target temperature is exceeded, the fan speed increases; if the current temperature falls below the target, the fan speed decreases, dynamically adjusting the forced convection. This approach ensures rapid response times while avoiding overshooting or abrupt temperature fluctuations. However, due to the inertia of the fans, they continue to rotate even after the power is cut off, providing a gradual reduction in convective heat transfer rather than an immediate cessation. This inertia effect helps maintain a stable temperature around the specimen, preventing sudden drops that could compromise the fatigue test results.

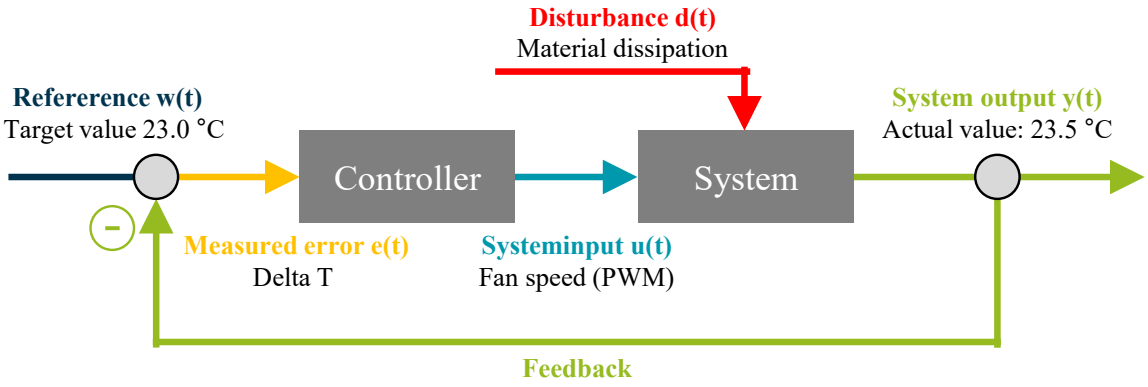

Fig. 8.2: Control loop for adjusting the fan speed to maintain a set target material's surface temperature.

The control unit is designed to allow any target temperature to be set via an integrated onboard user interface. Two different control strategies are implemented: bang-bang switching and PID control. In the experiments, both control strategies are evaluated, and it is concluded that the high processing speed of the Arduino, combined with the instantaneous temperature measurement provided by the infrared pyrometer, makes bang-bang switching sufficient for temperature regulation. This approach eliminates the need for complex determination of the PID controller parameters. A computer interface for logging and monitoring the cooling unit is

also developed. The electrical power for the Arduino is supplied via the USB interface of the control computer. Since the power supply via USB is insufficient for the dynamic operation of the fans, an additional power supply for the fans is used. The electronics are galvanically isolated from the control unit through a photodiode circuit to prevent any interferences regarding the different power supply sources. For the generation of airflow, two parallel configurations, each consisting of three high-performance fans (maximum airflow of 93.6 m³) connected in series to increase static pressure, are used.

The functionality of the developed thermo-adaptive testing methodology for quasi-stationary isothermal material characterization is exemplified in the diagram shown in Figure 8.3. Here, a longitudinal specimen is subjected to a dynamic-cyclic load of 78 N/mm² and a frequency of 60 Hz. In conventional tests, as presented in Chapter 7, the specimen fails within the first minute due to progressive temperature development, reaching temperatures exceeding 45 °C. However, with the newly developed quasi-stationary isothermal testing methodology, it can be observed that the temperature is maintained at a constant 23 °C throughout the entire testing duration. Given the significant dissipative power generated by the material and the load conditions, the ambient temperature is required to be set to 16 °C to keep the fans within their operational range. The specimen heats up during the first 30 seconds until the target temperature is reached, at which point the fans start to cool the specimen additionally. In this case, it is observed that the fan operates at approximately 20 % of its maximum power to maintain the specimen's temperature. Additionally, the fan power gradually increases as the dissipated energy within the specimen rises due to ongoing damage progression within the material, yet the specimen's temperature remains constant throughout the test. This advancement enables, for the first time, testing at high loads and frequencies without temperature increases.

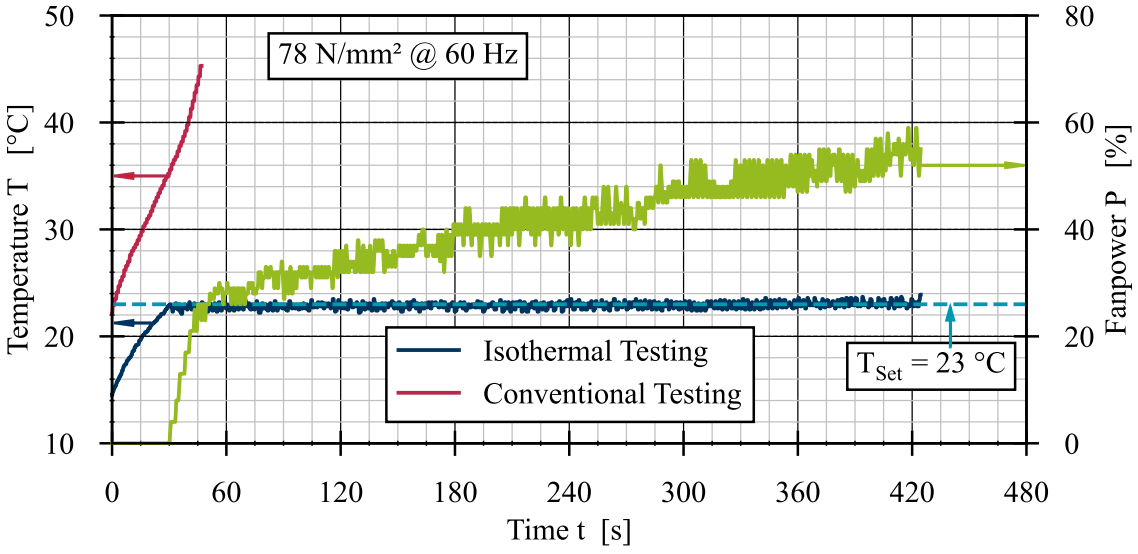

Fig. 8.3: Comparison of the temperature development in conventional experiments and tests with applying the thermo-adaptive cooling system. The applied load is 78.0 N/mm² at a frequency of 60 Hz.

Although in the previous Chapter 7.3, it has already been shown through the *Biot* number that the temperature distribution within the specimen is negligible, the next step will involve examining the temperature distribution across the cross-section of the specimen. This analysis is essential to ensure that uniform thermal conditions prevail throughout the entire cross-section (quasi-isothermal testing), thereby ensuring the damage processes occur under thermally homogeneous and comparable conditions.

8.2 Verification of the homogeneous temperature distribution within the specimen during quasi-stationary isothermal material characterization

To verify the temperature distribution within the specimen while using the thermo-adaptive cooling system for quasi-stationary isothermal tests, the finite element model previously applied in Chapter 7.3 is used since it has already been validated through experimental data obtained through the conventional fatigue tests. However, for calculating the temperature distribution during quasi-stationary isothermal testing, the previously applied approach must be modified since the convection rate can no longer be determined from the cooling curve after the specimen fails since the convective heat transfer coefficient is changed dynamically during the tests depending on the dissipated power within the material. Instead, the surface temperature at the pyrometer measurement point is used as the reference. Given that a target temperature of 23 °C is consistently maintained during the tests, the convective heat transfer coefficient is determined iteratively in the simulation under the assumption of uniform convective heat transfer across the entire specimen surface. Due to the existing relationship between temperature development and convective heat transfer, this approach yields the same accuracy as defining a constant heat transfer coefficient and subsequently calculating the temperature.

In this context, the temperature distribution within the specimen and on its surface is calculated for an applied stress of 68.5 N/mm² and a frequency of 60 Hz. Experimental validation of the temperature distribution is only feasible on the specimen's surface, which is achieved using the thermographic camera as before (Chapter 7.2). In Figures 8.4 and 8.5, the comparison between the simulated and experimentally measured temperature distributions shows that a highly accurate prediction of the temperature distribution is achieved. However, the experimental thermographic analysis reveals a slight tilt in the temperature field, most likely resulting from the airflow generated by the additional fans. Despite this, the surface temperature distribution remains highly uniform at 23 °C, validating the simulation model.

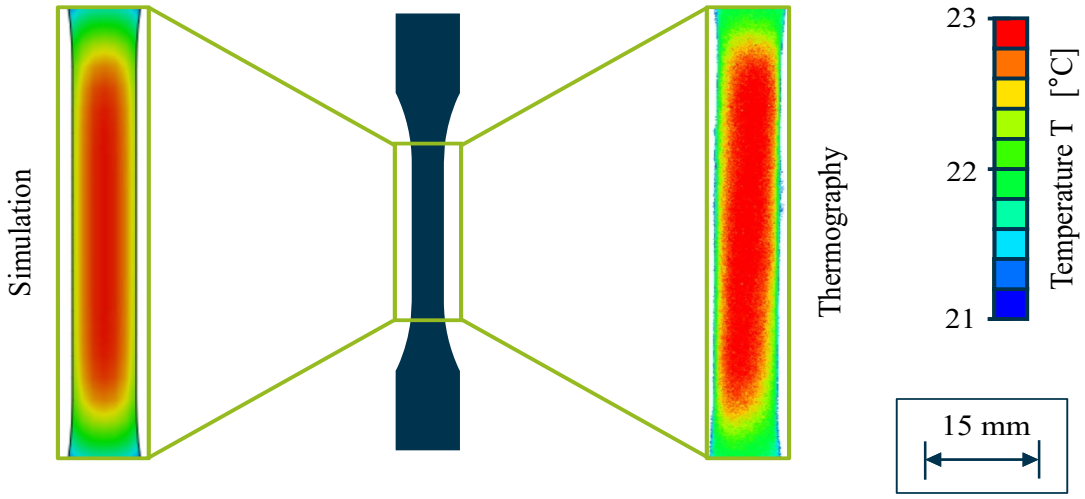

Fig. 8.4: Qualitative comparison of the simulated (left) and experimentally (right) determined temperature distribution of the specimen surface while quasi-stationary isothermal testing. At an applied stress of 68.5 N/mm² and a frequency of 60 Hz.

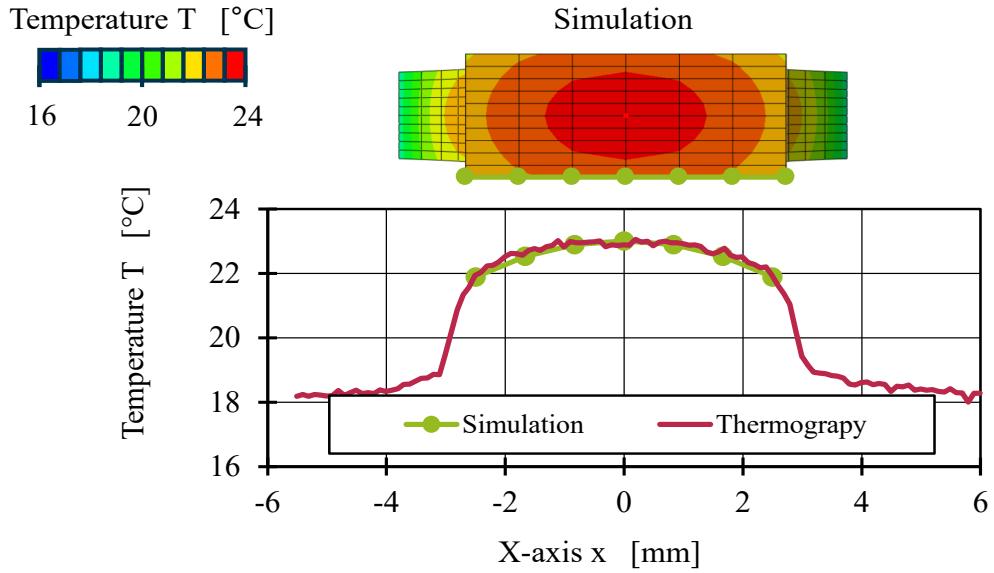

Fig. 8.5: Quantitative comparison of the simulated and experimentally determined temperature distribution of the specimen surface while quasi-stationary-isothermal testing. At an applied stress of 68.5 N/mm² and a frequency of 60 Hz.

Given that the temperature distribution on the surface can be accurately predicted via simulation, it is reasonable to assume that the temperature distribution within the specimen, governed by thermal conduction, is also accurate. However, it is important to note that the specimen exhibits a fiber orientation distribution across its thickness. This means that depending on the loading direction, certain areas will experience higher stress while others will experience less, leading to localized variations in energy dissipation across the cross-section. Nevertheless, due to the *Biot* number, it can be assumed that the overall temperature difference across the cross-section remains small (compare Chapter 7). Consequently, any temperature

inhomogeneity induced by the fiber orientation distribution is expected to be negligible, which is why the thermo-mechanical influence of the fiber orientation distribution is not taken into account.

Since the temperature distribution within the specimen also depends on thermal conductivity, a sensitivity analysis of the temperature distribution is performed. Figure 8.6 shows the temperature distribution across the cross-section in both thickness and width directions for three different thermal conductivities: 0.22 W/mK, 0.27 W/mK, and 0.32 W/mK. It is important to note that an average thermal conductivity of 0.278 W/mK was determined experimentally for the thickness direction using the LFA method over a temperature range of 20 °C to 50 °C. At 20 °C, the experimentally measured thermal conductivity was 0.290 W/mK. These experimentally determined values are used as a material input in the simulation. Across the width and thickness of the specimen, a temperature difference of approximately 1.5 °C is observed. However, cooler temperatures are particularly observed in the corners of the specimen, where the reduced volume-to-surface ratio contributes to more distinct heat transfer per volume. The maximum temperature variation across the entire specimen is found to be 3 °C, indicating a minimal impact of the thermal conductivity. Furthermore, the temperature distribution across the cross-section is volumetrically averaged. The resulting averaged temperature matches the measured surface temperature, consistently remaining at 23.0 ± 0.1 °C.

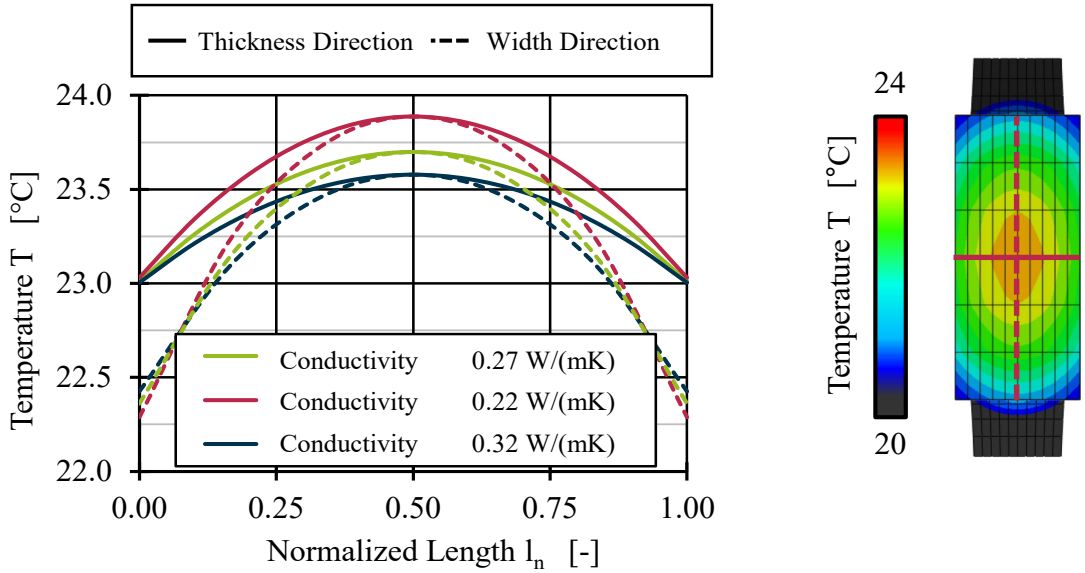

Fig. 8.6: The numerically determined local temperature distribution within the specimen, as a function of thermal conductivity, demonstrates that temperature deviation within the material is negligible.

Thus, the infrared pyrometer positioned in the center of the specimen always measures the volumetrically averaged temperature, making it representative of the entire temperature distribution. Initially, it was thought that a correction function would be required to bring the measured temperature to align with the actual average temperature within the specimen.

However, this step is unnecessary, allowing the controller to use the pyrometer's measurements directly to adjust the convective heat transfer.

Additional investigations into the time-dependent temperature distribution are performed using the time-dependent loss energy as input. This analysis reveals a negligible maximum temperature increase of 0.1 °C due to increased dissipation. The details of these results can be found in the work of *Fritsche* [Fri21]. Therefore, it can be concluded that a quasi-stationary temperature distribution is maintained within the specimen throughout the entire duration of the fatigue tests.

With this analysis, temperature deviations of up to 3 °C have been identified (quasi-isothermal) and maintained consistently throughout the test duration (quasi-stationary), even with increased energy dissipation due to damage progression, using the newly developed thermo-adaptive cooling device for an accurate material suitable characterization under dynamic-cyclic loads. Hence, this novel methodology enables, for the first time, the quasi-stationary isothermal characterization of the material behavior, effectively eliminating the negative effects of interacting material and load-induced temperature rises.

8.3 Load and frequency-dependent material characterization applying extended dynamic mechanical analysis (EDMA)

In this work, discussions of fatigue behavior have primarily focused on the load state, specifically load magnitude and frequency, and their correlation with resulting cyclic lifespan, or as time to failure. Additionally, dissipated energy has been considered as a key indicator of damage progression and a contributing factor to self-heating during dynamic-cyclic load. However, the deformation behavior of short glass fiber-reinforced thermoplastics is also crucial when analyzing failure, both under static and fatigue conditions. The stiffness properties of the individual constituents, alongside the micro-structure of the material, are important in governing the local stress distribution, thereby initiating crack propagation and contributing to the material’s mechanical degradation over the dynamic-cyclic load duration. Given that this study examines the influence of load frequency and considering that viscoelastic deformation behavior inherently exhibits time-dependent characteristics, it is important to assess whether variations in frequency induce changes in stiffness behavior. Such alterations could potentially affect the damage mechanisms at the micro-scale, which may subsequently propagate as material degradation at the macroscale.

Dynamic Mechanical Analysis (DMA) is typically employed to assess the temperature and time dependence of mechanical behavior as influenced by frequency [DHM22, GS15]. Similar to fatigue testing, a dynamic-cyclic load is applied to the specimen under controlled experimental conditions, with frequency and temperature sweeps conducted to measure the resulting material

behavior. Essentially, the storage and loss moduli are determined, as previously described in Chapter 7. The primary distinction is that conventional DMA characterizes the deformation behavior within the linear viscoelastic range without accounting for damage effects and generally does not consider load magnitude dependencies.

The thermo-adaptive test methodology developed here allows testing across the entire load range of the material without the negative effects of temperature increases due to hysteretic material dissipation. This approach is thus referred to as extended DMA (EDMA). The objective of these investigations is to analyze the dynamic-cyclic behavior of PBT-GF30, focusing on the influence of frequency, load magnitude, and temperature without incorporating the effects of damage. However, since the viscoelastic properties are primarily governed by the thermoplastic matrix, the non-reinforced PBT material is also characterized at this point.

To effectively utilize the developed methodology for assessing material behavior across different frequencies, load magnitudes, and temperatures, a specific testing protocol must be established. Unlike fatigue tests, which typically operate under constant conditions, this characterization involves varying parameters, requiring a tailored approach. The characterization is designed to cover a frequency range while minimizing the need for multiple specimens. Therefore, a combined frequency-load sweep is performed using a single specimen for each temperature. The testing program is structured so that a frequency sweep (1 Hz to 60 Hz) is conducted at each load level. For each frequency, 50 load cycles are applied before progressing to the next higher frequency. Subsequently, the load level is incrementally increased after each frequency sweep. Moreover, this procedure induces minimal damage to the material as it progressively increases both load and frequency from low to high levels.

To prevent overheating, load pauses are implemented for frequencies above 30 Hz, during which the specimen is held at a controlled zero-load state, allowing it to cool down, despite the use of the thermo-adaptive cooling system. This is essential because the ambient temperature within the test chamber is kept constant due to the thermal inertia of the chamber over all parameter sets and, hence, is not adjusted for different load levels and frequencies, as discussed before. This approach ensures that the specimen can endure the entire testing sequence without significant temperature-induced variability, thereby maintaining the integrity of the results. To avoid potential transient effects, only the last ten load cycles are considered for evaluating the mechanical behavior of the material. This ensures that the data reflects a stabilized state, providing more accurate and reliable insights into the material's response under the testing conditions.

In Figure 8.7, the resulting temperature across all load cycles during an EDMA test for a non-reinforced PBT specimen at a set target temperature of 23 °C is illustrated. It is evident that for nearly all load levels, the temperature is maintained within a range of ±1 °C. Only at the highest

load level, localized temperature increases of up to 2.5 °C occur, just before the cooling phases start. Additionally, it was observed during these preliminary investigations that the infrared pyrometer's measurement rate of 1 s is insufficient to capture these temperature peaks accurately. Consequently, the measurement rate is adjusted to 0.125 s to ensure accurate detection of temperature fluctuations.

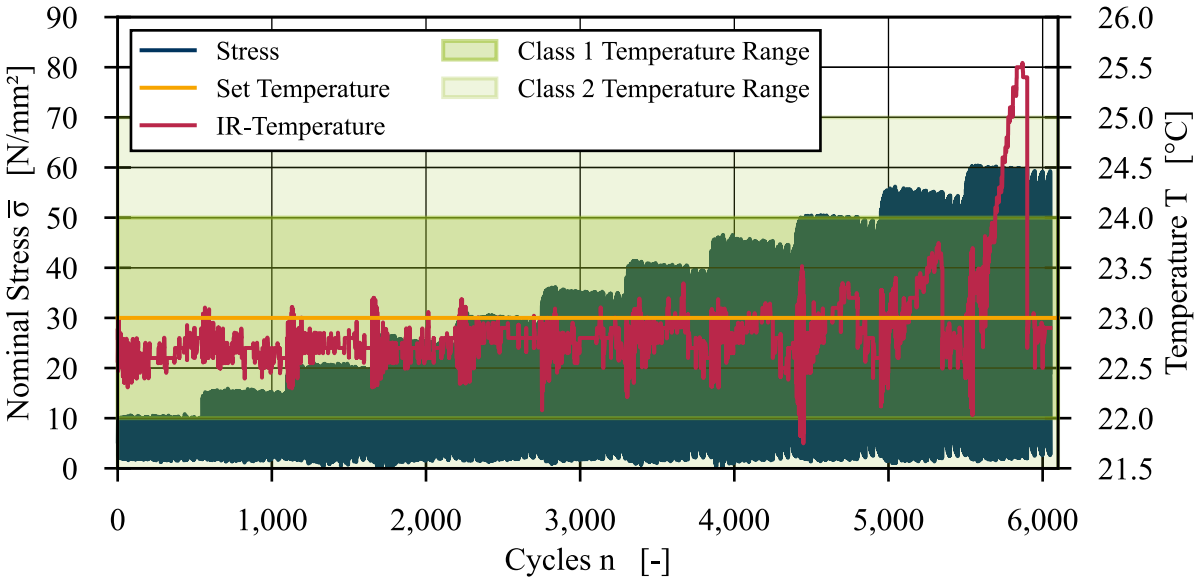

Fig. 8.7: Temperature development over load cycles while conducting the extended dynamic mechanical analysis for a set temperature of 23 °C. The green backgrounds indicate the class 1 (±1 °C) and class 2 (±2 °C) temperature ranges after DIN ISO 291.

In the following diagrams, Figure 8.8, the averaged temperature development for the selected last ten cycles during the evaluation of dynamic-cyclic mechanical properties for each parameter set across the load levels and frequencies is presented in the form of heatmaps. Since two materials, PBT-GF30 and non-reinforced PBT, are characterized at three different temperatures, a total of six diagrams are shown.

It is noteworthy that for a significant majority of the test points, the target temperature is maintained within the desired range of ±1.0 °C. However, as load levels and frequencies increase, there is a noticeable rise in temperatures. The implementation of cooling phases from 30 Hz onwards has proven effective in preventing temperature increases. Even at the temperature level at the glass transition temperature, where the viscous material properties are more pronounced, the pauses successfully controlled the temperature rise within acceptable limits.

However, the test protocol, initially evaluated and established using non-reinforced PBT specimens at 23 °C, where the temperature increase remained within acceptable limits, was subsequently applied to the EDMA tests for both materials using the same testing program, including pauses for frequency steps above 30 Hz. As a result, during the tests conducted at

47 °C, temperatures exceeding 11 °C are observed. To minimize experimental complexity, an adaptation of the ambient temperature to maintain the target temperature, as previously described, is not applied. It is also important to note that due to the generally reduced strength of the specimens at higher temperatures, failure occurs at lower load levels compared to the experiments at 23 °C, which explains the missing data points at higher temperatures as the specimens fail prematurely. Furthermore, as load levels increase and the specimens have undergone a considerable number of load cycles, it cannot be assumed that the specimens are entirely undamaged as the testing progresses. Nevertheless, it can be assumed that the specimen remains nearly undamaged for most load levels due to the low number of applied cycles compared to the corresponding fatigue life.

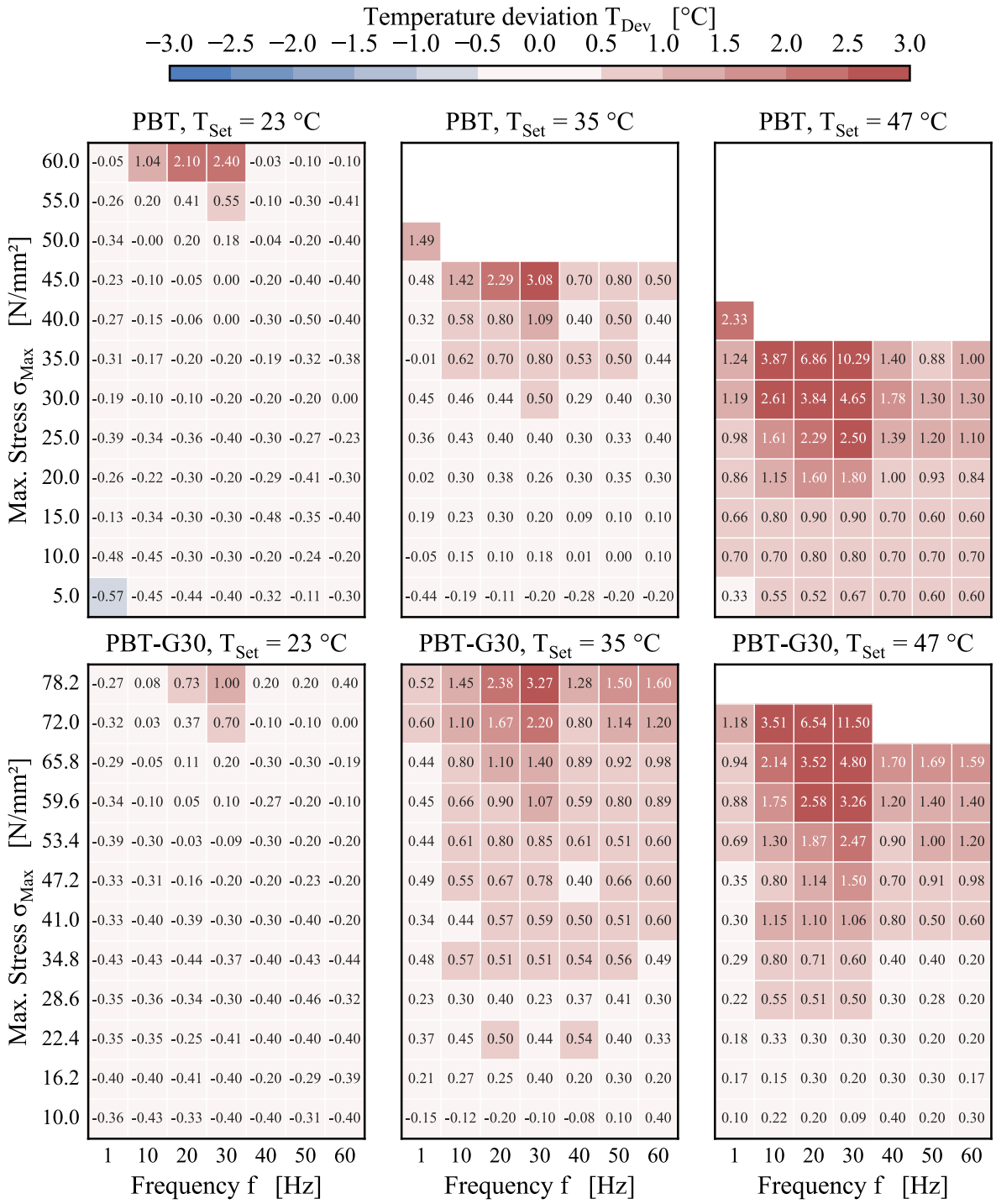

Fig. 8.8: Evaluation of the temperature control during EDMA characterization for non-reinforced PBT and longitudinal PBT-GF30 specimens.

However, it should also be noted that, in addition to damage, the material is subjected to a superimposed creep load under the applied tensile-tensile load cases. Given the relatively short test duration, it can be assumed that this superimposed creep load does not significantly affect the measured experimental data.

In conclusion, the results indicate that the material behavior can be effectively characterized using the proposed EDMA methodology by means of the observed temperature increases. Moreover, the insights to be gained regarding the material's response under dynamic-cyclic loading can be reliably interpreted without the adverse influence of temperature increases.

As previously discussed, a comprehensive understanding of the fatigue behavior in SFRT materials necessitates an in-depth analysis of the underlying fatigue mechanisms primarily determined by the interaction between the material's constituents and the resulting micro-mechanical stress states. These stress states are inherently dependent on the load paths within the material and, consequently, on the stiffness properties of both the fiber and matrix phases. The glass fibers are assumed to exhibit idealized linear-elastic behavior, independent of strain-rate. In contrast, the thermoplastic matrix, being viscoelastic, exhibits a complex non-linear response that is influenced not only by temperature but also by strain-rate dependence. Typically, when subjected to higher strain rates, the thermoplastic matrix shows increased resistance to deformation, leading to an overall stiffer material response. As a result, under dynamic-cyclic loads at higher frequencies, the deformation behavior is expected to show greater stiffness than at lower frequencies due to the strain-rate sensitivity inherent in the viscoelastic matrix. Hence, the progression and accumulation of damage due to crack growth can also be influenced by the changes in stiffness behavior, potentially impacting the overall fatigue performance of the material.

Therefore, using EDMA, the dynamic stiffness is analyzed under the previously presented load conditions (frequency and load sweep at three temperatures) to capture the material's stiffness response and to gain a deeper understanding of the relationship between loading frequency and the resulting stiffness behavior (see Figure 8.9). When comparing the dynamic stiffness data with temperature profiles, it becomes evident that even minor temperature fluctuations are reflected in the dynamic stiffness, indicating the material's sensitivity to thermal variations. This effect is particularly pronounced at higher stress levels, where the thermo-adaptive test methodology reaches its limits in compensating for temperature increases, resulting in noticeable artifacts. These findings not only underscore the sensitivity of dynamic stiffness in the tested PBT material to temperature variations but also demonstrate the repeatability and accuracy of the developed thermo-adaptive testing methodology.

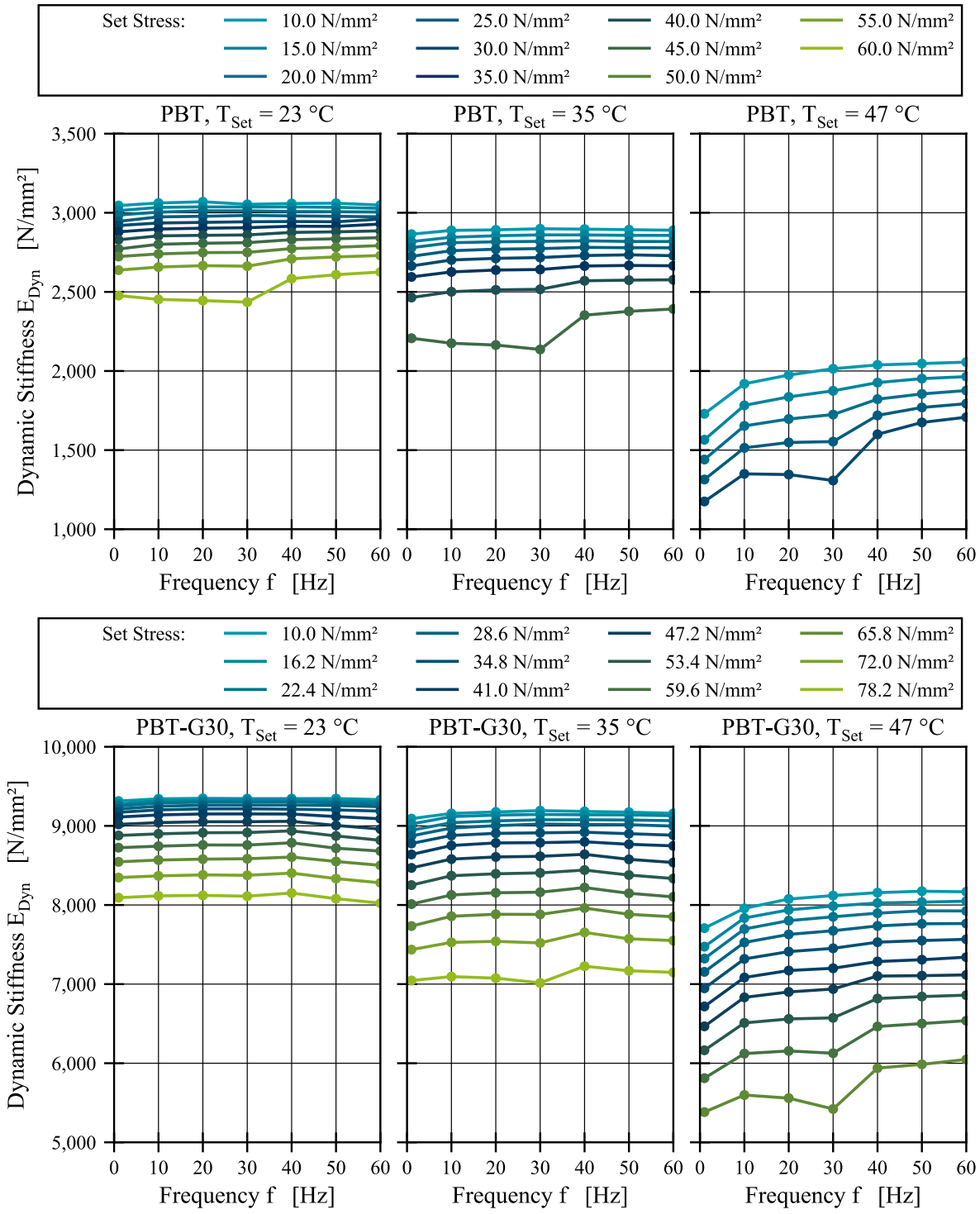

Fig. 8.9: Dynamic stiffness in dependency of the frequency for both non-reinforced PBT and reinforced PBT-G30 at various set stress levels and test temperatures (23 °C, 35 °C, and 47 °C). The diagrams show the effect of increasing frequency and temperature on the material stiffness across different stress levels, showing the viscoelastic response of the thermoplastic matrix.

While analyzing the material behavior, a distinction must be drawn between the non-reinforced and reinforced PBT, as the applied nominal stress in reinforced materials is reflected in a complex micro-mechanical stress state, thereby inducing different stress levels at the micro-

scale. In non-reinforced materials, the induced stress state is more homogeneous due to the nearly uniform stiffness throughout the entire cross-section.

For the non-reinforced PBT at 23 °C, a slight increase in dynamic stiffness, amounting to significantly less than 100 N/mm² across the frequency range of 1 to 60 Hz, is observed. This corresponds to a relative increase of less than 5 %. However, when the non-reinforced PBT is subjected to the glass transition temperature of 47 °C, the dynamic stiffness behavior changes more pronounced. Not only is the level of dynamic stiffness reduced to approximately half of its value at 23 °C, but with increasing frequency, the dynamic stiffness increases by up to 600 N/mm². This behavior can be attributed to the reduction in intermolecular forces between the polymers within the amorphous areas, which leads to a significantly more viscous material behavior and, consequently, being more sensitive to loading rates [WS12].

In addition to the frequency-dependent changes, it becomes apparent that dynamic stiffness decreases as the stress level increases. Since the dynamic stiffness is calculated using the maximum and minimum stresses and strains (compare Equation 7.6), and differs fundamentally from the elastic modulus - typically determined from the secant modulus at discrete strain levels (0.05 % and 0.25 %) within the linear elastic range [NN12] - this behavior reflects the degressive stress-strain response of the material. Hence, as the applied stress increases, the dynamic stiffness decreases.

For the reinforced material PBT-GF30, the dynamic stiffness exhibits a substantially higher value, approximately three times that of the unreinforced material, across all stress levels. At both 23 °C and 35 °C, no significant change in dynamic stiffness is observed as the frequency increases. The stiffness remains relatively constant over the entire frequency range. However, at 47 °C, the material exhibits behavior similar to that of non-reinforced PBT. As the frequency increases, the dynamic stiffness rises, although the overall stiffness at this elevated temperature is also lower.

These results demonstrate that both temperature and load frequency show, as expected, a significant influence on the dynamic stiffness of non-reinforced and reinforced PBT. Even small fluctuations in temperature lead to measurable changes in stiffness, particularly at higher load levels, where the thermo-adaptive test system is no longer able to fully compensate for the self-heating effect. This is most evident at 47 °C, where the deviations are most pronounced. Furthermore, the results clearly show that dynamic stiffness decreases as the applied stress increases, a trend that is consistent across all temperature conditions and could be quantified using the thermo-adaptive test system. Based on the results for the dynamic stiffness, it can be concluded that also during fatigue loads at approximately 23 °C, and assuming no significant temperature increase occurs, the matrix behavior and induced stress states are unlikely to substantially alter the prevailing damage mechanisms, even at higher strain rates resulting from

increased frequency. It is assumed that, in the presence of a crack, as long as the far-field stress remains the same, the crack growth will also proceed at a consistent rate without any change. Therefore, the progression of damage is expected to remain unaffected by higher loading frequencies, apart from the scaling effect related to the applied load cycles.

In addition to dynamic stiffness, the loss energy, calculated as the integral of the experimentally obtained stress-strain behavior, can also be evaluated and analyzed. This means that using the developed thermo-adaptive test method, the material-inherent hysteresis behavior can be examined without the influence of the self-heating effect. As previously discussed, EDMA allows for the characterization of energy loss due to viscoelasticity without the interference of damage mechanisms ($\mathcal{D}$), thereby enabling the determination of the dependencies between stress, frequency, and temperature (compare Equation 8.3),

$$w_L = w_L(\boldsymbol{\sigma}, f, T, \mathcal{D}) \qquad \textit{(Eq. 8.3)}$$

The results for the hysteretic loss energy are shown in Figure 8.10. A comparison between the reinforced and non-reinforced materials reveals that with increasing temperature, the loss energy also rises. Furthermore, it becomes evident that loss energy decreases with increasing frequency. It is crucial to emphasize that the data is presented on a logarithmic scale, which magnifies the observed variations in loss energy as a function of frequency, thereby showing that the reduction in loss energy is more pronounced. The observed rise in loss energy with temperature can be explained by the reduction of intermolecular forces by increasing free volume, which facilitates greater molecular interaction and promotes slippage at the molecular level. In contrast, the reduction in loss energy with increasing frequency can be attributed to the limited time available for molecular interaction at higher loading rates, leading to lower intermolecular friction.

The observation that loss energy decreases with increasing frequency may initially appear counterintuitive, given that higher frequencies are typically associated with greater thermal self-heating within the material. However, Equation 7.15 shows that the rate of temperature change $\dot{T}$ is governed not only by heat exchange with the environment $\{-div(\boldsymbol{q})\}$ and hysteretic loss energy w_L but also by the load frequency f itself, which acts as an external factor independent of the material properties. Consequently, the temperature change is driven by the loss power, which in turn is influenced by the frequency of the applied load. For this reason, Figure 8.11 illustrates the loss power across the tested parameter space, revealing that the loss power increases with rising frequency, thereby explaining the associated temperature rise.

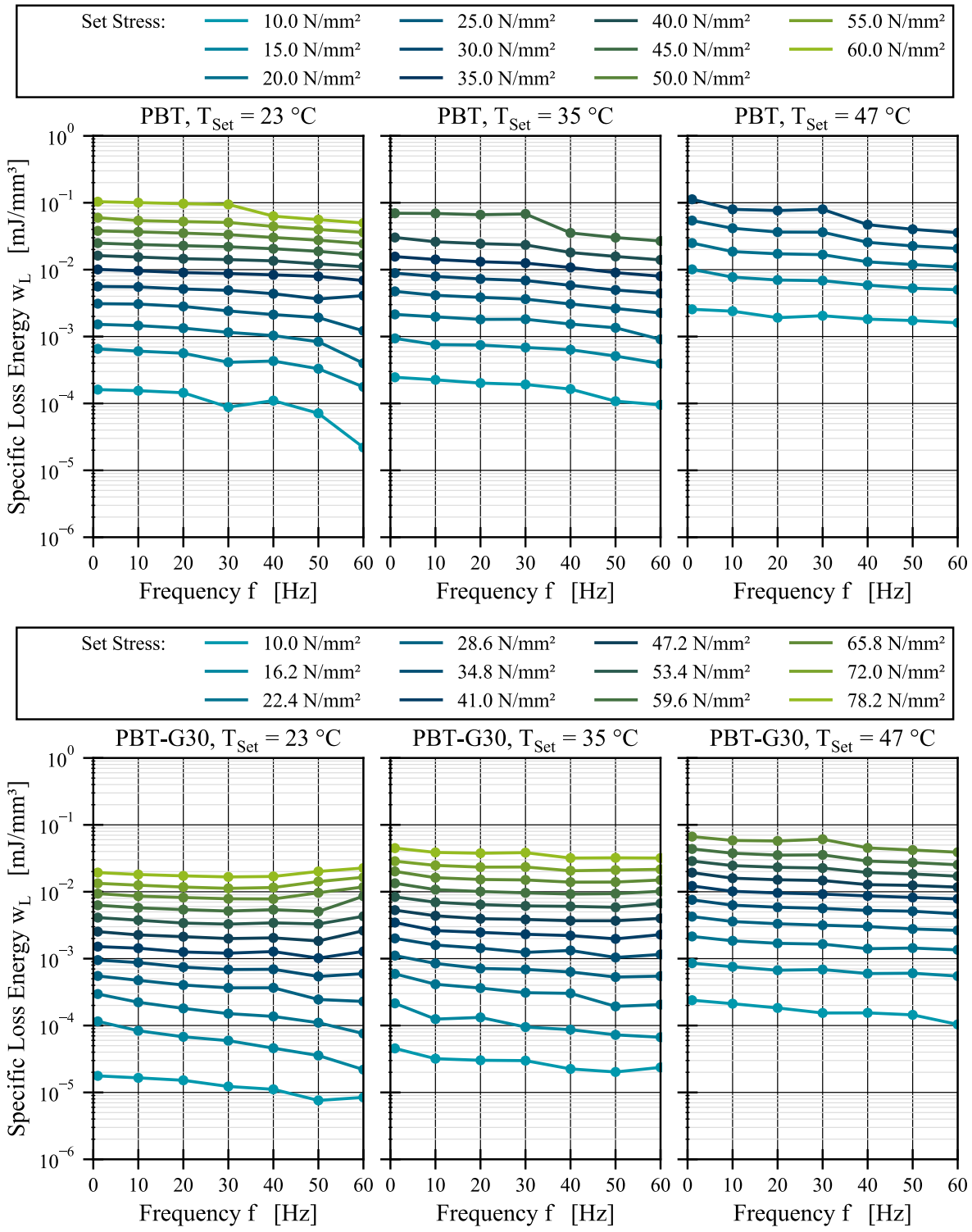

Fig. 8.10: Loss energy in dependency of the frequency for both non-reinforced PBT and reinforced PBT-G30 at various set stress levels and test temperatures (23 °C, 35 °C, and 47 °C).

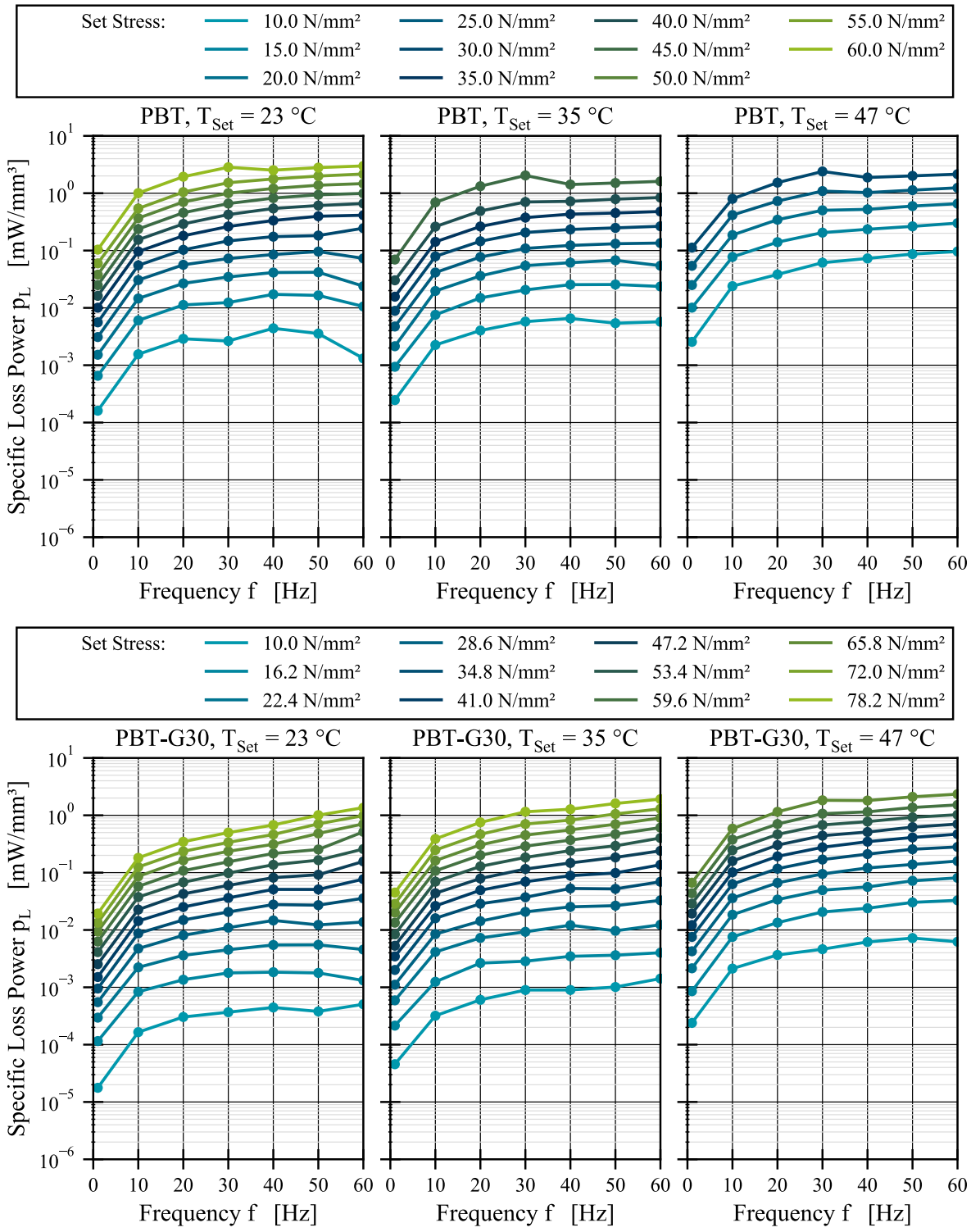

Fig. 8.11: Loss power in dependency of the frequency for both non-reinforced PBT and reinforced PBT-G30 at various set stress levels and test temperatures (23 °C, 35 °C, and 47 °C).

From these observations, it can be concluded that, for the tested PBT material, although the loss energy per cycle decreases with increasing frequency, the rate of decrease is not as pronounced as the corresponding increase in loss power at higher loading frequencies. Consequently, the

overall loss power shows a total increase with frequency, why the temperature development is more pronounced at higher frequencies during dynamic-cyclic loading of the material.

8.4 Conclusion on the thermo-adaptive test methodology for quasi-stationary isothermal material characterization and dynamic-cyclic material behavior of PBT

The development of the thermo-adaptive test methodology represents a significant advancement in the characterization of dynamic-cyclic properties of viscoelastic material across the entire stress range and at varying frequencies without significant interference of temperature fluctuations. The thermo-adaptive cooling system applied as an isothermal EDMA test method significantly extends the frequency and maximum load range that can be tested compared to conventional DMA. As a result, it facilitates the investigation of linear and non-linear hysteresis behavior, enabling comprehensive material characterization. Furthermore, the data generated by the EDMA testing are highly valuable for understanding material behavior. For example, the loss energy values obtained in this manner can be used to determine the temperature increase within the material using Equation 7.18. Despite the advantages offered by the thermo-adaptive methodology, the system can be further optimized. Enhancing the cooling system's performance or integrating additional holding phases into the testing protocol to eliminate residual self-heating during high-stress conditions would improve the fidelity of the measurements. Furthermore, adjusting the ambient temperature within the testing chamber, in conjunction with adapting the air velocity, could further eliminate temperature fluctuations at high loads and frequencies, ensuring more stable thermal conditions during testing.

With regard to the material, the experiments conducted on both non-reinforced PBT and fiber-reinforced PBT-GF30 quantified the mechanical response behavior to dynamic-cyclic loading. Across the tested frequency range of 1 Hz to 60 Hz, for temperatures of 23 °C and 35 °C, no significant frequency dependence of the dynamic stiffness was observed. However, at 47 °C, an increase in dynamic stiffness with frequency was determined, showing the material's sensitivity to temperature near its glass transition phase. Consequently, it can be assumed that the damage mechanisms within the tested frequency range are not significantly altered by the increased strain-rate. Additionally, it was found that while loss energy decreases with increasing frequency, the loss power rises due to the linear relationship between frequency and loss energy. Therefore, it can be stated that the temperature increase due to self-heating is mainly induced by the load frequency rather than by the material behavior. Thus, the behavior induced by the material's deformation characteristic is quantified and confirmed under high load conditions and frequencies using the thermo-adaptive test methodology. Consequently, in the next step, this methodology will be applied to investigate the fatigue behavior at different frequencies, independent of temperature effects.

9 DESCRIPTION OF THE FREQUENCY-DEPENDENT FATIGUE LIFE

In Chapter 7, fatigue results for specimens extracted longitudinally and transversely from injection-molded specimen plates were examined in fatigue tests conducted at frequencies ranging from 2 Hz to 90 Hz. In addition to evaluating the resulting fatigue life, the temperature evolution was also measured and correlated with the results, highlighting that, aside from cyclic damage progression, temperature-induced mechanical behavior changes in the material occurred, influencing the overall fatigue life. Distinctions could be made between a stable temperature state and progressively increasing temperature developments. Furthermore, the experimental data at higher frequencies indicated that different mechanisms became more pronounced in distinct load ranges, resulting in nonlinear SN curves. This observation implies that elevated temperatures have a substantial influence on the cyclic fatigue life of the material.

By employing the developed thermo-adaptive testing methodology, the intrinsic hysteresis behavior of the material under dynamic-cyclic loading was quantified and analyzed, effectively isolating the deformation response from the influence of self-heating effects in the EDMA test (Chapter 8). The results demonstrate that the induced micro-mechanical stress state remains mostly independent of the frequency, as the macroscopic behavior of both the reinforced and non-reinforced PBT shows no significant alteration across the frequency range of 1 Hz to 60 Hz. This indicates that the stress conditions at crack initiation and progression are independent of frequency for the tested PBT-GF30 material. Consequently, it is assumed that occurring solely cyclic damage mechanisms and fatigue processes are not impacted by the load frequency. Therefore, it is concluded that damage resulting from crack initiation and growth scales predominantly with the number of cycles and not with the rate of the dynamic-cyclic load, respectively frequency.

However, due to the nature of tensile-tensile loading under dynamic-cyclic conditions, the material is also subjected to creep. Nevertheless, the creep behavior cannot be investigated directly using the applied EDMA method. The following experimental analysis aims to determine how crack-controlled material degradation interacts with creep within the material, thereby influencing the resulting overall fatigue life. Since both the creep behavior and crack growth are influenced by the temperature-dependent deformation characteristics of the thermoplastic matrix, the thermo-adaptive test methodology is applied to investigate the impact of these mechanisms on fatigue life while eliminating material behavior alterations induced by temperature changes due to self-heating. This approach allows for a controlled and more profound analysis of fatigue behavior, enabling precise conclusions to be made regarding the material’s general fatigue and mechanical degradation process. Consequently, the experimental

fatigue tests from Chapter 7 are repeated using the thermo-adaptive test system, maintaining the material at a constant target temperature of 23 °C.

9.1 Characterization of frequency-dependent fatigue behavior under isothermal conditions

The generated results of the fatigue tests under isothermal conditions are presented in Figures 9.1 and 9.2 for both orientations, longitudinal and transversal. Since negligible temperature increase is observed at frequencies of 2 Hz and 5 Hz (compare Chapter 7), these tests are not repeated with the thermo-adaptive testing methodology. It is important to note that, similar to the previous tests, the 90 Hz experiments exhibit superimposed transversal loads in addition to the intended tensile loading caused by the oscillations of the test setup, as previously discussed. As a result, the data from these experiments do not accurately represent the material's fatigue life under defined loading conditions. Furthermore, it is evident that the experimental data exhibit increased scatter (compare 15 Hz, transversal specimens) despite the implementation of the procedure and measurement methodology outlined in Chapter 6, which was specifically designed to enhance and ensure high reproducibility of fatigue characterization across all tests. This emphasizes the high sensitivity of fatigue testing, where even minimal, often imperceptible variations can substantially affect the outcomes, potentially leading to significant deviations in the accuracy and reliability of the results. Additionally, it should be noted that the number of parameters involved in the application of the thermo-adaptive testing methodology is higher than in conventional tests, as it requires adjusting the ambient temperature to keep the cooling system in the operational range of the ventilation. At the same time, it must be ensured that the fans are positioned in such a way that they uniformly distribute the airflow around both sides of the specimen. Although the fan unit is equipped with adjustable end stops, it is essential to ensure that the setting is not changed over time. Nevertheless, the experimental data obtained can still be used to determine the influence of loading frequency on the number of cycles to failure since the overall behavior is still assumed to be represented correctly.

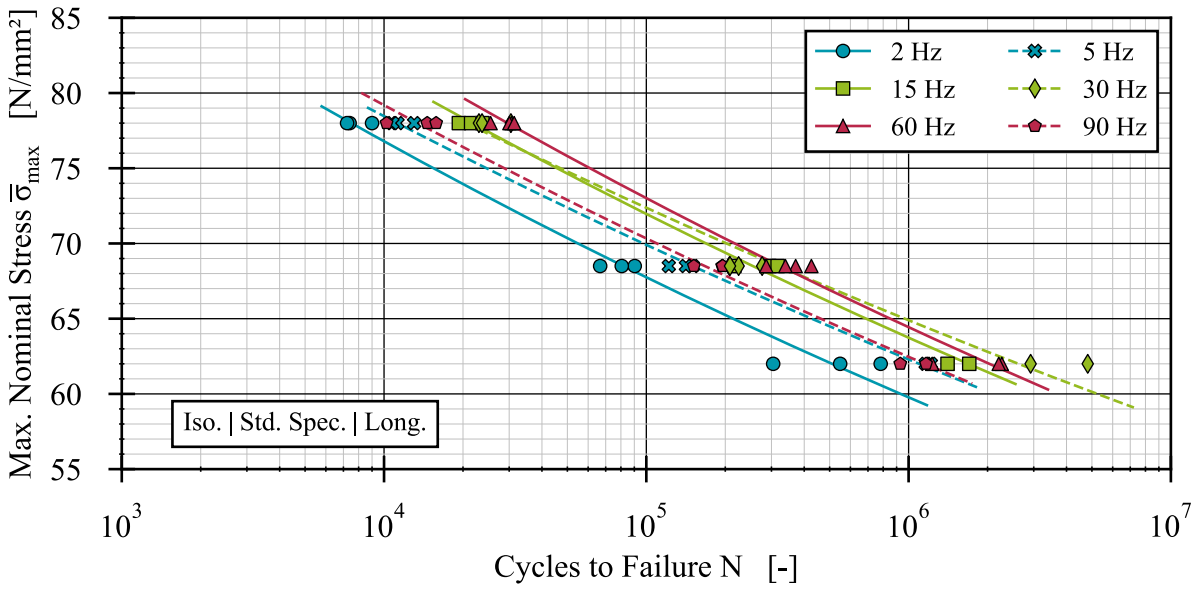

Fig. 9.1: Isothermal fatigue results over cycles to failure for varying frequencies between 2 Hz and 90 Hz for the longitudinal specimens made of PBT-GF30.

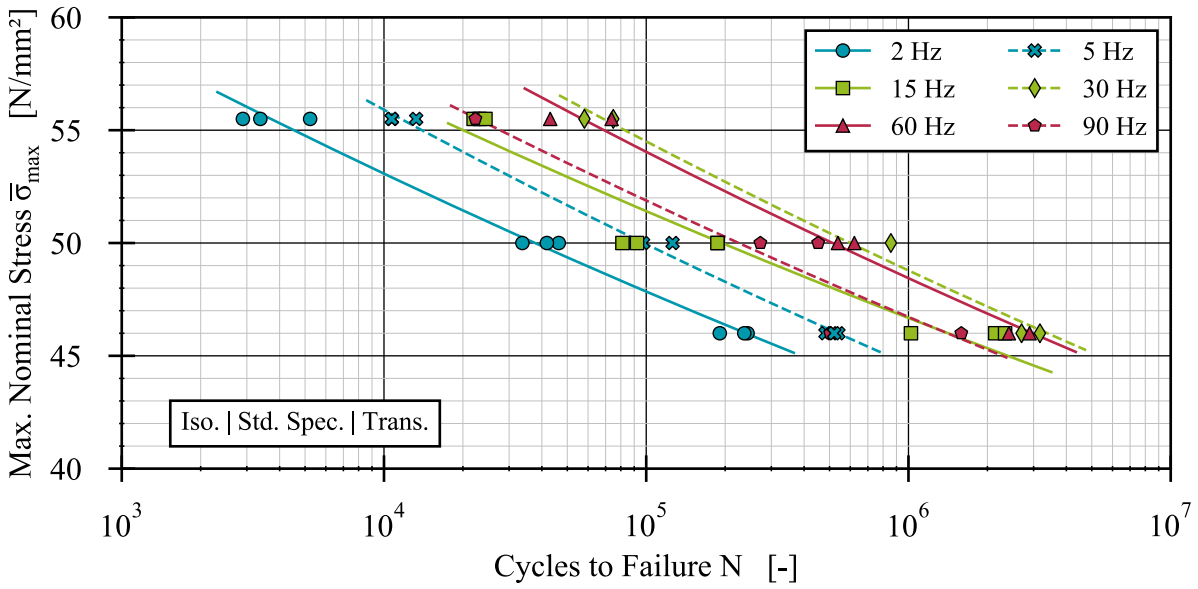

Fig. 9.2: Isothermal fatigue results over cycles to failure for varying frequencies between 2 Hz and 90 Hz for the transversal specimens made of PBT-GF30.

In comparison to the conventional tests, it is evident for both orientations that the trends of the experimental data does not exhibit a curvature at higher loading frequencies (15 Hz, transversal specimens excluded). This serves as further confirmation that the curvatures observed in previous tests (compare Figure 7.1 and 7.2) were caused by the induced temperature increase caused by self-heating. The experimental data points are fitted using the *Basquin* equation, as shown in Equation 9.1, where k describes the slope and C the shifting of the SN curve. The fits reveal that the slopes of the SN data are very similar across all frequencies for each orientations.

$$\sigma = CN^{-k} \qquad \textit{(Eq. 9.1)}$$

Additionally, it becomes evident that the cyclic lifetime, with the exception of the 90 Hz tests, increases with higher loading frequencies. However, it also appears that at the higher frequencies, the resulting cycles to failure converge closer together. This trend is observed for both longitudinal and transversal specimens. Moreover, the results also depict that the data for the longitudinal specimens show a more pronounced convergence with respect to load frequency compared to the transversal specimens. The shift in the longitudinal SN data is approximately 0.8 decades, while for the transversal specimens, it is around 1.5 decades in the same frequency range.

In the studies by *Kanters* and *Pastukhov*, it is postulated that the number of fatigue cycles to failure is independent of the loading frequency [Kan15, Past19]. However, when analyzing the isothermal fatigue data for PBT-GF30, it becomes apparent not only that the number of cycles to failure varies but also that the micro-structure, characterized by the prevailing fiber orientation distribution, seems to have a significant influence on fatigue behavior and, hence, to the number of cycles to failure (compare Figure 9.3). This is further shown when the results, similar to *Kanters'* approach, are plotted as the number of cycles to failure against frequency. The data reveal the emergence of two distinct regions: one showing a linear increase in the number of cycles to failure with increasing frequency, and another, starting at around 30 Hz, where this increase appears to stagnate. Furthermore, the linear increase is steeper for transversal specimens than for longitudinal specimens, indicating a higher frequency dependency. At 90 Hz, a noticeable decrease in the number of cycles to failure is observed, likely due to the additional transverse oscillation experienced by the specimens. As a result, these data are excluded from further analysis to maintain the integrity of the overall findings.

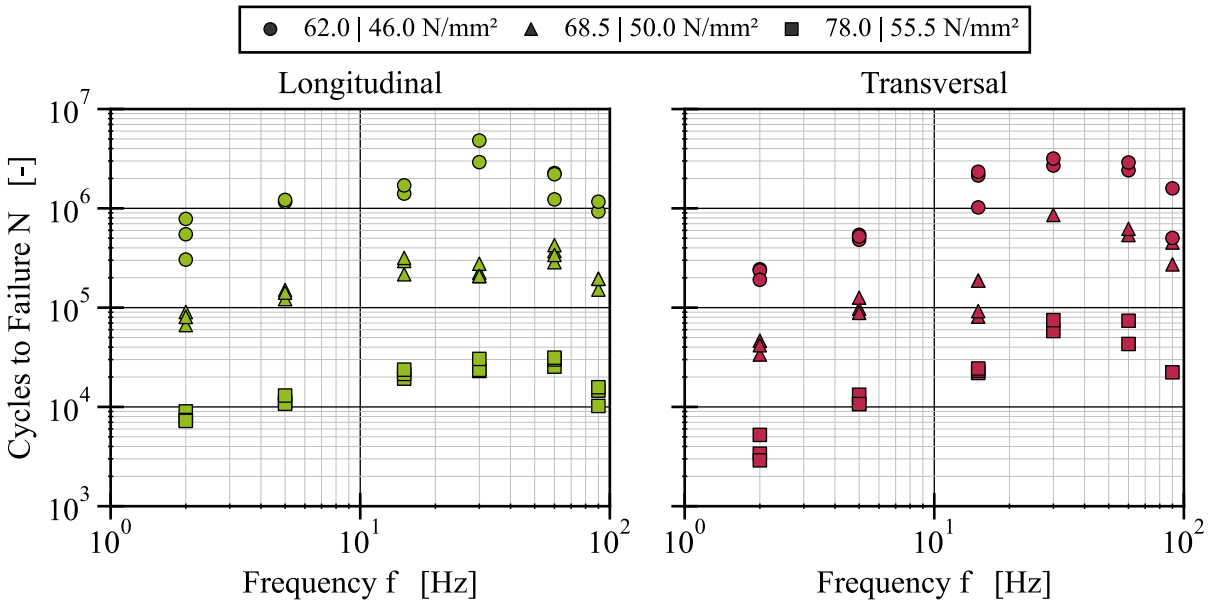

Fig. 9.3: Cycles to failure as a function of frequency for longitudinal and transversal specimens at various stress levels.

When analyzing the *Basquin* parameters over frequency (compare Figure 9.4), it becomes evident that the slope parameters k for the longitudinal specimens consistently exhibit higher values compared to the transversal specimens. A larger slope parameter indicates that the fatigue curve is steeper, meaning the material experiences a less rapid decrease in fatigue life with increasing stress compared to curves with lower slope values. Thus, a flatter SN curve is more sensitive to small changes in stress, making it mathematically less well-conditioned for accurate predictions of the cyclic fatigue life. When analyzing the shift parameter C, slight increasing trends can be observed with increasing frequency. However, these trends do not exhibit and represent the well-defined pattern, as seen in Figure 9.3.

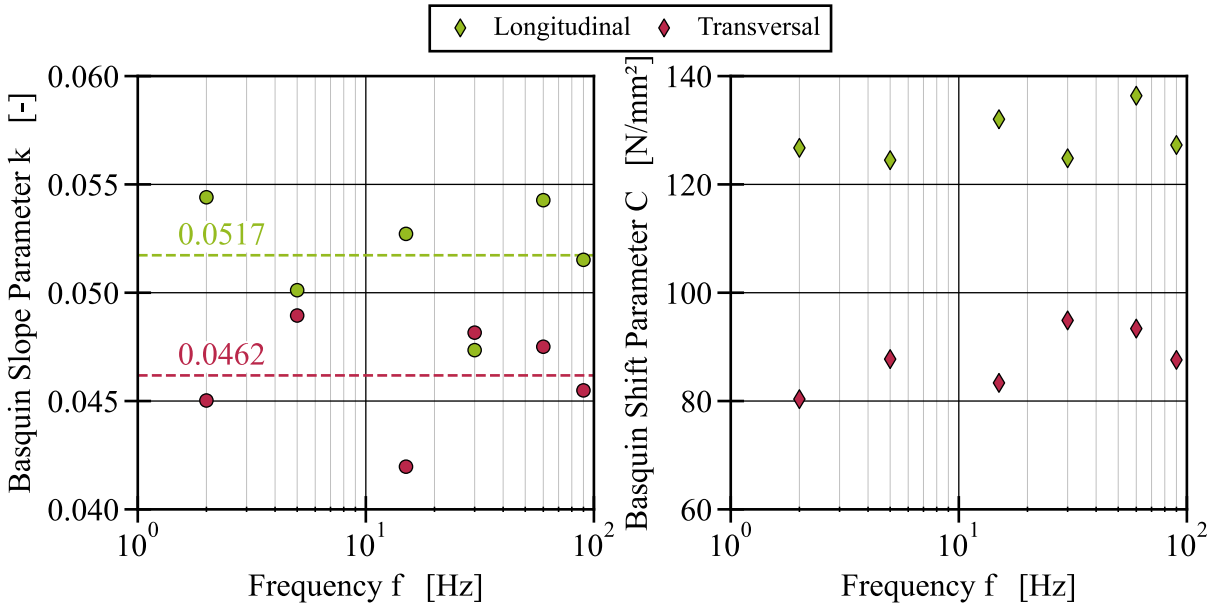

Fig. 9.4: Fitted Basquin parameters for the isothermal fatigue experiments conducted on longitudinal and transversal specimens.

A more detailed analysis of the *Basquin* equation reveals that, within the range of 10^3 to 10^7 cycles, small variations in the slope parameter k have a considerable impact on the shift parameter C. As a result, mathematically, the shift parameter C is poorly conditioned for fitting. However, since the fatigue tests indicate that the slope of the SN data remains nearly constant across varying loading frequencies, an average slope parameter for each orientation can be calculated, allowing the *Basquin* equations to be refitted with only the shift parameter C being adjusted by the fitting process. When the fitted shift parameters are subsequently plotted against frequency, the resulting trend closely matches the results that are shown in Figure 9.3, where the experimentally determined cycles to failure were plotted against the load frequency.

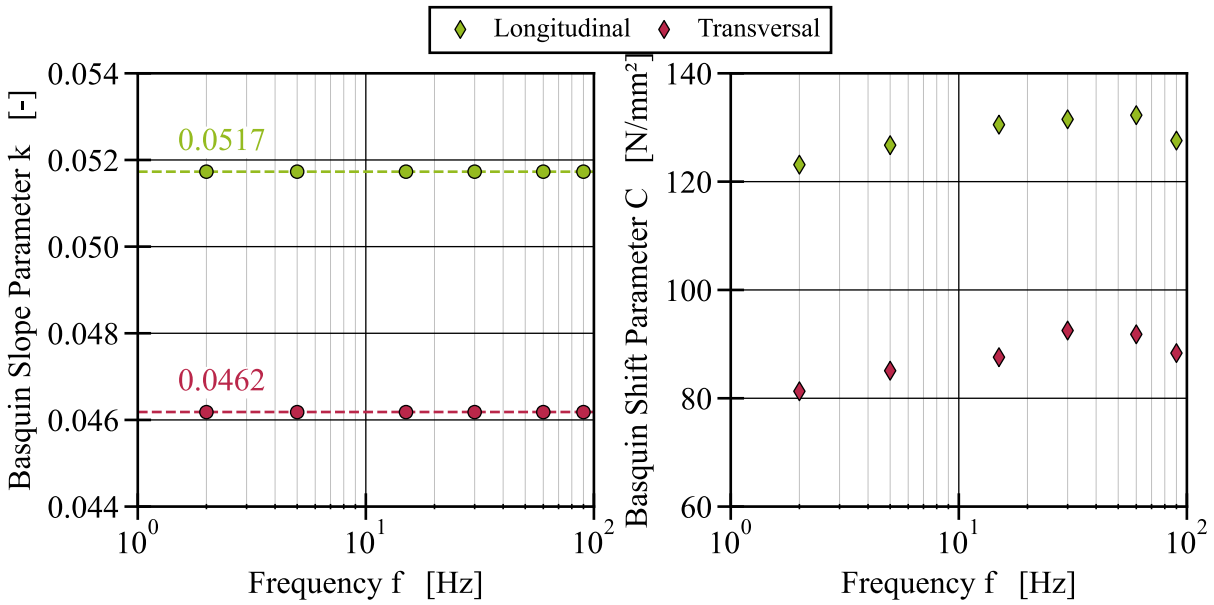

Fig. 9.5: Basquin parameters after using a constant slope parameter for each orientation.

In addition, when the *Basquin* fits determined in this manner are plotted against the results of stress versus cycles to failure, it is evident that the fitted data continues to align very well with the experimental data (compare Figure 9.6). This confirms that the shift in frequency can indeed be represented solely by the *Basquin* parameter C.

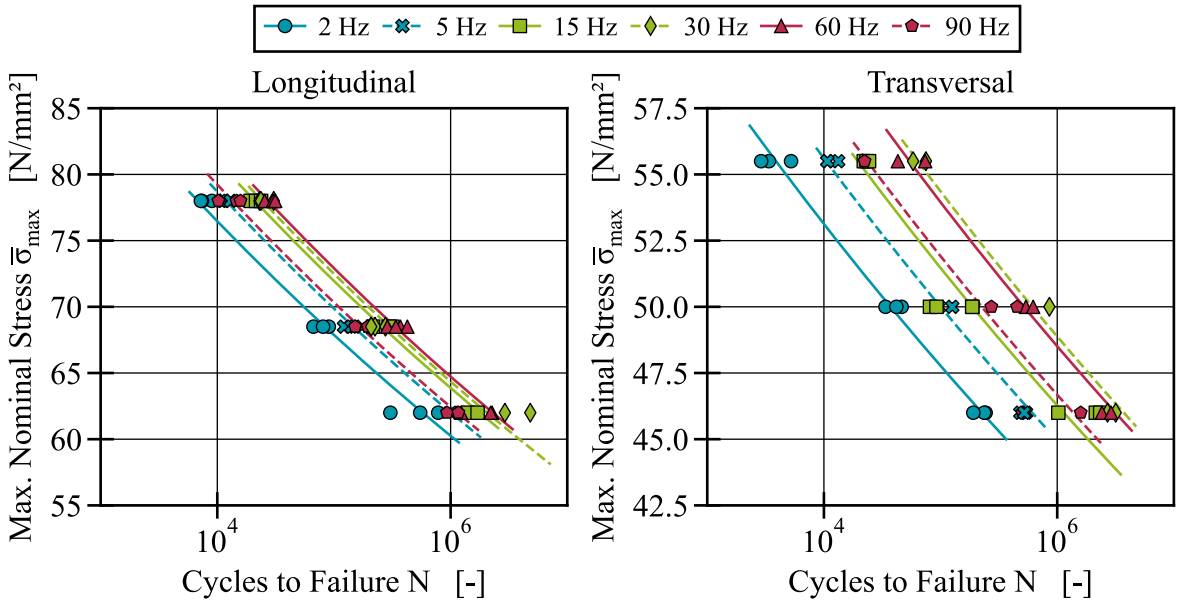

Fig. 9.6: Agreement between experimental data and Basquin equation fit with a constant slope across frequencies for each orientation.

In summary, through the isothermal fatigue tests, it can be further confirmed that the *Basquin* slope remains consistent in describing the fatigue behavior across different load frequencies for each respective orientation. Therefore, the frequency dependence of the number of cycles to failure can be captured using only the shift parameter C of the *Basquin* equation. Additionally, the isothermal experimental fatigue data indicate that the number of cycles to failure deviates

significantly more for the same frequency range in transversal specimens compared to longitudinal ones. The next step is to determine the shift parameter $C = C_{Shift}(f)$ as a function of load frequency.

9.2 Derivation of a phenomenological model for the frequency-dependent shift in describing and predicting cyclic fatigue life

To determine the parameters describing the frequency shift, it is necessary first to discuss the mechanisms governing fatigue behavior. Since temperature effects can be excluded in these mechanical investigations due to the application of the thermo-adaptive testing methodology, ensuring that all processes within the material occur under quasi-isothermal conditions, the overall fatigue behavior can be reduced to two fundamental mechanisms. It is assumed that fatigue behavior under a tensile-tensile dynamic-cyclic load is primarily influenced by cycle-driven crack initiation and progression and the time-dependent superimposed creep behavior of the thermoplastic matrix. From a fracture mechanics perspective, this relationship can be approximated by Equation 9.2, where the total change in crack length per cycle is described as the sum of the partial changes in crack length, induced by the crack length increase $\partial a/\partial n|_{cyclic}$ due to each individual applied load cycle and creep $\partial a/\partial n|_{creep}$ [Past19]. Both mechanisms are assumed to contribute, at this point linearly, to crack progression and, consequently, to the accumulation of damage within the material.

$$\frac{da}{dn} = \left.\frac{\partial a}{\partial n}\right|_{cyclic} + \left.\frac{\partial a}{\partial n}\right|_{creep} \qquad \textit{(Eq. 9.2)}$$

According to linear fracture mechanics, crack growth can be empirically described by Equation 9.3, utilizing the cyclic stress intensity factor ΔK. This equation is also commonly known as the *Paris* law [Gdo05, GS07]. The stress intensity factor K describes representative the local stress state at the crack tip as a function of the far-field stress σ. At this point, no distinction is made between the three different fracture modes, as the complex and heterogeneous material structure of SFRT does not allow for a clear identification of the individual fracture modes due to its statistical nature. Nonetheless, the underlying relationships remain valid and can be used here to derive an appropriate phenomenological model describing the mechanism for damage progression for fatigue predictions.

$$\left.\frac{\partial a}{\partial n}\right|_{cyclic} = C_{cyclic}\,\Delta K^{m_{cyclic}} = C_{cyclic}\left((1-r)\,K_{Max}\right)^{m_{cyclic}} \qquad \textit{(Eq. 9.3)}$$

For crack growth to occur under static loading, the K-factor must exceed a threshold K_C. Under dynamic-cyclic loading, it is assumed that each applied cycle contributes to crack growth [Gdo05, GS07]. Hence, the cyclic stress intensity factor ΔK is the difference between

$K_{Max} - K_{Min}$, which is equivalent to the stress difference $\sigma_{Max} - \sigma_{Min}$, thereby allowing the stress ratio r to be considered as well. The *Paris* equation includes two material-specific model parameters, C_{cyclic} and m_{cyclic}, which must be determined individually for each material. With this equation, it is assumed that the damage progression rate due to cyclic loads is constant in the secondary phase of fatigue. The secondary phase accounts for the majority of the material's fatigue life. [Gdo05].

At this point, crack growth induced by creep is formulated analogously, with the distinction that the crack growth is not driven by the applied cycles but by material stressing over time t (compare 9.4). Thereby, the induced stress state characterized by K_{Max} is multiplied by a reduction coefficient C_{eff}, as the applied peak stress intensity due to dynamic-cyclic loading only partially contributes to the creep process. Since the creep behavior scales nonlinearly with stress [Bra06, Haa18, Kue12], a simple averaging approach, for instance through $\frac{1}{2}K_{Max}$ would be insufficient [PKE+20b, TX07]. Similar to Equation 9.3, there are also two additional model parameters C_{creep} and m_{creep} that need to be determined in this context.

$$\left.\frac{\partial a}{\partial t}\right|_{creep} = C_{creep}\left(C_{eff.}\, K_{Max}\right)^{m_{creep}} \qquad \textit{(Eq. 9.4)}$$

To solve the differential equation in Equation 9.2, the time-dependent creep must be expressed as a function of the number of applied cycles. With $t = n/f$, this results in Equation 9.5, which incorporates the loading frequency into the equation of crack growth induced by creep.

$$\left.\frac{\partial a}{\partial n}\right|_{creep} = \frac{C_{creep}}{f}\left(C_{eff.}\, K_{Max}\right)^{m_{creep}} \qquad \textit{(Eq. 9.5)}$$

By utilizing the definition (Equation 9.6) of the stress intensity factor K which relates the far-field stress σ, geometry factor Y, and the prevailing crack length a, the total crack growth can then be described as a function of maximum stress σ_{max} of the dynamic-cyclic load and a set of coefficients [Gdo05, GS07]. Hence, the Equation 9.7 provides a basis for describing crack propagation under varying load conditions dependent on the applied load height and frequency.

$$K = Y\,\sigma\,\sqrt{\pi\, a} \qquad \textit{(Eq. 9.6)}$$

$$\frac{da}{dn} = C_{cyclic}\left((1-r)\, Y_{cyclic}\,\sigma_{max}\,\sqrt{\pi\, a}\right)^{m_{cyclic}} + \frac{C_{creep}}{f}\left(Y_{creep}\,\sigma_{max}\,\sqrt{\pi\, a}\right)^{m_{creep}} \qquad \textit{(Eq. 9.7)}$$

Based on the experimental results and the analysis of the fitting data of the *Basquin* equation, it was determined that the fatigue behavior, characterized by the number of cycles to failure as a function of stress, exhibits a consistent slope across all frequencies, confirming its frequency

independence. Furthermore, the linear approximation of fatigue behavior as a function of applied stress, characterized by this constant slope, suggests that the resulting macroscopic stress dependence can also be modeled using one constant exponent. Therefore, the simplification of $m_{cyclic} = m_{creep} = m$ can be assumed for the total crack growth equation.

In addition, the exponents of the remaining factors are considered negligible, as these parameters are effectively treated as arbitrary constants. This allows the parameters stress ${\sigma_{max}}^{m}$ and crack length $a^{m/2}$ to be distributively separated, resulting in a more mathematically manageable representation of the formula (compare Equation 9.8).

$$\frac{da}{dn} = \left(\frac{C_{creep}}{f}\left(C_{eff.}\, Y_{creep}\, \sqrt{\pi}\right)^{m} + C_{cyclic}\left((1-r)\, Y_{cyclic}\, \sqrt{\pi}\right)^{m}\right) a^{m/2} {\sigma_{max}}^{m} \qquad \textit{(Eq. 9.8)}$$

Since C_i, Y_i and $\sqrt{\pi}$ are pre-factors that act as phenomenological parameters, encapsulating fracture processes, material morphology, and other intrinsic material and damage properties, they can be consolidated into single terms. This additional simplification preserves the model's descriptive function while streamlining the overall equation. Consequently, the phenomenological fitting parameters are reduced to C_{static} and $C_{dynamic}$, describing crack growth induced by static creep and dynamic-cyclic contributions to the overall damage progression.

$$\frac{da}{dn} = \left(\frac{C_{static}}{f} + (1-r) C_{dynamic}\right) a^{m/2} \sigma^{m} \qquad \textit{(Eq. 9.9)}$$

Through this simplification, the total differential equation can now be solved by separation of variables and integration, leading to the Equation 9.10.

$$\int_{n_i=0}^{N} dn = \frac{1}{\left(\frac{C_{static}}{f} + (1-r)\, C_{dynamic}\right)} \sigma^{-m} \int_{a_i}^{a_f} a^{-m/2} da \qquad \textit{(Eq. 9.10)}$$

As the integral term on the right-hand side essentially describes crack growth, and there is no precise information about the initial crack length or the crack length at failure, the integral can be simplified and represented by a constant C_{crack} (compare Equation 9.11).

$$\int_{a_i}^{a_f} a^{-m/2} da = C_{crack} \qquad \textit{(Eq. 9.11)}$$

Since C_{static} and $C_{dynamic}$ are phenomenological pre-factors, the constant C_{crack} can be incorporated into these parameters, thereby describing the frequency-dependent cyclic fatigue life through Equation 9.12.

$$N = \frac{1}{\left(\frac{C_{static}}{f} + (1-r)C_{dynamic}\right)}\sigma^{-m} \qquad \textit{(Eq. 9.12)}$$

This equation shows an analogy to the *Basquin* equation $\sigma = CN^{-k}$ so it can be transformed into the same form, as depicted in Equation 9.13.

$$\sigma = \frac{1}{\left(\frac{C_{static}}{f} + (1-r)C_{dynamic}\right)^{\frac{1}{m}}}N^{-\frac{1}{m}} \qquad \textit{(Eq. 9.13)}$$

The equation is further simplified by neglecting the exponent for the pre-factor like conducted before and using $\frac{1}{m} = k$. Hence, the relationship in Equation 9.14 can be used in the concept of the *Basquin* equation.

$$\begin{aligned}\sigma = \frac{1}{\frac{C_{static}}{f} + (1-r)C_{dynamic}}N^{-\frac{1}{m}} &= C_{shift}(f,r\,)N^{-\frac{1}{m}} \\ &= C_{shift}(f,r\,)N^{-k}\end{aligned} \qquad \textit{(Eq. 9.14)}$$

Since only $r \approx 0$ is considered in this work, the pre-factor can be further simplified for the results discussed in this work (see Equation 9.15).

$$C_{shift}(f,r\,) = \frac{1}{\left(\frac{C_{static}}{f} + (1-r)C_{dynamic}\right)} \overset{r\,\approx\,0}{=} \frac{1}{\left(\frac{C_{static}}{f} + C_{dynamic}\right)} \qquad \textit{(Eq. 9.15)}$$

Thus, a phenomenological model has been derived to describe the shift parameter C_{shift} as a function of frequency and the two coefficients, C_{static} and $C_{dynamic}$.

When the equation is plotted over frequency (Figure 9.7), two distinct regimes emerge. In the first regime, the shift parameter exhibits a nearly linear increase with frequency, predominantly capturing the time-dependent creep contribution to the overall damage progression. At lower frequencies, the influence of creep becomes more pronounced, resulting in a linear reduction of the shift parameter with decreasing frequency and giving the material more time to creep, which corresponds to a decreasing cyclic lifespan of the material. As the parameter C_{static} increases, the linear region shifts towards higher frequencies, representing an increased creep influence on the fatigue process. As the frequency tends toward infinity ($f \to \infty$), the shift parameter $C_{shift}(f\,)$ asymptotically approaches a limiting value, reflecting the behavior of the material in a purely cycle-driven fatigue regime. Therefore, $C_{dynamic}$ serves as an indirect representation of an assumed intrinsic fatigue life $C_{shift}(f \to \infty) = C_{intrinsic} = 1/C_{dynamic}$, unaffected by any creep. It is assumed that this intrinsic cyclic life is determined solely by the

material composition and configuration, thereby defining the theoretical maximum bearable cycles of the material at a specific temperature not considering self-heating effects.

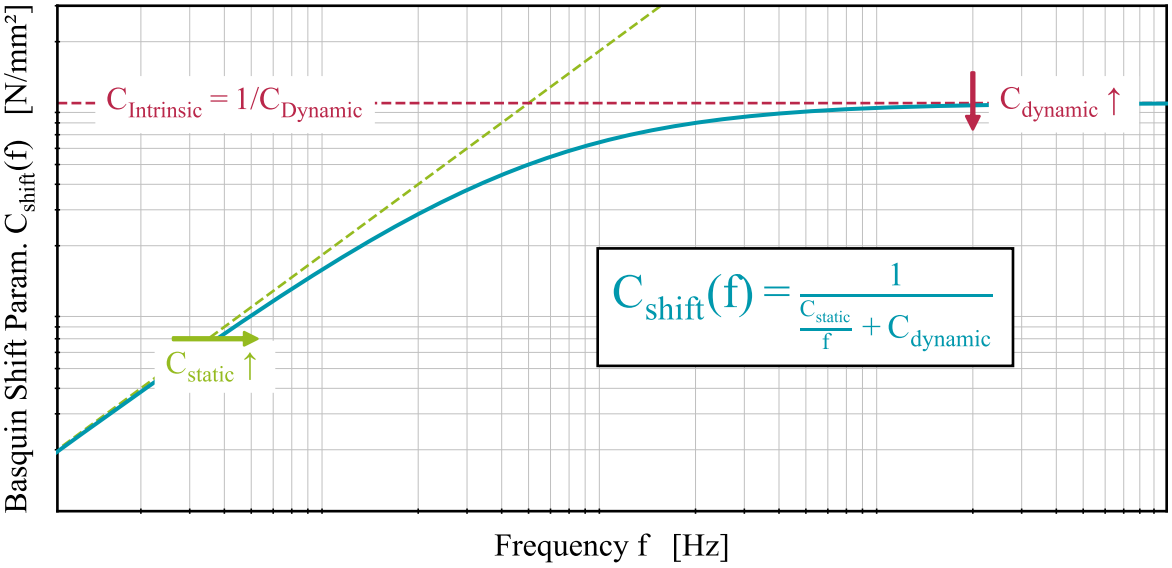

Fig. 9.7: Schematic evaluation of the frequency-dependent shift function for phenomenological description of the fatigue life for tensile-tensile load conditions.

Nevertheless, this formulation has a limitation. While the two parameters, C_{static} and $C_{dynamic}$, allow for the scaling of the shift function $C_{shift}(f)$, the slope of the linear increase remains constant, implying that all materials exhibit the same influence on creep-induced damage, irrespective of their specific properties. To refine this model, an additional factor q, can be introduced to enable further adjustment of the curve's slope (compare Equation 9.16 and Figure 9.8).

$$C_{shift}(f) = \frac{1}{\left(\frac{C_{static}}{f^{q}} + C_{dynamic}\right)} \qquad \textit{(Eq. 9.16)}$$

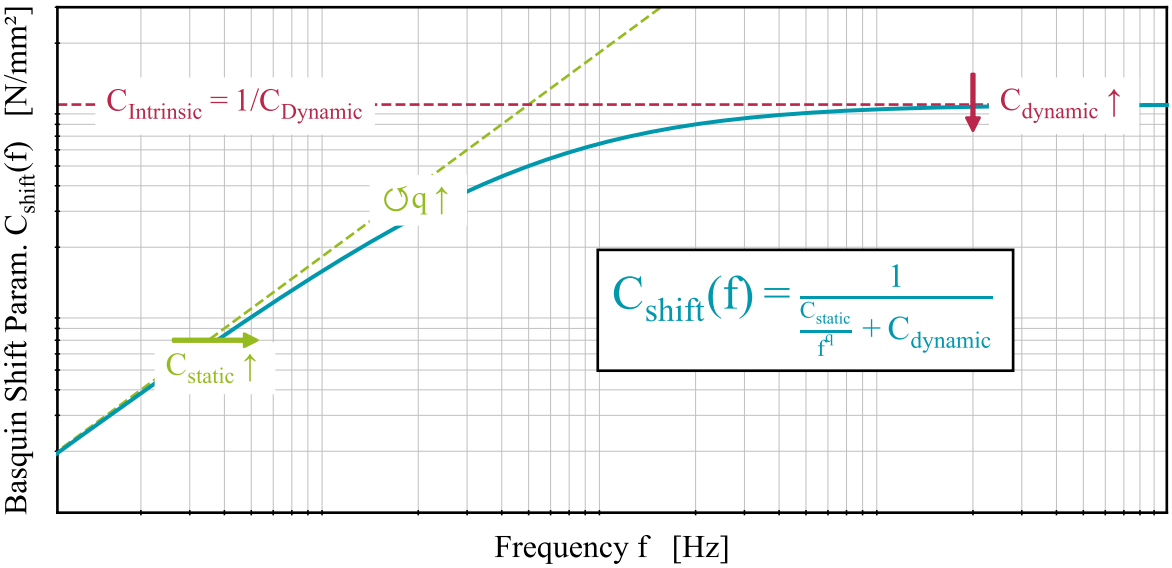

Fig. 9.8: Schematic evaluation of the modified frequency-dependent shift function for phenomenological description of the fatigue life for tensile-tensile load conditions.

However, by appropriately adjusting the shift function, also the creep-dominated data points can be represented by the shift function without an additional slope parameter q through the transition region where the shift function deviates from the ideal time-dependent description described by C_{static} (green line). Therefore, given the limited number of tested lower frequencies, the further analysis will be based on the relationship outlined in Equation 9.13. Nevertheless, it would be interesting to investigate the fatigue behavior at significantly lower frequencies than 2 Hz, and whether the phenomenological relationship remains valid at these very low frequencies, where the time of load increases substantially.

In the following, the developed phenomenological model is employed to quantify the frequency-dependent shift of the *Basquin* equation based on the experimentally determined fatigue data under isothermal material conditions. Thereby, the 90 Hz fatigue data are not included from the fitting process. Figure 9.9 shows the fitted shift function curves $C_{shift}(f)$ for both longitudinal and transversal oriented specimens. Given that the fitting process adjusts the parameters of the equation to match the experimentally observed data averagely, the determined asymptotic shift parameter $C_{shift}(f \to \infty)$ is lower than the experimentally derived *Basquin* parameters C for the single frequencies. Therefore, this suggests that the creep-independent shift parameter $C_{shift}(f \to \infty)$ used for predicting intrinsic cyclic fatigue life may be underestimated due to experimental scattering.

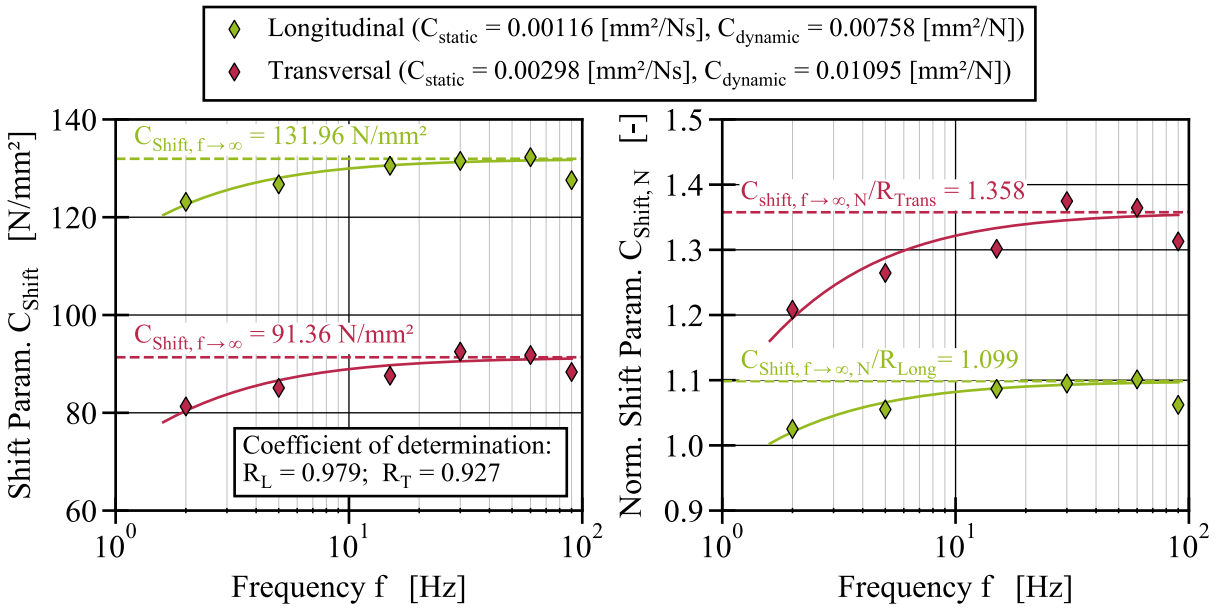

Fig. 9.9: Comparison of the fitted frequency-dependent shift function for longitudinal and transversal orientations in absolute terms and normalized by quasi-static strength

Despite this, the results clearly show that as frequency increases, the rate of change in the shift function $C_{shift}(f)$ decreases, and the SN data at higher frequencies converge compared to lower frequencies. At lower frequencies, the material has more time for creep to develop, leading to a greater influence on the overall fatigue life. On the right-hand side of the Figure 9.9, the shift parameter is also normalized using the quasi-static strength of each orientation, making the pronounced creep effects in the transversal oriented specimens more evident, as reflected in the broader spread over ca. 1.5 decades in the experimental SN data (compare Chapter 9.1). As discussed in Section 7.1, the relative fatigue life in relation to quasi-static strength is significantly greater for transversal specimens than for longitudinal ones, and this also becomes particularly evident through the normalization process. The normalized shift parameter $C_{shift,f\to\infty}/R$ is 28 % higher for the transversal orientation compared to the longitudinal orientation.

By quantifying the frequency- and, respectively, time-dependent creep-induced shift in the cyclic fatigue life, also the influence of the material's micro-structural configuration, characterized by the fiber orientation distribution, can now be better investigated and understood. Identical frequencies can have different impacts on the fatigue life shift depending on the material's morphological structure, even if the constituent materials are the same. For instance, a change to lower load frequencies leads to a more pronounced shift of cyclic fatigue life in transversal specimens compared to longitudinal ones, considering the calibrated phenomenological model. This leads to the conclusion that the phenomenological parameters are dependent on the material structure and exhibit distinct behaviors based on the micro-structural configuration. Nevertheless, based on the derived relationship for the frequency-

dependent shift of the cyclic fatigue data, it can be assumed that there also exists an intrinsic, frequency-independent, but solely cycle-driven fatigue life for the material. The experimentally determined intrinsic fatigue life for both orientations is shown in Figure 9.10. As described before, due to the experimental scatting and the fitting procedure, the determined intrinsic fatigue life is not the highest possible SN curve.

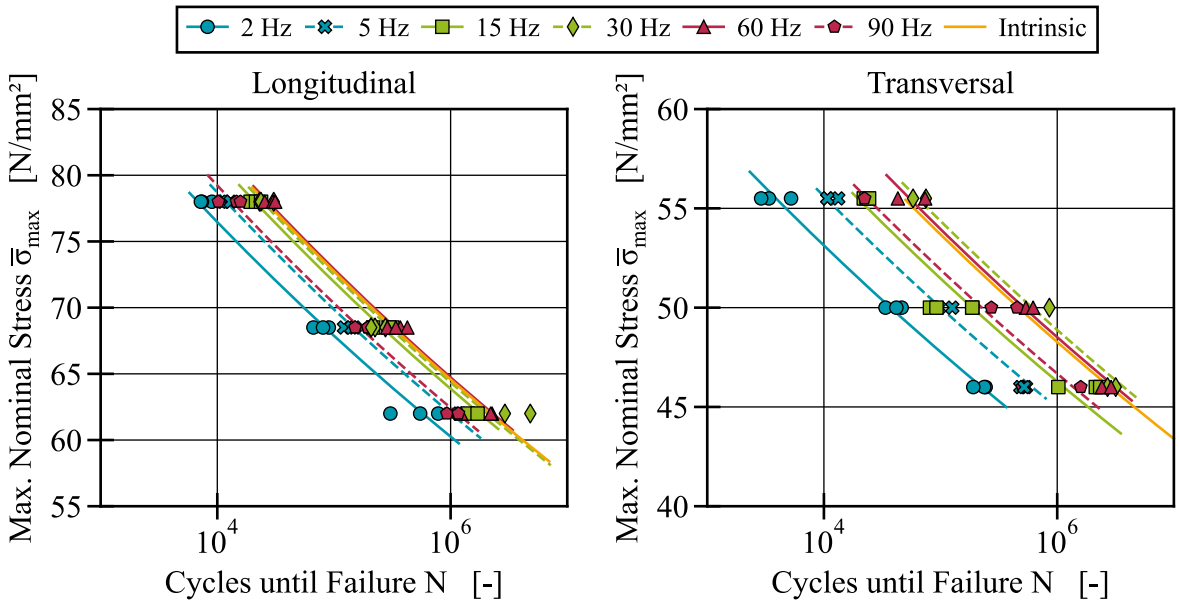

Fig. 9.10: Determined intrinsic fatigue life for both longitudinal and transversal specimens.

This concept of the intrinsic fatigue life offers the potential to systematically gather and compare cyclic fatigue life data under conditions where creep is effectively eliminated, thereby enabling a focused investigation into the material's structural behavior, including interactions between fibers and matrix inducing crack initiation and progression, in relation to purely cycle-driven damage mechanisms. The experimental findings indicate that the intrinsic fatigue life of the tested PBT-GF30 material is close to the determined fatigue data at a frequency of 60 Hz under isothermal conditions. Hence, the use of thermo-adaptive temperature control allows for the precise isolation and examination of the specific fatigue mechanisms. However, for frequencies beyond 60 Hz, further experimental studies are necessary to validate and clarify the relationship between frequency-dependent and intrinsic fatigue life.

9.3 Accelerated fatigue life characterization of short fiber-reinforced thermoplastics

In addition to improving the understanding of the fatigue behavior and damage mechanisms of SFRT materials, the characterization methodology developed here, together with the derived phenomenological shift function for fatigue data, also provides significant practical advantages for the fatigue dimensioning of structural components. The dimensioning process of structural components requires strength values to assess the stress states induced by external load cases. For fatigue life dimensioning, SN data are utilized as the basis for determining the fatigue

strength. However, the generation of comprehensive SN data for fatigue life is traditionally a time-consuming and costly process, especially if different material orientations and temperatures need to be tested. This makes the development of efficient methods for the fatigue characterization of materials crucial in order to reduce testing time while maintaining the accuracy necessary for reliable predictions of the mechanical behavior of the designed components before prototypes can be produced and tested. The methodology developed in this work has the potential to accelerate the fatigue characterization process substantially.

Essentially, as discussed before, the relationship between applied stress and the resulting fatigue life strength can be represented by the *Basquin* equation, uniquely defined by the parameter C and the slope, characterized by the parameter k. Provided that the material's cyclic deformation behavior does not exhibit a distinct frequency dependence (compare Chapter 8), and thus the induced micro-mechanical stress state is not altered by a change in test frequency, the material's intrinsic frequency-independent *Basquin* slope parameter $k(f) = k$ can be determined applying the thermo-adaptive testing methodology at very high frequencies under isothermal conditions. In the next step, the phenomenological shift function can be calibrated through additional fatigue tests in the required frequency range to determine the frequency-dependent *Basquin* parameter $C = C_{shift}(f)$. Given the consistent slope parameter across the different frequencies, it is not necessary to test the entire load range at each frequency as it was conducted in Chapter 9.1. Instead, the focus can be on specific load levels with significantly lower cycles to failure, thereby drastically minimizing the testing time. This methodology was previously introduced and validated in [HDÇ22], where a reduction in testing time for predicting the fatigue life is achieved using three load levels with triplicate testing at each level. In this case, the pure testing time is successfully reduced from approximately 25 days to around 5 days for generating a complete 5 Hz SN dataset for a cycle range between 10^4 and 10^6 without losing any accuracy.

Moreover, this approach not only significantly reduces the test time required for fatigue characterization but also delivers deeper insights by generating fatigue life data across a broader frequency range, compared to traditional testing conducted at one single specific frequency. However, the self-heating effect also needs to be considered while applying the accelerated fatigue characterization. This can be conducted using the EDMA data and the equation 7.17.

9.4 Conclusion on the isothermal characterization and the phenomenological modeling of the frequency-dependent fatigue life

In this chapter, the developed thermo-adaptive testing methodology was applied to fatigue experiments, enabling, for the first time, the characterization of fatigue life at very high frequencies, which would typically result in self-heating and premature thermal failure of the

material when tested in conventional fatigue experiments. The developed approach enables fatigue tests to be conducted over a broad frequency range, spanning up to 90 Hz, without the influence of temperature-induced changes in damage mechanisms for the tested PBT-GF30. It was observed that when the temperature increase due to material dissipation is eliminated, the slope parameter of the *Basquin* equation remains constant across all frequencies for each orientation. Furthermore, the isothermal fatigue data revealed that cyclic fatigue life increases with frequency. However, at higher frequencies, the number of cycles to failure tends to converge, while at lower frequencies, the shift between the SN data is increased.

This behavior can be explained through the interaction of two competing mechanisms within the material: mechanical degradation induced by cyclic load and time-dependent creep. Thereby, the load frequency serves as a link between the number of applied load cycles and the duration of applied stress. At lower frequencies, the material has more time to creep before reaching a critical number of cycles to failure while also undergoing cyclic damage over the same time period. Both mechanisms contribute to the irreversible material degradation, with one mechanism, creep or cyclic degradation, becoming more or less dominant depending on the applied frequency.

With this understanding of the fatigue behavior, a phenomenological equation was derived based on fundamental fracture mechanics principles to model the frequency-dependent shift of the cyclic fatigue life. Analysis of the experimental data and the derivation of the phenomenological equation revealed that the shift function approaches an asymptotic limit as the frequency increases. This limit can be interpreted as the material's intrinsic fatigue life, which is governed solely by cyclic material damage progression without any influence from creep effects. The theoretical value of this intrinsic fatigue life is very close to the results obtained at the tested frequencies, specifically at 60 Hz. However, it should be noted that the determination of the assumed intrinsic fatigue life is highly dependent on the input data for the fitting process and needs to be further investigated and confirmed in terms of material behavior. Furthermore, additional experiments are required to investigate and validate the concept of intrinsic, solely cyclic fatigue life.

The thermo-adaptive testing methodology facilitates a more comprehensive analysis of the material's fatigue behavior and provides deeper insights into the underlying damage mechanisms. Additionally, the knowledge gained from this approach allows for a significant acceleration in fatigue characterization. The frequency-independent slope parameter k of the *Basquin* equation can be determined at high frequencies under isothermal conditions testing the required load range. The shift function $C_{shift}(f)$ for different frequencies can be calibrated using a substantially reduced number of load cycles at higher stress levels. This approach is feasible since the fatigue behavior at stress levels corresponding to approximately 10^6 cycles

can be reliably predicted through extrapolation due to the consistency of the slope parameter across the range. Compared to conventional fatigue testing at low frequencies, such as the industry-standard 5 Hz, this approach delivers a faster and more comprehensive understanding, as well as more detailed data for dimensioning.

The investigations further showed that fatigue behavior is significantly influenced by the properties of the material constituents and, more importantly, by the material morphology, particularly the process-dependent fiber orientation distribution. This was demonstrated by the different fatigue behavior of longitudinally and transversely extracted specimens. For instance, the data indicated a greater frequency dependence in the creep regime for the transverse specimens. The heterogeneous and process-dependent micro-structure complicates the direct correlation of the damage mechanisms and interactions with the material behavior at the macroscopic level. Although the isothermal fatigue characterization has substantially reduced the complexity of interactions, the underlying structural intricacies of the material persist, making it challenging to fully deconstruct and understand the fatigue and, hence, the damage process of SFRT materials.

Characterization and testing directly at the meso-scale, where a uniform and high degree of fiber orientation prevails, would eliminate the interactions between different orientations and provide a deeper and more profound insight into the damage processes induced by dynamic-cyclic loads. Therefore, in the next chapter, a new methodology is introduced to directly manufacture specimens with a high fiber orientation and a uniform distribution across the thickness using injection molding.

10 NOVEL METHODOLOGY FOR MANUFACTURING SPECIMENS WITH UNIFORM AND HIGH FIBER ORIENTATION

The mechanical properties, specifically stiffness and strength, of short glass fiber-reinforced thermoplastics are strongly influenced by the process-dependent morphology of the material, as discussed and shown in the chapters before. This means that the damage process and degradation behavior under static, dynamic, and dynamic-cyclic loading are closely tied to the material constitution and, hence, the prevailing fiber orientation distribution. To investigate the influence of material structure on the damage mechanisms in detail, it is desirable to characterize the material behavior of SFRT materials directly at the meso-scale, where the fibers are uniformly and highly oriented, allowing investigations and analysis without the interactions of regions with different fiber orientations. This approach would ensure that the applied external loads reflect the corresponding stresses on the material level, unaffected by the varying stiffness resulting from different fiber orientations. Furthermore, the local stiffness behavior can also change due to damage progression throughout dynamic-cyclic loading. However, caused by the process-induced flow patterns in injection molding, SFRP compound materials and, thus, test specimens are characterized by a layered fiber orientation structure, as previously discussed (compare Chapters 5 and 6). Therefore, although the mechanical behavior can be examined by measuring the macroscopic elongation and the loads applied to the test specimen, it is not possible to directly observe the actual prevailing local state of stress or strain and internal interactions. Also, analyzing material changes, such as stress redistributions, damage progression, and mechanisms, is not possible without further ado or complicated measurement systems, like in-situ µCT analysis [RSR+18]. For this reason, there is an ongoing effort to be able to produce test specimens with uniform and highly oriented fiber orientation distribution across the thickness. The purpose is to investigate the material behavior and the resulting damage mechanisms directly at the meso-level without interacting layers of different fiber orientations, as it is already the case with continuously fiber-reinforced plastics.

In order to achieve meso-level specimens, a method was presented in [CMH+23], in which the layers of interest with a homogeneous and highly oriented fiber distribution are obtained by mechanical post-processing of the specimens through additional machining. This process involves milling the surface of the specimen and thus removing material layer by layer to obtain regions with a uniform fiber orientation distribution. The procedure was applied on a polyamide with 50 wt.-% glass fibers. Although the constitution and the production parameters in terms of cooling rates, crystallization, and actual fiber orientation are not changed by the mechanical removal, the authors point out that this additional and highly invasive mechanical milling process causes damage to the material and alters the material properties. Thus, a

characterization of the material behavior, particularly the fatigue behavior, of specimens produced using this technique is not promising.

Land and *Krumpholz* [Lan24, LK20] presented an alternative manufacturing process where the fiber orientation distribution in the injection molding process is manipulated by inducing a relative movement of the two cavity walls to each other while filling the cavity. This requires a cavity in a tube geometry and, thus, a tubular specimen design. The relative movement is achieved by rotating the core element on the ejector side of the injection mold, which reorients the fibers in the circumferential direction of the thin-walled tube through additional melt shearing (compare Figure 10.1). Hence, an overlaid *Couette* flow is induced, which causes the fibers to reorient in the direction of rotation. Although the fiber orientation can be manipulated in this way, there is still a layer formation with perpendicular orientations to each other across the thickness due to the overlaid melt flows in different directions. However, the proportions between the edge and the core regions can be adjusted. Nevertheless, this method does not lead to uniform fiber orientation distributions, and conventional test specimens cannot be taken since a thin-walled tube geometry is manufactured in the methodology.

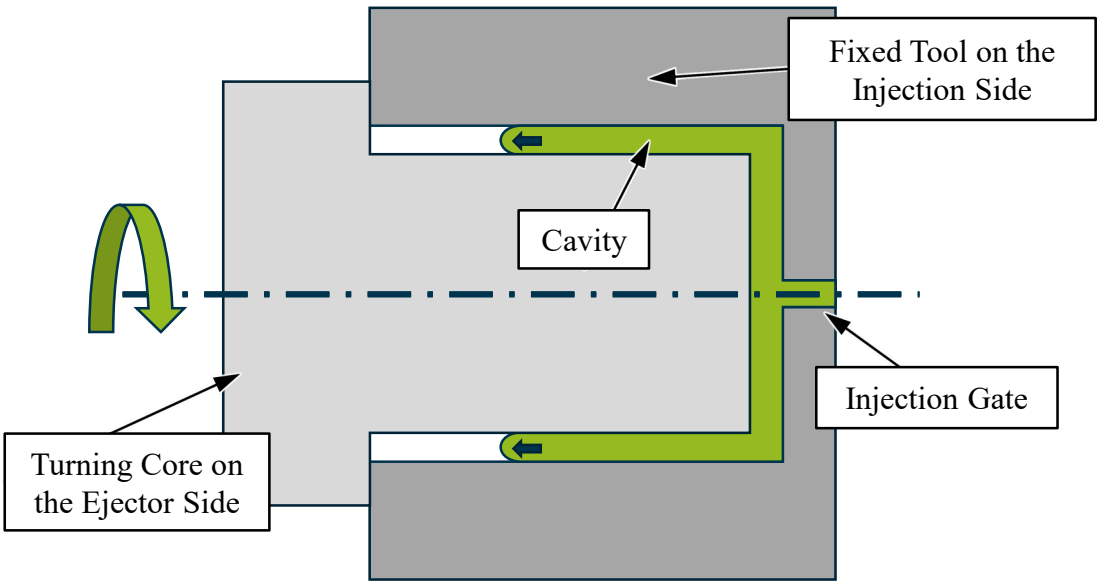

Fig. 10.1: *Schematic representation of the methodology to manipulate the fiber-orientation distribution across the thickness by turning the core after Land and Krumpholz.*

In [RKD+22, Roo24], a methodology was developed to produce highly oriented test specimens that closely align with the conventional injection molding procedure. An injection mold is designed to accelerate the melt while cavity filling. The acceleration is achieved by spreading the melt widely first, staunching it, and then letting it flow through the cavity region with tapering width, which results in a cross-section that decreases along the flow path (see Figure 10.2). The resulting convergent flow pattern induces high-velocity gradients and reorients the fibers into the main flow direction. However, the application of a strongly

convergent tapered area leads to significant restrictions on the dimensions of the test specimen. As a result, only test specimens with a maximum length of 40 mm transverse to the flow direction can be extracted.

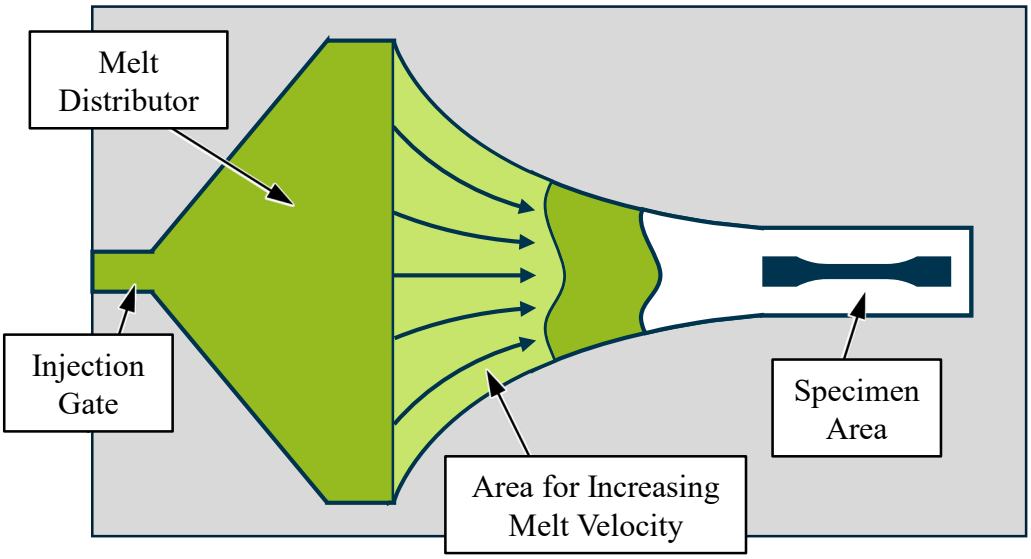

Fig. 10.2: After [RKDA22, Roo24], a schematic representation of the strongly tapered cavity geometry is shown. This geometry is designed to induce high-velocity gradients, thereby enabling the production of uniformly high-oriented specimen plates.

A comparable approach was applied by *Kaiser* and *Stommel*, developing a tube specimen geometry [Kai13]. However, in this case, the tube geometry tapering was achieved by reducing the wall thickness along the flow path, as shown in Figure 10.3. With this tube specimen, a uniform and highly oriented fiber orientation can be achieved in the test area of the specimen. The tube geometry also allows the characterization of the mechanical behavior under shear stresses by applying torsional loads. Nevertheless, testing the mechanical behavior of the material in the transverse direction is only possible with the application of internal pressure within the tube specimen, which is rather impractical for characterization under dynamic-cyclic loading in the transverse direction.

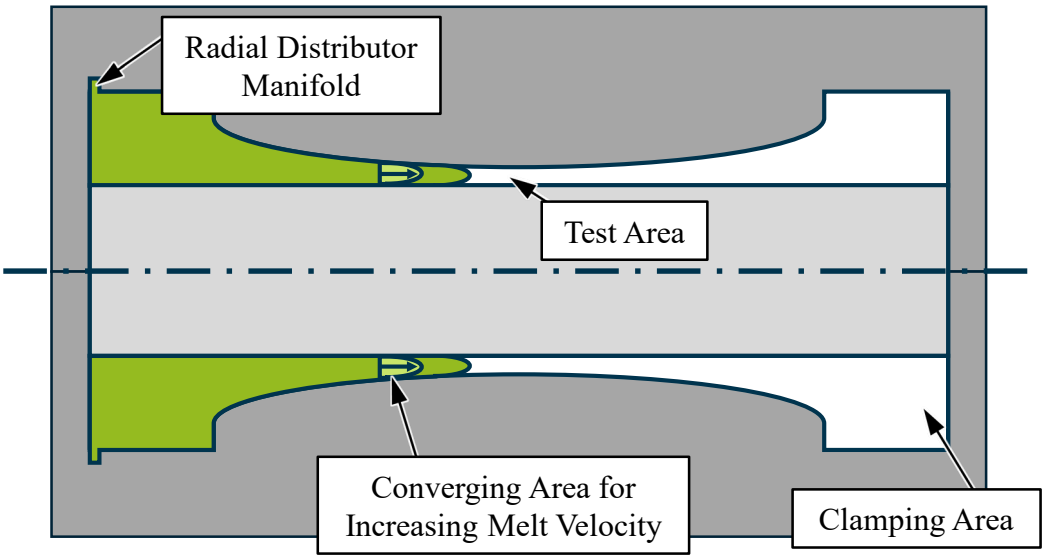

Fig. 10.3: A schematic representation of the tube specimen with a tapered cross-section to induce convergent melt flow and, hence, high-velocity gradients within the test area of the tubular specimen after [Kai13].

Consequently, within the framework of this work, it is aimed to develop a methodology to be able to produce specimen plates with a uniform and high fiber orientation along the thickness direction through injection molding, taking into account that standard specimens of the type 1BA can be extracted in different orientations regarding the fiber orientation.

Hence, in this chapter, a newly developed methodology for manufacturing specimen plates with uniform and high fiber orientation is presented. First, the main mechanisms of fiber orientation formation through melt flow processes occurring in injection molding are discussed. Subsequently, the concept and mold development for producing uniform and highly oriented specimen plates are presented. Following this, a parameter study using injection molding simulations is conducted to determine the manufacturing parameters for the reliable production of the specimen plates. At the end of this chapter, the developed methodology is validated with manufactured specimen plates.

10.1 Formation of fiber orientation distributions in injection molding

The description of fiber orientation development in the injection molding process is of great importance for fiber-reinforced thermoplastics, as the mechanical properties are inherently linked to the material structure resulting from the process. For the development of structural components, predicting the resulting material properties before the production of tools and molds is desirable to enhance component development as effectively and cost-efficiently as possible. Therefore, over the past decades, many models for predicting the fiber orientation

distribution have been researched and developed, which are based on the description of melt flow behavior and state while injection molding [FT84, Tuc22].

During the injection molding process, a melt velocity distribution develops within the flow gap of the cavity, as illustrated in Figure 10.4. For simplification purposes, *Newtonian* fluid behavior, laminar flow conditions, and adhesion of the melt at the cavity wall or the frozen melt areas are assumed. Additionally, an ideal, infinitely wide gap is considered for reducing the problem to two-dimensional. Due to wall adhesion, it is presumed that the melt exhibits zero velocity along the contact area, resulting in a parabolic velocity profile induced by the applied volumetric flow rate $\dot{V}$. The volumetric flow rate $\dot{V}$ is usually constant over the cavity filling caused by the position-controlled translation of the screw of the plasticizing unit during the melt injection. However, the velocity gradients across the thickness induce the shearing of the melt. Hence, the shear-rate quantifies the intensity of the velocity gradient within a fluid flow.

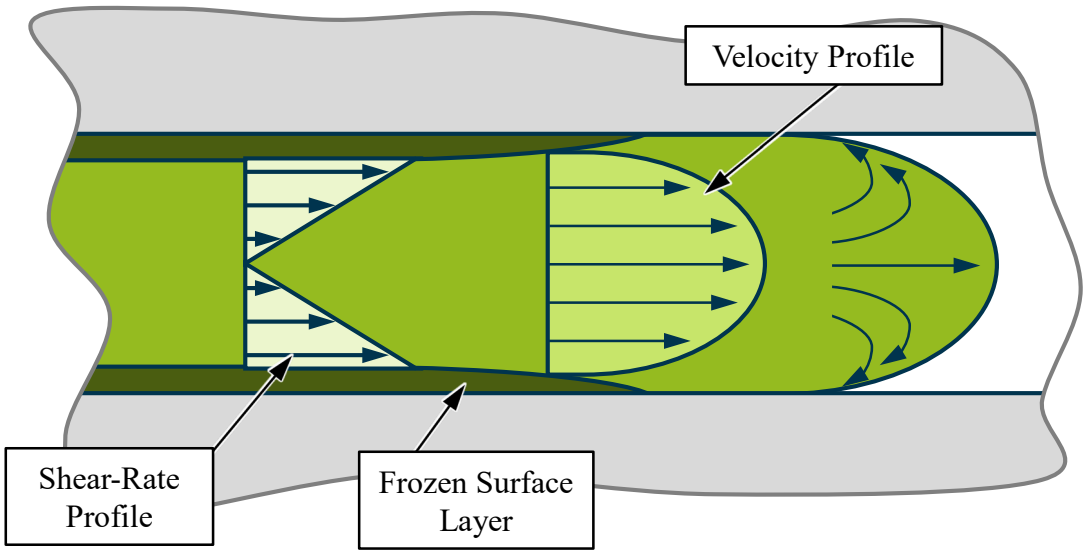

Fig. 10.4: Developed velocity and shear-rate distribution within the flow gap between two plates.

To demonstrate how melt-shearing causes the reorientation of the fibers into the direction of the main melt flow, another simplification of the velocity profile can be achieved using the *Couette* flow model, as depicted in Figure 10.5. In this case, one tool wall is fixed, while the opposite wall undergoes a constant translational movement relative to the first. This translation induces a velocity profile characterized by a constant shear-rate $\dot{\gamma} = \partial u(z)/\partial z$ in the melt fluid due to wall adhesion. When a fiber is placed in this *Couette* flow, the differing velocities, respectively, and the shearing of the melt acting on the fiber during its translational movement cause it to rotate. Assuming the fiber is infinitesimally thin, it will continue to rotate until it is completely aligned with a streamline (isotach), where no velocity differences of the melt-flow

can act on the fiber. Therefore, in sheared melts, the fibers are oriented in the direction of the main flow of the melt.

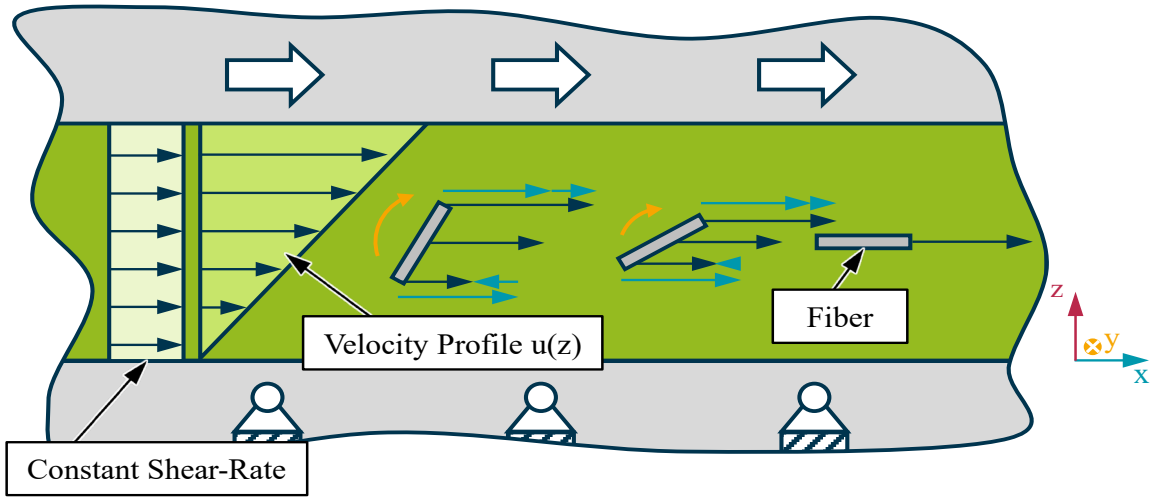

Fig. 10.5: *Mechanism of fiber orientation due to melt shearing within the Couette flow.*

However, the melt and the fibers exhibit different behavior when the previously described flow pattern is superimposed by radially propagating source flow, which is the case at the injection gate of mold cavities. A radial source (as shown in Figure 10.6) describes a fluid with a uniformly diverging flow within the cavity plane. This means that the melt spreads equally in all directions, with a flow front of the melt characterized by decreasing velocity due to the constant injection speed and the increasing cross-sectional area along the flow path. In contrast to the flow pattern discussed before, where all flow vectors are parallel along the flow length, radial source flow induces velocity components that are also perpendicular to the primary flow direction in the fibers caused by the diverging flow lines. This results in the fibers rotating until the rotation momentum is zero, thereby aligning them completely perpendicular to the primary flow direction of the melt. It is essential to note that the likelihood of in-plane fiber rotation around the z-axis decreases with increasing distance from the injection point caused by the diminishing velocity components resulting from the diverging flow pattern while keeping the volumetric flow rate constant.

Subsequently, both main mechanisms that lead to the orientation formation of the fibers were described in terms of the fundamental flow patterns occurring while cavity filling. For the quantitative descriptions, models to describe the fiber orientation procedure by the melt flow behavior are discussed in the following.

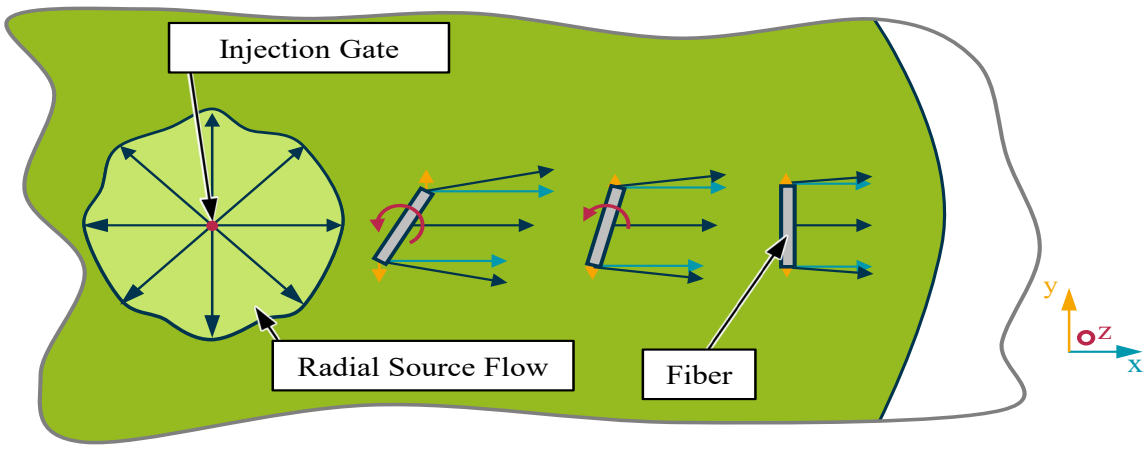

Fig. 10.6: Mechanism of fiber orientation perpendicular to the main flow direction due to diverging flow.

In 1922, *Jeffery* provided a mathematical solution for the motion equation of a single rigid ellipsoidal particle embedded in a viscous *Newtonian* fluid to describe the rotation of particles depending on the flow state. Most of the existing models for the prediction of fiber orientation in injection molding processes are based on *Jeffrey's* motion equation. The equation is derived from the solution of the *Stokes* flow equations under the following assumptions: the flow is characterized by low *Reynolds* numbers, indicating laminar flow conditions, and the rigid body is not subjected to any external forces other than the hydrodynamic forces applied by the surrounding fluid [Jeff22]. In accordance with the described assumptions, the time-dependent orientation change $\dot{\boldsymbol{p}}$ of a rigid ellipsoid can be described by Equation 10.1:

$$\dot{\boldsymbol{p}} = \boldsymbol{W} \cdot \boldsymbol{p} + \xi(\boldsymbol{D} \cdot \boldsymbol{p} - (\boldsymbol{D} \cdot \boldsymbol{p})(\boldsymbol{p} \cdot \boldsymbol{p})) \qquad \textit{(Eq. 10.1)}$$

Thereby, the change in orientation $\dot{\boldsymbol{p}}$ is determined by the current orientation state $\boldsymbol{p}$ of the rigid inclusion, and the flow conditions, characterized by $\boldsymbol{W}$ for the vorticity tensor and $\boldsymbol{D}$ for the rate of the deformation tensor, which is the symmetric part of the velocity gradient tensor. The required two tensors for the vorticity and deformation can be determined using the tensor for the velocity gradient $\nabla\boldsymbol{u}$ (equation 10.2) in accordance with equations 10.3 and 10.4.

$$\nabla\boldsymbol{u} = \begin{bmatrix} \frac{\partial u_x}{\partial x} & \frac{\partial u_x}{\partial y} & \frac{\partial u_x}{\partial z} \\ \frac{\partial u_y}{\partial x} & \frac{\partial u_y}{\partial y} & \frac{\partial u_y}{\partial z} \\ \frac{\partial u_z}{\partial x} & \frac{\partial u_z}{\partial y} & \frac{\partial u_z}{\partial z} \end{bmatrix} \qquad \textit{(Eq. 10.2)}$$

$$\boldsymbol{W} = \frac{1}{2}(\nabla\boldsymbol{u}^T - \nabla\boldsymbol{u}) \qquad \textit{(Eq. 10.3)}$$

$$\boldsymbol{D} = \frac{1}{2}(\nabla\boldsymbol{u}^T + \nabla\boldsymbol{u}) \qquad \textit{(Eq. 10.4)}$$

The geometric factor ξ describes the shape of the rigid inclusion and is defined by the aspect ratio, which can be formulated for fibers as stated in Equation 10.5, where l_F is the length and d_F the diameter of the fiber.

$$\xi = \frac{\left({}^{l_F}/_{d_F}\right)^2 - 1}{\left({}^{l_F}/_{d_F}\right)^2 + 1} \qquad \textit{(Eq. 10.5)}$$

However, for fiber-reinforced thermoplastics, the fiber-fiber interactions within the melt cannot be neglected while processing in injection molding. These interactions lead to a limitation in the possible orientation state, which is not accounted for by the original *Jeffery's* equation. Therefore, *Folgar* and *Tucker* [FT84] developed an orientation model to incorporate fiber-fiber interactions by introducing a phenomenological interaction parameter. They transferred the original motion equation of a rigid body into a formulation for orientation tensors to describe the statistical distributions for the orientation of the fibers. Thus, equation 10.6 describes the change of the orientation tensor $\dot{\boldsymbol{A}}$ depending on the flow state, described by the vorticity $\boldsymbol{W}$, deformation rate $\boldsymbol{D}$ and the shear-rate $\dot{\gamma}$ and the phenomenological interaction parameter C_i.

$$\dot{\boldsymbol{A}} = (\boldsymbol{W}\cdot\boldsymbol{A} - \boldsymbol{A}\cdot\boldsymbol{W}) + \zeta(\boldsymbol{D}\cdot\boldsymbol{A} + \boldsymbol{A}\cdot\boldsymbol{D} - 2\mathbb{A}\!:\!\boldsymbol{D}) + 2C_i\dot{\gamma}(\boldsymbol{I} - 3\boldsymbol{A}) \qquad \textit{(Eq. 10.6)}$$

In addition, the change in the orientation tensor is also influenced by the fourth-order orientation tensor $\mathbb{A}$. To calculate the change of the second-order orientation tensor $\dot{\boldsymbol{A}}$, it is necessary to determine the fourth-order tensor $\mathbb{A}$. Various closure approximations have been developed over the years to address this need and provide solutions to estimate the fourth-order orientation tensor $\mathbb{A}$. While these closure methods are required for solving the orientation models, a detailed discussion of these methods is beyond the scope of this work, hence, the reference to the literature [AÇN+22, Tuc22].

Since the objective of this chapter is to achieve a uniform and highly oriented fiber distribution in specimen plates, the mechanisms and analytical descriptions of fiber orientation formation as a function of thickness along the flow path are discussed, and the application to a conventional specimen plate geometry is provided as a case study in the following sections. This analysis provides a more formal but detailed understanding and an analytical description of the formation of different fiber orientation states while injection molding. Such a plate geometry, including both of the previously described corresponding dominant flow patterns, is illustrated in Figure 10.7. The melt of the SFRP compound is injected through the gate and is spread radially within the melt distributor area (radial source flow). Hence, a diverging flow pattern is present in this area of the cavity, which is why the melt and the fibers in the melt are experiencing crossflow stretching.

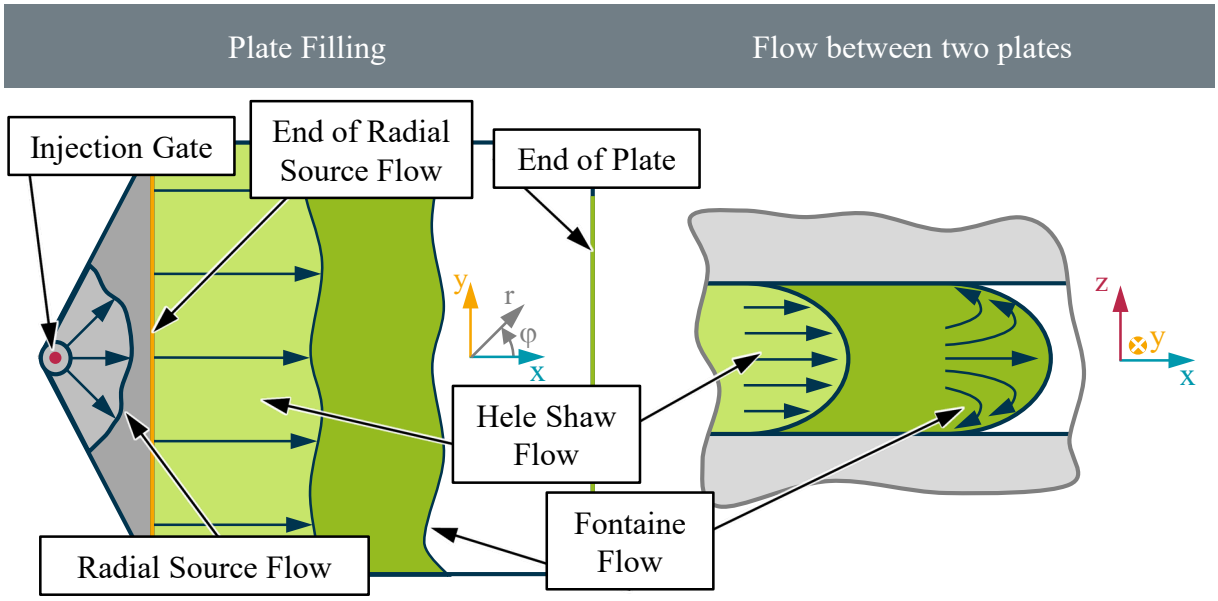

Fig. 10.7: Occurring flow patterns while injection molding of plates.

The fully developed flow velocity profile $u_{RSF}(r,z)$ depending on the radial position r and the cavity height position z can be analytically described by Equation 10.7 [OH06]. Thereby, an opening angle of 120° is considered for the triangle region, representing one-third of a center-gated disk. $\dot{V}$ represents the volumetric melt flow and h is the half of the cavity height H. As the melt progresses, the equation describes a progressive decline in the melt velocity, as a consequence of the reciprocal dependency of the radial position r caused by the increase of the circumferential cross-section. The corresponding velocity gradient tensor $\nabla \boldsymbol{u}_{RSF}$, required for solving the *Folgar-Tucker* equation for the time and flow dependent change of the orientation state $\dot{\boldsymbol{A}}$, is described in Equation 10.8.

$$u_{RSF}(r,z) = \frac{9}{8\pi}\frac{\dot{V}}{h\,r}\left(1-\frac{z^2}{h^2}\right) \qquad \textit{(Eq. 10.7)}$$

$$\nabla \boldsymbol{u}_{RSF} = \frac{9}{8\pi}\frac{\dot{V}}{h\,r^2}\begin{pmatrix} -\left(1-\frac{z^2}{h^2}\right) & 0 & -\frac{2\,r\,z}{h^2} \\ 0 & \left(1-\frac{z^2}{h^2}\right) & 0 \\ 0 & 0 & 0 \end{pmatrix} \qquad \textit{(Eq. 10.8)}$$

In a similar fashion, the velocity profile u_{HSF} and the corresponding tensor for the velocity gradient $\nabla \boldsymbol{u}_{HSF}$ are formulated for the parallel area of the specimen plate geometry using the Equations 10.9 and 10.10. The parameter w describes the geometric width of the parallel region of the specimen plate cavity. The relationship for the velocity profile is also known as the *Hele-Shaw* equation [OH06]. In a parallel flow gap, the cross-section remains constant, and thus the velocity profile u_{HSF} is solely a function of the height coordinate z.

$$u_{HSF}(z) = \frac{3}{4}\frac{\dot{V}}{h\,w}\left(1 - \frac{z^2}{h^2}\right) \qquad \textit{(Eq. 10.9)}$$

$$\nabla \boldsymbol{u}_{HSF} = \frac{3}{2}\frac{\dot{V}}{h\,w}\begin{pmatrix} 0 & 0 & -\frac{z}{h^2} \\ 0 & 0 & 0 \\ 0 & 0 & 0 \end{pmatrix} \qquad \textit{(Eq. 10.10)}$$

A comparison of the velocity gradient tensors (Equations 10.8 and 10.10) indicates the presence of two additional shear components ($\partial u/\partial x$ and $\partial v/\partial y$) acting in different directions within the radial flow region on the melt and describing the cross-flow behavior. For the *Hele-Shaw* equation, only one component ($\partial u/\partial z$) quantifies the shearing along the flow path. The orientation development along the flow direction for both the radial and parallel regions of the cavity is calculated using those flow equations to demonstrate the impact of these differences in flow patterns on fiber orientation.

For the geometric factor ξ, an average fiber length of 250 µm and a fiber diameter of 15 µm are assumed. Additionally, the interaction coefficient C_i is set to 0.0055, as determined by *Wilhelm* using experimental µCT scans for the PBT-GF30 compound material [Wil21]. The injection volumetric flow rate $\dot{V}$ is set to 40 cm³/s, and the cavity height H is specified as 2 mm. The hybrid closure hypothesis is used for the approximation of the fourth-order orientation tensor $\mathbb{A}$. The initial state of the fibers at the injection gate is set to be random ($a_{11} = a_{22} = a_{33} = 1/3$). In reality, the melt passes through the sprue, resulting in an oriented state of the fibers at the injection point of the cavity, which is neglected here. Also, no changes in viscosity due to shear-rate dependency or temperature are taken into account in this example.

Figure 10.8 shows the calculated development of the tensor components A_{11} and A_{22} of the second-order orientation tensor $\boldsymbol{A}$ for different relative coordinates in thickness direction z/h along the center streamline of the melt flow within the specimen plate geometry. The radial source flow area is depicted in gray, while the parallel area is represented by a green background in the diagram. Additionally, Figure 10.9 shows the orientation component A_{11} across the thickness for the three distinct positions along the flow path: injection gate, end of the radial flow and end of the plate.

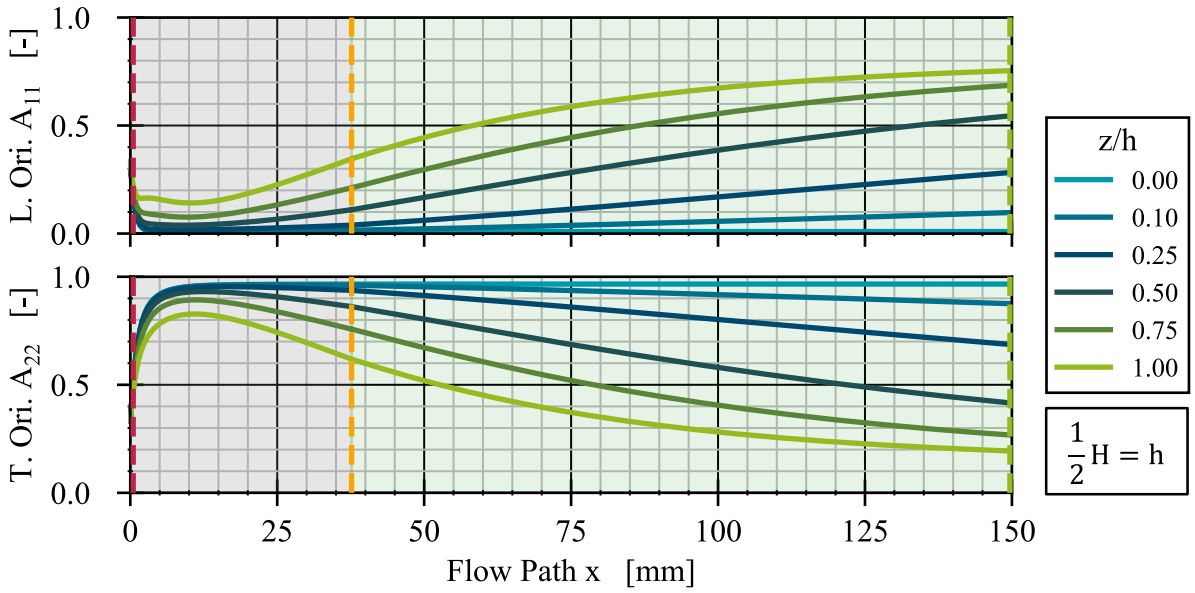

Fig. 10.8: Orientation development along the flow path of an exemplary specimen plate.

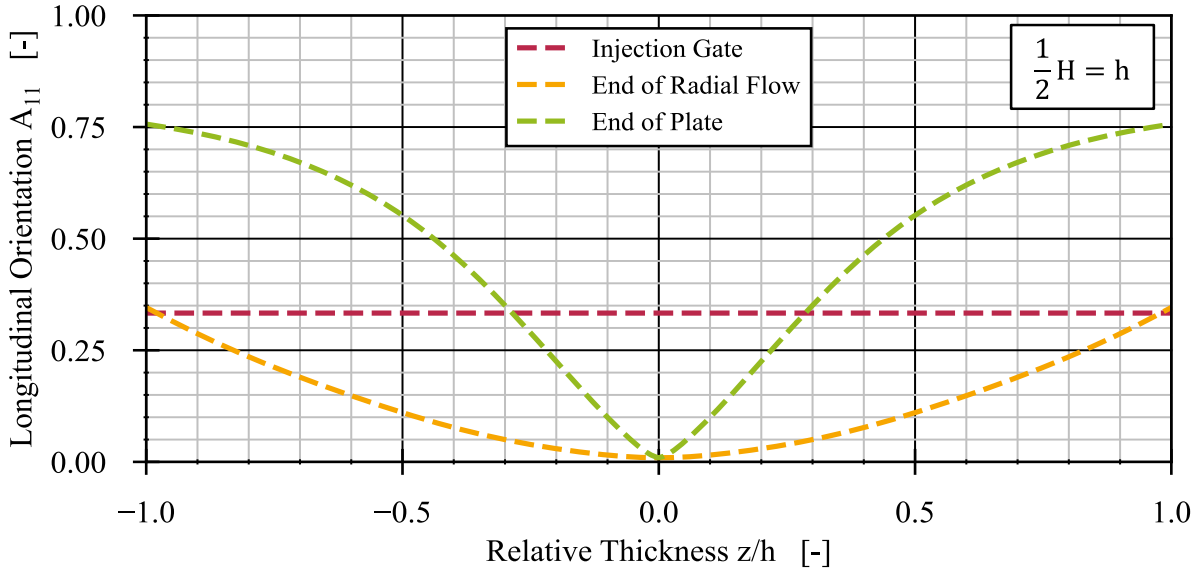

Fig. 10.9: Longitudinal fiber orientation distribution across the thickness at three different points along the flow path as a result of radial and parallel flow patterns.

In the region of radial melt flow, it is evident that across the entire thickness of the cavity, the fibers initially reorient perpendicular to the primary flow direction. Subsequently, beginning at approximately 10 mm along the flow path, there is a notable increase in fiber orientation in flow direction within the regions close to the cavity walls. In contrast, in the region of the parallel flow front, fiber orientation increases steadily along the flow path. However, as higher fiber orientations are achieved, the development becomes more degressive, particularly near the cavity walls. The behavior in the radial melt flow can be explained by the initial dominance of cross-flow stretching. However, due to the quadratic reciprocal components of the gradient tensor $\nabla \boldsymbol{u}_{RSF}$ (compare Equation 10.8), this effect diminishes rapidly. Subsequently, the shearing in the primary flow direction becomes more dominant, leading to a reorientation of

the fibers along the primary flow direction of the melt. It is also evident that in the core region ($z/h \approx 0$), the reorientation of the fibers in the longitudinal direction progresses very slowly or not at all, as the velocity gradients are very low or nonexistent for the case of the middle streamline. In summary, the radial and parallel flow patterns result in a perpendicular and layered fiber orientation distribution across the thickness, which is typical for the morphology of injection molded components (compare Figure 10.9).

It becomes clear that the injection molding of components, and also of specimen plates, through a point-shaped gate leads to a transverse orientation of the fibers, and that this behavior is then counteracted along the following flow through the shear-rate acting in the main flow direction on the melt, so that a longitudinal fiber orientation can develop. Therefore, to achieve a high degree of fiber orientation in one direction, the melt must be spread radially early, and a pure parallel flow needs to be maintained along the entire flow path. This allows the reorientation of the fibers into the primary flow direction.

As stated in Equation 10.10, the shear-rate in the parallel flow region is a function of the volumetric flow rate $\dot{V}$ and two geometric parameters: cavity width w and height h. In [RKD+22, Roo24], an increasing shear-rate is achieved by convergent changes in width, and in [Kai13] by reducing the thickness, respectively height. However, it is evident that cavity height enters the equation with a cubic reciprocal component, resulting in higher shear-rates and, hence, higher orientation degrees when the cavity height is reduced. To demonstrate this behavior, the previously discussed example ($H = 2\,mm$) was recalculated for various plate thicknesses down to $H = 0.5\,mm$ and evaluated at the end of the plate. It becomes apparent that decreasing plate thickness leads to very high orientations across the thickness. Especially, the fraction of high orientation relative to the thickness also increases with decreasing plate thickness. Nevertheless, due to the diminishing velocity gradient in the middle of the cavity height, a singularity is present, which does not occur in reality due to fiber-melt interactions. This singularity exists since the orientation equation does not account for the bidirectional dependence of the melt and fiber orientation, and the change in fiber orientation is calculated solely as a consequence of melt behavior.

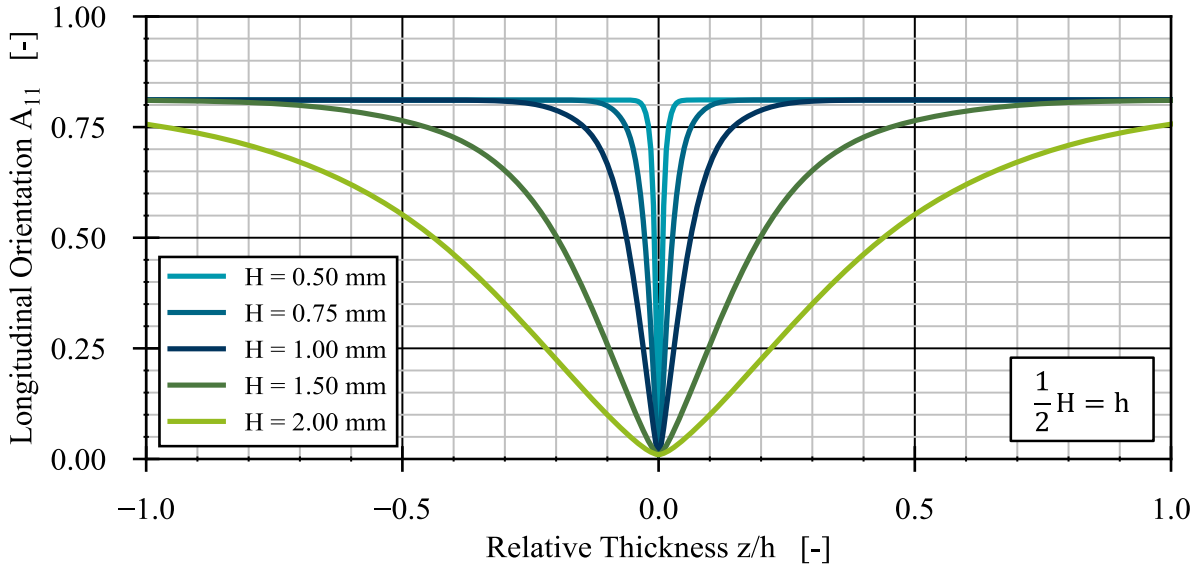

Fig. 10.10: Orientation distribution for A_{11} as a function of the cavity height, demonstrating that smaller gaps induce higher orientation across the thickness.

Consequently, the highest influence on fiber orientation formation is achieved by reducing the cavity height. However, it must be considered that the plate thickness cannot be made arbitrarily thin. There are process-related reasons for this, such as the increasing injection pressure required to fill the cavity. Additionally, there are mechanical reasons, as the SFRP compound material needs to be evaluated as a continuum, and the size effect should not affect the material behavior negatively when subjected to mechanical loads, as aimed in this work.

10.2 Conceptual process design and mold development for uniform and high fiber orientation

In this subchapter, based on the prior discussion of the formation of the fiber orientation, a methodology is developed for manufacturing injection molded specimen plates that exhibit uniform and high fiber orientation across their thickness. These plates should allow for the extraction of standardized 1BA test specimens after DIN EN ISO 527 in various orientations without necessitating changes to the specimen dimensions. The specimen plate thickness is set to 2 mm to be consistent with previous mechanical fatigue experiments conducted on specimens with typical fiber orientation distributions to minimize the influence of geometric factors. Moreover, the plate is to be manufactured by injection molding in order to maintain the process-related influences on the material morphology, such as crystallinity due to high cooling rates. Consequently, alternative manufacturing processes other than injection molding can be excluded from consideration.

Given that in the previous analysis, the height defined by the cavity dimensions in the thickness direction is identified as a key factor for achieving high shear-rates and, consequently, high fiber orientations. This dependency will be utilized here as well, although without altering the

tool cavity height or thickness in its dimensions. To achieve a reduction of the flowable height, the solidification process of the melt is taken advantage of. The melt solidification occurs simultaneously with the cavity filling, as the mold cools the melt, causing solidification to proceed from the outside to inwards (compare Figure 10.11). Hence, once the melt solidifies, the frozen material forms a new boundary layer for the remaining molten melt, effectively decreasing the core region where melt flow induced by the constant volumetric melt flow rate can still take place due to the temperature gradient across the thickness direction. Consequently, as solidification advances, the effective flowable height of the melt decreases.

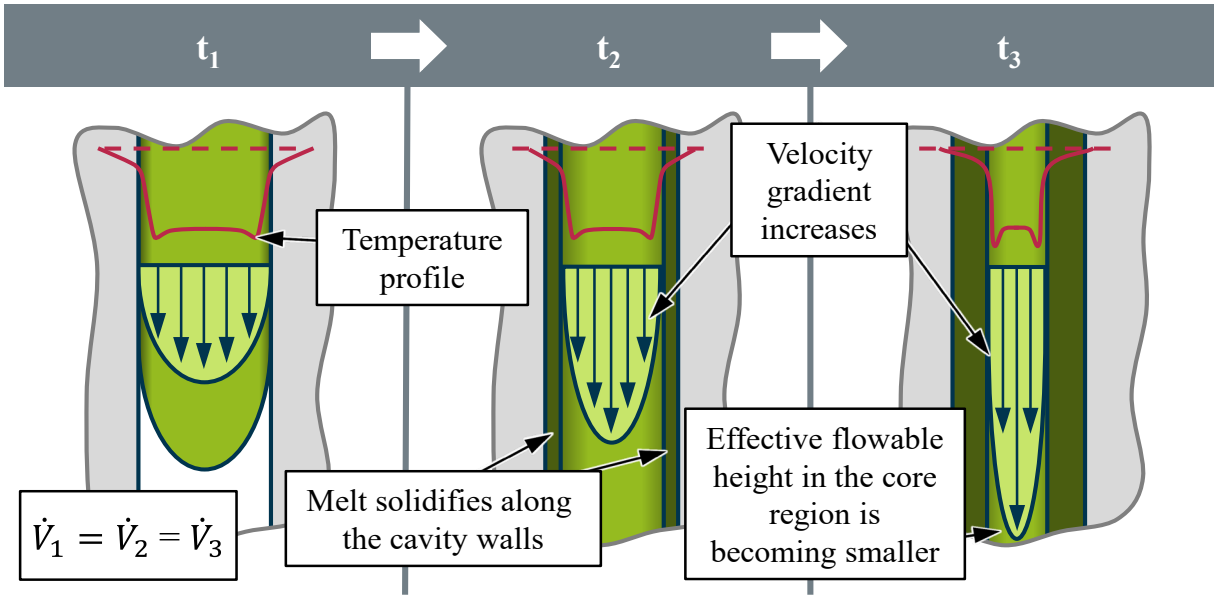

Fig. 10.11: Reduction of the effective flowable height as a result of the simultaneous solidification process of the melt.

The conceptual foundation involves both mechanisms, solidification and melt flow, so that the effective flowable height can decrease, thereby inducing high shear-rates in the melt and reorienting the fibers in the flow direction despite keeping the injection volume rate constant. In addition, as the effective flowable height narrows, the region of high shear gradients shifts toward the core of the cavity, allowing high shear-rates to act there as well. Consequently, the edge regions with high velocity gradients and corresponding high fiber orientation are solidified continuously while flowing through the cavity.

To achieve such continuous flow through the core region, a new injection mold concept is necessary. The concept developed here (compare Figure 10.12) is based on a conventional specimen plate mold, but unlike usual designs, the mold is not closed at the flow end initially. Instead, it remains open and can be closed at a defined time. This allows the melt to continue flowing through the core region of the specimen plate even though the cavity is filled completely. Meanwhile, the melt solidifies progressively at the mold walls, continuously reducing the effective flowable height and thereby achieving increasing shear-rates. At a pre-

determined time after the cavity is completely filled and flown through, the slider closes the cavity, and the holding pressure can be applied. In essence, this open-end injection molding pretend to manufacture specimen plates with theoretically infinite length, as long as the mold is kept open, the solidification process is not completed over the entire thickness and sufficient injection pressure can be applied by the injection molding machine. In addition, the mold is to be installed vertically in the injection molding machine so that the melt can flow out from below and the parallel flow front is not disturbed by the force of gravity. The developed tool concept for open-end injection molding enables to set high fiber orientations throughout the thickness of the specimen plate while eliminating transverse fiber orientation in the core region.

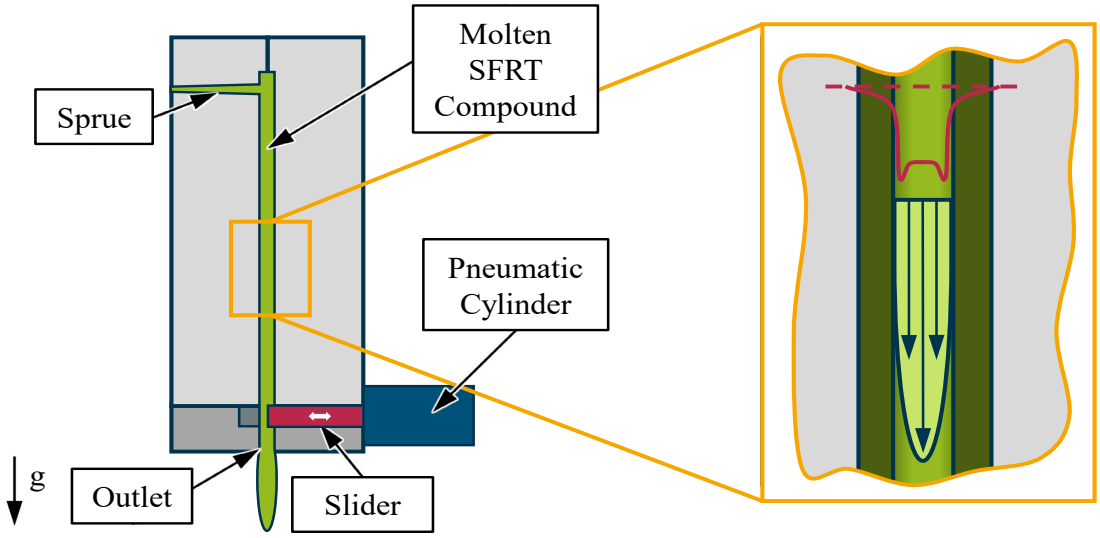

Fig. 10.12: Open-end injection molding concept to manufacture specimen plates with uniform and high fiber orientation across the thickness of the specimen plates.

This concept is subsequently transferred to a mold insert for an existing base tool. Special attention is given to ensure that a flow front parallel to the main flow direction is generated in the plate's parallel region without any radial flow. Furthermore, all elements of the mold are designed modular, allowing for subsequent optimization of the tool. The numerical investigations for the mold development are carried out using the SFRP material PBT-GF30, as it is used for all mechanical investigations in this work. The development and the realization of the required flow profiles are comprehensively described in the work of *Wilhelm* [Wil21].

The developed mold for the open-end injection molding is depicted in Figure 10.13. The mold comprises two fundamental components that can be integrated into an existing main base tool. The nozzle-side mold half features the cavity in a plate configuration with a flat rear surface. A guiding element is also located at the end of the mold to accommodate the slider to close the cavity at the predefined time. The opposing mold half is equipped with a slider, which is actuated by a pneumatic cylinder. In this configuration, the slider's opposing surface is offset relative to the mold surface, enabling the slider to fully close the mold and prevent any further

melt from leaving the cavity. Thus, when the mold closes, the melt flowing out is separated from the melt remaining inside the cavity. Also, the melt distributor and a further balancer element designed to ensure a uniform flow pattern with a parallel flow front without abrupt discontinuities are integrated into this mold half. Additionally, the mold contains three ejectors.

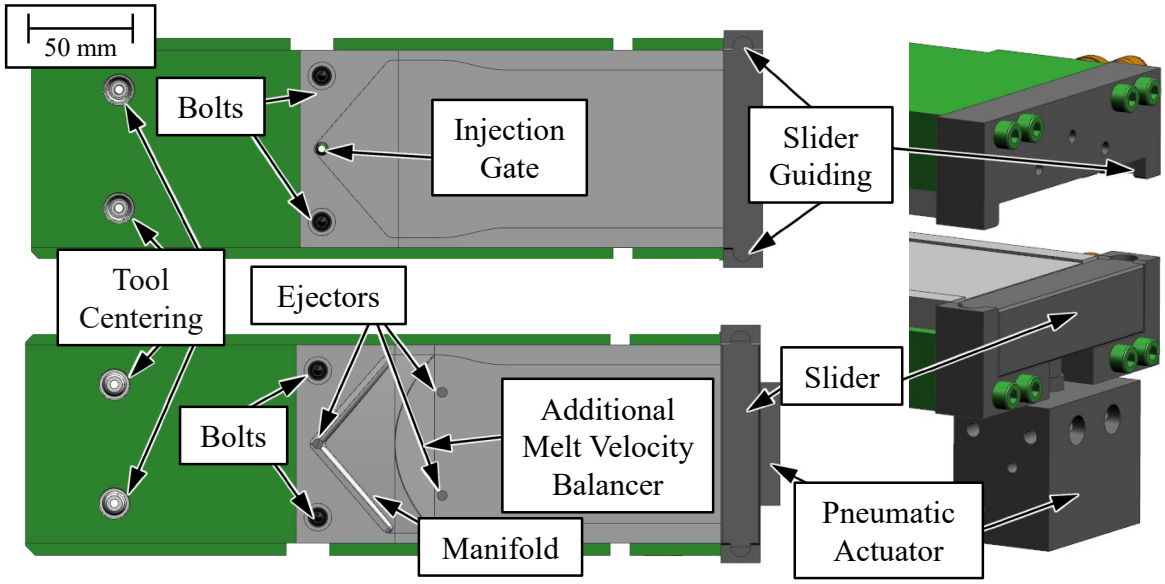

Fig. 10.13: Developed mold for open-end injection molding, including slider mechanism

10.3 Numerical analysis for the determination of the process parameters to manufacture specimen plates with uniform and highly oriented fiber orientation

Before the newly developed mold is used to produce specimen plates with a uniform and high oriented fiber orientation , numerical simulations are conducted to investigate the sensitivity of the manufacturing parameters to be able to reduce the experimental effort in finding the appropriate machine settings. This is necessary since the analytical case study conducted in Chapter 10.1 does not account for all influencing factors that contribute to the nonlinear system behavior of injection molding, affected by, for instance, the shear-rate-dependent viscosity or the solidification process of the injected melt. For the sensitivity analysis, the factors mold temperature T_{Mold} and volumetric flow rate $\dot{V}$ are selected, as experimental studies [BCF78, CCC+11, LZY14] have demonstrated that these parameters have the most significant impact on fiber orientation distribution in injection molded plates. In addition, the flow time t_{Flow}, which describes when the mold is closed by the pneumatic cylinder after the melt injection started and, hence, how much melt has flown through the cavity (additional melt throughflow V_{AMT}), is taken into account. This selection of parameters is also aligned with the mechanisms regarding the fiber orientation development discussed previously.

For the numerical sensitivity analysis, a second-order Central Composite Design (CCD) test plan is applied since it can also depict nonlinear relationships between the varied parameters. Applying the CCD method for the Design of Experiment (DoE), an experimental space is defined based on a classical full factorial design plan. However, to effectively capture the nonlinear behavior, the experimental space is extended by central and axial points [DVD17]. With three factors (mold temperature T_{Mold}, volumetric flow rate $\dot{V}$ and flow time t_{Flow}), this results in an analysis with 15 individual study points. The central and axial points are defined based on the two selected levels of the factorial design of the experiment.

The solidification process is mainly driven by the plate thickness and also by the mold temperature [HMG+17]. The plate thickness is set to 2 mm. In accordance with the manufacturer's processing recommendations for PBT-GF30, the mold temperature levels are set to 80 °C and 95 °C.

The specified levels for volumetric flow rate $\dot{V}$ are 25 cm³/s and 50 cm³/s. A volumetric flow rate of 25 cm³/s is selected based on findings by [BCF78], which indicate that lower injection flow rates increase the fiber orientation in the flow direction within the core region. This may seem counterintuitive, as the analytical analysis presented in the previous chapters demonstrated that high velocity gradients, which increase with the volumetric flow rate $\dot{V}$, are required for the reorientation of the fibers. However, the conducted analytical study does not take into account the solidification process and, hence, the resulting continuous reduction of the available flowable height during injection molding. The flowable height has a greater influence on the velocity gradients and, hence, on the orientation formation (compare Chapter 10.2). Nevertheless, to investigate the effects associated with higher volumetric flow rates, the second level for the flow rate is set at 50 cm³/s. For comparison, the specimen plates with the conventional fiber orientation distribution are manufactured at a volumetric flow rate of 40 cm³/s (compare Chapter 6).

To quantify the amount of melt that flows through the cavity before the slider closes, it is necessary to define the flow time t_{Flow}. In conventional injection molding, flow time is typically a resultant parameter, influenced by the melt volume required to fill the cavity at a constant flow rate and the switching from velocity (fill) to a pressure-controlled process (packing) [HM17]. However, in the developed open-end injection molding simulation model, the flow time is defined as a governing variable for evaluating the predicted results of the fiber orientation distribution across the plate cross-section. Since in the open-end injection molding the cavity continues to be flown through after it is completely filled, the melt volume that flows out of the cavity is also taken into account for a better understanding of the process. The melt volume leaving the cavity is described as an additional melt throughflow V_{AMT}. The resulting parameter sets for the numerical study of the development of the fiber orientation distribution

in the open-end injection molding process are given in Table 10.1. It is noteworthy that the cavity is not entirely filled at the specified parameters of the run 13. However, this test point is a consequence of the application of the CCD plan.

	Run	Mold Temperature T_{Mold} [°C]	Volumetric Flow Rate $\dot{V}$ [cm³/s]	Flow Time t_{Flow} [s]	Additional Melt Throughflow V_{AMT} [cm³]
Factorial Points	1	80.0	25.0	1.73	0.00
	2	80.0	25.0	3.45	43.25
	3	80.0	50.0	0.86	0.00
	4	80.0	50.0	1.73	43.25
	5	95.0	25.0	1.73	0.00
	6	95.0	25.0	3.45	43.25
	7	95.0	50.0	0.86	0.00
	8	95.0	50.0	1.73	43.25
Axial Points	9	77.0	37.5	1.73	21.63
	10	98.0	37.5	1.73	21.63
	11	87.5	20.0	3.24	21.63
	12	87.5	55.0	1.18	21.63
	13	87.5	37.5	0.92	-8.75
	14	87.5	37.5	2.54	52.00
Central Point	15	87.5	37.5	1.73	21.63

Table 10.1: Central Composite Design of Experiment for analyzing the influence of the manufacturing parameters on the fiber orientation distribution.

The open-end injection molding process is numerically investigated in the simulation environment of Moldflow 2021, Autodesk, Inc., San Rafael, USA. For this purpose, the three-dimensional model of the newly developed open-end mold depicted in Figure 10.13 is transferred to Moldflow. Since the closing mechanism of the cavity and the outlet to the environment cannot be modeled without further ado, the outlet is represented as an additional cavity with substantially larger dimensions to approximate the actual behavior of the open-end injection molding process. As the primary focus is to analyze the formation of the fiber orientation distribution, the simulations solely consider both the filling and the flowing through phases, thereby neglecting the application of the holding pressure and the cooling phase. The specimen plate geometry is discretized with an element edge length of 1.3 mm and a specified number of 20 elements across the plate thickness of 2 mm to obtain high-resolution data of the fiber orientation distribution across the thickness of the specimen plate. The Reduced Strain

Closure (RSC) model for predicting the fiber orientation is used, which is an extension of the previously introduced *Folgar-Tucker* model (compare Chapter 10.1). The RSC model was developed to incorporate the slow orientation kinetics of fiber reorientation [TCH13, Tuc22]. The parameters for the fiber orientation models are calibrated through reverse engineering, based on experimental trials conducted on injection molded specimen plates with conventional fiber orientation distribution across the thickness (Chapter 6) and specified as $C_i = 0.0055$ und $\kappa = 0.227$. For details regarding the configuration of the simulation model and parameter calibration, it is referred to the work of *Wilhelm* [Wil21].

In order to be able to quantitatively evaluate the fiber orientation with regard to high orientation and uniformity across the thickness, two parameters are defined for the assessment of the numerically and also experimentally determined fiber orientation distribution in the injection-molded specimen plate. The degree of orientation is described by the volumetric average of the orientation tensor component A_{11} denoted as $\overline{A_{11}}$. Considering that the orientation tensor provides pointwise information, the orientation is evaluated in all three directions (across the thickness and also in the in-plane direction) using the volumetric mean value. A high $\overline{A_{11}}$ value corresponds with a high degree of fiber orientation within the specimen plate. The uniformity of the orientation distribution is characterized by the standard deviation $A_{11,SD}$ of the orientation component A_{11}. Similarly, the evaluation of the standard deviation $A_{11,SD}$ is conducted in a volumetric manner. A low standard deviation $A_{11,SD}$ indicates a high degree of uniformity, whereas a high standard deviation signifies low orientation homogeneity. For instance, a standard deviation of zero would indicate a perfectly uniform orientation across the thickness, without any deviating fiber orientations across the thickness but also in the in-plane direction. The evaluation considers the entirety of the specimen plate in which test specimens can be taken out. This results in the assessment of a total of 6,400 local information points for the fiber orientation tensor derived in the simulation of the specimen plate to calculate both quantifying parameters for high orientation degree $\overline{A_{11}}$ and uniformity of the fiber orientation $A_{11,SD}$ for every parameter set of the DoE.

Subsequently, the second-degree polynomial (compare Equation 10.11) with the target variable y_i for both parameters $\overline{A_{11}}$ and $A_{11,SD}$ is fitted as a function of the three factors: mold temperature T_M, volumetric flow rate $\dot{V}$, additional melt throughflow V_{AMT} taking into account the flow time t_{Flow} for the entire experimental design using regression.

$$\begin{aligned} y_i = {} & C_1 + C_2\,T_M + C_3\,\dot{V} + C_4\,V_{AMT} \\ & + C_5\,T_M^2 + C_6\,\dot{V}^2 + C_7\,V_{AMT}^2 \\ & + C_8\,T_M\,\dot{V} + C_9\,T_M\,V_{AMT} + C_{10}\,\dot{V}\,V_{AMT} \end{aligned} \qquad \textit{(Eq. 10.11)}$$

For each of both target variables, ten proportionality constants C_1 to C_{10} of the polynomial function are determined. Furthermore, to show the validity of this approach, both of the fitted relationships are also evaluated by predicting the input calibration data, which results in coefficients of determination (CoD) R^2 of 0.994 and 0.987, indicating a good agreement between the predicted and the actual data (see Figure 10.14).

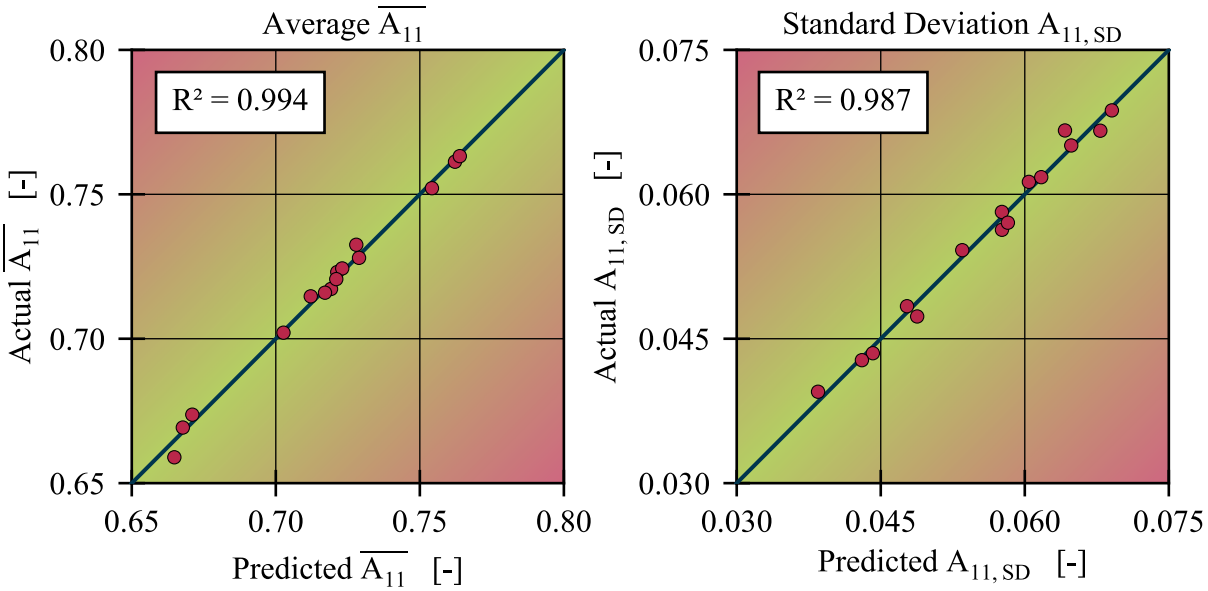

Fig. 10.14: Comparison of the actual explicit fitting data with the data predicted by the regression.

In order to obtain a more comprehensive understanding of the dependencies, Figure 10.15 illustrates the effects of the three influencing factors on orientation evaluation using the objective function Equation 10.11 and the determined coefficients. The plots are presented for the three different levels for the additional melt throughflow V_{AMT} (0 cm³, 21.63 cm³ and 43.25 cm³). For the average fiber orientation $\overline{A_{11}}$, the contour plots show that higher values are achieved with lower volumetric flow rates and mold temperatures. This trend is consistent across all three levels for V_{AMT}, whereby a higher melt throughflow leads to higher fiber orientations. The absolute maximum ($\overline{A_{11,\mathrm{Max}}} = 0.763$) of the function for the average fiber orientation is evaluated at 80 °C mold temperature, flow rate of 25 cm³/s and an additional melt throughflow of 37.85 cm³. With a value of $V_{AMT} = 43.25\ cm^3$, but otherwise identical process parameters an average orientation of $\overline{A_{11}} = 0.762$ is reached. Thus, the difference is negligible small. Equally, lower standard deviations $A_{11,SD}$, respectively higher uniformity of fiber orientation are achieved with lower volumetric flow rates and mold temperatures. However, when comparing the additional melt throughflow, the lowest value $A_{11,SD}$ is at a $V_{AMT} = 24.99\ cm^3$, rather than at $V_{AMT} = 43.25\ cm^3$, although the difference of the evaluated target value is also small (0.0417 vs 0.0430) compared to the range of 0.04 to 0.07.

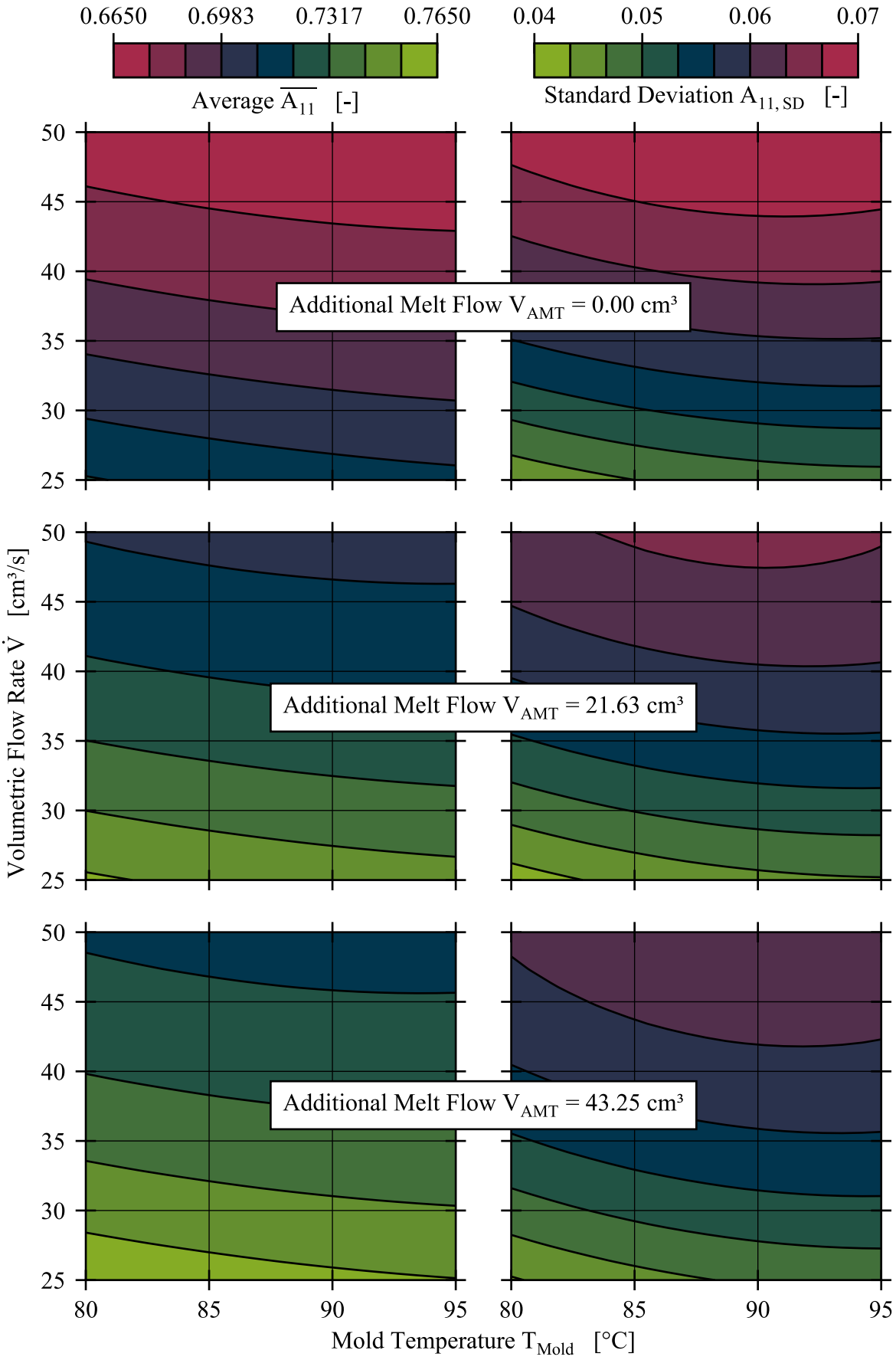

Fig. 10.15: Impact of volumetric flow rate and mold temperature on the fiber orientation distribution of the plates at varying degrees for additional melt flow.

It can thus be concluded that lower mold temperatures and lower injection rates result in a significantly enhanced fiber orientation formation. The resulting behavior can be explained by two factors. First, the slower volumetric injection rate allows more time for the melt to cool down and solidify. Second, a lower mold temperature also contributes to the solidification of the melt. Consequently, the flowable height reduces in size over time, resulting in an increase in velocity gradients and a subsequent reorientation of the fibers within the core. This effect becomes even more apparent if the DoE data is used to depict the average orientation and uniformity over the flow time (compare Figure 10.16). In both figures, a general trend can be seen that as the flow time increases, the melt also has more time to solidify, resulting in a higher and more homogeneous orientation.

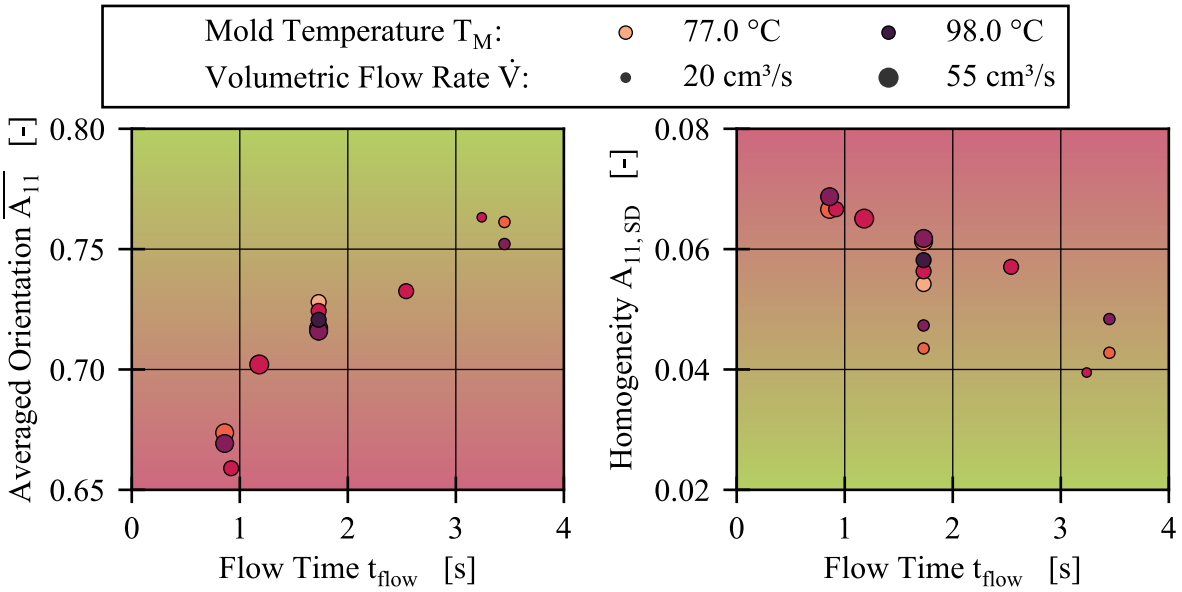

Fig. 10.16: The averaged orientation and the uniformity of fiber orientation distribution across the thickness improve both with increasing flow time.

Furthermore, the detailed analysis of the conducted simulations also indicates that increased shear-rates lead to higher shear dissipation, which in turn results in a stagnation of the reduction in flowable height at high flow rates due to the introduced additional heat. In some cases, the flowable height even shows again a slight increase after certain flow times. This also provides an explanation as to why the simulation demonstrates that the optimal values are not reached at the lowest flow rates and highest melt throughflows. In addition, it should be noted that the applied fiber orientation model is calibrated using conventional fiber orientation distributions via reverse engineering. Therefore, it is not possible to entirely disregard the discrepancy between the predicted fiber orientation and the actual prevailing distribution, which is why also in the experimental validation, a parameter variation is needed to analyze the actual process. To get a more detailed process understanding, also some parameter values beyond the defined DoE parameters are simulated. For example, a parameter set is taken with even lower volume rates

(12.5 cm³/s and 6.25 cm³/s). However, this parameter setting leads to a strong dominance of the solidification processes since the material has even more time to cool down, which results in the inability to maintain a uniform and parallel flow front over the cavity width during the melt throughflow of the cavity.

In summary, achieving high and uniform fiber orientation across the thickness using the open-end injection molding methodology is a complex problem, including fluid dynamics, heat transfer, and solidification processes. Nevertheless, the numerical DoE analysis provides a good understanding of the process parameters and their influence on the orientation formation within the open-end injection molding process.

10.4 Experimental validation of the open-end injection molding process

In accordance with the previously conducted numerical parameter study and the insights gained, the open-end injection molding process is experimentally tested in the following section, and the process for manufacturing specimen plates with uniform and high fiber orientation across the thickness is thus validated.

For the validation experiments, the injection molding machine Arburg Allrounder 520 A 1500 - 400 from ARBURG GmbH + Co. KG, Loßburg, Germany, with a clamping force of 150 tons is used. To experimentally confirm the findings of the numerical investigations discussed in the previous section, the process parameters are aligned with the simulated DoE plan. Since the injection molding simulation was conducted without modeling the sprue bushing, it is not expected that the filling times in the simulation match the experiments. Furthermore, the flow time for the production process of the uniform and highly oriented test specimen plates is particularly important, as it also defines the time when the cavity is closed by moving the slider translationally via the pneumatic cylinder. For this reason, a filling study is conducted first. The mold is set to a temperature of 95 °C. The injection volumetric flow rate $\dot{V}$ is kept constant at 50 cm³/s while the injected melt volume is continuously increased. In addition, the flow time determination can also be used to analyze and verify the flow pattern. The partially filled injection molded specimen plates show that a constant parallel flow front is achieved across the entire specimen plate, ensuring that no diverging source flow occurs in the parallel flow region, which can negatively influence the fiber orientation distribution (compare [Wil21]). The polymer melt reaches the end of the specimen plate (cavity is filled) after 1.2 s. For comparison, in the simulation, without considering the sprue system but with otherwise identical boundary conditions, a filling time of 0.85 s is calculated. The maximum flow time results from the maximum achievable injection volume of 95 cm³ and a melt cushion of 5 cm³. Hence, for a volumetric flow rate of 50 cm³/s, a flow time of 1.8 s is derived. Thus, the lower limit of the flow time is set to 1.2 s and the upper limit to 1.8 s. Due to the limitations of the injection

molding machine, the experimental parameter set deviates slightly from the simulation. The difference in flow time between degree of filling $V_{AMT} = 0.0\ cm^3$ and $V_{AMT} = 43.1\ cm^3$ should be identical in the experimental trials and numerical simulations to ensure the same amount of additional melt throughflow after the cavity is filled completely. However, the throughflow time of 0.86 s from the numerical investigations cannot be fully achieved. The cavity can be flown through at a volumetric flow rate of 50 cm^3/s for a maximum of 0.6 seconds after the cavity is completely filled. Since similar values for fiber orientation were obtained for longer flow times, it is assumed that the slightly shorter flow times will not have a negative impact. The settings for the flow rate of 25 cm^3/s are also derived proportionally from the determined parameters.

In the numerical studies, the mold temperature is varied in addition to the flow times, respectively, additional melt throughflow and flow rates. However, within the preliminary experimental tests, a mold temperature of 80 °C resulted in a significant increase in the required injection pressure at high flow times. The injection pressure exceeds the preset pressure limit of 1600 bar of the injection molding machine. According to numerical studies, injection pressures up to approximately 1250 bar are predicted. Nevertheless, considering the numerical results from the previous chapter, the effect of mold temperature on fiber orientation is less significant, which is why the validation experiments are only conducted at a mold temperature of 95 °C.

Since the experiments are evaluated through µCT examinations analyzing the resulting fiber orientation distribution of the injection molded test specimen plates, a reduced experimental test plan is deliberately chosen to minimize the experimental effort required for µCT measurements (compare Table 10.2). Based on the preliminary investigations, it is to be expected that the best results for the manufacturing of a uniform and highly oriented specimen plate can be achieved with the parameter set of experiment four.

Experiment	**Mold Temperature T_{Mold} [°C]**	**Volumetric Flow Rate $\dot{V}$ [cm³/s]**	**Flow Time t_{Flow} [s]**	**Additional Melt Throughflow V_{AMT} [cm³]**
1	80.0	50.0	1.2	0.00
2	80.0	25.0	2.4	0.00
3	80.0	50.0	1.8	30.00
4	80.0	25.0	3.6	30.00

Table 10.2: Experimental plan for validating the open-end injection molding process to manufacture specimen plates with uniform and high fiber orientation.

The first two experiments (1 and 2) are intended to investigate the fundamental influence of the volumetric flow rate and to assess how accurately the fiber orientation is predicted by the model parameters fitted through reverse engineering based on conventional plates. Thus, the quality of the previously conducted numerical analysis can be assessed. However, it should be noted that although experimental parameters are used where the closed cavity is fully filled, thus no melt flow can occur through the open end of the mold; the µCT scans are conducted on specimens located centrally, at a distance of 55 mm from the end of the plate. This means that while the cross-section at the end of the cavity cannot be flown through by the melt, the evaluation point experiences a flow through of a melt volume of approximately 8.8 cm³. Consequently, the previously discussed mechanisms still apply even with a just-fully-filled cavity, allowing the influence on the fiber orientation distribution formation to be investigated.

The evaluation of the fiber orientation distributions for experiments 1 and 2 is shown in Figures 10.17 and 10.18. The fiber orientation distribution is not fully met quantitatively by the simulation for both test points. In the outer regions, the fiber orientation component A_{11} is underestimated by up to 0.05, while in the central regions, it is overestimated by up to 0.2. Nevertheless, the prediction quality is good enough to allow the numerical study of the interactions and mechanisms within the processes, especially since the trend directions are predicted correctly. When reducing the volumetric flow rate from 50 cm³/s to 25 cm³/s, it can be seen that the fibers in the core also align more strongly in the main flow direction of the melt. Therefore, it is to be expected that, as shown in the conducted simulations, a more uniform fiber orientation distribution across the thickness of the specimen plate will result when the flow time is increased by an additional melt throughflow.

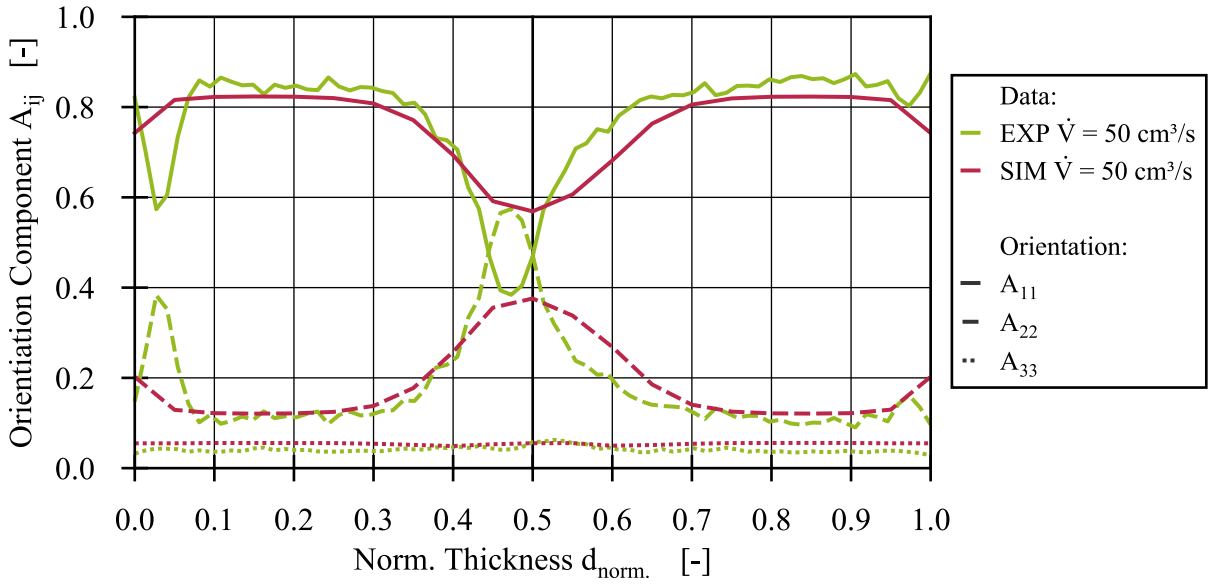

Fig. 10.17: A comparison of the numerically and experimentally determined fiber orientation distribution for a volumetric flow rate of 50 cm³/s for the closed mold.

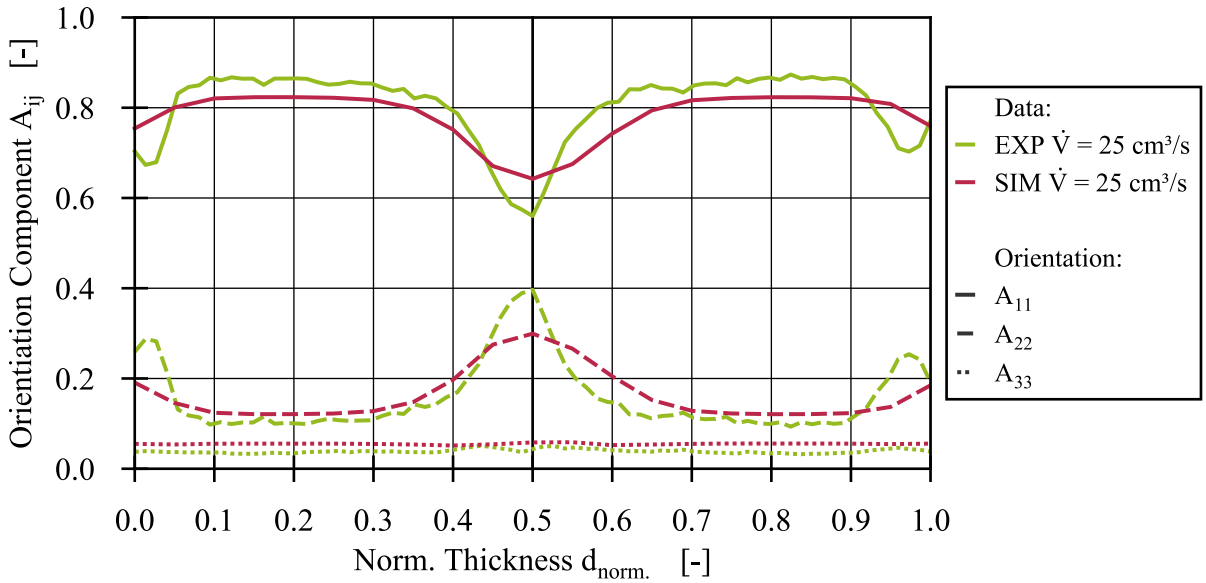

Fig. 10.18: A comparison of the numerically and experimentally determined fiber orientation distribution for a volumetric flow rate of 25 cm³/s for the closed mold.

For a quantitative description, Table 10.3 shows both the mean fiber orientation and the standard deviation across the thickness, and Figure 10.18 shows the µCT measurements of the fiber orientation distribution across the thickness of all four experiments.

Experiment	**Mold Temperature** T_{Mold} [°C]	**Volumetric Flow Rate** $\dot{V}$ [cm³/s]	**Flow Time** t_{Flow} [s]	**Additional Melt Throughflow** V_{AMT} [cm³]	$\overline{A_{11}}$ [-]	$A_{11,SD}$ [-]
1	80.0	50.0	1.2	0.00	0.7761	0.1225
2	80.0	25.0	2.4	0.00	0.8026	0.0811
3	80.0	50.0	1.8	30.00	0.8190	0.0405
4	80.0	25.0	3.6	30.00	0.8340	0.0496

Table 10.3: Quantitative comparison of the experimentally determined fiber orientation distribution.

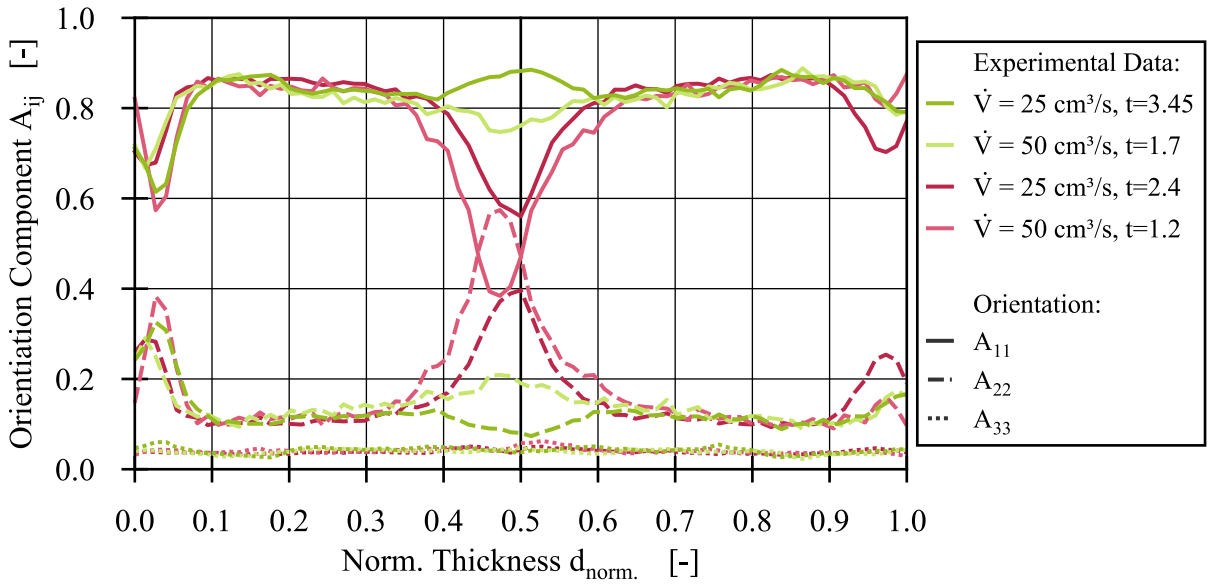

Fig. 10.19: Influence of the process parameters on the fiber orientation distribution.

Comparing the experiment, it can be seen that reducing the volumetric flow rate and increasing the flow time leads to an increase in the fiber orientation into the main flow direction of the melt within the core area of the specimen plate. As expected, the highest orientation distribution is obtained for the experimental test 4. Here, neglecting the edge areas that were in direct contact with the cavity wall, a uniform orientation for A_{11} of over 0.8 was achieved over the entire thickness of the test specimen. To ensure that in the entire area where test specimens are taken out of the specimen plate, µCT samples are extracted and evaluated for four different positions on the specimen plates (compare Figure 10.20). The µCT samples are also extracted from two different plates, one produced at the beginning and one at the end of the production batch. The measurements show that uniform and high fiber orientation can be achieved even over the different positions in the test area of the specimen plates.

This means that the process parameters of experiment 4 can be used to injection mold specimen plates that, unlike conventional test specimen plates, are characterized by a uniform and high fiber orientation across the thickness. Thus, the developed novel open-end injection molding process is successfully experimentally validated, and the desired aim of manufacturing UH-FOD injection molded specimen plates without any transversally oriented core is achieved.

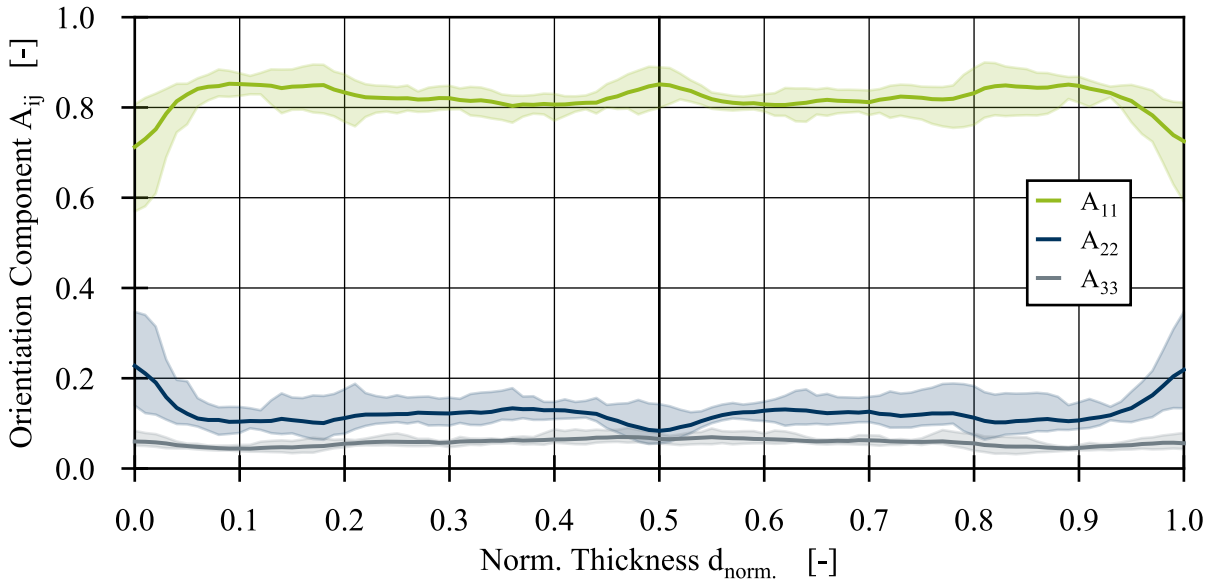

Fig. 10.20: µCT evaluation of the fiber orientation of the specimen plates manufactured with the open-end injection molding, showing a uniform and high fiber orientation across the thickness.

The discussed investigations for the open-end injection molding are carried out with the SFRT material PBT-GF30 of the type Pocan® B3235 provided by Envalior GmbH, Düsseldorf, Germany, as it is used for all mechanical investigations in this work. The mold and processing concept is also validated with a polyamide 6 containing 60 wt% glass fibers of the type ULTRAMID B3WG12 from BASF SE, Ludwigshafen, Germany (compare [Wil21]).

However, the mechanical behavior under dynamic-cyclic loading under different frequencies is of interest in this work, and these properties are influenced not only by the matrix and fiber characteristics but also by the micro-configuration of the material morphology, mainly determined by fiber mass content and orientation distribution. Furthermore, the material microstructure is also characterized by the fiber length distribution [TV96]. In the injection molding process, the complex flow conditions and high shear-rates during cavity filling result in irreversible fiber length degradation [PAK+13, Phe09]. In the newly developed open-end injection molding process, fiber reorientation into the main flow direction in the core region is achieved by inducing additional shear-rates compared to conventional injection molding. Therefore, it is essential to ensure that the newly developed process does not cause significantly more fiber damage compared to conventional injection molding, resulting in a mesomechanically different material morphology regarding fiber length. Hence, the fiber length distribution is also experimentally investigated.

For the analysis of fiber length distribution in this study, the FASEP Eco Ed. 2013 measurement system from xyz high precision, Darmstadt, Germany, is used. To determine fiber lengths and their distributions, individual fibers are measured and assigned to predefined length categories.

Specimens are taken from areas of the plates where test specimens for the µCT scans and specimens for mechanical testing are also extracted. This study investigates and compares plates with conventional fiber orientation distribution and those produced using the open-end injection molding process, belonging to the production parameters of experiment 4 (compare Figure 10.21). For each fiber orientation distribution, two specimens were examined, resulting in a total of four specimens.

In the comparison, it is observed that the number-based average fiber length L_n is decreased by 23.2 µm, and the weight-based average fiber length L_w is lower by 125.6 µm for the UH-FOD specimen plates. The width of the distribution is described by the quotient L_w/L_n of both parameters [Tuc22]. A comparison of the two different specimen types reveals a ratio L_w/L_n of 1.588 for the conventional and 1.556 for the high orientation, indicating a comparable outcome. The distributions for the relative counts intersect at approximately 380 µm. This shows that more fibers break from lengths greater than 380 µm during the open-end injection molding process.

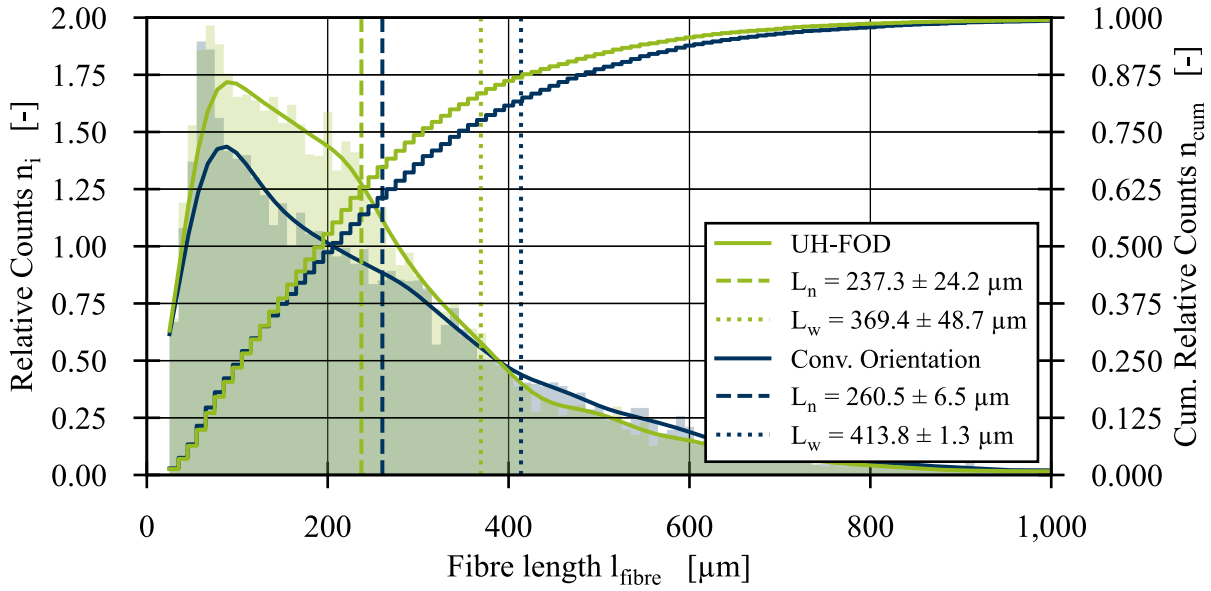

Fig. 10.21: Comparison of the number-based fiber length distribution between conventionally manufactured specimens and specimens produced via open-end injection molding.

Due to the higher average shear experienced by the melt in the open-end injection molding process, which aligns the fibers into the main melt flow direction throughout the entire thickness, a shorter fiber length distribution was expected. However, the data obtained from the applied experimental measurement method using the FASEP system is unable to provide any information regarding the height-dependent fiber length distribution. As demonstrated in [SO20], a varying fiber length distribution is observable across the thickness for long-fiber-reinforced thermoplastics. The average fiber length is notably increased in the core region of injection-molded plates when compared to the edge areas. The higher fiber length in the core

area is also explained in [SO20] by the decreased shear-rate in the core area of the specimen plates. Since in open-end injection molding, the melt is sheared over a larger region across the thickness due to the decreasing flowable height over the flow time, it is assumed that a comparable fiber length is present in the core area as in the edge areas. Nevertheless, the fiber length distributions are not fundamentally different and it can still be assumed that the specimen plates produced in the open-end process represent the meso-mechanical behavior of the conventionally produced specimen plates.

With the availability of a manufacturing process for test specimens that enables the direct determination of meso-mechanical material properties, tensile tests are conducted on specimens extracted from specimen plates at seven different angles in 15 ° increments. These tests are performed using the same testing machines as the tensile tests on specimens with conventional fiber orientation (Chapter 6.3). Here, the specimen geometry 1BA is also used. As expected, the longitudinal specimens exhibit higher stiffness and strength properties. Specifically, the stiffness increase of 776.51 N/mm² (+9.65 %) compared to specimens with conventional fiber orientation distribution falls within the anticipated range, given that approximately 80 % of the fibers within the specimens with conventional fiber orientation distribution are oriented in the melt flow direction and a gradual transition to transverse orientation in the core area. The strength has increased by 7.97 N/mm² (+6.64 %), although proportionally not as significantly as the stiffness. Due to the generally higher fiber orientation in the UH-FOD specimens, the applied load is more uniformly distributed across the cross-section, resulting in reduced overall stress despite the same applied loads as in the conventional specimens. This behavior is particularly evident in the transversal specimens, where the stiffness difference is -453.95 N/mm² (-9.83 %), while the strength reduction is at 10.94 N/mm² (-16.26 %). The influence of longitudinal orientation is more pronounced, as the longitudinally loaded regions are characterized by higher stiffness, thereby channeling the load path predominantly through these regions, where the local strengths are higher. Furthermore, the fracture strain is of interest. In the conventional specimens, with an approximately 0 °/90 °/0 ° material structure, similar strains at failure are observed for both longitudinal and transversal directions, approximately $\varepsilon_f \approx 3.0$ %. This behavior cannot be seen for the UH-FOD specimens. The longitudinal test specimens exhibit a strain at failure of 2.5 %, while the transverse samples maintain a strain at failure of approximately 3.0 %. Furthermore, by examining the angle dependency between 0° and 90°, it becomes evident how the material properties for stiffness and strength decrease with increasing angle. Consequently, the angular dependence for meso-mechanical properties of SFT materials can now be directly quantified analogously to continuous fiber-reinforced composites [Sch07].

Since the fatigue behavior is characterized by local damage events and their progression, and the number of load cycles achievable has a strong exponential dependence on the applied load respectively stress in the material, it is assumed that even if the tensile strength values vary in the range of approximately -10 % to +16 %, the differences in fatigue life and behavior will be significantly more pronounced.

Orientation	**Young's Modulus E [N/mm²]**	**Difference Young's Modulus E - $E_{Conv.}$ [N/mm²]**	**Tensile Strength R [N/mm²]**	**Difference Strength R - $R_{Conv.}$ [N/mm²]**
Longitudinal - 0°	8,824.41 (468.36)	+ 776.51	128.02 (0.78)	+ 7.97
15°	7,912.45 (-)	-	112.16 (-)	-
30°	5,984.42 (422.20)	-	85.04 (0.34)	-
Diagonal - 45°	4,837.70 (121.44)	- 262.28	70.51 (0.71)	- 7.80
60°	4,395.09 (123.82)	-	61.85 (0.08)	-
75°	4,340.61 (-)	-	57.58 (-)	-
Transversal - 90°	4,164.12 (111.37)	- 453.95	56.35 (0.06)	-10.94

Table 10.4: Tensile test results for the specimens with uniform and high fiber orientation for seven different extraction angles relative to the main flow direction, including the standard deviations.

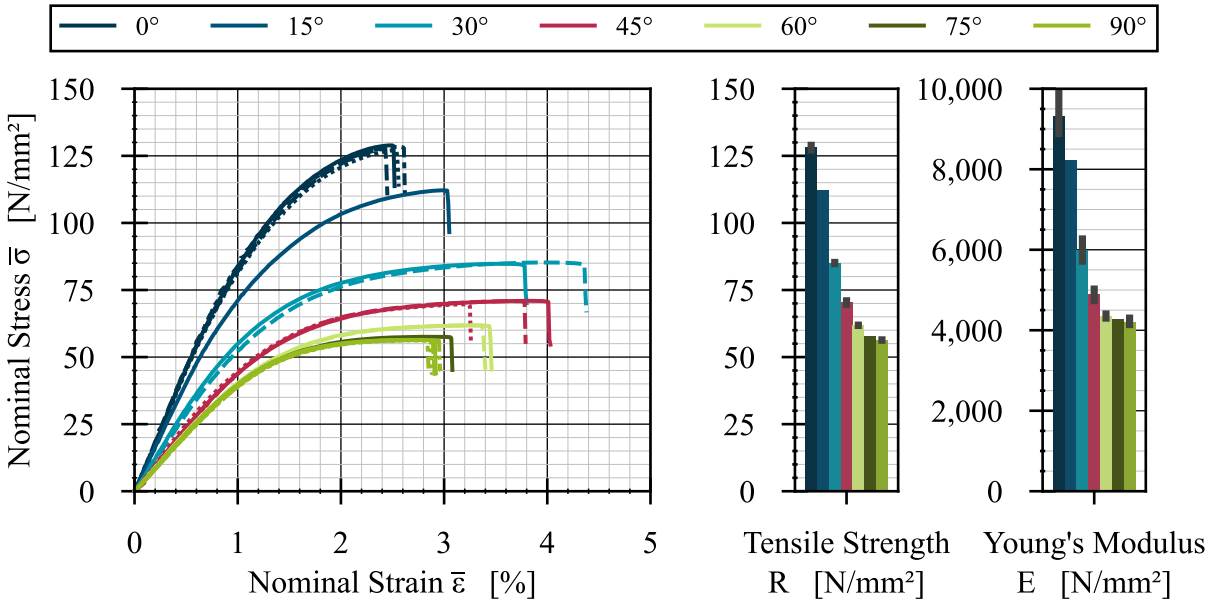

Fig. 10.22: Tensile test results for the specimens with uniform and high fiber orientation for seven different extraction angles relative to the main flow direction. Left: Stress-strain curves, Middle: Tensile strength, and Right: Young's modulus.

10.5 Conclusion on the developed novel injection molding process for specimen plates with uniform and high fiber orientation

The complex material structure of SFRT, resulting from the melt flow processes within the injection molding process, presents numerous open research questions (fiber orientation development, fiber breakage, fiber-matrix separation) that are currently being investigated. These findings are being translated into usable methods for the development and, primarily, the dimensioning of technical components. In particular, the heterogeneous fiber orientation distribution and the lack of a methodology to directly characterize SFRT materials at the meso-level is a significant gap in the field of material modeling for the designing of injection molded structural parts. Most methods for calibrating material models to describe deformation behavior are based on reverse engineering approaches [Bra06, Haa18], which risk identifying parameter sets that provide an adequate approximation of the material behavior for specific load applications but can yield significantly divergent results under different conditions since the derived input parameters for the models are physically not sufficiently valid.

With the newly developed open-end injection molding process, it is now possible to specifically manufacture specimen plates with uniform and high fiber orientation, allowing the material behavior of SFRT to be characterized and examined directly at the meso-level, dependent on discrete fiber orientations without the interaction of differing fiber orientations. For instance, the inherent strength values for anisotropic strength criteria could not be directly determined before but are now enabled by the UH-FOD specimens. In addition to characterizing the deformation behavior and directly calibrating material models for component dimensioning in the industry, it is also possible to characterize the damage behavior and development directly at the meso-level. Previously, only the resultant macroscopic behavior could be analyzed to study locally occurring damage events at the micro- and meso-levels. The open-end injection molding process allows the investigation of the material and damage behavior on a finer material scale than usual. Thus, it is now feasible, as with continuous fiber-reinforced materials, to understand the material's primary properties at the meso-level and then derive mechanical properties for the process-dependent complex material structure at the macro level, characterized by an infinitely large parameter space through homogenization approaches.

Additionally, the dimensions of the manufactured specimen plates are the same as those of established specimen plates, allowing existing routines and experimental equipment to be used in the same manner as before. This is a significant advantage over other presented manufacturing methods, allowing the adjustment of fiber orientation distribution in specimens.

Consequently, the developed open-end injection molding process provides a methodology for an improved material characterization that can be applied to calibration routines for

dimensioning methods of SFRT components and the ability to eliminate influencing factors, such as differing fiber orientation, to investigate and understand the damage behavior of SFRT materials in a material-appropriate manner. Hence, in the next chapter, specimens produced with the new methodology will be experimentally characterized in isothermal fatigue experiments to analyze the orientation dependence for the frequency-dependent fatigue behavior of SFRT materials.

11 INFLUENCE OF FIBER ORIENTATION DISTRIBUTION ON THE FATIGUE BEHAVIOR

The newly developed injection molding methodology enables the production of specimens with uniform and high fiber orientation across the entire thickness (compare Chapter 10). This advancement in tailored specimen production allows for the direct investigation of meso-mechanical material morphology and its influence on both general mechanical and specifically fatigue behavior at the macroscopic scale while eliminating the effects arising from interactions between different fiber orientations, which otherwise lead to more complex load paths and damage processes within the material. When combined with the thermo-adaptive testing methodology at high frequencies, the number of influencing factors regarding temperature or creep can be further minimized, allowing for a more conclusive analysis of the fatigue behavior in SFRT materials. By synthesizing the insights of the cyclic degradation at the meso-level and transferring it to conventional fiber orientation distributions, it paves the way for the development of mechanism-based models for predicting the fatigue behavior of SFRT materials of any configuration occurring in injection molded components.

In this chapter, a preliminary approach will be taken to investigate the meso-mechanical behavior at varying frequencies in isothermal conditions. Additionally, the meso-mechanically determined fatigue data will be compared with conventional results, considering their dependence on the micro-structure, particularly the fiber orientation distribution.

11.1 Isothermal fatigue characterization of specimens with uniform and high fiber orientation across the thickness

The fatigue tests using the UH-FOD specimens are conducted using the same thermo-adaptive testing methodology analogous to the previous investigations in Chapter 9. Consistent with those fatigue experiments with isothermal conditions, the experiments at 2 Hz and 5 Hz are performed without the thermo-adaptive test equipment due to the negligible temperature increase caused by hysteretic self-heating. For the longitudinal specimens, the same load levels are applied as in the tests with the specimens characterized by conventional fiber orientation. However, for the transversal specimens, the nominal load levels are reduced compared to the conventional specimens, as the original load levels led to premature failure, preventing them from reaching the desired cycle ranges up to 10^6 load cycles (compare Table 11.1). Hence, the same kind of occurring damage mechanisms are expected to be maintained since the material is tested for similar time and cycle ranges, whereby the direct comparison of the different orientation configurations is still possible. Also, it is noteworthy that the UH-FOD specimens are extracted from the injection molded specimen plates using a less stiff milling

machine than for the conventional specimens potentially resulting in slightly different surface qualities. However, the milled surfaces of the specimen edges are not further analyzed or quantified but can have an impact on the experimental fatigue results, as discussed in Chapter 6.

	Longitudinal specimen		Transversal specimen	
Targeted number of cycles to failure N [-]	**Applied loads F_i [N]**	**Relative to the quasi-static strength F_i/R_L [-]**	**Applied loads F_i [N]**	**Relative to the quasi-static strength F_i/R_T [-]**
10^4	780	0.609	460	0.816
10^5	685	0.535	400	0.710
10^6	620	0.484	340	0.603

Table 11.1: Defined load levels for evaluation of the frequency effect on the fatigue behavior for longitudinal and transversal UH-FOD specimens.

The obtained results of the isothermal fatigue tests for both orientations are presented in Figures 11.1 and 11.2. In comparison to the previous tests conducted on the identical testing machine with the same equipment, the obtained fatigue life data for the specimens with uniform and high fiber orientation are characterized by a higher degree of scattering. Additionally, the frequency-dependent shift at 2 Hz to lower cyclic lifetime is more pronounced than in the fatigue tests with conventional fiber orientation distributions. It is assumed that the overall behavior remains largely unchanged, as the analysis is based on the averaged behavior obtained through the fitting procedure. Nevertheless, for both longitudinal and transversal orientations, an increase in cyclic fatigue life is observed with rising test frequency.

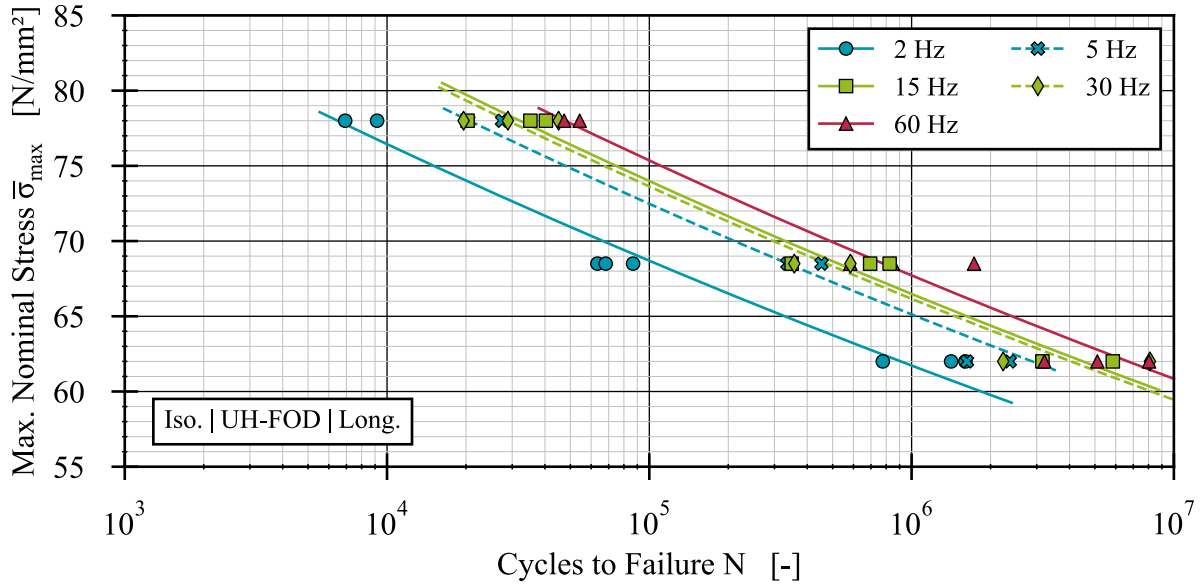

Fig. 11.1: Isothermal fatigue results over cycles to failure for varying frequencies between 2 Hz and 60 Hz for the longitudinal UH-FOD specimens.

For the longitudinal specimens, it becomes apparent that when tested at the same nominal stress levels as applied for the conventional fiber orientation, a general shift in the fatigue life data is observed. Specifically, an increase of approximately 1/3 of a decade in the number of load cycles can be achieved, reflecting an improved fatigue resistance compared to specimens with conventional fiber orientation distribution. Furthermore, the reduction of the applied load levels for the transversely oriented UH-FOD specimens results in an overall lower fatigue life. This is attributed to the missing of the longitudinally oriented fibers in the core region of the specimens, which reduces the absolute load-bearing capacity of the material. The applied nominal stresses are approximately 10 N/mm² lower compared to specimens with conventional fiber orientation distribution for the same range of cycles to failure. This corresponds to an approximate 17 % reduction in the transverse strength of the material.

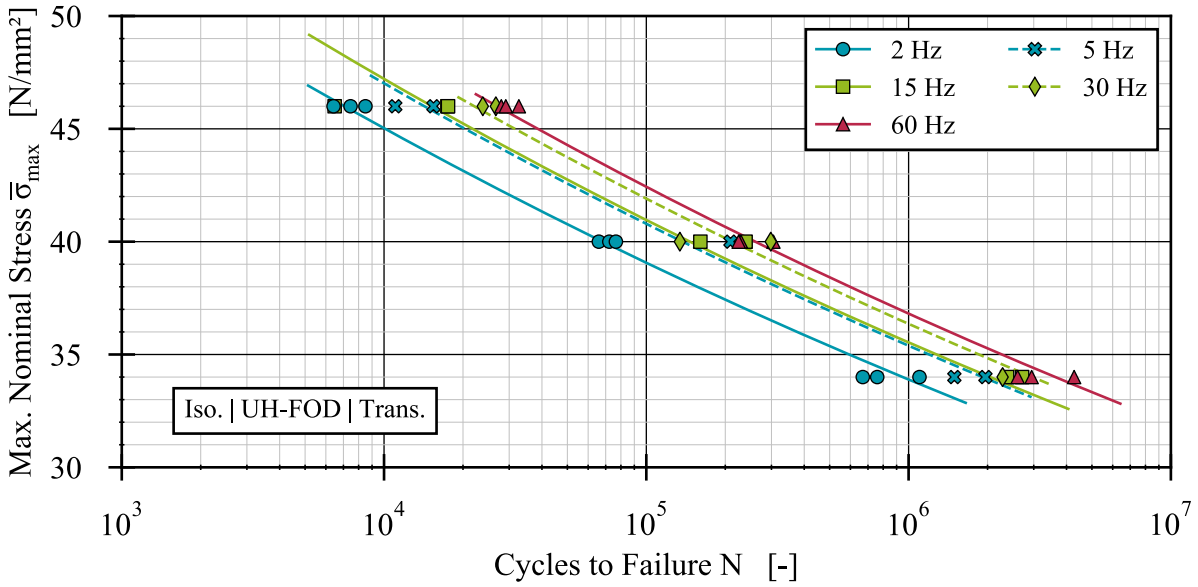

Fig. 11.2: Isothermal fatigue results over cycles to failure for varying frequencies between 2 Hz and 60 Hz for the transversal UH-FOD specimens.

When the obtained fatigue data is plotted against frequency (compare Figure 11.3), it becomes evident, alongside the increased scattering of the results, that the cyclic lifespan also increases with rising frequency. Nevertheless, compared to conventional tests, the trends are less pronounced.

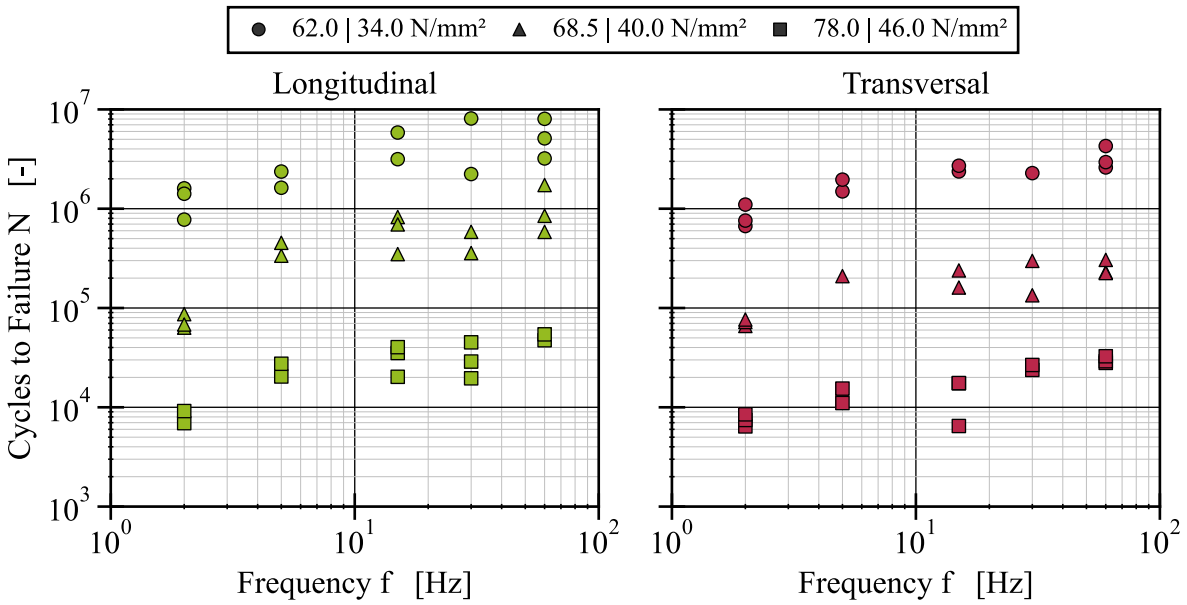

Fig. 11.3: Cycles to failure as a function of frequency for longitudinal and transversal specimens at various stress levels for the UH-FOD specimens.

The fatigue data obtained from these tests are analyzed using the *Basquin* equation, following the same approach as in the isothermal tests with conventional fiber orientation distributions (compare Chapter 9). However, this time, the slope parameters for the longitudinal SN data are consistently lower than those for the transversal specimens (see Figure 11.4, left). The average slope parameter for the longitudinal specimens is $m_{Long} = 0.0464$, while for the transversal specimens it is $m_{Trans} = 0.0617$. In contrast, the specimens with conventional fiber orientation show the opposite trend, with slope parameters $m_{Long} = 0.0517$ for longitudinal and $m_{Trans} = 0.0462$ for transversal specimens. Hence, the slopes for the UH-FOD specimens differ more significantly. The large difference between the slope parameters could be attributed to the fundamental differences in the orientation distributions, as the newly developed specimens do not have a perpendicularly oriented core layer. However, given the observed inverse dependence for the main orientation directions, an explanation based on the morphology of the SFRT for this phenomenon is not provided at this stage.

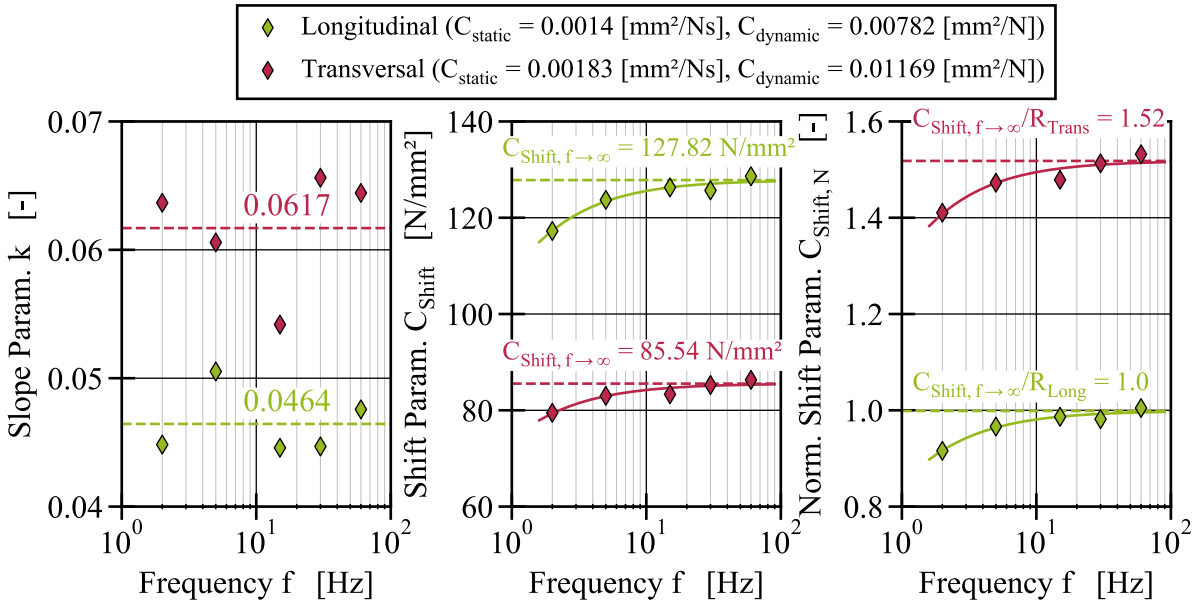

Fig. 11.4: Comparison of the slope parameters (left) and fitted frequency-dependent shift function $C_{shift}(f)$ for longitudinal and transversal orientations in absolute terms (center) and normalized by quasi-static strength (right).

For the UH-FOD specimens, the *Basquin* fitting is performed using an averaged slope parameter for each orientation, followed by the determination of the frequency-dependent shift factor $C_{shift}(f)$. The comparison of the normalized shift parameters $C_{shift,f\to\infty}/R$ shows a larger deviation between longitudinal and transversal specimens, with a factor of 1.52 compared to 1.23 for the specimens with conventional orientation, regardless of the potentially more deviating intrinsic value $C_{Intrinsic}$ for the transversal orientation. Since the quasi-static strength R is already significantly determined by the micro-structure, the normalization reveals that the micro-structure has a distinctly different impact on failure under static loading compared to dynamic-cyclic loading. For the uniformly high-oriented material structure, the longitudinal specimens have more fibers aligned in the load direction, enhancing their load-carrying capacity. In contrast, the transversal specimens lack longitudinally oriented fibers, which reduces their resistance against mechanical loads when compared to specimens with conventional fiber orientation distributions.

Despite these findings, the results from Chapter 9 are also confirmed for the meso-mechanical configuration of the tested PBT-GF30. For specimens with uniform and high fiber orientation, the slope of the obtained SN data remains consistent across all frequencies for each orientation. Additionally, the calibrated phenomenological shift function shows a degressively increasing asymptotic trend, suggesting that the cyclic fatigue life approaches a convergence at higher frequencies. Hence, the results obtained with the UH-FOD specimens can now be compared to those of other orientation configurations characterized by the conventional shell-core structure,

thereby improving the fundamental understanding of how the material configuration affects the overall fatigue behavior of SFRT-material.

11.2 Influence of fiber orientation state on the cyclic fatigue performance

Following the experimental characterization of the longitudinal and transversal specimens with uniform and high fiber orientation, the fatigue behavior can now be compared across four different orientation states, characterized by the varying thickness-averaged fiber orientation tensor value $\overline{A_{11}}$, for the same constitutive PBT-GF30 material system. However, it should be noted, as shown in Chapter 10.4, that the material morphology also exhibits micro-structural differences in terms of fiber length distribution, irrespective of the intentionally varied fiber orientation distribution. Nevertheless, it is assumed that the general mechanical properties and the fatigue behavior are predominantly influenced by the prevailing fiber orientation distribution, since the difference in fiber-length of $\Delta L_n = 23.2\ \mu m$ is negligible.

Furthermore, the creep behavior depends not only on the load-frequency or respective duration but also significantly on the fiber-orientation-dependent stress state at the micro-scale. However, the exact contribution of creep, in competition with cyclic damage progression, to the overall fatigue life is not yet quantified. Therefore, at this point, only the predominantly cyclic fatigue behavior, characterized by the extrapolated *Basquin* parameter $C_{Intrinsic}$, will be compared to initially disregard most of the superimposed influence of creep on fatigue life.

For this purpose, the orientation dependent tensile strength R obtained from quasi-static tensile tests, the *Basquin* parameter $C_{Intrinsic}$ for the intrinsic fatigue life, the strength-normalized value $C_{Intrinsic}/R$, and the frequency-independent slope k of the *Basquin* equation are compared as a function of the average orientation tensor value $\overline{A_{11}}$ (compare Figure 11.5).

When analyzing these values based on the averaged fiber orientation distribution $\overline{A_{11}}$, it is important to recognize that the mechanical properties are not represented here over the fiber orientation angle but by the material composition specified by the structural configuration of the “material layers”. For example, a fiber orientation distribution in which one fiber direction occupies half of the material thickness, while the other half is oriented perpendicularly, would result in an average orientation tensor value of $\overline{A_{11}} = 0.5$. Therefore, the data in Figure 11.5 illustrates the effect of the biaxial structural arrangement on the material’s orientation-dependent characteristics, rather than on individual fiber orientation angles.

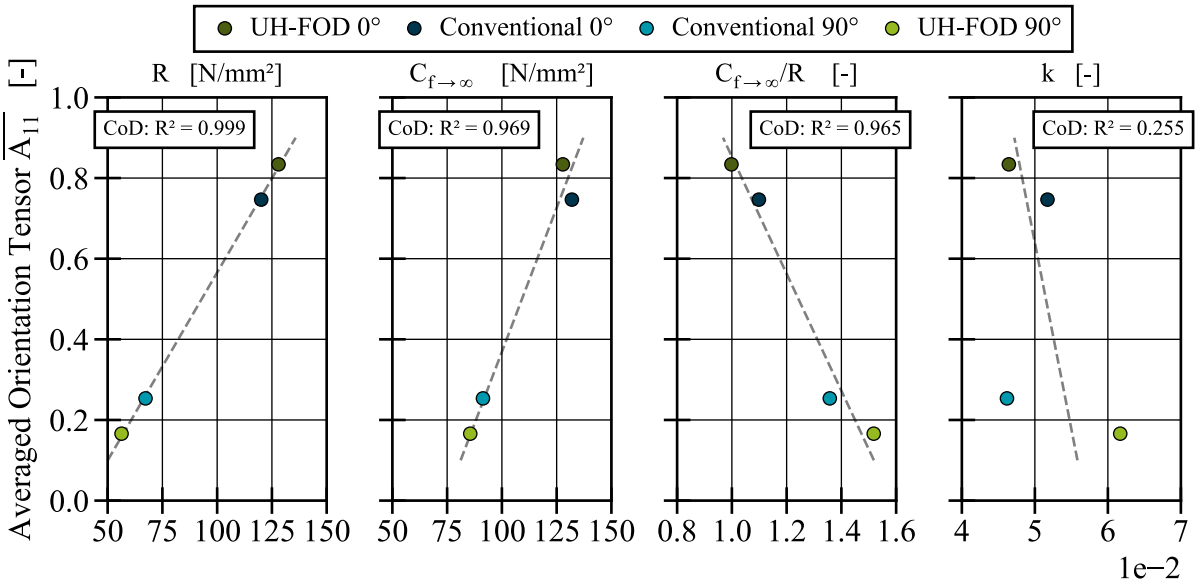

Fig. 11.5: Comparison of tensile strength R, intrinsic Basquin parameter $C_{Intrinsic}$, strength-normalized intrinsic parameter $C_{Intrinsic}/R$, and Basquin Slope k as functions of average orientation tensor value $\overline{A_{11}}$. Grey dashed line represents the linear regression applied to the dataset.

A linear correlation is observed between the material strength R and the state of fiber orientation $\overline{A_{11}}$. With increasing fiber alignment into the longitudinal direction, higher strength values are achieved. This is quantitatively supported by a coefficient of determination of $R^2 = 0.999$. In the context of the *Basquin* parameter $C_{Intrinsic}$, which characterizes intrinsic fatigue life, a similar trend is observed with increasing orientation tensors. However, a key distinction arises. Conventionally longitudinal oriented specimens exhibit higher values for the *Basquin* parameter compared to the UH-FOD specimens, indicating, at first, that the SN curve of the UH-FOD specimens is positioned below that of specimens with a conventional fiber orientation distribution. This would imply that, despite the higher proportion of longitudinally oriented fibers in the material, it would exhibit a shorter fatigue life. However, it should be noted that, as previously explained (see Chapter 9), the parameter C is highly sensitive to the slope of the *Basquin* equation. Therefore, particular caution is required when interpreting deviations, especially when the data points are closely clustered, as is the case here.

When the intrinsic parameter $C_{Intrinsic}$ is normalized using the respective quasi-static strength R, the relative intrinsic parameter increases with decreasing fiber orientation state and, hence, the dependence on the fiber orientation distribution is reversed. This demonstrates that, relative to their quasi-static strength, the transversely oriented specimens exhibit a significantly greater fatigue life compared to the longitudinally oriented specimens. Even the conventionally oriented transversal specimens, where the core area still contains fibers aligned in the load direction despite predominantly transversal orientation, show a lower $C_{Intrinsic}/R$. In addition, given that the quasi-static strength is also influenced by the fiber orientation distribution, it

could be expected that normalization would mitigate the effect of material configuration. However, this is not observed. This suggests that the mechanisms of damage initiation and progression under cyclic loading differ fundamentally from those governing quasi-static loading. It is also important to note that, in quasi-static tensile tests, the specimen is strained to failure under displacement control, whereas in these fatigue tests, conducted under load control, damage accumulation occurs progressively. Moreover, fibers aligned in the load direction are primarily load-bearing due to their higher stiffness, which induces load transfer across the fiber/matrix-interface, leading to significant shear stress concentrations at the interfaces, which are more sensitive to dynamic-cyclic loads. In contrast, for transversely oriented fibers, the matrix predominantly carries the load, as the small fiber diameter is insufficient to effectively attribute to load transfer into the fibers [FLM19, LF99].

When examining the slope k of the *Basquin* relationship, it is observed that the slopes for the longitudinal and transversal conventional specimens and the longitudinal UH-FOD specimen lie within a narrow range of 0.0462 to 0.0517 (approximately ±4 %), while the entirely transversely oriented samples show a slope of 0.0617, deviating by an average of around 28 %. It is important to note that the predominantly transversely oriented specimens with a conventional fiber orientation distribution still contain a longitudinally oriented core, which is subjected to higher stresses compared to the transversely oriented regions. As a result, these longitudinal layers may show a more dominant influence on the overall fatigue behavior.

Examining the fatigue data in the SN plot in Figure 11.6 that, although the $C_{Intrinsic}$ parameter of the *Basquin* equation for the conventional specimen is higher than that for the UH-FOD specimen, the fatigue strength for the same cycle range of 10^4 to 10^6 is greater for the UH-FOD specimen. This underlines the sensitivity of the C parameter in the *Basquin* equation, as discussed before. The slight difference in the slope between the two longitudinal material configurations gives the misleading impression that the conventional samples can withstand higher loads for the same number of cycles. The UH-FOD specimens exhibit the highest fatigue life, closely followed by the conventional specimens, where the fatigue strength is only marginally lower. A more pronounced difference is observed in the transversely oriented specimens. Here, the specimens with a conventional fiber orientation distribution show approximately 20 % higher fatigue strength compared to the transversely oriented UH-FOD specimens. The longitudinally oriented fibers in the core play a significant role in fatigue performance and contribute to this increase in fatigue strength.

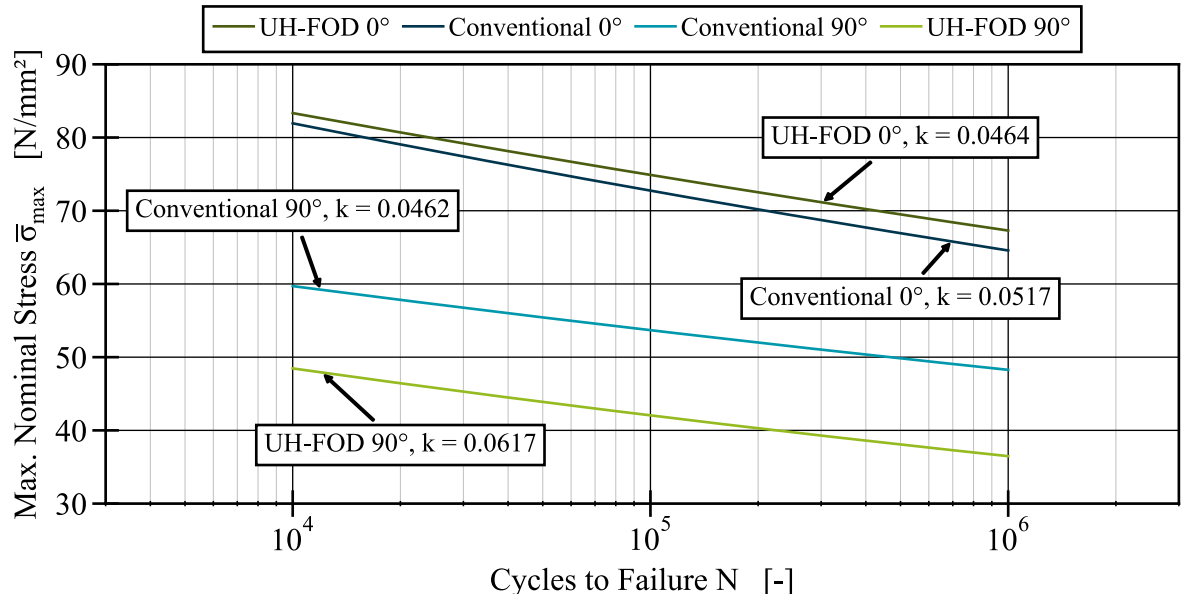

Fig. 11.6: Comparison of the intrinsic fatigue behavior of specimens with uniform and high fiber orientation to those with conventional fiber orientation distribution.

As dimensioning using the strength hypothesis often relies on normalizing stress states relative to material strengths, the SN curves are examined in these normalized domains. It becomes apparent that the transverse oriented specimens with conventional FOD demonstrate the highest fatigue life relative to their quasi-static strength. This shows that the relatively higher load-bearing capacity of the core layer significantly contributes to an extended fatigue life also beyond the quasi-static measure. In contrast, the UH-FOD specimens are characterized by the lowest relative fatigue strength, with a reduction of approximately 25 % on average within the cycle range of 10^4 to 10^6 compared to the transversally orientated conventional specimen.

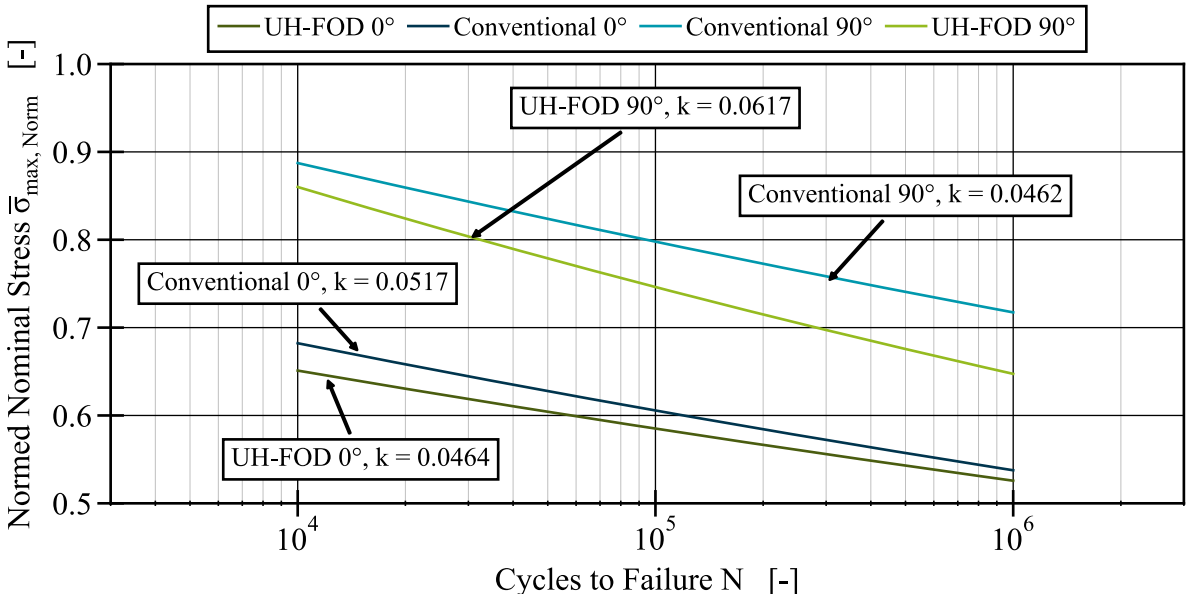

Fig. 11.7: Intrinsic SN data normalized by quasi-static strength for specimens with uniform high and conventional fiber orientation.

It can initially be concluded that the *Basquin* parameter C, acting as the y-axis intercept parameter, can result in misleading analyses regarding fatigue life when differing slope parameters are analyzed. However, when all slope parameters are identical or very similar, this parameter can be effectively utilized, as discussed in Chapters 9.2 and 11.2. The parameter C, however, shows a strong tendency to correlate with quasi-static strength R and the averaged fiber orientation distribution $\overline{A_{11}}$.

From a material perspective, it becomes clear that, in terms of absolute fatigue strength, the more fibers are oriented in the load direction, the higher the fatigue resistance. However, this correlation is no longer apparent when examining the relative fatigue life due to the normalization by the respective quasi-static strength. The fatigue strength no longer presents a clear trend in the dependency of the fiber orientation distribution. The highest relative fatigue life is observed in the transversally oriented specimens with conventional FOD, where the longitudinally oriented fibers in the core seem to have a more pronounced effect on improving fatigue life relative to quasi-static strength. In contrast, the lowest relative fatigue strength is obtained for the longitudinal UH-FOD specimens. This suggests that the influence of material configuration on quasi-static mechanical properties and fatigue behavior scales differently depending on the fiber orientation distribution.

For a conservative design methodology, it would be sufficient to characterize only the UH-FOD specimens in the longitudinal direction, as they represent the lower bound of relative fatigue life while still describing the absolute load-bearing capacity of the material. To provide a more detailed quantitative explanation, more investigations but at micro-level are necessary, as fatigue is primarily driven by damage accumulation at the micro-scale and the interactions between fibers and the matrix.

11.3 Fractographic analysis for understanding fatigue damage progression and the influence of creep

In the following, fractographic investigations are conducted on the fracture surfaces of failed specimens subjected to dynamic-cyclic loads. UH-FOD specimens oriented both longitudinally and transversely, tested under isothermal conditions (23 °C) at frequencies of 2 Hz and 60 Hz, are examined. Specimens subjected to the lowest tested load levels (62 N/mm² and 34 N/mm²) are selected to obtain test durations with the highest influence of the creep in the analysis. The objective of these investigations is to determine whether the varying load durations have an influence on the resulting fracture surfaces, as the specimens shown in Figure 11.8 exhibited differing degrees of creep deformation. For both specimen orientations, the fatigue tests conducted at 2 Hz exhibited a time-dependent fatigue life approximately five times longer than those at 60 Hz. Furthermore, it becomes clear that the transversally oriented specimens

experience greater creep strain and a higher creep rate compared to the longitudinally oriented UH-FOD specimens. As discussed earlier, the uniform transverse fiber orientation causes the load to be primarily carried by the matrix, which, due to its viscoelastic properties, leads to a higher degree of creep, also influencing the fatigue behavior of the material.

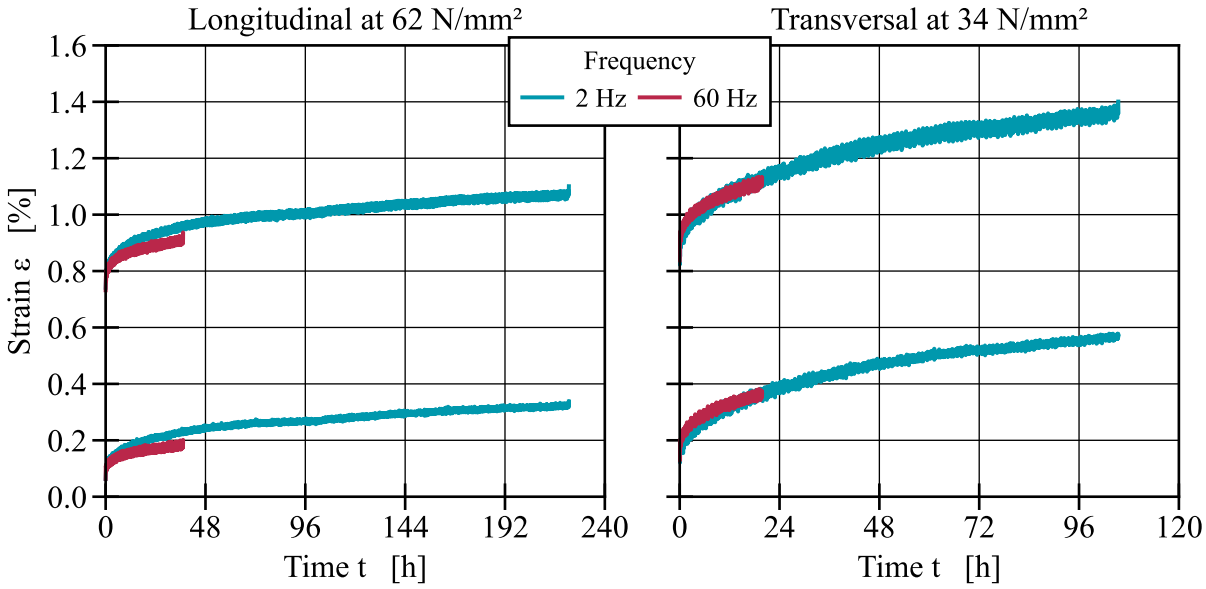

Fig. 11.8: Comparison of the maximum and minimum strain over load time for longitudinal and transversal UH-FOD specimens at a load frequency of 2 Hz and 60 Hz. The tests are conducted at a material temperature of 23 °C.

Upon examining the fracture surfaces of the specimens using reflected light microscopy (compare Figure 11.9). It is important to note that the fatigue experiments were conducted under load-controlled conditions in the tensile-tensile regime. This implies that the already fractured and opened surfaces were not compressed as significantly as they would have been in a displacement-controlled test.

It becomes evident that all four specimens exhibit distinct regions: one characterized by significant plastic deformation (ductile) and another by a relatively brittle appearance, with a fine micro-structure and minimal deformation. The transition between these regions occurs across the width of the specimen. It is reasonable to assume that the ductile regions were induced by the overstress during the moment of final specimen failure. The brittle region constitutes approximately one-third of the fracture surface, while the remainder is dominated by ductile areas. It is, therefore, assumed that the fine micro-structure in the brittle region was induced by dynamic-cyclic fatigue. However, no recognizable, distinct differences are observed between the two test frequencies. Hence, upon initial observation, the prolonged creep exposure in the 2 Hz specimens, compared to the 60 Hz specimens, does not appear to exert any noticeable macroscopic influence on the fracture surface.

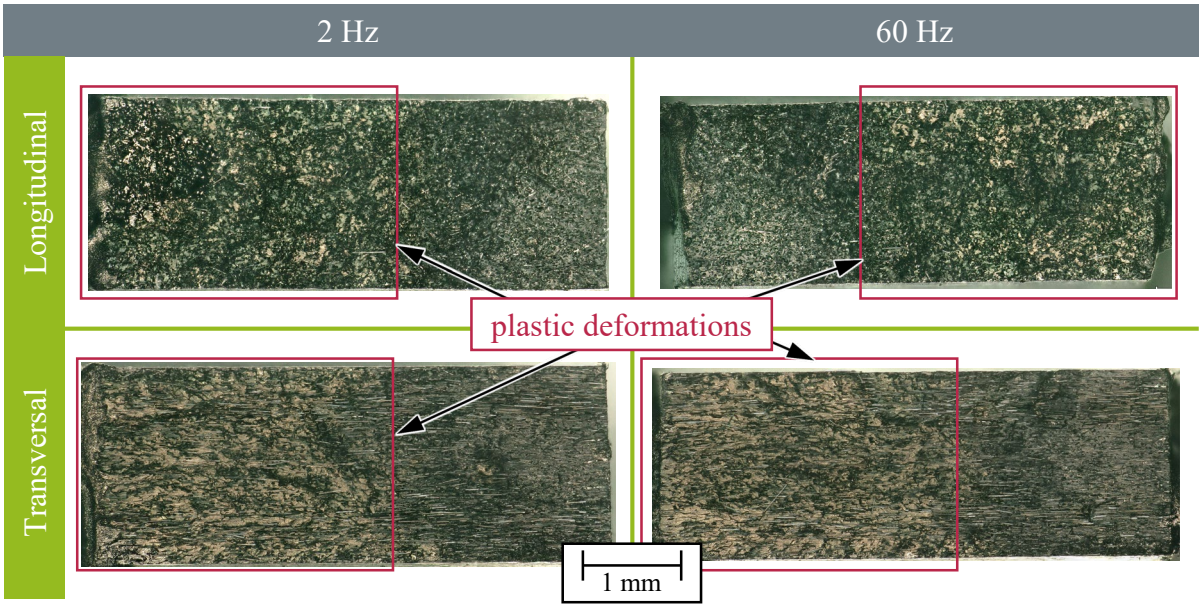

Fig. 11.9: Examination of fracture surfaces of longitudinal and transversal UH-FOD specimens from 2 Hz and 60 Hz fatigue tests using reflected light microscopy.

Since no differences between the two test frequencies are recognizable through reflected light microscopy, a series of fracture surface images are captured using a field emission scanning electron microscope (FESEM). The images were obtained using a Sigma VP FESEM from Carl Zeiss Microscopy GmbH, Jena, Germany. A total of 51 images are taken, with magnifications ranging from 50x to 5000x, capturing both the brittle and ductile regions of the fracture surfaces.

As shown in the previous diagram (Figure 11.8), the longitudinal orientation is characterized by overall lower creep deformation. When examining the FESEM images for the brittle fracture regions (compare Figure 11.10, top), areas with slight striations, indicative of less brittle failure, can be observed for both frequencies. However, no significant difference in the shape or formation of striations and ridges between the two frequencies could be detected. The images in the ductile regions are also comparable (Figure 11.10, bottom), showing significantly more ductile fibrils and greater deformations. Flow patterns, particularly micro-tears, are especially visible at larger distances from the fibers. Notably, detachment effects are visible at the fiber-matrix interface. In the FESEM image in Figure 11.10, lower left, it can be seen that in regions where the adhesion between fiber and matrix remains intact, the fibrils are more finely developed compared to areas where the fiber-matrix bond has already been compromised. There is also evidence of matrix material rolling up along the interface of the fiber, likely a result of the dynamic-cyclic load. Despite these observations, the fracture surfaces of the longitudinal UH-FOD specimens appear similar for both the 2 Hz and 60 Hz tests.

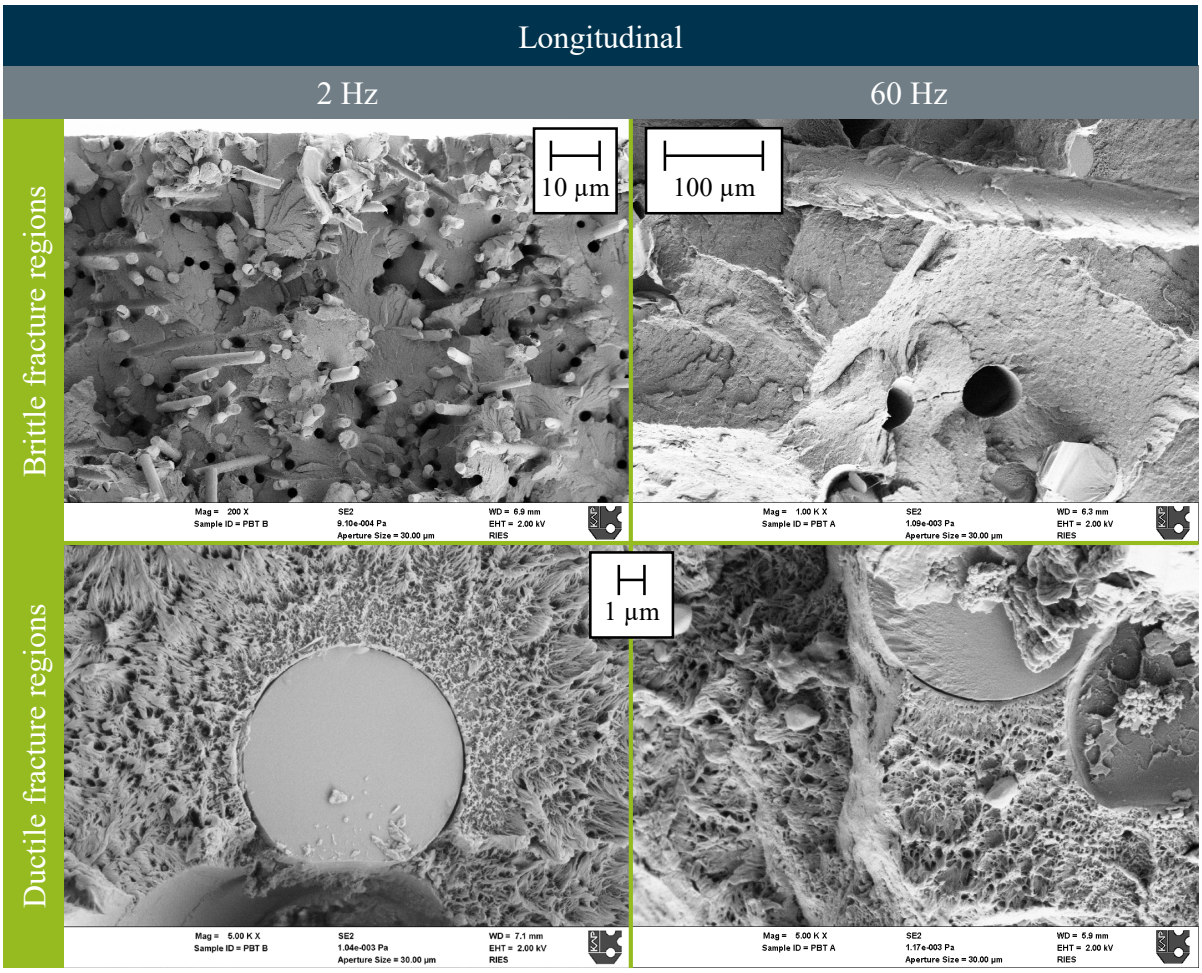

Fig. 11.10: Comparison of FESEM images of fracture surfaces in longitudinal UH-FOD specimens under 2 Hz and 60 Hz dynamic-cyclic loading. Images are taken from brittle and ductile fracture regions.

When examining the fracture surfaces of the transversely oriented specimens (compare Figure 11.11), a similar pattern is observed as with the longitudinal specimens. The brittle regions are characterized by striations and ridges, displaying fine fracture surfaces with minimal plastic deformation. Additionally, vertical striations are slightly visible, suggesting crack propagation in a horizontal direction. However, no significant differences between the 2 Hz and 60 Hz frequencies are observed in the brittle areas. The ductile regions are marked by extensive tearing and plastic deformation. The micro-tears are larger compared to the longitudinal specimens, further emphasizing that the matrix plays a more dominant load-bearing role in the transversely oriented specimens.

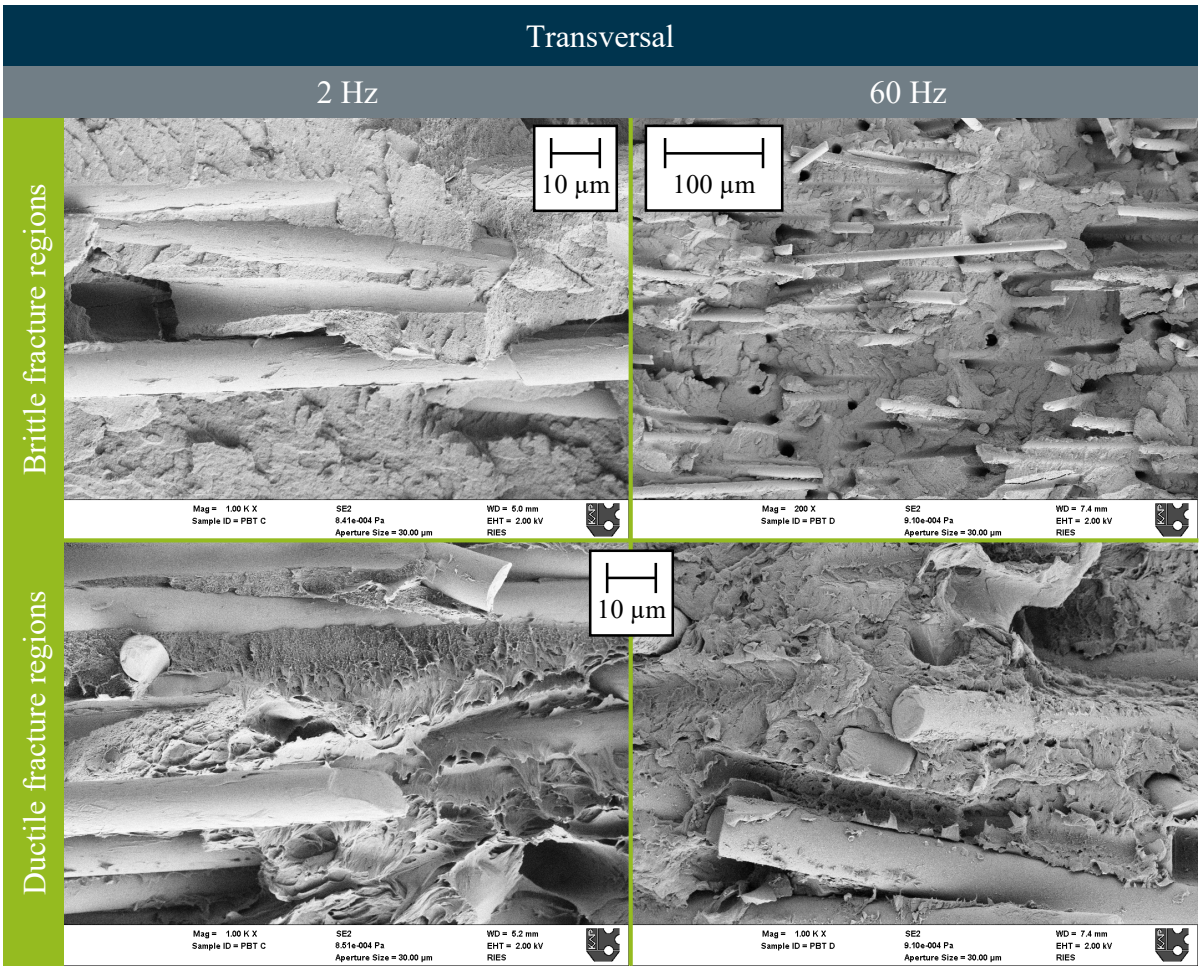

Fig. 11.11: Comparison of FESEM images of fracture surfaces in transversal UH-FOD specimens under 2 Hz and 60 Hz dynamic-cyclic loading. Images are taken from brittle and ductile fracture regions.

A cyclic induced, distinct grid-like striation pattern, often observed in classic brittle fracture pathways [EEK+11], could not be identified, although the transverse specimens exhibit slight vertical deformation bands. It is assumed that the complex material morphology prevents the induction of uniform stress states, leading to a range of interactions instead. Additionally, the fibers may act as crack stoppers. Since the FESEM images capture only the fracture surface conditions after the final failure of the specimens, it is presumed that cyclic crack growth initiated in the brittle fracture region, though precise localization could not be determined [BDB+07, SDH+14].

Ultimately, definitive conclusions about the influence of creep behavior on the fracture surfaces of the four specimens tested at 2 Hz and 60 Hz cannot be established, as significant differences in fracture surface characteristics were not observed.

11.4 Conclusions on the fiber orientation distribution and its impact on cyclic fatigue behavior

In this chapter, the two newly developed methodologies, thermo-adaptive testing and the manufacturing of the UH-FOD specimens were combined, allowing for the first time direct experimental investigations of both longitudinal and transversal meso-mechanical fatigue behavior of SFRT materials under isothermal conditions in the frequency range of 2 Hz to 60 Hz through macroscopic fatigue tests. The experimental results were then analyzed using the phenomenological frequency shift model and the concept of cycle-driven intrinsic fatigue life. Furthermore, the fracture surfaces were examined exemplarily using FESEM to investigate the impact of creep on the material failure.

The results demonstrate that when the micro-structure is characterized by a uniformly high fiber orientation across the entire cross-section, the mechanical behavior, particularly in terms of fatigue properties, differs accordingly. The fatigue resistance varies significantly more than in specimens with a conventional fiber orientation distribution due to the more distinct material configuration. As observed with the conventional specimens in Chapter 9, it was also found here that with increasing frequency, the number of load cycles to failure tends to converge.

In absolute terms, it was observed that the more fibers are oriented in the load direction, the higher the fatigue resistance. Simultaneously, it was also determined that, while the *Basquin* parameter C scales with fiber orientation in a manner similar to quasi-static strength, the fatigue data exhibits a different behavior when normalized by quasi-static strength R. Here, the transversally oriented specimens perform significantly better than the longitudinally oriented ones. To withstand the same number of load cycles, the relative load level, in comparison to quasi-static strength, must be reduced by approximately 25 % for the longitudinal specimens.

In the fractographic investigations using FESEM, no significant and clear differences in the fracture surfaces related to creep were observed. The surfaces for both frequencies exhibit brittle and ductile regions, with the brittle areas likely induced by dynamic-cyclic loading, while the ductile regions are assumed to result from the final fracture at the end of the fatigue life.

12 CONCLUSIONS AND OUTLOOK

The prediction of the fatigue life of short fiber-reinforced thermoplastics requires a profound understanding of the cross-scale and simultaneously occurring deformation and damage processes within the material. To improve this understanding, experimental methods were developed in this work to investigate individual mechanisms through macroscopic approaches by reducing interactions related to temperature or material composition. Emphasis has been placed on load frequency as it plays a critical role in fatigue behavior under dynamic-cyclic loads in the tensile-tensile regime by determining the ratio of applied load cycles to load duration, thereby governing the interaction between creep and cyclic degradation.

The investigations confirmed that increasing the load frequency initially leads to an increase in the number of load cycles the material can withstand. However, beyond a specific threshold frequency, identified as 15 Hz within the range of 10^3 to 10^6 load cycles for the tested PBT-GF30, the cyclic fatigue life begins to decrease. This behavior is attributed to self-heating effects arising from hysteretic energy losses within the material, which significantly impact the fatigue strength under continuous dynamic-cyclic loads. The analysis revealed two distinct temperature development regimes: stabilized and progressive. In the stabilized regime, thermal equilibrium is reached, and the material's temperature remains constant during dynamic-cyclic loads. In contrast, the progressive regime is characterized by a continuous and accelerated rise in temperature due to self-heating, leading to a decline in fatigue lifespan once significant heating occurs. Accurate temperature predictions can be made if the material's loss energy and heat exchange with the environment are known, highlighting the importance of understanding thermal effects in fatigue characterization at higher frequencies.

To reduce the superimposed temperature influence on fatigue investigations, a thermo-adaptive testing methodology was developed, allowing for the characterization of dynamic-cyclic properties of viscoelastic materials across the entire stress range and at varying frequencies without significant interference from temperature fluctuations. Experiments using this method revealed that the loss energy per cycle decreases with increasing frequency while the dissipated power increases in turn. Notably, no significant frequency dependence of dynamic stiffness was observed at 23 °C, which suggests that in the tested frequency range, the micro-mechanical stress state, as the driving parameter for damage progression, can be considered constant for the tested material. Furthermore, it was observed that the cyclic fatigue life increases with frequency and converges at higher frequencies. This behavior can be explained by the interaction of two competing mechanisms: mechanical degradation induced by cyclic load and time-dependent creep. Therefore, an intrinsic, solely cyclic fatigue life can be assumed and considered as a fundamental material property representing the maximum achievable lifetime.

Recognizing that the heterogeneous and process-dependent micro-structure of SFRT complicates the correlation of damage mechanisms with macroscopic behavior, a novel injection molding process was developed. This open-end injection molding technique enables the production of specimen plates with a uniform and high fiber orientation across the thickness, eliminating the interactions between different fiber orientations inherent in conventional specimens. This advancement allows for direct characterization and examination of the material behavior at the meso-level, dependent on discrete fiber orientations. Combining the thermo-adaptive testing methodology with the UH-FOD specimens allowed for direct experimental investigations of both longitudinal and transverse meso-mechanical fatigue behavior under isothermal conditions across a frequency range of 2 Hz to 60 Hz. In absolute terms, specimens with more fibers oriented in the load direction exhibited higher fatigue resistance. However, when normalized by quasi-static strength, transversely oriented specimens performed significantly better than longitudinally oriented ones. This indicates that fatigue strength does not scale with the degree of fiber orientation in the same manner as quasi-static strength, suggesting differing damage mechanisms between quasi-static and fatigue load conditions.

In conclusion, this research provides new characterization methodologies and a comprehensive understanding of the fatigue behavior of SFRT materials by isolating and analyzing the individual mechanisms that determine material degradation under dynamic-cyclic loads. The development of the thermo-adaptive testing methodology and the novel injection molding process for UH-FOD specimens represent significant advancements in material characterization techniques. The findings also have important implications for the design and dimensioning of injection-molded SFRT components. By understanding the intrinsic fatigue life and the interplay between cyclic degradation and creep, engineers can make more informed decisions regarding material selection and component design.

In future research, the concept of intrinsic fatigue life introduced here must be further investigated and validated. Should the concept of solely cyclic fatigue life be confirmed and linked to the existing micro-structure, it would be a significant step forward in understanding the fatigue processes of SFRT materials. Furthermore, the UH-FOD specimens allow the description of the fatigue at the meso-mechanical scale, enabling the development of models that can later be applied to more complex macro-mechanical configurations characterized by the fiber orientation distribution. This would enable comprehensive fatigue prediction within the parameter space of material configurations at the macroscopic level.

On the other hand, the UH-FOD specimens also offer the opportunity to bridge the gap to the micro-scale, where many fatigue processes originate. For example, with meso-mechanical characterization, failure mechanisms can now be numerically examined using representative volume elements and directly compared to experiments, allowing the investigation of the

impact of micro-mechanical interactions between fibers and matrix on the material behavior at the meso-scale.

Only by linking material behavior across all material scales can a fundamental understanding of fatigue processes in short fiber-reinforced thermoplastics be achieved, ultimately translating this knowledge into applicable predictive models.

13 ABBREVIATIONS, SYMBOLS, INDICES

13.1 Abbreviations

Abbreviations	Meaning
ABS	Acrylonitrile butadiene styrene
CCD	Central Composite Design
DoE	Design of Experiment
DSC	Differential scanning calorimetry
EDMA	Extended dynamic mechanical analysis
FESEM	Field emission scanning electron microscope
FLD	Fiber length distribution
FOD	Fiber orientation distribution
FWC	Fiber weight content
GF	Glass fiber
HD-PE	High-Density Polyethylene
IKV	Institut für Kunststoffverarbeitung (IKV-Aachen)
LEFM	Linear elastic fracture mechanics
LFA	Light flash analyzer
µCT	Micro-computed tomography
NC	New Configuration
OC	Old Configuration
PA6	Polyamide 6
PA66	Polyamide 6.6
PBT	Polybutylene terephthalate
PC	Polycarbonate
PEEK	Polyether ether ketone
PEI	Polyetherimide
PID	Proportional-integral-derivative
PMMA	Polymethyl methacrylate
PP	Polypropylene
PWM	Pulse-width modulation
RCR	Radiation and convection ratio
RVE	Representative volume element
SFRT	Short fiber-reinforced thermoplastics
SN	Stress/number of cycles

UH	Uniform-high
USB	Universal Serial Bus

13.2 Symbols

Symbols	Unit	Meaning
A	[m²]	Area
$\boldsymbol{A}$	[-]	Orientation tensor of second order
$\mathbb{A}$	[-]	Orientation tensor of forth order
a	[m/s^2]	Acceleration
a	[m]	Crack length
B	[m³]	Body volume
Bi	[-]	*Biot* number
C	[-]	*Basquin* Parameter, Constant
$C_{Intrinsic}$	[N/mm²]	Intrinsic fatigue life constant
C_{crack}	[-]	Phenomenological parameter, describing crack
C_{creep}	[N/mm^2 mm$^{m/2}$]	Crack growth parameter, creep induced
C_{cyclic}	[N/mm^2 mm$^{m/2}$]	Crack growth parameter, cycle induced
$C_{dynamic}$	[mm²/N]	Phenomenological parameter, dynamic-cyclic load
$C_{eff.}$	[-]	Effective load coefficient
C_i	[-]	Interaction parameter
$C_{shift}(f)$	[N/mm²]	Frequency shift function for *Basquin* equation
C_{static}	[mm²/Ns]	Phenomenological parameter, static load
c_v	[J/kg K]	heat capacity at constant volume
c_p	[J/kg K]	heat capacity at constant pressure
c_ε	[J/kg K]	heat capacity at constant strain
D	[-]	Damage state
$\boldsymbol{D}$	[1/s]	Deformation tensor
$\mathcal{D}$	[J/m³]	Dissipation
d	[m]	Thickness
∂B	[m²]	Surface area of Body
E	[N/mm²]	*Young's* Modulus
E'	[N/mm²]	Storage modulus
E''	[N/mm²]	Loss modulus
E^*	[N/mm²]	Complex modulus

E_{dyn}	[N/mm²]	Dynamic stiffness
F	[N]	Force
f	[Hz]	Frequency
H	[m]	Cavity height
h	[m]	Cavity height, half
g	[m/s^2]	Gravitational acceleration
K	[N/mm$^{3/2}$]	Stress intensity factor
k	[-]	*Basquin* Parameter
l	[m]	Length
m	[kg]	Mass
m_{creep}	[-]	Slope parameter crack growth, creep induced
m_{cyclic}	[-]	Slope parameter crack growth, cycle induced
N	[-]	Number of cycles to failure
n	[-]	Number of cycles
$\boldsymbol{n}$	[-]	Normal vector
p_L	[W/m³]	Volume specific loss power
$\boldsymbol{p}$	[-]	Unit vector
Q	[J]	Heat
q	[-]	Frequency dependency factor
$\boldsymbol{q}$	[W/m^2]	Heat flux vector
R	[N/mm²]	Quasi-static strength
R^2	[-]	Coefficient of determination
r	[-]	Load-ratio
r	[m]	Position coordinate, radial
s	[m]	Position coordinate, translational
S	[J/K]	Entropy
s	[J/kgK]	Specific entropy
T	[°C]	Temperature
t	[s, h]	Time
U	[J]	Internal energy
u	[J/kg]	Specific internal energy
V	[m³]	Volume
$\dot{V}$	[m³/s, cm³/s]	Volumetric flow rate
$\boldsymbol{V_k}$	[-]	Internal material variables
v	[m/s]	Velocity

W	[J]	Work
$\boldsymbol{W}$	[m/s]	vorticity tensor
w	[m]	Width
w_L	[J/m³]	Volume specific loss energy
w_S	[J/m³]	Volume specific stored energy
x	[m]	Position coordinate
y	[m]	Position coordinate
Y	[-]	Geometric factor
z	[m]	Position coordinate
α	[W/m²K]	Convective heat transfer coefficient
$\dot{\gamma}$	[1/s]	Shear-rate
Δ	[mm]	Change, Difference
$\dot{\Delta}$	[W/m³s]	Dissipation rate
δ	[rad]	Phase angle
$\varepsilon, \boldsymbol{\varepsilon}$	[-]	Strain
ϵ	[-]	Emissivity
λ	[W/mK]	Heat conductivity
ξ	[-]	Geometric factor ξ
ρ	[kg/mm³]	Density
$\sigma, \boldsymbol{\sigma}$	[N/mm²]	Stress, stress tensor
σ_{SB}	[W/m²K⁴]	Stefan-Boltzmann constant
τ	[-]	Dimensionless time
ψ	[J/kg]	*Helmholtz* free energy
$\dot{\blacksquare} = \frac{d\blacksquare}{dt}$		Time derivative
$\overline{\blacksquare}$		Averaging

13.3 Indices

Indices	**Meaning**
0	Time t = 0
Amb	Ambient
Amp	Amplitude
AMT	Additional melt throughflow
Clamp	Clamping
Dyn, dyn	Dynamic

e	Elastic
F	Fiber
HSF	*Hele-Shaw* flow
i	Counting variable
k	Counting variable
L	Longitudinal
L	Loss
M	Mold
Max, max	Maximum
mech.	Mechanical
Min, min	Minimum
n	Number based
norm.	Normalized
p	Plastic
Prod.	Production
RSF	Radial source flow
SD	Standard deviation
Surf	Surface
T	Transversal
therm.	Thermal
w	Weight based

14 LITERATURE

[AÇN+22] AL-QUDSI, A.; ÇELIK, H.; NEUHAUS, J.; HOPMANN, C.: A comparative study between fiber orientation closure approximations and a new orthotropic closure. *Polymer Composites* 43 (2022) 11, S. 7669-7700

[AML+13] Abello, L.S.; Marco, Y.; Le Saux, V.; Robert, G.; Charrier, P.: Fast Prediction of the Fatigue Behavior of Short Fiber Reinforced Thermoplastics from Heat Build-up Measurements. Procedia Engineering 66 (2013), S. 737-745

[AT87] ADVANI, S.G.; III, C.L.T.: The Use of Tensors to Describe and Predict Fiber Orientation in Short Fiber Composites. *Journal of Rheology* 31 (1987) 8, S. 751-784

[Bau17] BAUER, C.: *Charakterisierung und numerische Beschreibung des nichtlinearen Werkstoff- und Lebensdauerverhaltens eines kurzglasfaserverstärkten Polymerwerkstoffes unter Berücksichtigung der im µCT gemessenen lokalen Faserorientierung*. Technische Universität Kaiserslautern, Dissertation, 2017

[BCF78] BRIGHT, P.F.; CROWSON, R.J.; FOLKES, M.J.: A study of the effect of injection speed on fibre orientation in simple mouldings of short glass fibre-filled polypropylene. *Journal of Materials Science* 13 (1978) 11, S. 2497-2506

[BCR14a] BENAARBIA, A.; CHRYSOCHOOS, A.; ROBERT, G.: Fiber orientation effects on heat source distribution in reinforced polyamide 6.6 subjected to low cycle fatigue. *Journal of Engineering Mathematics* 90 (2014), S. 13-36

[BCR14b] BENAARBIA, A.; CHRYSOCHOOS, A.; ROBERT, G.: Kinetics of stored and dissipated energies associated with cyclic loadings of dry polyamide 6.6 specimens. *Polymer Testing* 34 (2014), S. 155-167

[BDB+07] BERNASCONI, A.; DAVOLI, P.; BASILE, A.; FILIPPI, A.: Effect of fibre orientation on the fatigue behaviour of a short glass fibre reinforced polyamide-6. *International Journal of Fatigue* 29 (2007) 2, S. 199-208

[BK09] BERNASCONI, A.; KULIN, R.M.: Effect of frequency upon fatigue strength of a short glass fiber reinforced polyamide 6: A superposition method based on cyclic creep parameters. *Polymer Composites* 30 (2009) 2, S. 154-161

[Bra06] BRANDT, M.: *CAE Methoden für die verbesserte Auslegung themoplastischer Spritzgussbauteile*. RWTH Aachen, Dissertation, 2006 - ISBN: 978-3-86130-850-8

[BW15] BÖCKH, P.; WETZEL, T.: *Wärmeübertragung: Grundlagen und Praxis*. Berlin, Heidelberg: Springer-Verlag, 2015

[CB75] CRAWFORD, R.J.; BENHAM, P.P.: Some fatigue characteristics of thermoplastics. *Polymer* 16 (1975) 12, S. 908-914

[CCC+11] CHEN, C.-S.; CHEN, T.-J.; CHEN, S.-C.; CHIEN, R.-D.: Optimization of the injection molding process for short-fiber-reinforced composites. *Mechanics of Composite Materials* 47 (2011) 3, S. 359-368

[Cen04] CENGEL, Y.: *Heat Transfer: A Practical Approach*. McGraw-Hill Education, 2004

[Che23] CHEN, J.: *Entwicklung neuer Methoden zur mikromechanischen Ermüdungsanalyse für endlosfaserverstärkte Kunststoffe.* RWTH-Aachen, Dissertation, 2023

[Chr12] CHRYSOCHOOS, A.: Thermomechanical Analysis of the Cyclic Behavior of Materials. *Procedia IUTAM* 4 (2012), S. 15-26

[CK02] CHUNG, D.H.; KWON, T.: Fiber orientation in the processing of polymer composites. *Korea-australia Rheology Journal* 14 (2002), S. 175-188

[CMH+23] CANEGRATI, A.; MARTULLI, L.M.; HINE, P.J.; GRASSINI, C.; BERNASCONI, A.: On the use of milled shell-only specimens to study the effect of fiber orientation on the fatigue behavior of a short fiber-reinforced polyamide. *Fatigue & Fracture of Engineering Materials & Structures* 46 (2023) 2, S. 616-630

[DHM22] DAHLMANN, R.; HABERSTROH, E.; MENGES, G.: *Menges Werkstoffkunde Kunststoffe*. München: Carl Hanser Verlag, 2022

[Dil19] DILLENBERGER, F.: *On the anisotropic plastic behaviour of short fibre reinforced thermoplastics and its description by phenomenological material modelling*. Technische Universität Darmstadt, Disseration, 2019

[DJB+09] DREIßIG, J.; JASCHEK, K.; BÜTER, A.; DE MONTE, M.: Fatigue life estimation for short fibre reinforced polyamide components under variable amplitude loading. *Proceedings of the 2nd International Conference on Material and Component Performance under Variable Amplitude Loading.* Darmstadt, Germany, 2009

[DP01] DEGRIECK, J.; PAEPEGEM, W.V.: Fatigue Damage Modelling of Fibre-reinforced Composite Materials: Review. *Applied Mechanics Reviews* 54 (2001) 4, S. 279-300

[DVD17] DEAN, A.; VOSS, D.; DRAGULJIĆ, D.: *Design and Analysis of Experiments*. Cham: Springer International Publishing AG, 2017

[EAT+21] ERARTSIN, O.; ARNTZ, S.A.J.J.; TROISI, E.M.; PASTUKHOV, L.V.; VAN DRONGELEN, M.; WARNET, L.; GOVAERT, L.E.: Long-term failure of transversely loaded glass/iPP. *Journal of Applied Polymer Science 138* (2021) 35, S. 50878

[EEK+11] EHRENSTEIN, G.W.; ENGEL, L.; KLINGELE, H.; SCHAPER, H.: *SEM of Plastics Failure: REM Von Kunststoffschäden*. München: Carl Hanser Verlag, 2011

[Erik90] ERIKSEN, E.: The influence of surface roughness on the mechanical strength properties of machined short-fibre-reinforced thermoplastics. *Composites Science and Technology* 60 (2000) 1, S. 107-113

[FHY99] FU, S.-Y.; HU, X.; YUE, C.-Y.: Effects of Fiber Length and Orientation Distribution on the Mechanical Properties on the Mechanical Properties of Short-Fiber-Reinforced Polymers - A Review. *Journal of the Society of Materials Science, Japan* 48 (1999) 6, S. 74-83

[FLM19] FU, S.; LAUKE, B.; MAI, Y.W.: *Science and Engineering of Short Fibre-Reinforced Polymer Composites*. Elsevier Ltd., 2019

[FM15] MORTAZAVIAN, S.; FATEMI, A.: Fatigue behavior and modeling of short fiber reinforced polymer composites: A literature review. *International Journal of Fatigue* 70 (2015), S. 297-321

[Fri21] FRITSCHE, D.: *Development of a phenomenological superpositon principle for the determination of fatigue properties for short glass fibre reinforced thermoplastics at high frequencies*. Institut für Kunststoffverarbeitung, RWTH Aachen, unveröffentlichte Masterarbeit, 2021 – Betreuer: H. Çelik

[FT84] FOLGAR, F.; TUCKER, C.L.: Orientation Behavior of Fibers in Concentrated Suspensions. *Journal of Reinforced Plastics and Composites* 3 (1984) 2, S. 98-119

[Gdo05] GDOUTOS, E.E.: *Fracture Mechanics - An Introduction*. Dordrecht: Springer, 2005

[GGJ+15] GAO, X.; GILLESPIE, J.W.; JENSEN, R.E.; LI, W.; HAQUE, B.Z.; MCKNIGHT, S.H.: Effect of fiber surface texture on the mechanical properties of glass fiber reinforced epoxy composite. *Composites Part A: Applied Science and Manufacturing* 74 (2015), S. 10-17

[GGO+16] GORIS, S.; GANDHI, U.; SONG, Y.Y.; OSSWALD, T.A.: Analysis of the Process-Induced Microstructure in Injection Molding of Long Glass Fiber-Reinforced Thermoplastics. *SPE Proceedings of the ANTEC 2016. Indianapolis, USA, 2016*

[GHS+18] GROSS, D.; HAUGER, W.; SCHRÖDER, J.; WALL, W.A.; BONET, J.: *Engineering Mechanics 2: Mechanics of Materials*. Berlin, Heidelberg: Springer-Verlag, 2011

[GO18] GORIS, S.; OSSWALD, T.A.: Process-induced fiber matrix separation in long fiber-reinforced thermoplastics. *Composites Part A: Applied Science and Manufacturing* 105 (2018), S. 321-333

[GS07] GROSS, D.; SEELIG, T.: *Bruchmechanik - Mit einer Einführung in die Mikromechanik*. Berlin, Heidelberg: Springer-Verlag, 2007

[GS11] GROSS, D.; SEELIG, T.: *Bruchmechanik*. Heidelberg, Dordrecht, London,New York: Springer, 2011

[GS15] GRELLMANN, W.; SEIDLER, S.: *Kunststoffprüfung*. München: Carl Hanser Verlag, 2015

[Gün13] GÜNZEL, S.: *Analyse der Schädigungsprozesse in einem kurzglasfaserverstärkten Polyamid unter mechanischer Belastung mittels Röntgenrefraktometrie, Bruchmechanik und Fraktografie*. Technische Universität Berlin, Dissertation, 2013

[Gus09] GUSTER, C.: *Ansätze zur Lebensdauerberechnung von kurzglasfaserverstärkten Polymeren*. Montanuniversität Leoben, Dissertation, 2009

[Haa18] HAAG, J.V.: *Modellierung des zeitabhängigen thermomechanischen Steifigkeitsverhaltens spritzgegossener kurz- und langfaserverstärkter Thermoplaste*. RWTH Aachen, Dissertation, 2018 - ISBN: 978-3-95886-267-8

[Hai06] HAIBACH, E.: *Betriebsfestigkeit - Verfahren und Daten zur Bauteilberechnung*. Berlin, Heidelberg: Springer-Verlag, 2006

[Har77] HARRIS, B.: Fatigue and accumulation of damage in reinforced plastics. *Composites* 8 (1977) 4, S. 214-2

[HÇ21] HOPMANN, C.; ÇELIK, H.: Cumulative Failures Prevention. *Kunststoffe International* (2021) 01, S. 44-46

[HDÇ22] HOPMANN, C.; DAHLMANN, R.; ÇELIK, H.: Accelerated fatigue characterisation of technical thermoplastics by temperature controlled fatigue tests at high frequencies. *Proceedings of the 31st International Colloquium Plastics Technology.* Institute for Plastics Processing in Industry and Craft at RWTH Aachen University, Aachen, Germany, 2022

[HKN99] HANDA, K.; KATO, A.; NARISAWA, I.: Fatigue characteristics of a glass-fiber-reinforced polyamide. *Journal of Applied Polymer Science* 72 (1999) 13, P. 1783-1793

[HM17] HOPMANN, C.; MICHAELI, W.: *Einführung in die Kunststoffverarbeitung*. München: Carl Hanser Verlag, 2017

[HM19] HERWIG, H.; MOSCHALLSKI, A.: *Wärmeübertragung: Physikalische Grundlagen und ausführliche Anleitung zum Lösen von Aufgaben*. Wiesbaden: Springer Fachmedien Wiesbaden, 2019

[HM80] HERTZBERG, R.W.; MANSON, J.A.: *Fatigue of Engineering Plastics*. Academic Press, 1980

[HMB11] HARTMANN, J.; MOOSBRUGGER, E.; BÜTER, A.: Variable amplitude loading with components made of short fiber reinforced polyamide 6.6. *Procedia Engineering* 10 (2011), S. 2009–2015

[HMG+17] HOPMANN, C.; MICHAELI, W.; GREIF, H.; EHRIG, F.: *Technologie des Spritzgießens*. München: Carl Hanser Verlag, 2017

[HS20] HOPMANN, C.; SCHMITZ, M.: *Plastics Industry 4.0: Potentials and Applications in Plastics Technology*. München: Carl Hanser Verlag, 2020

[Jeff22] JEFFERY, G.B.: The Motion of Ellipsoidal Particles Immersed in a Viscous Fluid. *Proceedings of the Royal Society of London A: Mathematical, Physical and Engineering Sciences* 102 (1922) 715, S.161-179

[JGM08] JANSSEN, R.P.M.; GOVAERT, L.E.; MEIJER, H.E.H.: An Analytical Method To Predict Fatigue Life of Thermoplastics in Uniaxial Loading: Sensitivity to Wave Type, Frequency, and Stress Amplitude. *Macromolecules* 41 (2008) 7, S. 2531-2540

[JK98] JIA, N.; KAGAN, V.A.: Effects of time and temperature on the tension-tension fatigue behavior of short fiber reinforced polyamides. *Polymer Composites* 19 (1998) 4, S. 408-414

[JML+12] JEGOU, L.; MARCO, Y.; LE SAUX, V.; CALLOCH, S.: Thermomechanical identification of a threshold in the cyclic response of "SFRP": Fast identification of the fatigue properties and correlation to microstructural data. *Proceedings of the 15th European Conference on Composite Materials.*Venice, Italy, 2012

[JMS+13] JEGOU, L.; MARCO, Y.; LE SAUX, V.; CALLOCH, S.: Fast prediction of the Wöhler curve from heat build-up measurements on Short Fiber Reinforced Plastic. *International Journal of Fatigue* 47 (2013), S. 259-267

[JW11] JIANG, Q.; WEN, Z.: *Thermodynamics of Materials*. Berlin, Heidelberg: Springer-Verlag, 2011

[Kai13] KAISER, J.M.: *Beitrag zur mikormechanischen Berechnung kurzfaserverstärkter Kunststoffe*. Universität des Saarlands, Dissertation, 2013

[Kan15] KANTERS, M.J.W.: *Prediction of long-term performance of load-bearing thermoplastics*. Eindhoven University of Technology, Dissertation, 2015

[Kaw04] KAWAI, M.: A phenomenological model for off-axis fatigue behavior of unidirectional polymer matrix composites under different stress ratios. *Composites: Part A* 35 (2004), S. 955-963

[KKG16] KANTERS, M.J.W.; KUROKAWA, T.; GOVAERT, L.E.: Competition between plasticity-controlled and crack-growth controlled failure in static and cyclic fatigue of thermoplastic polymer systems. *Polymer Testing* 50 (2016), S. 101-110

[KKS+91] SATO, N.; KURAUCHI, T.; SATO, S.; KAMIGAITO, O.: Microfailure behaviour of randomly dispersed short fibre reinforced thermoplastic composites obtained by direct SEM observation. *Journal of Materials Science* 26 (1991) 14, S. 3891-3898

[KLC+20] KUGLER, S.K.; LAMBERT, G.M.; CRUZ, C.; KECH, A.; OSSWALD, T.A.; BAIRD, D.G.: Macroscopic fiber orientation model evaluation for concentrated short fiber reinforced polymers in comparison to experimental data. *Polymer Composites* 41 (2020) 7, S. 2542-2556

[KMA+21] KÖBLER, J.; MAGINO, N.; ANDRÄ, H.; WELSCHINGER, F.; MÜLLER, R.; SCHNEIDER, M.: A computational multi-scale model for the stiffness degradation of short-fiber reinforced plastics subjected to fatigue loading. *Computer Methods in Applied Mechanics and Engineering* 373 (2021), S. 113522

[KS19] KAISER, W.; SCHLACHTER, W.: *Energie in der Kunststofftechnik: Grundlagen und Anwendungen für Ingenieure*. München: Carl Hanser Verlag, 2019

[KSO+18] KÖBLER, J.; SCHNEIDER, M.; OSPALD, F.; ANDRÄ, H.; MÜLLER, R.: Fiber orientation interpolation for the multiscale analysis of short fiber reinforced composite parts. *Computational Mechanics* 61 (2018) 6, S. 729-750

[Kue12] KÜSTERS, K.: *Modellierung des thermo-mechansichen Langzeitverhaltens von Thermoplasten*. RWTH Aachen, Dissertation, 2012 - ISBN: 978-3-86130-513-2

[Lan24] LAND, P.: *Spritzgießen von faserverstärkten Kunststoffen mit drehendem Werkzeugkern: Rheologie - praktische Untersuchungen - Auslegungsmethodik*. Kassel University, Dissertation, 2024

[LC94] LEMAITRE, J.; CHABOCHE, J.-L.: *Mechanics of solid materials*. New York: Cambridge University Press, 1994

[Len16] LENKE, K.: *Kurzfaserverstärktes Polyamid - Charakterisierung der Mikroschädigungsentwicklung unter zweiachsiger mechanischer Last*. Technische Universität Berlin, Dissertation, 2016

[LF99] LAUKE, B.; FU, S.-Y.: Strength anisotropy of misaligned short-fibre-reinforced polymers. *Composites Science and Technology* 59 (1999) 5, S. 699-708

[LK20] LAND, P.; KRUMPHOLZ, T.: Targeted Manipulation of Fibre Orientation Through Relative Movement in an Injection Mould. *Advances in Polymer Processing 2020: Proceedings of the International Symposium on Plastics Technology.* Aachen, Germany, 2020

[LMH87] LANG, R.W.; MANSON, J.A.; HERTZBERG, R.W.: Mechanisms of fatigue fracture in short glass fibre-reinforced polymers. *Journal of Materials Science* 22 (1987) 11, S. 4015-4030

[LMN09] NOURI, H.; MERAGHNI, F.; LORY, P.: Fatigue damage model for injection-molded short glass fibre reinforced thermoplastics. *International Journal of Fatigue* 31 (2009) 5, S. 934-942

[LZY14] LI, X.-P.; ZHAO, G.-Q.; YANG, C.: Effect of mold temperature on motion behavior of short glass fibers in injection molding process. *The International Journal of Advanced Manufacturing Technology* 73 (2014) 5-8, S. 639-645

[McK16] MCKEEN, L.W.: *Fatigue and Tribological Properties of Plastics and Elastomers (Third Edition)*. Kidlington, Cambridge: William Andrew Publishing, 2016

[MFM+15] MORTAZAVIAN, S.; FATEMI, A.; MELLOTT, S.R.; KHOSROVANEH, A.: Effect of cycling frequency and self-heating on fatigue behavior of reinforced and unreinforced thermoplastic polymers. *Polymer Engineering and Science* 55 (2015) 10, S. 2355-2367

[MMJ+10] DE MONTE, M.; MOOSBRUGGER, E.; JASCHEK, K.; QUARESIMIN, M.: Multiaxial fatigue of a short glass fibre reinforced polyamide 6.6 – Fatigue and fracture behaviour. *International Journal of Fatigue* 32 (2010) 1, S. 17-28

[MML+15] MASQUELIER, I.; MARCO, Y.; LE SAUX, V.; CALLOCH, S.; CHARRIER, P.: Determination of dissipated energy fields from temperature mappings on a rubber-like structural sample: Experiments and comparison to numerical simulations. *Mechanics of Materials* 80 (2015), S. 113-123

[MMQ10] MONTE, M.D.; MOOSBRUGGER, E.; QUARESIMIN, M.: Influence of temperature and thickness on the off-axis behaviour of short glass fibre reinforced polyamide 6.6 – cyclic loading. *Composites Part A: Applied Science and Manufacturing* 41 (2010) 10, S. 1368–1379

[MO12] OSSWALD, T.A.; MENGES, G.: *Material Science of Polymers for Engineers*. München: Carl Hanser Verlag, 2012

[Mur12] MURAKAMI, S.: *Continuum Damage Mechanics: A Continuum Mechanics Approach to the Analysis of Damage and Fracture*. Dordrecht, Heidelberg, London, New York: Springer Science+Business Media, 2012

[NLB15] NOTTA-CUVIER, D.; LAURO, F.; BENNANI, B.: Modelling of progressive fibre/matrix debonding in short-fibre reinforced composites up to failure. *International Journal of Solids and Structures* 66 (2015), S. 140-150

[NN08] N.N.: *DIN EN ISO 291: Kunststoffe - Normklimate für Konditionierung und Prüfung*. Berlin, DIN Media GmbH, 2008

[NN12] N.N.: *DIN EN ISO 527-1: Kunststoffe - Bestimmung der Zugeigenschaften - Teil 1: Allgemeine Grundsätze.* Berlin, DIN Media GmbH, 2012

[NN15] N.N.: *Dokumentation Zwick TestControl 2*. Datasheet, Zwick GmbH & Co. KG, Ulm, Germany, 2015

[NN16] N.N.: *DIN 50100: Schwingfestigkeitsversuch - Durchführung und Auswertung von zyklischen Versuchen mit konstanter Lastamplitude für metallische Werkstoffproben und Bauteile*. Berlin, DIN Media GmbH, 2016

[NN19] N.N.: *Pocan B3235 000000, PBT, 30 % Glasfasern, Spritzguss*. Datasheet, Envalior GmbH, Düsseldorf, 2019

[NN90] N.N.: *DIN 53442 - Prüfung von Kunststoffen; Dauerschwingversuch im Biegebereich an flachen Probekörpern*. Berlin, Din Media GmbH, 1990

[Oec16] ÖCHSNER, A.: Continuum Damage and Fracture Mechanics. Singapore: Springer Science+Business Media Singapore, 2016

[OH06] OSSWALD, T.A.; HERNÁNDEZ-ORTIZ, J.P.: *Polymer Processing: Modeling and Simulation*. Müchnen: Carl Hanser Verlag, 2006

[PAK+13] PHELPS, J.H.; ABD EL-RAHMAN, A.I.; KUNC, V.; TUCKER, C.L.: A model for fiber length attrition in injection-molded long-fiber composites. *Composites Part A: Applied Science and Manufacturing* 51 (2013), S. 11-21

[Past19] PASTUKHOV, L.: Long-term performance of fibre-reinforced thermoplastics. Eindhoven University of Technology, Dissertation, 2019

[PB81] PENN, L.S.; BOWLER, E.R.: A new approach to surface energy characterization for adhesive performance prediction. *Surface and Interface Analysis* 3 (1981) 4, S. 161-164

[PCD+20] PIETROGRANDE, R.; CARRARO, P.A.; DE MONTE, M.; QUARESIMIN, M.: Modelling the influence of the microstructure on the high cycle fatigue crack initiation in short fibre reinforced thermoplastics. *Composites Science and Technology* 201 (2021), S. 108533

[PD01] PAEPEGEM, W.V.; DEGRIECK, J.: Modelling Strategies for Fatigue Damage Behaviour of Fibre-reinforced Polymer Composites. *European Journal of Mechanical and Environmental Engineering* 46 (2001) 4, S. 217-227

[PD02] PAEPEGEM, W.V.; DEGRIECK, J.: Coupled Residual Stiffness and Strength Model for Fatigue of Fibre-reinforced Composite Materials. *Composite Science and Technology* 62 (2002) 5, S. 687-696

[PG21a] PASTUKHOV, L.V.; GOVAERT, L.E.: Crack-growth controlled failure of short fibre reinforced thermoplastics: Influence of fibre orientation. *International Journal of Fatigue* 143 (2021). S. 105982

[PG21b] PASTUKHOV, L.V.; GOVAERT, L.E.: Plasticity-controlled failure of fibre-reinforced thermoplastics. *Composites Part B: Engineering* 209 (2021), S. 108635

[PGB+13] PUPURS, A.; GOUTIANOS, S.; BRONDSTED, P.; VARNA, J.: Interface debond crack growth in tension-tension cyclic loading of single fiber polymer composites. *Composites Part a-Applied Science and Manufacturing* 44 (2013), S. 86-94

[Phe09] PHELPS, J.H.: *Processing - Microstructure Models for Short- and Long-Fiber Themoplastic Composite*. University of Illinois at Urbana-Champaign, Dissertation, 2009

[PKE+20a] PASTUKHOV, L.V.; KANTERS, M.J.W.; ENGELS, T.A.P.; GOVAERT, L.E.: Influence of fiber orientation, temperature and relative humidity on the long-term performance of short glass fiber reinforced polyamide 6. *Journal of Applied Polymer Science* (2020), S. 50382

[PKE+20b] PASTUKHOV, L.V.; KANTERS, M.J.W.; ENGELS, T.A.P.; GOVAERT, L.E.: Physical background of the endurance limit in poly(ether ether ketone). *Journal of Polymer Science* 58 (2020) 5, S. 716-736

[PMP+11] PIERANTONI, M.; DE MONTE, M.; PAPATHANASSIOU, D.; DE ROSSI, N.; QUARESIMIN, M.: Viscoelastic material behaviour of PBT-GF30 under thermo-mechanical cyclic loading. *Procedia Engineering* 10 (2011), S. 2141-2146

[PP03] PITARRESI, G.; PATTERSON, E.A.: A review of the general theory of thermoelastic stress analysis. *The Journal of Strain Analysis for Engineering Design* 38 (2003) 5, S. 405-417

[RKD+22] VAN ROO, T.; KOLLING, S.; DILLENBERGER, F.B.; AMBERG, J.: On short glass fiber reinforced thermoplastics with high fiber orientation and the influence of surface roughness on mechanical parameters. *Journal of Reinforced Plastics and Composites* 41 (2022) 7-8, S. 296-308

[Roo24] VAN ROO, T.: *Einfluss der Oberflächenrauigkeit auf die mechanischen Eigenschaften hochorientierter kurzglasfaserverstärkter thermoplastischer Polymere*. Technische Hochschule Mittelhessen (THM), Disseration, 2024

[RSL+16] ROLLAND, H.; SAINTIER, N.; LENOIR, N.; KING, A.; ROBERT, G.: Fatigue mechanisms description in short glass fibre reinforced thermoplastic by microtomographic observations. *Procedia Structural Integrity* 2 (2016), S. 301-308

[RSR+18] ROLLAND, H.; SAINTIER, N.; RAPHAEL, I.; LENOIR, N.; KING, A.; ROBERT, G.: Fatigue damage mechanisms of short fiber reinforced PA66 as observed by in-situ synchrotron X-ray microtomography. Composites Part B: Engineering 143 (2018), S. 217-229

[RV07] RADAJ, D.; VORMWALD, M.: *Ermüdungsfestigkeit - Grundlagen für Ingenieur*. Berlin Heidelberg, Springer-Verlag, 2007

[Sch07] SCHÜRMANN, H.: *Konstruieren mit Faser-Kunststoff-Verbunden*. Berlin, Heidelberg: Springer-Verlag, 2007

[Sch08] SCHIJVE, J.: *Fatigue of Structures and Materials*. Springer Science+Business Media, 2008

[Sch11] SCHOßIG, M.: *Schädigungsmechanismen in faserverstärkten Kunststoffen: Quasistatische und dynamische Untersuchungen*. Wiesbaden: Vieweg+Teubner Verlag, 2010

[Sch17] SCHÖNEICH, M.: *Charakterisierung und Modellierung viskoelastischer Eigenschaften von kurzglasfaserverstärkten Thermoplasten mit Faser-Matrix Interphase*. Universität des Saarlands, Dissertation, 2017

[SDB14+] SPANCKEN, D.; DECKER, J.; BECKER, P.; CONTEELL ASINS, C.; BÜTER, A.: Fatigue Design of Short Fibre Reinforced Polymers. *Proceedings of the 16th European Conference on Composite Materials (ECCM16).* Seville, Spain, 2014

[SDH+14] SCHAAF, A.; MONTE, M.D.; HOFFMANN, C.; VORMWALD, M.; QUARESIMIN, M.: Damage Mechanisms in PBT-GF30 under Thermo-Mechanical Cyclic Loading. *Proceedings of the 29th International Conference of the Polymer Processing Society*. Nürnberg, Germany, 2014

[SM08] SONSINO, C.M.; MOOSBRUGGER, E.: Fatigue design of highly loaded short-glass-fibre reinforced polyamide parts in engine compartments. *International Journal of Fatigue* 30 (2008) 7, S. 1279-1288

[SML+17] SERRANO, L.; MARCO, Y.; LE SAUX, V.; ROBERT, G.; CHARRIER, P.: Fast prediction of the fatigue behavior of short-fiber-reinforced thermoplastics based on heat build-up measurements: application to heterogeneous cases. 29 (2017) 5, S. 1113-1133

[SML+20] SANTHARAM, P.; MARCO, Y.; LE SAUX, V.; LE SAUX, M.; ROBERT, G.; RAOULT, I.; GUÉVENOUX, C.; TAVEAU, D.; CHARRIER, P.: Fatigue criteria for short fiber-reinforced thermoplastic validated over various fiber orientations, load ratios and environmental conditions. *International Journal of Fatigue* 135 (2020), S. 105574

[SO20] SENIOR, A.B.; OSSWALD, T.: Measuring Fiber Length in the Core and Shell Regions of Injection Molded Long Fiber-Reinforced Thermoplastic Plaques. *Journal of Composites Science* 4 (2020) 3, S. 104

[Son04] SONNER, M.: *Schädigungsmechanische Charakterisierung kunststoffvergossener Bauteile - Schädigungslokalisation und Lebensdauervorhersage*. Brandenburgische Technische Universität Cottbus, Dissertation, 2004

[SSK18] STOMMEL, M.; STOJEK, M.; KORTE, W.: *FEM zur Berechnung von Kunststoff- und Elastomerbauteilen*. München: Carl Hanser Verlag, 2018

[SVG16] SWOLFS, Y.; VERPOEST, I.; GORBATIKH, L.: A review of input data and modelling assumptions in longitudinal strength models for unidirectional fibre-reinforced composites. *Composite Structures* 150 (2016), S. 153-172

[SZS15] SCHÖNEICH, M.; ZAMANZADE, M.; STOMMEL, M.: Fiber-matrix interphase in applied short glass fiber composites determined by a nano-scratch method. *Composites Science and Technology* 119 (2015), S. 100-107

[TCH13] TSENG, H.-C.; CHANG, R.-Y.; HSU, C.-H.: Phenomenological improvements to predictive models of fiber orientation in concentrated suspensions. *Journal of Rheology* 57 (2013) 6, S. 1597-1631

[TCH17] TSENG, H.-C.; CHANG, R.-Y.; HSU, C.-H.: Numerical prediction of fiber orientation and mechanical performance for short/long glass and carbon fiber-reinforced composites. *Composites Science and Technology* 144 (2017), S. 51-56

[Tuc22] TUCKER III, C.L.: *Fundamentals of Fiber Orientation*. München: Carl Hanser Verlag, 2022

[TV96] THOMASON, J.L.; VLUG, M.A.: Influence of fibre length and concentration on the properties of glass fibre-reinforced polypropylene: 1. Tensile and flexural modulus. *Composites Part A: Applied Science and Manufacturing* 27 (1996) 6, S. 477-484

[TX07] TAO, G.; XIA, Z.: Mean stress/strain effect on fatigue behavior of an epoxy resin. *International Journal of Fatigue* 29 (2007) 12, S. 2180-2190

[Wil21] WILHELM, F.: *Entwicklung einer Methodik zur Herstellung hochorientierter Probekörper aus kurzfaserverstärkten Thermoplasten zur werkstoffgerechten Untersuchungen von mechanischen Eigenschaften*. Institut für Kunststoffverarbeitung, RWTH Aachen, unveröffentlichte Masterarbeit, 2021 – Betreuer: H. Çelik

[WS12] WARD, I.M.; SWEENEY, J.: *Mechanical Properties of Solid Polymers*. Chichester: John Wiley & Sons, Ltd., 2012

[ZM06] ZHOU, Y.; MALLICK, P.K.: Fatigue performance of an injection-molded short E-glass fiber-reinforced polyamide 6 6, I. Effects of orientation, holes, and weld line. *Polymer Composites* 27 (2006) 2, S. 230–237

[ZT00] ZHAO, F.M.; TAKEDA, N.: Effect of interfacial adhesion and statistical fiber strength on tensile strength of unidirectional glass fiber/epoxy composites. Part I: experiment results. *Composites: Part A* 31 (2000), S. 1203-1214

15 APPENDIX

15.1 Processing parameters for specimen plate production

Parameter	Unit	Value
Cylinder Temperature – Zone 1	[°C]	240
Cylinder Temperature – Zone 1	[°C]	240
Cylinder Temperature – Zone 2	[°C]	245
Cylinder Temperature – Zone 3	[°C]	250
Nozzle Temperature	[°C]	255
Melt Temperature	[°C]	255
Mold Temperature	[°C]	80
Volumetric Flow Rate	[cm³/s]	40
Velocity/Pressure Switch-Over-Point	[cm³]	10
Packing Pressure	[bar]	500
Packing Time	[s]	5
Cooling Time	[s]	32
Cycle Time	[s]	~ 46

Table 15.1: Processing parameters for the manufacturing of the conventional specimen plates.

15.2 Thermodynamic framework for thermo-mechanical interactions during dynamic-cyclic loading

As described in this work, the fatigue behavior of engineering thermoplastics depends on a number of factors (material constitution, morphology, load, frequency, temperature environmental effects, etc.). One of the most important aspects for materials made of polymers is the distinct temperature dependence of material properties and, consequently, the change in mechanical response with temperature. Due to material-specific dissipation mechanisms (friction at the molecular level, plastic deformation, damage, etc.), the material can heat up under mechanical and particularly dynamic-cyclic loads, depending on the type and level of the load and the heat exchange with the environment. For this reason, the framework for the thermomechanical description of systems and, hence, the temperature changes within the material as a function of the main influencing factors are discussed in the following.

Since temperature change is an energetic motivated problem, the relationship for describing temperature is derived from the first law of thermodynamics. This law states the conservation

of energy, postulating that different forms of energy can be converted into each other, but no new energy can be generated or diminished [JW11].

In this work, the material is considered as a solid with a volume B, and there are no mass flows across the system boundaries represented by the surface area ∂B. Hence, the material is treated as a closed system, and the interaction with the environment is described by the exchange of energy over the system's boundaries [KS19, Oec16]. Even though the focus is on composite materials consisting of reinforcing fibers and a polymer matrix, the material properties are considered homogenized at this point according to the principles of continuum mechanics [Oec16]. For simplification reasons, it is also assumed that the material under consideration is static but not rigid. Therefore, kinetic and potential energies can be neglected. The change in temperature over time is of particular interest in the context of this work. Hence, the rate dependent energy balance is used as the foundation for subsequent considerations. Accordingly, the energetic behavior can be described as in Equation 15.1, where the rate of the internal energy $\dot{U}$ corresponds to the sum of the rates of work $\dot{W}$ and heat $\dot{Q}$ [JW11, KS19].

$$\dot{U} = \dot{W} + \dot{Q} \qquad \textit{(Eq. 15.1)}$$

The internal energy U is a thermodynamic potential that describes the total energy of the system, regardless of its form. As a state function, the internal energy U characterizes the state of the system in the current thermodynamic equilibrium and is independent of the path the system has taken to reach that state [LC94]. The rate of the internal energy $\dot{U}$ can be described according to Equation 15.2 as a function of the density ρ, the specific rate of the internal energy $\dot{u}$ and the Volume V.

$$\dot{U} = \int_B \rho\, \dot{u}\, dV \qquad \textit{(Eq. 15.2)}$$

Both work W and heat Q result in changes in the state function and, hence, demonstrate path dependency. Therefore, these quantities are defined as process variables [KS19]. The rate of work $\dot{W}$, which is the total power in a mechanical manner introduced to the system, can be described under continuum mechanics assumptions, considering small strains, using Equation 15.3. Here, $\boldsymbol{\sigma}$ represents the stress tensor, and $\dot{\boldsymbol{\varepsilon}}$ stands for the strain rate tensor [LC94].

$$\dot{W} = \int_B \boldsymbol{\sigma} : \dot{\boldsymbol{\varepsilon}}\, dV \qquad \textit{(Eq. 15.3)}$$

Similarly, the rate of heat $\dot{Q}$ in the considered system is described by the relationship in Equation 15.4. It is comprised of two terms: the heat power r generated by external sources (e.g., inductive heating) and heat flux $\boldsymbol{q}$ through the boundaries of the system ∂B. In this context, the symbol $\boldsymbol{n}$ represents the normal vector to the surface dA. The divergence

relationship can be used to describe the heat flux $\boldsymbol{q}$ as volume-dependent rather than the surface-dependent quantity [LC94, Mur12].

$$\dot{Q} = \int_B r \, dV - \int_{\partial B} \boldsymbol{q}\, \boldsymbol{n} \, dA = \int_B \big(r - div(\boldsymbol{q})\big) \, dV \qquad \textit{(Eq. 15.4)}$$

Given that there are no external energy flows that induce heat internally within the material, it can be assumed that r is negligible. The terms for the rates of work and heat are both inserted into the fundamental Equation 15.1 [BCR14a, LC94].

$$\int_B \rho \, \dot{e} \, dV = \int_B \big(\boldsymbol{\sigma}\colon \dot{\boldsymbol{\varepsilon}} - div(\boldsymbol{q})\big) \, dV \qquad \textit{(Eq. 15.5)}$$

Consequently, Equation 15.6 can be derived to describe the energy balance for the material, since the Volume B is arbitrary.

$$\rho \, \dot{u} = \boldsymbol{\sigma}\colon \dot{\boldsymbol{\varepsilon}} - div(\boldsymbol{q}) \qquad \textit{(Eq. 15.6)}$$

Nevertheless, in order to describe the change in temperature $\dot{T}$ resulting from energy dissipation, it is necessary to consider entropy as an additional state function. The concept of entropy, as articulated by the second law of thermodynamics, describes the inherent irreversibility and directionality of thermodynamic processes.

Since a closed system is considered here, no external entropy can be added or removed by exchange of mass across the system boundary. As a consequence, the change of entropy in the system is only described by the internal entropy production $s_{Prod.}$. It should be noted here that entropy production is zero for reversible processes ($s_{Prod.} = 0$), whereas it is positive for irreversible processes ($s_{Prod.} > 0$). Hence, Equation 15.7 describes the rate of entropy for a closed system.

$$\dot{s}_{Prod.} \geq 0 \qquad \textit{(Eq. 15.7)}$$

The entropy production is inherently correlated with heat flux $\boldsymbol{q}$ at a specific temperature T. The application of the calculation rule for divergence $div\left(\frac{\boldsymbol{q}}{T}\right) = \frac{div(\boldsymbol{q})}{T} - \boldsymbol{q}\frac{grad(T)}{T^2}$ enables the transformation of right part of the Equation 15.8 [Mur12].

$$\rho\dot{s} \geq -div\left(\frac{\boldsymbol{q}}{T}\right) = -\frac{div(\boldsymbol{q})}{T} + \boldsymbol{q}\frac{grad(T)}{T^2} \qquad \textit{(Eq. 15.8)}$$

Then, the first law of thermodynamics in the form of Equation 15.6 can be used to substitute the divergence of the heat flux $div(\boldsymbol{q})$ in Equation 15.8 and consequently multiplied by the temperature T. The resulting Equation 15.9 contains two terms representing state variables (internal energy and entropy) and two process variables (work and heat flow).

$$\rho(T\dot{s} - \dot{u}) + \boldsymbol{\sigma}\colon \dot{\boldsymbol{\varepsilon}} - \boldsymbol{q}\frac{grad(T)}{T} \geq 0 \qquad \textit{(Eq. 15.9)}$$

At this point, the concept of *Helmholtz* free energy ψ is introduced. Equation 15.10 indicates that *Helmholtz* free energy ψ is defined as the difference between the internal energy u and the product of the system's temperature T and entropy s. This term describes the thermodynamic potential of a system that is available to perform work at a constant temperature and volume [LC94, Mur12].

$$\psi = u - Ts \qquad \textit{(Eq. 15.10)}$$

The time derivative of the Equation 15.9. yields the following relationship:

$$\dot{\psi} = \dot{u} - T\dot{s} - \dot{T}s \;\; or \;\; T\dot{s} - \dot{u} = -\left(\dot{T}s + \dot{\psi}\right) \qquad \textit{(Eq. 15.11)}$$

Thus, it can be concluded that this relationship can be used to express the second law of thermodynamics as a function of *Helmholtz* free energy ψ. This resulting Equation 15.12, known as the *Clausius-Duhem* inequality, describes the total dissipation $\mathcal{D}$ in the continuum [LC94, Mur12].

$$\mathcal{D} = \boldsymbol{\sigma}\colon\dot{\boldsymbol{\varepsilon}} - \rho\left(\dot{T}s + \dot{\psi}\right) - \boldsymbol{q}\frac{grad(T)}{T} \geq 0 \qquad \textit{(Eq. 15.12)}$$

In the following, the concept of *Helmholtz* free energy ψ will be explained in more detail in order to gain a more comprehensive understanding of the *Clausius-Duhem* inequality. The thermodynamic state of a material in equilibrium can be completely defined by a number of state variables. These variables can be divided into two categories: external (observable) and internal (hidden) [Mur12]. For instance, in the context of continuum mechanics, temperature T and total strain $\boldsymbol{\varepsilon}$ are external observable variables. In contrast, internal variables are chosen to describe alterations in the internal state of the material. Typical alterations in the material can be changes at the molecular level, of the configuration of dislocations, or of the distribution of defects, for instance [LC94, Mur12]. Consequently, the internal variables are descriptors of dissipative processes occurring within the material. Thus, even though the internal variables are not directly measurable, they can still potentially influence the observable external variables. It is assumed, that the internal variables can be expressed by a set of tensor variable $\boldsymbol{V_k}; k = 1, \dots, n$. The definition of the internal variables is dependent on the phenomena to be investigated in the context of the respective research question. However, the total strain $\boldsymbol{\varepsilon}$ is the sum of elastic and inelastic strain, $\boldsymbol{\varepsilon_e}$ and $\boldsymbol{\varepsilon_p}$. Hence, the inelastic strain $\boldsymbol{\varepsilon_p}$ induces irreversible material changes, it can be also expressed by internal variables $\boldsymbol{V_k}$. Thus, *Helmholtz* free energy ψ and its time derivative $\dot{\psi}$ can be described as a function (compare Equations 15.13 and 15.14) of the external and internal variables [LC94, Mur12].

$$\psi = \psi(\boldsymbol{\varepsilon}, T, \boldsymbol{V_k}) \text{ or } \psi = \psi(\boldsymbol{\varepsilon_e}, T, \boldsymbol{V_k}) \qquad \textit{(Eq. 15.13)}$$

$$\dot{\psi} = \frac{\partial\psi}{\partial\boldsymbol{\varepsilon_e}}\colon\dot{\boldsymbol{\varepsilon}}_{\boldsymbol{e}} + \frac{\partial\psi}{\partial T}\dot{T} + \frac{\partial\psi}{\partial\boldsymbol{V_k}}\colon\dot{\boldsymbol{V}}_{\boldsymbol{k}} \qquad \textit{(Eq. 15.14)}$$

The time derivative of the *Helmholtz's* free energy $\dot{\psi}$ the can now be used in Equation 15.11, which leads to the following relationship for the total dissipation $\mathcal{D}$:

$$\begin{aligned}\mathcal{D} = \rho\left(\boldsymbol{\sigma} - \frac{\partial\psi}{\partial\boldsymbol{\varepsilon_e}}\right):\dot{\boldsymbol{\varepsilon}}_{\boldsymbol{e}} + \boldsymbol{\sigma}:\dot{\boldsymbol{\varepsilon}}_{\boldsymbol{p}} - \rho\frac{\partial\psi}{\partial\boldsymbol{V_k}}:\dot{\boldsymbol{V}}_{\boldsymbol{k}} \\ -\rho\left(s + \frac{\partial\psi}{\partial T}\right)\dot{T} - \boldsymbol{q}\frac{grad(T)}{T} \geq 0\end{aligned} \qquad \textit{(Eq. 15.15)}$$

The equation presented here is universally valid for every thermodynamic process described with the function for the *Helmholtz* free energy in Equation 15.13.

The following Equation 15.16 can be derived for the special case of elastic deformation, i.e. when the boundary conditions are $grad(T) = 0, \dot{\boldsymbol{\varepsilon}}_p = 0, \dot{\boldsymbol{V}}_k = 0$.

$$\left(\boldsymbol{\sigma} - \rho\frac{\partial\psi}{\partial\boldsymbol{\varepsilon_e}}\right):\dot{\boldsymbol{\varepsilon}}_{\boldsymbol{e}} - \rho\left(s + \frac{\partial\psi}{\partial T}\right)\dot{T} \geq 0 \qquad \textit{(Eq. 15.16)}$$

As a consequence, the two thermoelastic laws can be derived in Equation 15.17, where the stress $\boldsymbol{\sigma}$ due to the summation of the elastic and inelastic strain, $\boldsymbol{\varepsilon}_e$ and $\boldsymbol{\varepsilon}_p$ is derived via the different partial derivatives of the respective strains.

$$s = -\frac{\partial\psi}{\partial T}, \qquad \boldsymbol{\sigma} = \rho\frac{\partial\psi}{\partial\boldsymbol{\varepsilon}_e} = \rho\frac{\partial\psi}{\partial\boldsymbol{\varepsilon}} = -\rho\frac{\partial\psi}{\partial\boldsymbol{\varepsilon}_p} \qquad \textit{(Eq. 15.17)}$$

With these two relationships, Equation 15.15 can then be simplified to Equation 15.18, whereby the total dissipation $\mathcal{D}$ is composed of the intrinsic mechanical and thermal dissipation, $\mathcal{D}_{mech.}$ and $\mathcal{D}_{Therm.}$. As previously stated, the inelastic strain $\dot{\boldsymbol{\varepsilon}}_{\boldsymbol{p}}$ can be interpreted as an internal variable $\boldsymbol{V_k}$ and the stress can be expressed by $\boldsymbol{\sigma} = -\rho\frac{\partial\psi}{\partial\boldsymbol{\varepsilon_p}}$. Therefore, the term for the mechanical dissipation can be further simplified. Consequently, any reduction in the *Helmholtz* free energy $\frac{\partial\psi}{\partial\boldsymbol{V_k}}$ leads to an increase in dissipation in the material [Chr12, Mur12].

$$\begin{aligned}\mathcal{D} &= \mathcal{D}_{mech.} + \mathcal{D}_{therm.} \\ &= \left\{\boldsymbol{\sigma}:\dot{\boldsymbol{\varepsilon}}_{\boldsymbol{p}} - \rho\frac{\partial\psi}{\partial\boldsymbol{V_k}}\dot{\boldsymbol{V}}_{\boldsymbol{k}}\right\}_{mech.} + \left\{-\boldsymbol{q}\frac{grad(T)}{T}\right\}_{therm.} \\ &= \left\{-\rho\frac{\partial\psi}{\partial\boldsymbol{V_k}}\dot{\boldsymbol{V}}_{\boldsymbol{k}}\right\}_{mech.} + \left\{-\boldsymbol{q}\frac{grad(T)}{T}\right\}_{therm.} \geq 0\end{aligned} \qquad \textit{(Eq. 15.18)}$$

The heat equation for temperature change $\dot{T}$ is derived by using the law of energy conservation (Equation 15.6) with the definition for the internal energy using the *Helmholtz* free and the entropy, $\dot{u} = \dot{\psi} + \dot{T}s + T\dot{s}$.

$$\rho\dot{\psi} + \rho\dot{T}s + \rho T\dot{s} = \boldsymbol{\sigma}:\dot{\boldsymbol{\varepsilon}} - div(\boldsymbol{q}) \qquad \textit{(Eq. 15.19)}$$

The time derivative of the *Helmholtz* free energy $\dot{\psi}$ and, additionally, the time derivative of the entropy $\dot{s}$ as a function of the *Helmholtz* free energy (Equation 15.20) can then be applied to Equation 15.19.

$$\dot{s} = -\frac{\partial}{\partial t}\frac{\partial \psi}{\partial T} = -\frac{\partial^2 \psi}{\partial T \partial \boldsymbol{\varepsilon_e}} : \dot{\boldsymbol{\varepsilon}}_{\boldsymbol{e}} - \frac{\partial^2 \psi}{\partial T^2}\dot{T} - \frac{\partial^2 \psi}{\partial T \partial \boldsymbol{V_k}} : \dot{\boldsymbol{V}}_{\boldsymbol{k}} \qquad \textit{(Eq. 15.20)}$$

The following Equation 15.21 results from the preceding equations.

$$\begin{aligned} &\rho\left(\frac{\partial \psi}{\partial \boldsymbol{\varepsilon_e}} : \dot{\boldsymbol{\varepsilon}}_{\boldsymbol{e}} + \frac{\partial \psi}{\partial T}\dot{T} + \frac{\partial \psi}{\partial \boldsymbol{V_k}} : \dot{\boldsymbol{V}}_{\boldsymbol{k}}\right) \\ &\qquad + \rho \dot{T} s \\ &+\rho\left(-T\frac{\partial^2 \psi}{\partial T \partial \boldsymbol{\varepsilon_e}} : \dot{\boldsymbol{\varepsilon}}_{\boldsymbol{e}} - T\frac{\partial^2 \psi}{\partial T^2}\dot{T} - T\frac{\partial^2 \psi}{\partial T \partial \boldsymbol{V_k}} : \dot{\boldsymbol{V}}_{\boldsymbol{k}}\right) = \boldsymbol{\sigma} : \dot{\boldsymbol{\varepsilon}} - div(\boldsymbol{q}) \end{aligned} \qquad \textit{(Eq. 15.21)}$$

The aforementioned Equation 15.21 can then be simplified by applying the thermoelastic relationships for stress $\boldsymbol{\sigma} = -\rho\frac{\partial \psi}{\partial \boldsymbol{\varepsilon}_e}$ and entropy $\frac{\partial \psi}{\partial T} = -s$, in addition to the introduction of heat capacity at constant strain, $c_\varepsilon = T\frac{\partial s}{\partial T}$. It should be noted that the heat capacity at constant strain c_ε is often considered similar to the heat capacity at constant volume $c_{\boldsymbol{v}}$. However, the heat capacity at constant strain c_ε is approximated by the heat capacity at constant pressure c_p here for simplicity, since the experimental determination of c_v is difficult [Mur12].

$$\begin{aligned} \rho c_p \dot{T} = &\left\{\boldsymbol{\sigma} : \dot{\boldsymbol{\varepsilon}}_{\boldsymbol{p}} - \rho\left(\frac{\partial \psi}{\partial \boldsymbol{V_k}} : \dot{\boldsymbol{V}}_{\boldsymbol{k}}\right)\right\}_{mech.} + \{-div(\boldsymbol{q})\}_{therm.} \\ &+ \left\{T\left(\frac{\partial \boldsymbol{\sigma}}{\partial T} : \dot{\boldsymbol{\varepsilon}}_{\boldsymbol{e}} + \rho\frac{\partial^2 \psi}{\partial T \partial \boldsymbol{V_k}} : \dot{\boldsymbol{V}}_{\boldsymbol{k}}\right)\right\}_{therm-mech.} \end{aligned} \qquad \textit{(Eq. 15.22)}$$

Equation 15.22 enables the description of temperature changes $\dot{T}$ as a function of the continuum mechanical processes occurring within the material in a thermodynamically manner. In the context of continuum mechanics, it is important to note that this relationship assumes that the temperature is uniform $grad(T) = 0$ throughout the continuum. The first two terms on the right-hand side of Equation 15.22 describe the mechanical dissipative components that lead to an increase in temperature. The temperature is also influenced by the heat exchange with the environment, which is described by heat flux $div(\boldsymbol{q})$. In addition, there are two terms that describe the thermomechanical couplings. The term $T\frac{\partial \boldsymbol{\sigma}}{\partial T} : \dot{\boldsymbol{\varepsilon}}_{\boldsymbol{e}}$ represents the thermoelastic coupling within the material. This term accounts for the effect of temperature on the stress response during elastic deformation. When a load is applied to the material, a decrease in temperature is observed. The last term $\rho T\frac{\partial^2 \psi}{\partial T \partial \boldsymbol{V_k}} : \dot{\boldsymbol{V}}_{\boldsymbol{k}}$ describes the interaction between temperature change and internal processes within the material [Chr12, Mur12].

LEBENSLAUF

Persönliche Daten

Name	Hakan Çelik
Geburtsdatum	14.05.1989
Geburtsort	Wuppertal

Berufserfahrung

Seit 2022	**Abteilungsleiter**
	Strukturberechnung und Werkstofftechnik
	Institut für Kunststoffverarbeitung (IKV) an der RWTH-Aachen
2017 – 2022	**Wissenschaftlicher Mitarbeiter**
	Betriebsfestigkeit und Vibroakustik technischer Thermoplaste
	Institut für Kunststoffverarbeitung (IKV) an der RWTH-Aachen
2012 – 2016	**Studentische Hilfskraft**
	Institut für Kunststoffverarbeitung (IKV) an der RWTH-Aachen
2013	**Praktikant**
	Produktions- und Werkstofftechnik, Kunststofftechnologie
	Mercedes-Benz Group AG, Sindelfingen
2010 – 2012	**Studentische Hilfskraft**
	Institut für Allgemeine Mechanik (IAM) der RWTH-Aachen

Ausbildung

2017 – 2025	**Promotionsstudium**
	RWTH-Aachen University
2016 – 2017	**Master of Science, Kunststoff- und Textiltechnik**
	Fachrichtung Kunststofftechnik
	RWTH-Aachen University
2017	**Visiting Scholar**
	zur Anfertigung der Masterarbeit
	University of Wisconsin-Madison, USA
2009 – 2016	**Bachelor of Science, Maschinenbau**
	Fachrichtung Kunststofftechnik
	RWTH-Aachen University
2014 - 2015	**Forschungspraktikum**
	zur Anfertigung der Bachelorarbeit
	National University of Ireland Galway (NUIG), Irland